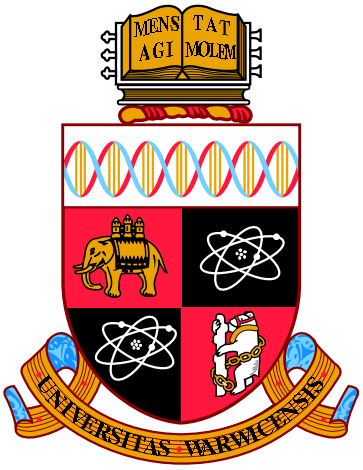

Quasi-Periodic Pulsations in Solar and Stellar Flares

by

Chloë Emma Pugh

Thesis

Submitted to the University of Warwick

for the degree of

Doctor of Philosophy

Department of Physics

April 2018

THE UNIVERSITY OF WARWICK

Contents

List of Tables

List of Figures

Acknowledgments

Firstly I would like to give a huge thank you to my supervisors, Prof Valery Nakariakov and Dr Anne-Marie Broomhall, for their guidance and continued support. Thank you also to my colleagues in the Centre of Fusion, Space and Astrophysics—in particular those who I shared an office with—who have provided many interesting discussions over the years. I am also grateful to my wonderful family and friends for their endless support.

Declarations

This thesis is submitted to the University of Warwick in support of my application for the degree of Doctor of Philosophy. It has been composed by myself and has not been submitted in any previous application for any degree or other university.

The work presented was carried out by the author except in the cases outlined below: the *Vernov*/DRGE data used in Chapter 5 were provided and prepared by A. V. Bogomolov and I. N. Myagkova. The stellar rotation periods used in Chapter 6 were determined by D. J. Armstrong.

The work presented in this thesis is based on the following peer-reviewed journal articles (4 published, 0 submitted):

- Pugh, C. E., Nakariakov, V. M., Broomhall, A.-M. (2015), "A multi-period oscillation in a stellar superflare", *Astrophysical Journal Letters*, 813, L5
- Pugh, C. E., Armstrong, D. J., Nakariakov, V. M., Broomhall, A.-M. (2016), "Statistical properties of quasi-periodic pulsations in white-light flares observed with *Kepler*", *Monthly Notices of the Royal Astronomical Society*, 459, 3659
- Pugh, C. E., Broomhall, A.-M., Nakariakov, V. M. (2017), "Significance testing for quasi-periodic pulsations in solar and stellar flares", *Astronomy & Astrophysics*, 602, A47
- Pugh, C. E., Nakariakov, V. M., Broomhall, A.-M., Bogomolov, A. V., Myagkova, I. N. (2017), "Properties of quasi-periodic pulsations in solar flares from a single active region", *Astronomy & Astrophysics*, 608, A101

Abstract

Quasi-periodic pulsations (QPPs) are a phenomenon commonly observed in solar flares, and are also occasionally observed in stellar flares. They are time variations in the intensity of the flare emission that repeat with approximately constant timescales, or timescales that increase or decrease monotonically in the special case of non-stationary QPPs. There are two main reasons for the interest in QPPs. First is the potential for the diagnosis of plasma parameters in the corona, such as the magnetic field strength and plasma density, which are otherwise difficult to observe directly. If the mechanism causing the QPPs can be inferred, then they would join MHD oscillations of coronal loops as a coronal seismology tool (e.g. Nakariakov & Ofman 2001). Secondly, since QPPs have been found to be a common phenomenon in flares, flares cannot be fully understood without knowing the origin of QPPs. This thesis presents statistical studies of QPPs in both solar and stellar flares, with the aim of learning more about the nature of this phenomenon.

The robust detection of QPPs in solar and stellar flares has been the topic of recent debate. In light of this, this thesis shows how a statistical method described by Vaughan (2005), originally developed to test for the presence of periodic variations of the X-ray emission from Seyfert galaxies, can be adapted to aid with the search for QPPs in flare time series data. The method identifies statistically significant periodic signals in power spectra, and properly accounts for red noise as well as the uncertainties associated with the data. The method has been further developed to be used with rebinned power spectra, allowing QPPs whose signal is spread over more than one frequency bin to be detected. An advantage of this method is that there is no need to detrend the data prior to creating the power spectrum. Examples are given where the method has been applied to synthetic data, as well as real flare data from the *Nobeyama Radioheliograph* (NoRH). These show that, despite the transient nature of QPPs, peaks corresponding to the QPPs can be detected at a significant level in the power spectrum without any processing of the original time series data, providing the background trends are not too steep.

The properties of a set of solar flares originating from a single active region (AR) that exhibit QPPs were investigated. In particular, any indication of QPP periods relating to AR properties was searched for, as might be expected if the characteristic timescale of the pulsations corresponds to a characteristic length scale of the flaring structure. The three AR properties used for this study were the area, bipole separation distance, and average magnetic field strength, which were all measured at the photosphere using SDO/HMI magnetogram data. The AR studied,

best known as NOAA 12192, was unusually long-lived and persisted for over three Carrington rotations. During this time a total of 181 flares were observed by GOES. Data from the GOES, SDO/EVE, *Fermi*, *Vernov* and NoRH observatories were used to determine if QPPs were present in the flares. For the soft X-ray GOES and EVE data, the time derivative of the signal was used so that any variability in the impulsive phase of the flare was emphasised. Power spectra of the time series data, without any form of detrending, were inspected and flares with a peak above the 95% confidence level in the power spectrum were labelled as having candidate QPPs. The confidence levels were determined taking full account of data uncertainties and the possible presence of red noise. A total of 37 flares (20% of the sample) showed good evidence of having stationary or weakly non-stationary QPPs, and some of the pulsations can be seen in data from multiple instruments and in different wavebands. Because of the conservative detection method used, this may be a lower bound for the true number of flares with QPPs. The fact that a substantial fraction of the flare sample showed evidence of QPPs, using a strict detection method with minimal processing of the data, demonstrates that these QPPs are a real phenomenon that cannot be explained by the presence of red noise or the superposition of multiple unrelated flares. No correlations were found between the QPP periods and the AR area, bipole separation distance, or average magnetic field strength. This lack of correlation with the AR properties implies that the small-scale structure of the AR (which was not accounted for in this study) is important and/or that different QPP mechanisms act in different cases.

Flares that are orders of magnitude larger than the most energetic solar flares have been observed on Sun-like stars, raising the question of whether the same physical processes are responsible for both solar and stellar flares, and hence whether the Sun is capable producing a devastating superflare. A study of QPPs in the decline phase of white-light stellar flares observed by *Kepler* was embarked upon. Out of the 1439 flares on 216 different stars detected in the short-cadence data using an automated search, 56 flares were found to have QPP-like signatures in the light curve, of which 11 had stable decaying oscillations. No correlation was found between the QPP period and the stellar temperature, radius, rotation period, or surface gravity, suggesting that the QPPs are independent of global stellar parameters. Hence they are likely to be the result of processes occurring in their local environment. There was also no significant correlation between the QPP period and flare energy, while there was evidence that the period scales with the QPP decay time for the Gaussian damping scenario, but not to a significant degree for the exponentially damped case. This same scaling has been observed for MHD oscillations on the Sun, suggesting that they could be the cause of the QPPs in those flares. Scaling laws of the flare energy were also investigated, supporting previous reports of a strong correlation between the flare energy and stellar temperature/radius. Additional analysis was performed on one flare with a rare multi-period QPP pattern. Two periodic signals were identified using the wavelet and autocorrelation techniques. The presence of multiple periods is an indication that the QPPs might have been caused by magnetohydrodynamic oscillations, and suggests that the physical processes operating during stellar flares could be the same as those in solar flares.

Abbreviations

AIA	Atmospheric Imaging Assembly
AR	Active Region
CCD	Charge-Coupled Device
CME	Coronal Mass Ejection
DFT	Discrete Fourier Transform
d.o.f.	degrees of freedom
DRGE	Detector of the Roentgen and Gamma-ray Emissions
ESA	European Space Agency
ESP	Extreme Ultraviolet Spectrophotometer
EUV	Extreme Ultraviolet
EVE	Extreme Ultraviolet Variability Experiment
GALEX	Galaxy Evolution Explorer
GBM	Gamma-ray Burst Monitor
GOES	Geostationary Operational Environmental Satellite
HMI	Helioseismic and Magnetic Imager
HXR	Hard X-ray
IDL	Interactive Data Language
KIC	Kepler Input Catalog

LS	Lomb-Scargle
MCMC	Markov chain Monte Carlo
MHD	Magnetohydrodynamic
NAOJ	National Astronomical Observatory of Japan
NASA	National Aeronautics and Space Administration
NOAA	National Oceanic and Atmospheric Administration
NoRH	Nobeyama Radioheliograph
NoRP	Nobeyama Radio Polarimeters
PDCSAP	Pre-search Data Conditioning Simple Aperture Photometry
QPF	Quasi-Periodic Propagating Fast Magnetoacoustic Waves
QPP	Quasi-Periodic Pulsation
RHESSI	Reuven Ramaty High Energy Solar Spectroscopic Imager
SAP	Simple Aperture Photometry
SDO	Solar Dynamics Observatory
SMART	Solar Monitor Active Region Tracking
SWPC	Space Weather Prediction Centre
SXR	Soft X-ray
TESS	Transiting Exoplanet Survey Satellite
TRACE	Transition Region and Coronal Explorer
XMM-Newton	X-ray Multi-Mirror Mission
XRS	X-ray Sensor

Chapter 1

Introduction

1.1 The structure of the Sun and stars

The Sun is a middle-aged main sequence dwarf star with a mass $M_\odot \approx 1.99 \times 10^{30}$ kg and a radius $R_\odot \approx 6.96 \times 10^8$ m (Severino 2017). An overview of the main structural features of the Sun is shown in Fig 1.1. In the centre is the extremely hot and dense core, where nuclear fusion converts hydrogen to helium and releases vast amounts of energy in the process. The core extends out to $\sim 0.25\,\mathrm{R}_\odot$. Above the core is the radiative zone, which extends out to $\sim 0.7\,\mathrm{R}_\odot$ and is the region where the dominant energy transfer mechanism is thermal radiation. Then the ~ 0.7–$1\,\mathrm{R}_\odot$ region is referred to as the convective zone, where the lower temperature and density mean that convection is the dominant energy transfer mechanism. Between the radiative and convective zones lies a transition layer called the tachocline. The transition in this layer is between the rigid-body rotation of the radiative zone and the differential rotation, where there is a latitudinal dependence of the rotation rate, of the convective zone. Hence there is a strong shear motion within this layer. The tachocline is believed to play a crucial role in the generation of the Sun's magnetic field through a dynamo process.

The solar atmosphere can be divided into four main regions: the photosphere, chromosphere, transition region, and corona. At the base of the atmosphere is the photosphere, the layer below which the Sun is opaque to visible light. Hence the photosphere is the solar surface as viewed in visible light. Images of the photosphere reveal a granular structure, where the granules are the tops of convection cells in the convective zone. The granules are brighter in the centre where hot gas rises from below, and darker around the edges where the gas has cooled and sinks back down. The effective temperature is measured from the light emitted from the photosphere, and has a value of 5,778 K (Severino 2017). The temperature decreases with height and reaches a minimum value of around 4,000 K in the temperature minimum region between the photosphere and chromosphere (Vernazza et al. 1976),

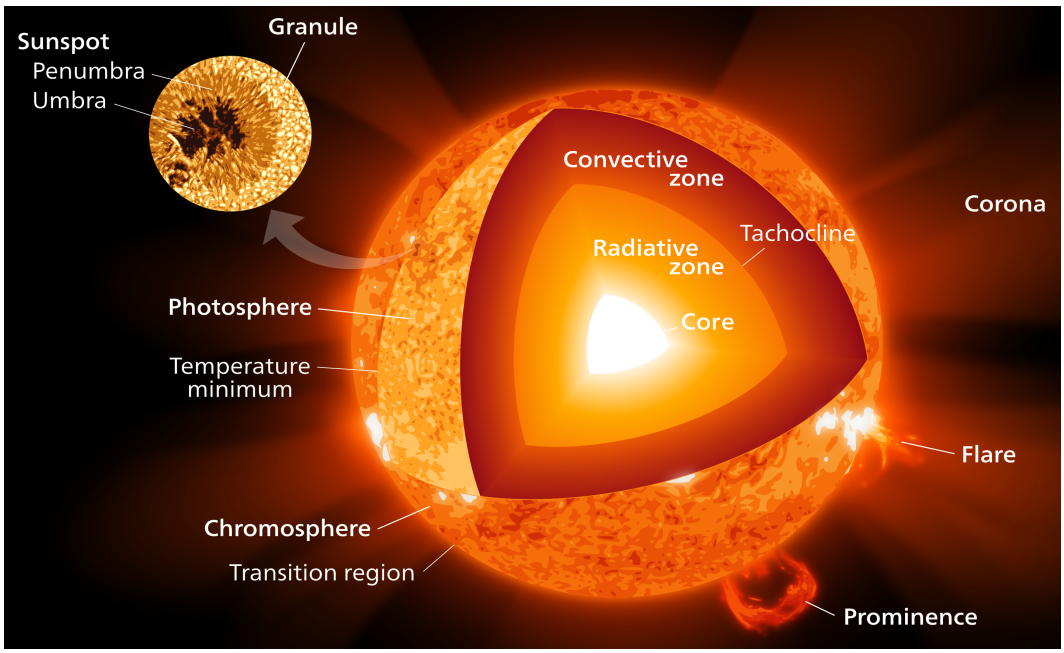

Figure 1.1: Interior and exterior structure of the Sun. *Image courtesy of Wikimedia Commons.*

above which it rises dramatically. The chromosphere is spectroscopically distinct from the photosphere as it is dominated by emission lines rather than absorption lines: in particular the Hα line and the Ca II H and K lines, the wavelengths of which are very suitable for viewing the chromosphere. When viewed using one of these spectroscopic emission lines, the chromosphere appears to have a dynamic 'hairy' structure, where the 'hairs' are short-lived jets of cool plasma and are referred to as spicules when viewed off-limb or fibrils when viewed on-disk (e.g. Judge et al. 2011). The chromosphere and corona are separated by the transition region, where the temperature increases from around 20,000 K to 1 MK and the density decreases by around two orders of magnitude. The mechanism of this dramatic rise in temperature is one of the great mysteries of solar physics, and popular explanations are heating by magnetohydrodynamic (MHD) waves or nanoflares (Narain & Ulmschneider 1990). Finally the outermost region of the Sun is the corona, where the material is in a plasma state and hence the magnetic field plays an important role in determining the structure. The complex and dynamic magnetic field in the corona is made up of a combination of closed and open magnetic field lines. The closed field lines, anchored inside the Sun, tend to be concentrated around active regions (see Section 1.1.1), while the open field lines connect to the interplanetary magnetic field and ultimately the interstellar magnetic field. The energy distribution of the hot plasma in the corona means a small fraction of particles will have enough energy to overcome the Sun's gravity and stream away into space. This continuous stream

Table 1.1: Harvard spectral classes of stars.

Class	Effective Temperature (Kelvin)
O	$\geq$ 30,000
B	10,000–30,000
A	7,500–10,000
F	6,000–7,500
G	5,200–6,000
K	3,700–5,200
M	2,400–3,700

of charged particles from the Sun is called the solar wind.

The majority of main sequence stars also have a core, radiative zone, and convective zone, although the relative thicknesses of the internal layers may vary substantially according to the mass of the star. Stars are classified according to the Harvard spectral classification system (Cannon & Pickering 1901; Payne 1925), which divides stars up based on the effective temperature derived from their spectrum, as shown in Table 1.1. The letter classes may be subdivided into ten numerical classes between 0 and 9, where 0 is hot and 9 is cool. According to this the Sun can be classed as a G2 dwarf star. Cooler stars have deeper convection zones relative to their size than hotter stars, with low-mass M dwarf stars ($\lesssim 0.35\,M_{\odot}$) being fully convective (e.g. Dorman et al. 1989; Chabrier & Baraffe 1997). Stars with a mass, M, in the range $0.35\,M_{\odot} \lesssim M \lesssim 1.5\,M_{\odot}$ have a similar structure to the Sun, with a radiative zone above the core and a convective zone above the radiative zone. Hotter and more massive stars have a thinner convective zone relative to their size, and the convective zone lies between the radiative zone and the core. Stars hotter than A-type lack a convective zone all together (Smalley 2004).

As a solar-type main sequence star evolves it eventually depletes the hydrogen in the centre, and hydrogen fusion continues in a shell around a helium core. The increasing mass of the helium core causes it to contract and increase in temperature, hence increasing the rate of fusion in the hydrogen-burning shell. As a result the star expands enormously and becomes more luminous; this is the red giant phase, and stars in this phase tend to a have a spectral type of K or M. Eventually the helium core becomes hot enough to initiate helium fusion, which continues until the helium in the core has been converted to carbon. Again the increasingly massive core contracts and heats up until it can be supported by electron degeneracy pressure. This carbon core forms a white dwarf star, while the helium and hydrogen-burning shells continue to expand until they eventually leave the star completely and become a planetary nebula. The different stages of a star's life are

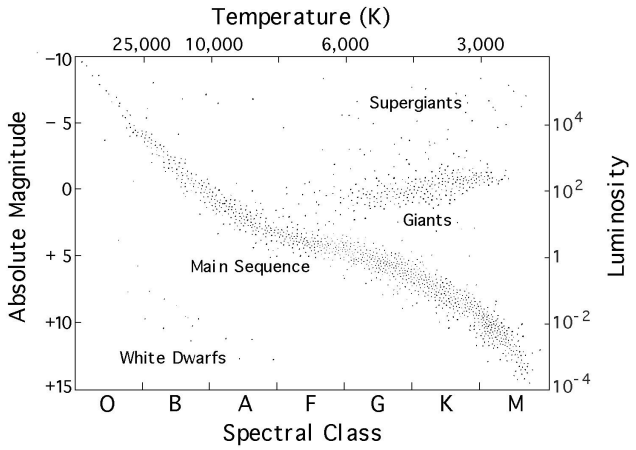

Figure 1.2: Hertzsprung Russell diagram showing populations of different kinds of stars, which can be distinguished based on their effective temperature and luminosity. *Image courtesy of NASA Goddard Space Flight Centre.*

characterised by different effective temperatures and luminosities, and as such the three main phases of a typical main sequence star's life can be seen as three different regions on the Hertzsprung-Russell diagram, as shown in Fig. 1.2. The universe is not old enough for the oldest low-mass stars to have evolved off the main sequence, but stellar evolution models suggest that low-mass stars ($< 0.5\,M_{\odot}$) cannot fully progress though the red giant phase as they cannot reach the necessary conditions for helium fusion in their core, and the lowest mass stars may bypass the red giant phase altogether. On the other hand, higher mass stars ($> 8\,M_{\odot}$) continue fusing elements in the core until iron is formed. The fusion of iron and heavier elements consumes energy rather than releasing it, so once iron is formed in the core there is no longer the thermal pressure required to balance gravity and a core-collapse supernova explosion occurs. The supernova remnant is either a neutron star or a black hole, depending on the original star's mass.

1.1.1 Solar and stellar active regions

Solar active regions (ARs) are regions of enhanced magnetic field strength, visible on or above the solar surface, that tend to appear at mid-latitudes. Typical lifetimes for ARs range from a few days to a few months, with larger ARs being longer lived than smaller ARs. In the photosphere (viewed at visible wavelengths), stronger ARs appear as a group of one or more dark sunspots accompanied by bright faculae. Weaker ARs may just appear as a cluster of faculae. Sunspots indicate regions of concentrated magnetic field, where a typical magnetic field strength in the centre of the spot is 3,000 G (Solanki 2003), and they can be split into two regions: an inner umbra and outer penumbra (see Fig. 1.1). Strong magnetic fields inhibit convec-

tion, so hot gas is slower to rise and cool gas is slower to sink, hence the gas inside a sunspot is cooler (with a temperature around 4,000 K) than in the surrounding photosphere (where the temperature is around 5,800 K). This cooler temperature means that the sunspot appears less bright than the surrounding photosphere. Because sunspots can be seen from the ground, reports of them have appeared in literature going back thousands of years. More complete records of the number of sunspots on the solar disk date back to the 17^{th} century. These provide information about historical activity levels of the Sun, and reveal an approximately 11 yr long activity cycle: referred to as the solar cycle (Hathaway 2010). Faculae are the next most obvious feature in visible-light images of the Sun. They appear bright in the photosphere and chromosphere (Steiner 2005), and indicate regions of more dispersed magnetic field. Because the number of faculae outnumbers the number of sunspots, during periods of greater solar activity the total solar irradiance is higher (Willson & Hudson 1988).

Higher up in the solar atmosphere, ARs appear bright where the strong magnetic field traps hot plasma. Because of this hot plasma, extreme ultraviolet (EUV) and soft X-ray (SXR) wavelengths tend to be best for viewing ARs in the chromosphere and corona. The most obvious structures associated with ARs in the solar atmosphere are coronal loops, which are magnetic flux tubes with a higher density of hot plasma inside than outside. These loops have their footpoints anchored in the photosphere and connect regions of opposite magnetic polarity. Coronal loops can either connect sunspots/faculae within an AR, or they can connect other separated regions of concentrated magnetic flux (that do not necessarily constitute an AR).

The formation of solar ARs stems from the dynamo process operating in the convective zone. Rotation and convective motions of the electrically conducting plasma induce and constantly regenerate the magnetic field, and so the solar magnetic field is continuously evolving. It can be thought of as beginning as an approximately bipolar poloidal field that is distorted by differential rotation (Bushby & Mason 2004). This distortion in the azimuthal direction generates a toroidal magnetic field, and when the toroidal field is strong enough some of the magnetic flux can become buoyant and rise towards the surface as a loop (see Fig.1.3). As the loops rise they are twisted by the Coriolis force, and this regenerates the poloidal magnetic field. This play off between the poloidal and toroidal magnetic field components is thought to be the source of the 11 yr solar cycle. The weaker buoyant magnetic flux elements will be dissipated by the turbulent motions in the convective zone, while those that are strong enough will penetrate through the surface and form a bipolar AR. ARs will eventually decay, mainly through Ohmic dissipation and flux cancellation processes. Flux cancellation is a combination of magnetic reconnection (see Section 1.2.2) and flux submergence, where very small and highly curved flux

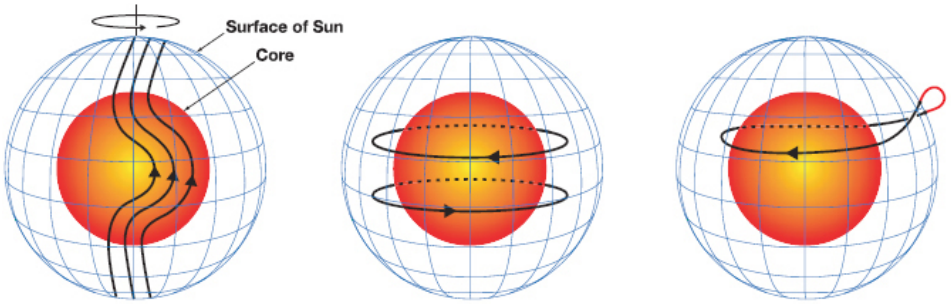

Figure 1.3: *Left:* Poloidal field lines being distorted and sheared in the azimuthal direction in the tachocline. *Middle:* The toroidal field generated from the shearing of the poloidal field. *Right:* Parts of the toroidal field can become buoyant and form loops of magnetic flux that rise towards the surface, twisting as they go. *Image adapted from Dikpati & Gilman (2007).*

elements retract back down due to the magnetic tension force overcoming magnetic buoyancy (Green et al. 2011; Van Driel-Gesztelyi & Green 2015).

A feature in the corona associated with ARs is a prominence (if viewed off-limb) or filament (if viewed on-disk). They are large strands of cool, dense plasma suspended by the magnetic field, and if viewed at wavelengths corresponding to chromospheric emission lines they appear bright when off-limb and dark when on-disk. The dark on-disk appearance is a result of the high density and cool temperature, meaning that the plasma is only partially ionised, causing the filament to be optically thick to many of the chromospheric emission line wavelengths (Parenti 2014). At hotter wavelengths, more suited to viewing the corona, prominences cannot be seen off-limb but they can still be seen as dark absorption features on-disk. Filaments are always directly above magnetic polarity inversion lines (which separate regions of opposite magnetic polarity), and the eruption of filaments/prominences is closely linked to solar flares (see Section 1.2.2) and coronal mass ejections (CMEs).

The two most notable and most energetic eruptive phenomena associated with solar ARs are solar flares and CMEs. Since flares are the main topic of this thesis they are discussed in detail in Section 1.2. CMEs are huge expulsions of coronal material with speeds ranging from less than 100 to over 1,000 km/s (Gosling et al. 1976), and are thought to result from a sudden reorientation of the coronal magnetic field (Gopalswamy et al. 2006). Coronagraph images reveal that CMEs expand to cover a greater area than the solar disk (Webb & Howard 2012). Although CMEs have long been known to be associated with solar flares—with the likelihood of a CME occurring increasing with more powerful flares (e.g. Kahler 1992; Yashiro et al. 2005)—the relationship is complex, as some powerful flares have been observed without accompanying CMEs (Sun et al. 2015) and some CMEs without accompanying flares (Munro et al. 1979).

Many stars show brightness modulations that are thought to be associated with the presence of ARs, since these modulations are associated with other proxies of magnetic activity (see Sections 1.2.3 and 1.2.4). Whether starspots or faculae are the dominant source of modulation depends on how active the star is, with the more active stars thought to have starspot dominated brightness modulation (Lockwood et al. 2007). For stars with clear sinusoidal modulations of the brightness, Notsu et al. (2015b) verified that these modulations allow the rotation period of the star to be estimated from photometric data, rather than requiring spectroscopic data.

1.2 Solar and stellar flares

Flares are sudden enhancements of emitted electromagnetic radiation and high energy charged particles from a region of strong magnetic field on the Sun/star, lasting from a few minutes to several hours. The first recorded observation of a solar flare was made by Carrington (1859) and Hodgson (1859), while both astronomers were independently studying a group of sunspots on a projected image of the Sun. Two patches of white light, brighter than the rest of the solar surface, appeared before them, then disappeared after five minutes. The appearance of white light emission during a solar flare is now known to be a fairly rare occurrence, and tends to be associated with the most energetic flares. The energy of this flare, referred to as the Carrington Flare, has retrospectively been estimated to be around 10^{32} erg, making it one of the most powerful solar flares ever observed. The effects of this flare and an associated CME were noticed on Earth, with intense aurorae visible at far lower latitudes than usual, and widespread failures of the telegram system (Green & Boardsen 2006). The measured disturbance of the Earth's magnetic field in the hours after the flare led both Carrington and Hodgson to suspect that there might be a link. Technological advancements mean that the Sun can now be monitored continuously from space, and huge numbers of solar flares have been observed since the beginning of the space age. The following section discusses the main features of flare observations.

1.2.1 Observational features of solar flares

Flare time profiles are mainly characterised by two phases: the impulsive phase and decay phase. During the impulsive phase, charged particles are accelerated to very high energies, resulting in non-thermal emission in the form of microwave radiation via the gyrosynchrotron mechanism, and hard X-ray (HXR) radiation via bremsstrahlung. Hence, during a flare the overall solar flux measured in HXR and certain microwave wavebands may be dominated by the emission produced by these non-thermal particles. This sudden release of energy results in heating and

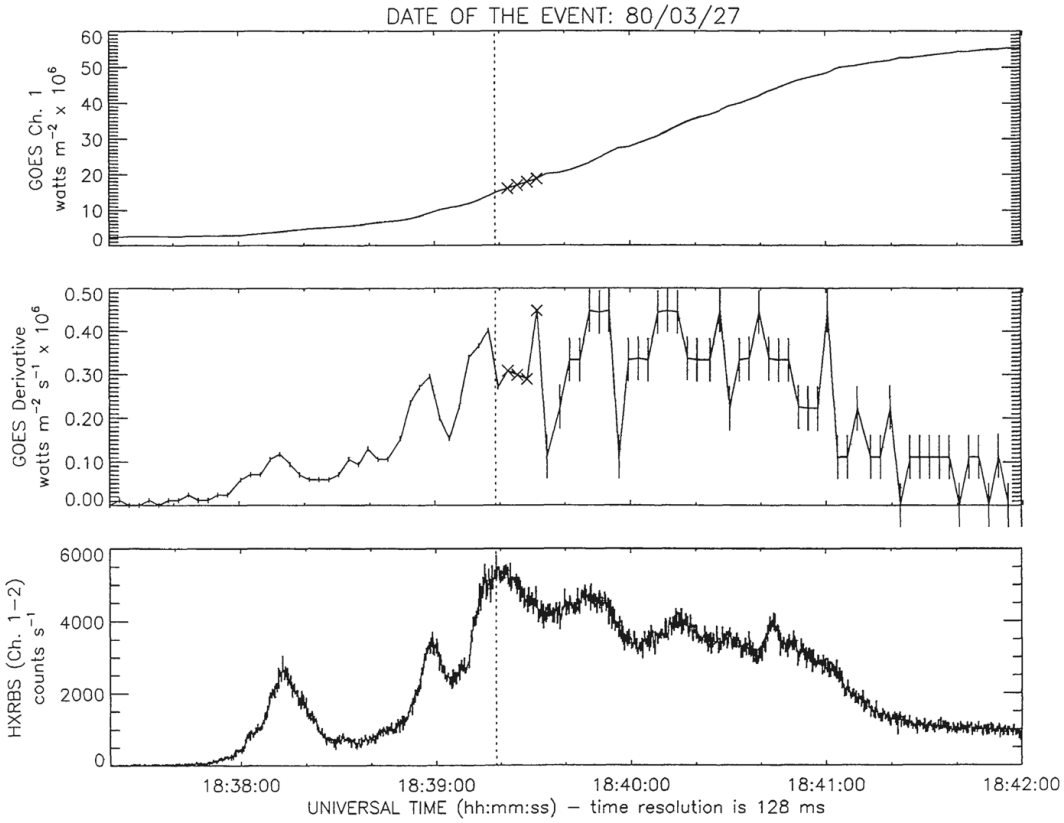

Figure 1.4: An example of the time profile of a flare and the Neupert effect. *Top*: Part of the SXR light curve observed by GOES in the 1–8 Å waveband during the impulsive phase of the flare. *Middle*: The time derivative of the above light curve. *Bottom*: The corresponding HXR light curve observed by the HXR Burst Spectrometer aboard the Solar Maximum Mission satellite in the 26–51 keV waveband. A correlation can be seen between HXR time profile and the derivative of the SXR profile, which is referred to as the Neupert effect. *Image courtesy of Dennis & Zarro (1993).*

the emission of thermal SXR, which peaks at the end of the impulsive phase and declines during the decay phase, and EUV radiation, which peaks shortly after the SXR emission (Benz 2017). The time integral of the microwave and HXR emission has been shown to correlate with the SXR emission during the impulsive phase in the majority of flares (see Fig. 1.4 for an example). This behaviour is known as the Neupert effect (Neupert 1968).

The most standardised classification system for solar flares is based on the peak intensity of the flare in the 1–8 Å waveband, as measured by the X-ray sensor (XRS) instrument aboard one of the GOES satellites (more information on the GOES satellites and the XRS instruments is given in Chapter 2). The different intensity categories are represented by different letters, as defined in Table 1.2, and the letters are usually accompanied by a number that indicates the strength

Table 1.2: GOES flare classes and the corresponding peak fluxes in the 1–8 Å waveband.

Class	Peak flux (Wm^{-2})
A	$< 10^{-7}$
B	10^{-7} up to 10^{-6}
C	10^{-6} up to 10^{-5}
M	10^{-5} up to 10^{-4}
X	$> 10^{-4}$

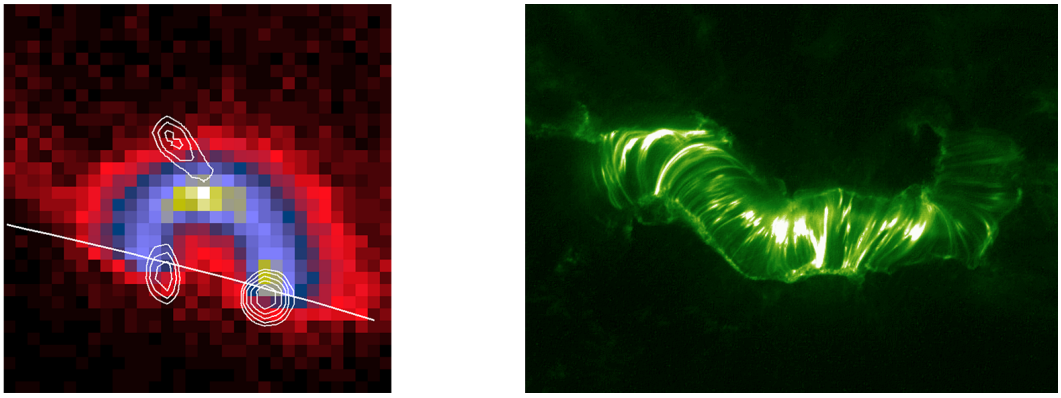

Figure 1.5: *Left*: A compact flare observed side-on by Yohkoh, with the colours representing SXR emission from the post-flare loop (red is weak emission, blue is medium, and yellow is strong), and the contour lines HXR emission from the loop footpoints and above the top of the loop. *Right*: A two ribbon flare arcade viewed from above, observed by TRACE in the 195 Å waveband on 2000 July 14. This flare is known as the Bastille Day flare, and has gained fame thanks to the formation of a clear coronal arcade that resembles the popular slinky toy. *Images courtesy of Masuda et al. (1994), NASA/TRACE and Stanford-Lockheed Institute for Space Research.*

within each category. The scaling is logarithmic so, for example, an M2.5 class flare represents a peak flux of $2.5 \times 10^{-5}\,\mathrm{Wm}^{-2}$.

In the imaging data flares can be seen as bright loop structures in the SXR, EUV, and microwave bands. While in the HXR waveband, sources of emission can be seen at the loop footpoints and occasionally above the top of the SXR loop as well. Solar flares are sometimes classed as either being compact or two-ribbon; compact flares consist of a single coronal loop whereas two-ribbon flares form an arcade of many loops, so emission from the footpoints in the chromosphere appears like two ribbons (Shibata & Magara 2011). Examples of these types of flares are shown in Fig 1.5.

1.2.2 The standard model of solar flares

The CSHKP model, named after some of the major contributors towards the development of the model (Carmichael 1964; Sturrock 1966; Hirayama 1974; Kopp & Pneuman 1976), is often referred to as the standard model of solar flares. The model can explain compact flares, as well as two-ribbon flares if the approximately 2D geometry for compact flares is extended into the third dimension.

The basic idea of the CSHKP model begins with a plasmoid or filament. A plasmoid is a compact structure consisting of cool, dense plasma, whereas a filament is similar but refers to the case where the plasmoid is elongated. The plasmoid/filament is suspended inside a twisted magnetic flux tube (referred to as a flux rope) in the corona above a magnetic polarity inversion line (also referred to as a neutral line) of an active region. The formation of a flux rope is illustrated in Fig. 1.6. In this scenario, proposed by Van Ballegooijen & Martens (1989), flux cancellation occurs in a highly sheared magnetic field, resulting in the formation of helical field lines that may support a cool, dense plasma structure within them. The strong shear required to form the flux rope means that when formed it lies almost parallel to the polarity inversion line. The sheared flux rope can be seen as the classic 'sigmoid' shape that often appears in SXR observations prior to a flare (Moore et al. 2001). Free magnetic energy is stored by the stretching and twisting of the flux rope, and this process is thought to be due to the perturbation of the flux rope by turbulent motion in the convective zone and/or emergence of new flux (the details of this are still a matter of debate). This stretching, twisting, and shearing of the magnetic field can be described quantitatively by magnetic helicity.

The plasmoid erupts if the system eventually evolves into a non-equilibrium state. Normally the flux rope will be surrounded by a much simpler magnetic field which runs perpendicular to the polarity inversion line, and since magnetic field lines move with perfectly conducting fluids (referred to as Alfvén's frozen-in theorem; Alfvén 1942), the erupting plasmoid drags the surrounding magnetic field upwards with it. As the magnetic field lines are stretched, the oppositely directed field lines below the filament are brought together and form a current sheet. This is illustrated in Fig. 1.7. The orange region of this figure represents the diffusion region, where the magnetic field approaches zero and hence the frozen-in condition no longer applies. The diffusion of plasma in this region allows the reconfiguration of the magnetic field into a lower energy state in a process known as magnetic reconnection.

During the impulsive phase of the flare, the magnetic reconnection process forms a post-flare coronal loop below the current sheet, and converts stored magnetic energy into kinetic energy by accelerating charged particles away from the reconnection site. Those particles that are accelerated downwards move along the field lines of the newly formed coronal loop. These particles (mainly electrons) may ap-

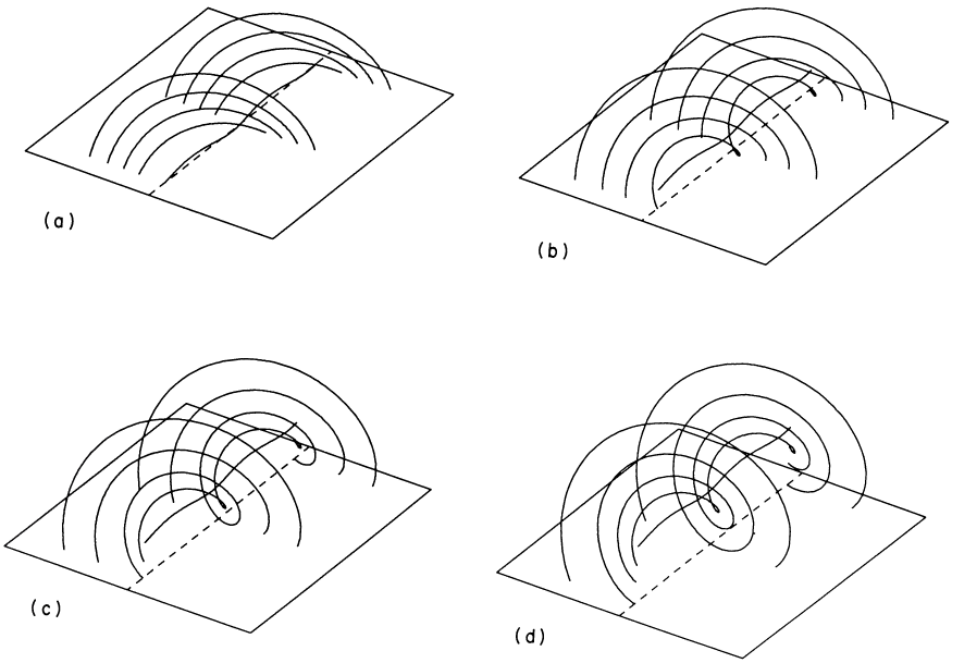

Figure 1.6: Different stages of the formation of a magnetic flux rope over a polarity inversion line. *Image courtesy of Van Ballegooijen & Martens (1989).*

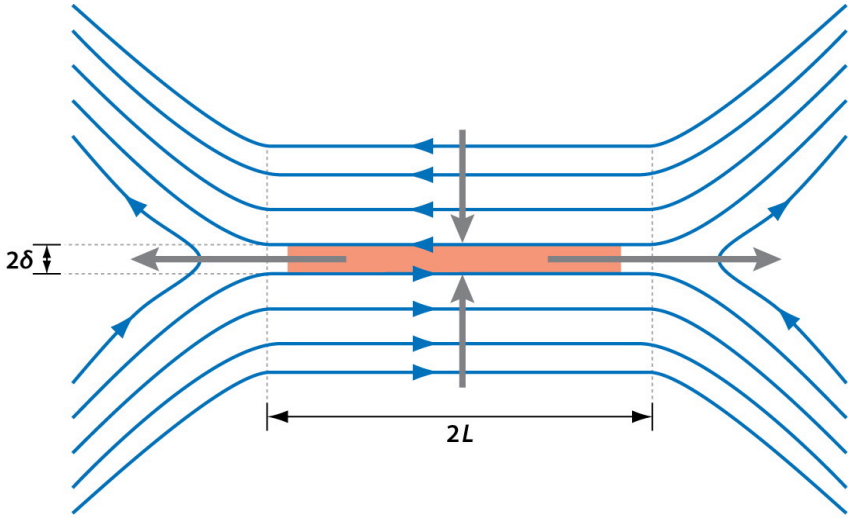

Figure 1.7: A simple illustration of 2D magnetic reconnection and associated plasma outflows in a current sheet (indicated by the orange region), where parallel but oppositely directed magnetic field lines (indicated by the blue lines) are brought together. *Image courtesy of Zweibel & Yamada (2009).*

proach relativistic speeds, meaning they release microwaves via the gyrosynchrotron mechanism as they spiral along the magnetic field lines of the post-flare loop, and when they reach the more cool, dense plasma of the chromosphere they are rapidly decelerated, emitting X-ray radiation via bremsstrahlung. Gamma rays may also be produced during this phase via collisions of accelerated protons and ions.

The thick-target model of Brown (1971) shows how the observed HXR source above the loop top can result from an outflow jet of charged particles produced by magnetic reconnection colliding with the top of the post-flare loop below and generating a shock. This shock causes the further acceleration of charged particles, and sends them spiralling down along the magnetic field lines of the post-flare loop. These charged particles are decelerated via coulomb collisions in the chromosphere until they reach thermal energies. This intense heating of the chromosphere causes an increase in gas pressure, since the energy cannot be dissipated away quickly enough by radiation, which allows the plasma to be able to overcome gravity and flow upwards. Due to the conservation of momentum, this upflow is accompanied by a downflow of plasma to the lower chromosphere. The upflow of hot plasma from the chromosphere, known as chromospheric evaporation, fills the post-flare coronal loop formed by magnetic reconnection (Hirayama 1974). This hot plasma in the post-flare loop is the source of the thermal SXR and EUV emission observed in flares. The decay phase of the flare begins after reconnection has ended, and in this phase the hot plasma cools down. The main features of the CSHKP model are shown in Fig. 1.8.

While the standard flare model has proved to be highly successful in explaining many observational features of solar flares, some inconsistencies have been found. The main example relating to this thesis is the presence of quasi-periodic pulsations observed in a large fraction of solar flares, which are not naturally explained by the current standard model. Several modifications to the standard model have been proposed to explain these pulsations, however, and these are discussed further in Section 1.3.

Other examples relate to the electron beam produced by magnetic reconnection that generates the HXR emission at the loop footpoints. Some studies suggest that the necessary beam density would result in an unstable beam (Krucker et al. 2011), and that in some cases the height of the beam source is too low to explain the deposited energy (Martínez Oliveros et al. 2012). An alternative mechanism for the transport of energy from the reconnection site to the loop footpoints via Alfvén waves could help avoid problems with the electron beam model (Fletcher & Hudson 2008).

Another limitation of the standard flare model is the failure to explain the often-observed second peak in the EUV emission, referred to as the EUV late phase

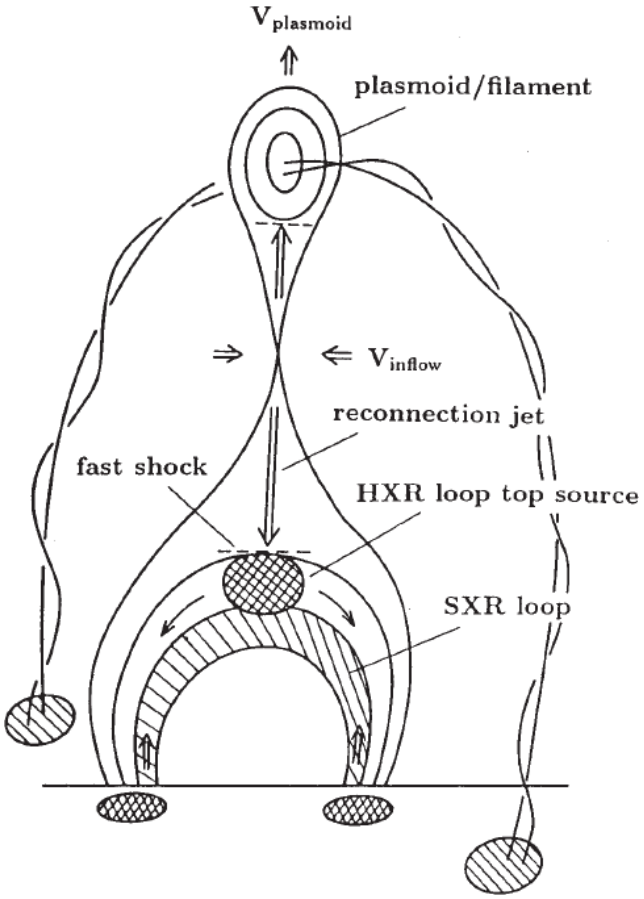

Figure 1.8: Diagram showing the basic geometry and various features of the standard model of a solar flare. *Image courtesy of Shibata et al. (1995).*

(Woods et al. 2011). There is evidence to suggest that this is the result of a more complex magnetic topology, where the main flaring structure is linked to another magnetic structure and triggers a second magnetic reconnection (Liu et al. 2013).

An ongoing mystery of solar flares is the origin of the white-light and infrared emission. Despite the first observed solar flare being viewed in the visual waveband, white-light emission from subsequent flares has been notoriously challenging to measure due to the poor contrast with the solar photosphere. While white-light emission tends to be associated with the more energetic solar flares, it has been observed in weak C-class flares as well (Matthews et al. 2003; Hudson et al. 2006), suggesting that white-light emission is common to all flares even if it cannot always be observed. The fact that the white-light emission tends to correlate well in both space and time with the HXR emission (Krucker et al. 2011) suggests that it is also a product of the non-thermal electrons, although some observations have shown that the white-light emission originates from a lower height, in the upper photosphere or lower chromosphere, than the HXR emission (Watanabe et al. 2010; Martínez Oliveros et al. 2012). As mentioned above, Martínez Oliveros et al. (2012) found that the source region of both the HXR and white-light emission for the studied flare was too low in the atmosphere to be explained by the thick-target model, since the model did not produce enough electrons with energies high enough to reach the source region to explain the observed white-light flux. Watanabe et al. (2010) also found that the source height of the white-light emission was too low to be explained by the standard thick-target model, and suggest that the ionisation enhanced continuum and radiative back-warming ideas discussed by Hudson (1972) and Metcalf et al. (2003) merit further development as a potential explanation.

There is currently a severe lack of observations of solar flares in the infrared waveband, although future observatories will remedy this (Simões et al. 2017). Despite this there has been recent progress in understanding the origin of the infrared emission. Current observations suggest that the infrared emission is impulsive and well-correlated with the HXR and white-light emission (Penn et al. 2016). Radiative hydrodynamic simulations of Simões et al. (2017) suggest that the origin of the infrared continuum emission is mainly in the chromosphere and via the thermal ion free-free emission mechanism (Ohki & Hudson 1975), which is consistent with the observations of Penn et al. (2016). The term 'free-free' is used as free electrons are scattered by ions, producing thermal bremsstrahlung, but remain free.

1.2.3 Flares on other stars

Impulsive brightness enhancements are frequently observed in the light curves of other main sequence stars, and because these sudden brightenings resemble solar flares they are assumed to be equivalent. The likelihood of observing a flare on

another star is highly dependent on the spectral type of the star; a higher proportion of small, cool M-type red dwarf stars are observed to flare compared to larger, hotter F- and A-type stars. In addition the magnetically active cooler stars tend to produce flares more frequently than the hotter stars (e.g. Candelaresi et al. 2014). This may have much to do with the internal structures of main sequence stars, since cooler stars have larger convective zones than hotter stars and a sufficiently deep convective zone is necessary for a dynamo process to generate a magnetic field. Hence the hotter stars tend to not be active, but despite this there may be some flaring A-type stars (Pedersen et al. 2017; Van Doorsselaere et al. 2017). The rotation rate and age also relate to the flaring rate, since younger stars tend to rotate faster and faster rotation means a stronger dynamo (Pettersen 1989; Candelaresi et al. 2014). Even without observing any flares, magnetically active stars can be distinguished from inactive stars as the Hα spectral line will be in emission rather than absorption.

It is generally agreed that stellar flares are produced by magnetic activity, similar to solar flares. Observations show solar and stellar flares to have very similarly shaped time profiles, proxies of magnetic activity to be enhanced for stars that frequently produce large flares (Karoff et al. 2016), and evidence of the Neupert effect for stellar flares observed simultaneously in two different wavebands (Hawley et al. 1995). The possibility that at least some stellar flares may be produced by slightly different mechanisms should still be considered, however, especially since many stellar flares are orders of magnitude more energetic than any recorded solar flare (see Section 1.2.4 for more discussion of the implications of these 'superflares'). So far the alternative mechanisms for stellar superflares include interactions of the magnetic field of the flaring star with that of a companion binary star (Simon et al. 1980), a close-in planet (Rubenstein & Schaefer 2000; Ip et al. 2004), or a disk (Hayashi et al. 1996). In addition, Cuntz et al. (2000) suggested that a tidal interaction between a star and a close-in planet could enhance the magnetic activity of the star by altering flows and turbulence in the convection zone of the tidal bulge region, which in turn could lead to locally increased heating and dynamo action.

Although the majority of stellar flare studies focus on main sequence stars, there have been observations of flares or flare-like phenomena on post-main sequence stars and more exotic objects. Since flares are observed on stars across the main sequence, it is not surprising that as stars start to evolve off the main sequence they continue to flare. Some examples of early observations of flares on red giants in the white-light and radio wavebands were collected by Schaefer et al. (2000). In addition, Karovska et al. (2005) reported the observation of a SXR flare on the red giant Mira A. The recent observations from *Kepler* (see Section 2.6) have helped vastly expand the number of giants observed to flare (Van Doorsselaere et al. 2017). There is currently nothing to suggest that these red giant flares are fundamentally different

to solar flares and main sequence stellar flares, although a different mechanism cannot be ruled out.

The dramatic changes that a star undergoes as it transitions to a white dwarf, and the very different physics operating inside white dwarfs, mean that it is difficult to imagine how solar-like flares could continue into this phase of a star's life. Although some white dwarfs have extremely strong magnetic fields (Hollands et al. 2015), there are no observations of typical stellar flares on white dwarf stars. There have been reports of 'outbursts' on white dwarfs by Hermes et al. (2015), however. These occur on much longer timescales than typical magnetic reconnection flares, with a rise phase that lasts several hours. The outbursts were found to be linked to asteroseismic g-mode pulsations of the star, with the pulsations having shorter periods and larger amplitudes during the outburst. Hermes et al. (2015) suggest that the mechanism behind the outbursts could be resonant mode coupling of the pulsations to daughter modes, which could then be rapidly damped by turbulence in the convective zone, thus depositing energy there.

In a more exotic case, flares are frequently detected from the supermassive black hole at the centre of the Milky Way, Sgr A* (e.g. Degenaar et al. 2013). It has been suggested that these could still result from some magnetic reconnection process in the accretion disk, although other mechanisms such as the infall of matter have also been proposed. Flares have also been detected on magnetars (neutron stars with extremely strong magnetic fields), which are attributed to large-scale reordering of the magnetic field (Woods et al. 2001). A particularly intriguing observed feature (with respect to this thesis) of some of these flares is the presence of quasi-periodic oscillations (e.g. Huppenkothen et al. 2013). Duncan (1998) suggested that these quasi-periodic oscillations might link to global seismic waves that could be initiated by the huge flares (referred to as 'starquakes' and synonymous to sunquakes; Matthews et al. 2015), and hence that they could be used for asteroseismology.

1.2.4 Superflares

While solar flares typically release 10^{29} to 10^{32} erg of energy, stars not dissimilar from the Sun have been observed to produce flares several orders of magnitude more powerful than any solar flare on record. The first of these were reported by Schaefer et al. (2000), who identified nine superflares on stars with a similar spectral type to the Sun (in the range F8 to G8) with estimated energies ranging from 10^{33} to 10^{38} erg. These stars did not have close binary companions, and they were not very young or rapidly rotating. There is potential for substantial damage on Earth and in the near-Earth environment associated with powerful flares. Therefore it is important to work towards determining whether a superflare could occur on the Sun, and if so what the probability of one occurring at a given time would be and what

the precursors might be. Based on order-of-magnitude estimates and a theoretical model of the solar dynamo, Shibata et al. (2013) found that, in principle, a 10^{34} erg superflare could occur on the Sun if the necessary magnetic flux were stored over one solar cycle period (∼11 yrs), while it would take around 40 yrs to accumulate enough magnetic flux for a 10^{35} erg superflare. It is not completely understood how magnetic flux could be prevented from emerging from the base of the convection zone for such a long period of time, hence additional observational data and theoretical constraints are needed to support or disprove these findings. Further work in this area was made by Aulanier et al. (2013), who used 3D MHD simulations of eruptive flares to obtain a relationship between maximum flare energy and sunspot area, and suggested a maximum solar flare energy of $\sim 6 \times 10^{33}$ erg based on the largest sunspot group that has been imaged. They also argue that the current solar dynamo is probably not capable of producing a sunspot group large enough to produce a superflare.

Although these studies suggest that it is highly unlikely that the present Sun could produce a superflare, there is some evidence that solar superflares may have occurred in the past. Miyake et al. (2012) and Miyake et al. (2013) reported two cosmic ray events evidenced in the tree rings of Japanese cedars. They found enhancements of carbon-14 in the years AD 774–775 and AD 993–994, and discussed possible causes. A supernova event was concluded to be an unlikely cause due to the lack historical records reporting a bright object in the northern hemisphere around this time, and the lack of a supernova remnant observed in the present day that is sufficiently bright and close. Other suggested causes were solar proton events (Miyake et al. 2013), short gamma-ray bursts (Hambaryan & Neuhäuser 2013), and comet collisions (Liu et al. 2014). Since there have been no significant changes in the concentration of atmospheric radiocarbon associated with observed solar flares, including the Carrington Event, a solar flare and associated proton event would have to be vastly more powerful than any observed before to have such an effect. Following the work of Miyake *et al.*, Mekhaldi et al. (2015) found matching enhancements of beryllium-10 during the periods AD 774–775 and AD 993–994 in both Arctic and Antarctic ice cores, along with chlorine-36 measurements from an Arctic ice core. They rule out the comet hypothesis because the associated enhancement of radionuclides would be mostly restricted to one hemisphere of the Earth. Moreover, a gamma-ray burst event would not produce the observed increase of beryllium-10 (Pavlov et al. 2013). Hence they conclude that the most likely source is a solar proton event that would have been at least five times stronger that any event measured by a spacecraft.

Due to the limited history of solar observations, one can also look at populations of other stars to infer information about the Sun. With the release of the

Kepler data, a huge number of superflares have been observed on a variety of different stars. The first set of superflares from solar-type stars in the 30 min cadence *Kepler* data were reported by (Maehara et al. 2012), where they selected G-type stars with a surface gravity, $\log g$, greater than 4.0. Their sample of 365 flares on 148 stars had amplitudes around 0.1–1% of the stellar luminosity and estimated energies of 10^{33} to 10^{36} erg. They paid closer attention to 14 superflares on Sun-like stars, which had effective temperatures in the range 5,600–6,000 K and were slowly rotating, and found that the 10^{34} erg flares occurred on average once every 800 yrs, and the 10^{35} erg flares once every 5,000 yrs. This work was extended by Shibayama et al. (2013), who increased the number of observed superflares on the Sun-like stars to 44. After the end of the *Kepler* mission, Maehara et al. (2015) searched the full set of 1 min cadence data and found 187 superflares on 23 solar-type stars with an average occurrence rate for 10^{33} erg flares of once in every 500–600 yrs. Notsu et al. (2015a) used the Subaru High Dispersion Spectrograph (HDS) to make spectroscopic observations of 50 of the solar-type superflare stars observed by *Kepler* and found that 9 were Sun-like (with $5,600 \leq T_{\rm eff} \leq 6,000$, $\log g \geq 4.0$, a rotation period greater than 10 days, and no binary companion). (Karoff et al. 2016) studied Ca II H and K spectral emission lines (which are a proxy for magnetic activity in the chromosphere) of 48 solar-type superflare stars observed by the Large Sky Area Multi-Object Fibre Spectroscopic Telescope (LAMOST). They found that the majority of the superflare stars showed higher chromospheric emission than the Sun, but 12 stars observed to produce superflares with energies below 2×10^{34} erg, or 4 stars with superflare energies above 2×10^{34} erg, had similar chromospheric emission levels to the Sun. Hence based on these studies it seems that, in principle, the Sun is capable of producing a superflare.

The occurrence of superflares also has implications for the search for other planets that might harbour life, especially since a high proportion of exoplanets in the habitable zone are detected around M-type stars. For example, Armstrong et al. (2016) detected superflares on the host star of the most Earth-like exoplanet found at the time, Kepler-438b. Seven flares were identified with energies ranging from $(4 \pm 2) \times 10^{32}$ to $(1.4 \pm 0.6) \times 10^{33}$ erg, and given that the exoplanet orbits at a distance of 0.166 AU from the host star it is likely more vulnerable to the effects of stellar activity than the Earth. Another example of flares on the host star of an exoplanet in the habitable zone was reported by Davenport et al. (2016), who studied flares on Proxima Centauri after the discovery of the small exoplanet Proxima b in the habitable zone (Anglada-Escudé et al. 2016). They extrapolated the cumulative flare frequency distribution as a function of energy to conclude that a 10^{33} erg superflare should occur around 8 times per year, on average. Finally, following the recent highly-publicised announcement of seven planets orbiting the

cool M dwarf TRAPPIST-1 (Gillon et al. 2017), of which three are in the habitable zone, there were reports of flares with energies up to 1.24×10^{33} erg on the host star (Vida et al. 2017).

Several studies have made theoretical explorations of the impact that activity of a host star could have on planets in the habitable zone. Segura et al. (2010) investigated the potential effects of a 10^{34} erg superflare on an Earth-like exoplanet orbiting an M dwarf in the habitable zone. They found that the increased X-ray emission did not penetrate beyond the upper atmosphere, while the UV emission that reached the surface did not greatly surpass the levels on Earth (since the cooler stars have a lower UV flux contribution from the blackbody spectrum). In addition, the increased UV emission did not cause any significant depletion of the ozone layer. Therefore they concluded that the enhanced high-energy electromagnetic radiation incident on the planet would not have much of an impact on its habitability. On the other hand, their model planet had no magnetic field and so the influx of energetic charged particles (that are associated with powerful flares) could pose a threat to any life. In a different study, Lingam & Loeb (2017) investigated the effect that a 10^{37} erg superflare would have on Earth, and concluded that the ozone layer would be destroyed.

Flares and proton events are not the only activity phenomena that may affect habitability. Since CMEs are associated with powerful solar flares, it is expected that CMEs should occur on superflare stars as well. Although a magnetosphere can help protect a planet from the damaging effects of a CME, an Earth-like planet in the habitable zone of an M dwarf would be unlikely to have a large enough magnetosphere. This is because the M dwarf habitable zone is close in to the star, and so planets orbiting in this zone are likely to be tidally locked. This tidal locking would limit the rotation of the planet and thus limit the magnetic field that could be generated by a dynamo process. Even if the planet did have a magnetosphere, Khodachenko et al. (2007) showed that stellar winds and CMEs could compress a small magnetosphere on the star-facing side, such that the magnetopause entered the atmosphere. This would result in erosion of the atmosphere. In fact there is some observational evidence of atmospheric erosion associated with stellar activity reported by Lecavelier des Etangs et al. (2012). During two different observational periods of the star HD 189733, the authors measured spectra before, during, and after the transit of the exoplanet HD 189733b. They measured the Lyman-α emission line and found no significant changes during the first observational period. In the second observational period, however, they measured a strong absorption of the line during the transit phase, which suggested the presence of atmospheric hydrogen and thus an extended hydrogen cloud around the exoplanet resulting from evaporation of its atmosphere. In addition to this, they detected an X-ray flare from the host

star 8 hr before the second observational period, suggesting that enhanced stellar activity might be to blame for the atmospheric evaporation. Following from Khodachenko et al. (2007), Lammer et al. (2007) also found that CMEs could erode the atmospheres of exoplanets orbiting active M dwarfs in the habitable zone, and suggested that a planet could retain its atmosphere if was larger and more massive than the Earth. This would mean a greater gravitational pull and a stronger magnetic field could be generated.

1.3 Quasi-periodic pulsations

Quasi-periodic pulsations (QPPs) are time variations in the intensity of electromagnetic radiation emitted by a flare. The periodic modulation of a solar flare light curve was first reported by Parks & Winckler (1969), and with the development of increasingly high-precision instruments that observe the Sun, it emerged that these QPPs of the energy release are a common feature of flares (e.g. Kupriyanova et al. 2010; Simões et al. 2015; Hayes et al. 2016; Inglis et al. 2016; Pugh et al. 2017b). They are also occasionally observed in stellar flares (e.g Mathioudakis et al. 2003; Anfinogentov et al. 2013; Pugh et al. 2016; Doyle et al. 2018), with the first of these observations being made by Rodono (1974). A classic example of QPPs in a solar flare observed by Kane et al. (1983) is shown in Fig. 1.9 and is nicknamed the 'Seven Sisters Flare'. In this plot, very clear periodic pulsations with a period of around 8 s can be seen in several different wavelengths from two separate instruments.

Although there is no strict definition of QPPs, it is generally accepted for stationary QPPs that the impulsive and/or decay phase of the flare should contain, at the very least, three cycles of oscillation, or pulses with approximately equal time spacing, visible above the noise level. There may also be non-stationary QPPs, where the time spacing between pulses increases or decreases monotonically (e.g. Kupriyanova et al. 2010; Huang et al. 2014). Typical QPP periods for solar flares range from a few seconds to a few minutes, and they have been observed in many different wavebands, encompassing much of the electromagnetic spectrum. Stellar flare QPPs tend to be observed to have longer periods, which is likely to be due to a combination of the limited time cadence of the data and the longer duration of observable stellar flares compared to solar flares.

Despite the large number of observations of QPPs in solar and stellar flares, their nature remains mysterious. Since QPPs are a common feature of flares, the nature of them should be understood in order to fully understand flares, and flare models should allow for their production. In addition, it is expected that the properties of the QPPs should relate to the plasma parameters in the flaring region, such as the size of the flaring structure, magnetic field strength, and plasma den-

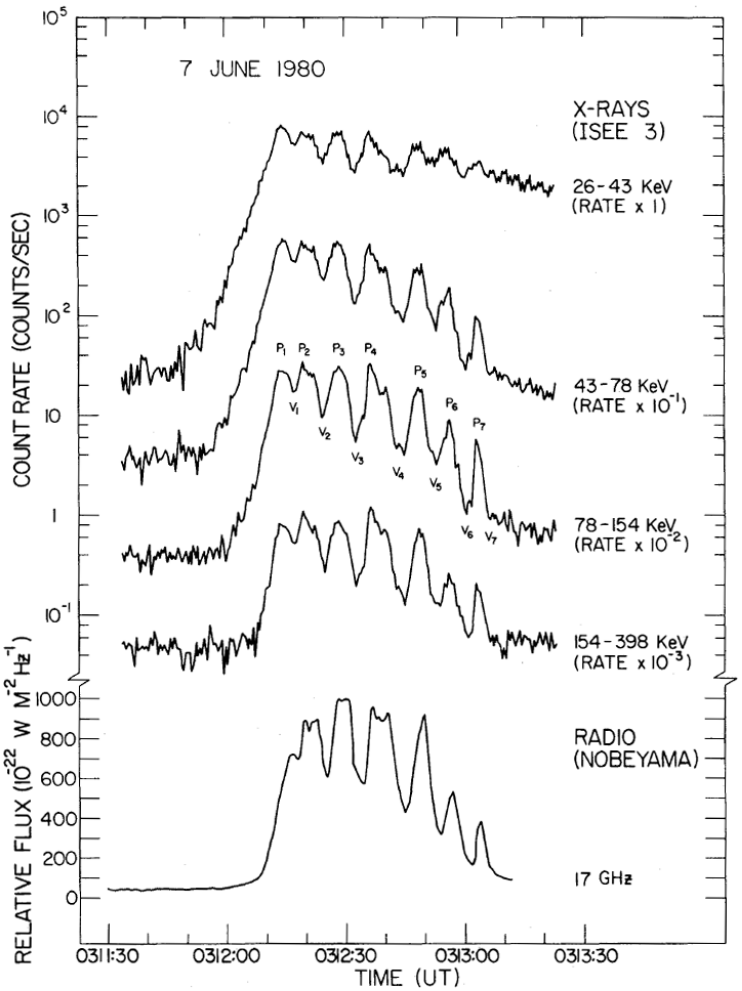

Figure 1.9: The Seven Sisters Flare, which exhibits QPPs in several different wavebands. *Image courtesy of Kane et al. (1983).*

sity. Therefore there is potential for the diagnosis of plasma parameters in the corona that are otherwise difficult to observe directly. If the mechanism causing the QPPs can be inferred, then they would join MHD oscillations of coronal loops (e.g. Nakariakov & Ofman 2001; Van Doorsselaere et al. 2008; De Moortel & Nakariakov 2012) as a valuable coronal seismology tool. Furthermore, the fact that QPPs have been observed in stellar flares suggests that the physical processes occurring in solar and stellar flares are similar (see Section 1.2.4 for a discussion of the importance of this). Another interesting possible impact of QPPs in solar flares is the effect on the near-Earth environment. Nakariakov et al. (2016) suggested that since solar flares alter high energy particle distributions and result in enhanced ionisation of the ionosphere, then QPPs of the flare intensity with a constant period could resonate with nature frequencies of geophysical systems and hence exaggerate the negative affects of the flare. Recently Hayes et al. (2017) for the first time observed QPPs in a solar flare resulting in corresponding pulsations of the electron density in the ionosphere, demonstrating the geoeffectiveness of QPPs.

While it is currently difficult to determine the exact cause of the QPPs for any given case, several possible mechanisms have been proposed. In the following sections these are split into three groups: those based on MHD oscillations of the flaring structure itself, those where magnetic reconnection is triggered periodically by MHD waves originating from outside of the flaring structure, and those based on regimes of repetitive magnetic reconnection that can be considered in terms of a 'magnetic dripping' model (Nakariakov & Melnikov 2009; Nakariakov et al. 2010; Van Doorsselaere et al. 2016; McLaughlin et al. 2018).

1.3.1 Modulation of the flare emission by MHD waves

MHD marries electromagnetism to fluid dynamics, and is used to describe the dynamics of plasmas on a macroscopic scale and at non-relativistic velocities. For a uniform plasma, if a small perturbation is introduced to the static equilibrium MHD equations and these equations are linearised, then the resulting equations can be reduced to wave equations. From these wave equations three kinds of waves emerge: these are the incompressible Alfvén wave, and the compressible fast and slow magnetoacoustic waves.

In the solar corona the plasma is highly structured; in particular, coronal loop structures are prevalent around active regions. Coronal loops can be approximated by a cylindrical geometry as a simple magnetic flux tube, with a different magnetic field strength, temperature, and density inside the tube compared to the outside. If the flux tube is perturbed from its equilibrium position—for example by a plasma flow, eruption, or reconfiguration of the magnetic field—it will oscillate about that equilibrium position with one or more of several possible wave modes. The different

possible modes can grouped into different types of wave, which include the sausage, kink, slow magnetoacoustic, torsional, and fluting/ballooning waves (Nakariakov & Verwichte 2005). Since the fluting/ballooning mode is difficult to observe and not expected to be common it is not discussed further.

The sausage mode is a type of fast magnetoacoustic wave and refers to the periodic expansion and contraction of the loop cross section without displacing the loop axis, as illustrated by Fig. 1.10 and the $m = 0$ mode of Fig. 1.11, hence this mode is compressive and can modulate the plasma parameters inside the loop. Typical periods of the sausage mode for solar coronal loops range from less than a second to several seconds.

Another fast magnetoacoustic mode is the kink mode (illustrated by the $m = 1$ mode of Fig. 1.11), which refers to the periodic transverse displacement of the loop axis. If the wavelength of a kink mode is much longer than the minor radius of the oscillating loop, then the kink mode is mostly incompressible. The horizontally polarised kink mode refers to the scenario where the loop sways sideways, without the loop length being altered, while for the vertically polarised kink mode the loop length oscillates. Typical kink mode periods for the Sun range from several seconds to a few minutes.

Slow magnetoacoustic waves are analogous to the acoustic waves that occur in other mediums. They refer to the periodic expansion and compression of the plasma in the direction of the loop axis, with typical periods ranging from several minutes to over half an hour.

Finally, Alfvén waves in a coronal loop are referred to as torsional modes, and are illustrated by Fig. 1.12. They describe the periodic motion in the azimuthal direction of the loop, where neither the loop axis nor the loop cross section are perturbed, while unlike for the slow magnetoacoustic mode the motion is not parallel to the loop axis either. Hence this mode is incompressible so long as the loop is not already twisted. Torsional modes have typical periods in the range from several seconds to several minutes.

Since QPPs often appear as an oscillatory process with periods in the range of seconds to minutes, it is natural to hypothesise that they may be linked to the MHD oscillations which are frequently detected in various coronal structures. MHD waves cause plasma parameters to vary periodically, which could either directly affect the emission, or could modulate the magnetic reconnection rate and acceleration of charged particles, and hence indirectly affect the flare emission.

For the cases of the sausage and slow magnetoacoustic modes of a coronal loop, the plasma density within the loop varies periodically, which in turn causes the magnetic field strength to vary. Hence the gyrosynchrotron emission in the microwave band would be modulated, since the emission intensity is related to the

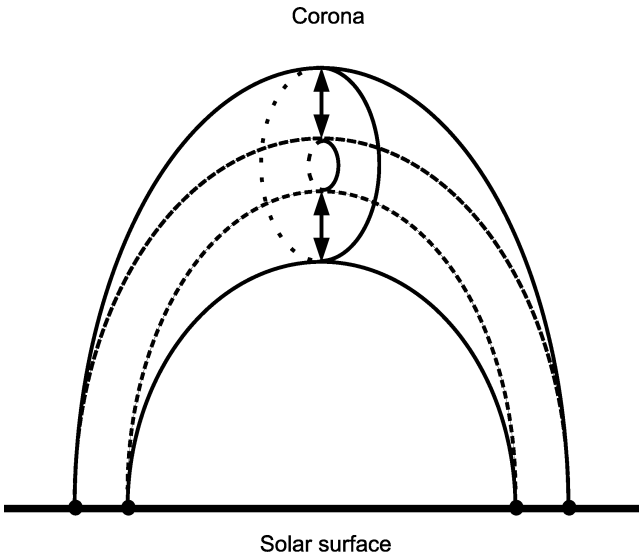

Figure 1.10: Illustration of a sausage mode in a coronal loop. *Image courtesy of Pascoe et al. (2007).*

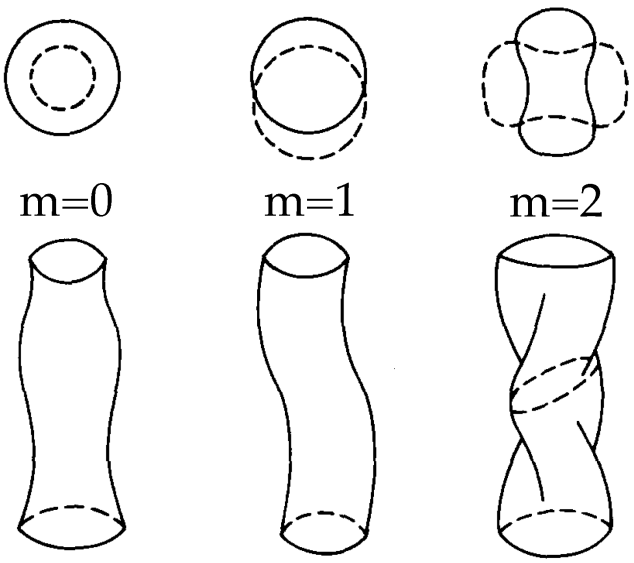

Figure 1.11: Cylindrical oscillation modes, where here m is the azimuthal wave number. The $m = 0$ mode is known as the sausage mode, $m = 1$ is the kink mode, and $m \geq 2$ is a ballooning or fluting mode. *Image courtesy Spruit (1982).*

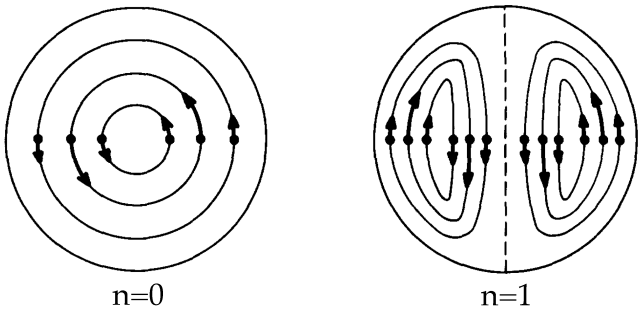

Figure 1.12: Two different torsional Alfvén modes, where n refers to the radial wave number. *Image courtesy of Spruit (1982).*

magnetic field strength. The variation of the magnetic field strength could also modulate the acceleration of charged particles (e.g. Zaitsev & Stepanov 2008), which would affect bremsstrahlung emission from the loop foot-points in the HXR and white-light wavebands.

The sausage mode may also affect bremsstrahlung emission via a magnetic mirror mechanism (Zaitsev & Stepanov 1982). In this case variations of the magnetic field strength along the loop could result in magnetic mirrors, which may trap the non-thermal electrons depending on their angle of incidence to the magnetic mirror (referred to as their pitch angle). Changes in the magnetic field strength will cause the critical pitch angle to vary, which will alter the proportion of electrons that remain trapped between the magnetic mirrors, and those that can escape and produce bremsstrahlung emission when they reach the loop footpoints.

Horizontally polarised kink modes vary the angle between the line-of-sight and magnetic field in the loop, and since gyrosynchrotron emission is directional this would result in the apparent modulation of the observed emission intensity (Nakariakov & Melnikov 2009). The vertically polarised kink mode, on the other hand, causes a periodic stretching of the loop which would alter the magnetic field strength within the loop, and thus could cause modulation of the gyrosynchrotron and bremsstrahlung emission in a similar manner to the sausage/slow magnetoacoustic mode case.

Finally, an LCR circuit model describes how QPPs could result from the torsional mode (Zaitsev et al. 1998; Zaitsev & Stepanov 2008). In this case the mode would cause oscillations of the electric current in the loop, which in turn would cause variations of the magnetic field and hence directly affect gyrosynchrotron emission. The oscillations of the electric field would also vary the acceleration of charged particles, affecting bremsstrahlung emission from the loop footpoints. In addition the electric current would dissipate by Ohmic heating, which would lead to an increase in temperature that could affect the emission.

These MHD oscillation mechanisms can naturally produce the multiple periods that are occasionally observed in some QPP signals (e.g. Kupriyanova et al. 2013; Pugh et al. 2015) from the presence of higher harmonics and the co-existence of different types of waves. They may also explain the time delays between QPP signals observed in different wavebands by Dolla et al. (2012) if the acceleration of charged particles is modulated, since the Neupert effect means there is a natural time delay between the HXR and SXR emission. It should be noted, however, that not all QPP signals show evidence of time delays between different wavebands (Hayes et al. 2016).

1.3.2 Periodic triggering of magnetic reconnection by MHD waves

The idea that QPPs could result from MHD oscillations from a external source perturbing the flaring structure was first proposed in Foullon et al. (2005). Oscillations from an external source could leak into the intermediate plasma, then as each wavefront reaches the flaring site, micro-instabilities could be formed which would result in anomalous resistivity and strong currents near the magnetic null point. This will trigger magnetic reconnection if the current cannot remain high enough to sustain the strong magnetic field gradient (according to Ampère's law: $\nabla \times \mathbf{B} = \mu_0 \left(\mathbf{J} + \epsilon_0 \frac{\partial \mathbf{E}}{\partial t}\right)$). McLaughlin & Hood (2004) demonstrated this for a single fast magnetoacoustic pulse approaching a null point, and found that the pulse was refracted towards the null point leading to the accumulation of electric current density. Nakariakov et al. (2006) expanded on this by considering the interaction of a periodic fast magnetoacoustic wave with a null point, and showed that even MHD waves that are low in amplitude when they approach the null point are able to cause strong spikes in the current due to non-linear effects.

Another possibility specific to two ribbon flares is propagations along the axis of the coronal arcade associated with slow magnetoacoustic waves, periodically triggering reconnection at the 'X' configuration null points of each of the arcade loops as they go (Nakariakov & Zimovets 2011). The principle of slow magnetoacoustic waves triggering reconnection was first shown by Chen & Priest (2006). Their simulations showed that five-minute p-mode oscillations (which convert to slow magnetoacoustic oscillations in a magnetised plasma) imposed at the base of the photosphere caused oscillations of the plasma density in the solar atmosphere, leading to anomalous resistivity and hence reconnection in the transition region. Although slow magnetoacoustic waves cannot propagate perpendicular to the magnetic field in a uniform medium, they can propagate slightly obliquely to the magnetic field. In a plasma structure such as a coronal arcade, slow magnetoacoustic waves can be reflected at the loop footpoints. These reflections, combined with the fact that these modes may propagate at a slight angle to the magnetic field, means that the coronal arcade can

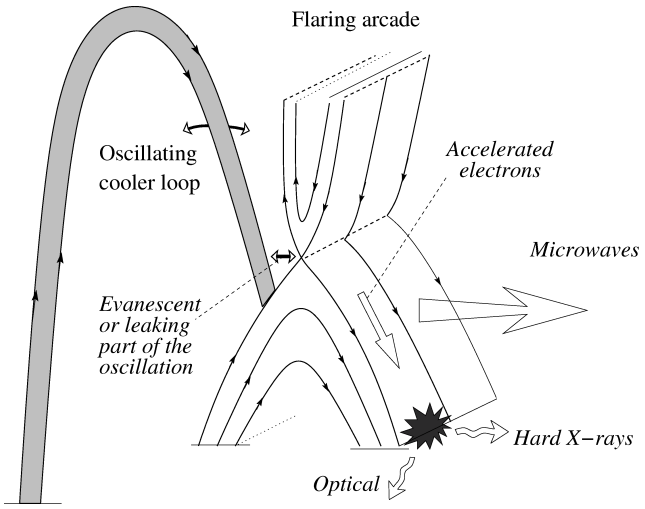

Figure 1.13: Illustration of repetitive reconnection being triggered in a flaring arcade by oscillations of a nearby loop. *Image courtesy of Nakariakov et al. (2006).*

act as a waveguide and allow propagation across the magnetic field. The propagation speed would be slow, however, and as such this mechanism could only explain long-period QPPs.

Due to the typically smaller amplitude of higher harmonics relative to the fundamental mode, it has not yet been shown that they could trigger periodic reconnection in addition to the fundamental mode. Hence it is not yet clear if these reconnection mechanisms driven by external MHD waves could explain QPPs with multiple periods. On the other hand, these mechanisms could explain the time delays between QPP signals observed in different wavebands, since non-thermal particles with a distribution of energies will be produced by each reconnection. The different energies will result in different speeds and different locations where the non-thermal particles lose the majority of their energy, and hence will result in time delays between emission in different wavebands.

1.3.3 Oscillatory regimes of magnetic reconnection

These mechanisms are also referred to as 'load/unload' mechanisms or 'magnetic dripping', since in the simplest case they can be imagined as a scenario where free magnetic energy continuously builds up but is released repetitively each time some threshold energy is surpassed (Nakariakov & Melnikov 2009; Nakariakov et al. 2016; Van Doorsselaere et al. 2016). The 'magnetic dripping' term arises because an analogy can be made between this mechanism and leaking water accumulating at a steady rate at the bottom of a surface, that drips each time the weight of the water is great enough to overcome the surface tension (Nakariakov et al. 2010).

Numerous MHD simulations have demonstrated the plausibility of these

regimes of repetitive reconnection that do not require a periodic driver. For example, McLaughlin et al. (2009) simulated a single non-linear fast magnetoacoustic wave front approaching a 2D X-type null point. By beginning with an incident annulus wave front that contracted around the null point, they found that the wave distorted the null point until eventually a current sheet formed. The outflow jets resulting from reconnection at the current sheet (see Fig.1.7) heated the plasma and caused it to expand. The expanding regions of plasma at either end of the current sheet caused the current sheet to first shrink and then reform another current sheet in a different orientation. This process repeated several times, as what was termed oscillatory reconnection. Based on this work, McLaughlin et al. (2012a) performed a parametric study and were able to obtain oscillation periods of the order of 1 min, with the specific value relating to the amplitude of the initial wave pulse. They found that the oscillatory behaviour was similar to that of a damped harmonic oscillator, with an exponential decay profile and a decay time of the order of the period. This decay was concluded to be a result of the finite energy input by the initial wave pulse, rather than due to a separate damping mechanism. It was also noted that the periods tended to decrease very slightly with time, although the reason for this was not clear. For this mechanism it is still an open question which parameters determine the period.

In a similar vein, Murray et al. (2009) and McLaughlin et al. (2012b) performed 2.5D simulations of the emergence of a flux rope into a coronal hole (with a vertical magnetic field), and found that a current sheet formed. Reconnection occurred, with outflows from the ends of the current sheet resulting in a build up of gas pressure in a quasi-bound region. The increase in the pressure gradient caused the inflow field lines to move apart, stopping reconnection, and brought the outflow field lines together, causing reconnection to recommence in a different configuration. This process repeated in a periodic manner until eventually an equilibrium state was reached. McLaughlin et al. (2012b) also made a parametric study, where they varied the magnetic field strength of the emerging flux tube. They found a lower limit on the magnetic field strength required for the flux tube to be buoyant and emerge into the atmosphere, thus triggering oscillatory reconnection. Above this threshold the period increased with magnetic field strength, with values around a few minutes, and the oscillatory signal followed an exponential decay profile, similar to the results of McLaughlin et al. (2012a). They also defined an upper bound for the field strength in this study, because above this upper threshold plasmoids are ejected from the current sheet. Although the authors still report some oscillatory behaviour, the system behaviour is very different and thus they aim to address this different regime in a future study. Recently, Thurgood et al. (2017) extended the work of McLaughlin et al. (2012b) by demonstrating that oscillatory reconnection

can also occur at a 3D magnetic null point.

Kliem et al. (2000) instead focussed on a long current sheet above a SXR flare loop, and found that instabilities caused anomalous resistivity and the formation of magnetic islands as a result of reconnection, which could then coalesce, forming one or more plasmoids which would then be ejected. The ejection of multiple plasmoids (and hence resulting flare emission) could either be sporadic or quasi-periodic. A more recent work by Guidoni et al. (2016) investigated charged particle acceleration in flares, based on the mechanism for electron acceleration via interactions with magnetic islands proposed by Drake et al. (2006). They found that this mechanism is capable of explaining the observed electron energies in flares, and also found that it results in sporadic flare emission because of the intermittent magnetic island formation, which could relate to observed flare pulsations.

Another example in this regime was put forward by Takasao & Shibata (2016). Their 2D simulation of a flare revealed oscillations of the plasma above the SXR post-flare loops that generated quasi-periodic propagating fast magnetoacoustic waves (QPFs), which have typical periods in the range of tens to hundreds of seconds. These oscillations were a consequence of shocks produced when the outflows of plasma resulting from reconnection reached the reconnected post-flare loops. These shocks could reflect in the region above the post-flare loops and thus multiple shocks were produced, which in turn excited the QPFs. They included the basic physics of flares—such as magnetic reconnection, chromospheric evaporation, and heat conduction—which is a step forward on previous models of the production of coronal waves. The multiple, quasi-periodically occurring shocks would result in a quasi-periodic variation of the acceleration of non-thermal electrons, and hence could result in QPPs of the non-thermal flare emission.

1.4 Thesis outline

The research presented in this thesis concerns the statistical properties of QPPs in both solar and stellar flares. Relating to this, another theme is methods of detection for quasi-periodic signals in time series data. Modern observations have increased both the quantity and quality of flare time series data, meaning that statistical studies can now be undertaken to get a sense of the general properties of the still poorly understood QPPs. Through this there is potential to make links with theoretical models of QPPs, and to determine whether the QPPs observed in solar and stellar flares are of the same nature.

In this chapter an overview of the general structure of the Sun and stars is given, followed by a more detailed description of solar/stellar flares and QPPs. A summary of the different instruments that provided the data for this thesis is

given in Chapter 2. These include solar flare observations from GOES, SDO/EVE, *Fermi*/GBM, *Vernov*/DRGE, and Nobeyama Radioheliograph, active region observations from SDO/HMI, and finally stellar flare observations from *Kepler*. Chapter 3 discusses the different data analysis techniques used in the subsequent chapters, including fitting models to data, spectral analysis, and data detrending considerations.

Chapter 4 presents a new method for the detection of QPPs in flares whose light curves cannot easily be fitted with a simple model, based on a technique used for the detection of quasi-periodic oscillations in the X-ray emission of Seyfert galaxies. This method assesses the significance of a peak in the power spectrum of the flare light curve, and accounts for the presence of coloured noise, trends, and data uncertainties such that the risk of a false detection in minimised. The method described in this chapter is applied to a set of solar flares in Chapter 5. The set of flares used for this study all originate from the same active region, so that a search for links between the QPP properties and the evolution of the active region can be made.

In Chapter 6 the *Kepler* data is searched for evidence of QPPs in stellar flares. A set of stellar flares containing QPP-like signature in their light curves is presented, and relationships between the QPP period, global stellar properties, and flare properties are checked for. A more detailed analysis of one of the flares which shows evidence of containing two simultaneous periodic signals is also given. Finally, Chapter 7 gives a summary of the results presented in this thesis and a discussion of potential avenues for future work.

Chapter 2

Instrumentation

2.1 GOES

The *Geostationary Operational Environmental Satellite* (GOES) program is a joint project of both the National Aeronautics and Space Administration (NASA) and the National Oceanic and Atmospheric Administration (NOAA) that has been ongoing since 1974. The GOES satellites carry a variety of different instruments, and are primarily used for weather forecasting and storm tracking. There are usually two spacecraft operating at a time, in geostationary orbits that give a continuous view of much of North and South America, as well as the Pacific and Atlantic oceans.

In addition to the terrestrial weather monitoring instruments, the GOES spacecraft also carry a set of space environment monitor (SEM) instruments, which include a magnetometer, energetic particle sensor, and two X-ray sensors (XRS). The X-ray sensors are gas-filled ion chambers with beryllium filters that make near continuous Sun-as-a-star observations of the solar flux in two SXR wavebands: 1–8 Å (1.5–12.4 keV) and 0.5–4 Å (3.1–24.8 keV) (Hanser & Sellers 1996). The lower energy limit is prescribed by the thickness of the beryllium filter, and the upper limit by the gas used in the ion chamber, the chamber window size, and the gas thickness along the line-of-sight.

The data from more recent versions of the XRS aboard the GOES 13–15 satellites have an excellent signal-to-noise ratio and a cadence of 2.048 s, meaning these data are highly suited to being searched for QPPs in solar flares. Chapter 5 of this thesis make use of XRS data for this purpose, and for the time interval used in that chapter, GOES-15 provided the XRS measurements.

Regarding the measurement uncertainties of the XRS aboard GOES-15, Simões et al. (2015) showed that the irradiance steps due to the digitisation of the XRS data are greater than the Poisson noise from counting statistics. Poisson noise is equal to the square root of the number of photon counts, so after converting the Poisson noise to be in units of irradiance, it could be directly compared with the

Table 2.1: Count step sizes due to digitisation corresponding to different photon counts for the XRS aboard GOES-15.

Counts	Step size
4095	1
8191	2
16383	4
32767	8
65535	16
131071	32
262143	64
524287	128
1048575	256
2097151	512
4194303	1024
8388607	2048
16777215	4096
33554431	8192
67108863	16384

irradiance step size as a function of irradiance. Table 2.1 shows the count digitisation step sizes corresponding to different count values, and these can be converted into the irradiance step size as a function of the irradiance using the following expression:

$$\text{X-ray flux} = S(\text{counts} - B)G/C, \tag{2.1}$$

where the X-ray flux units are Wm^{-2}, S is a scaling factor (equal to 0.85 for the 0.5–4 Å channel and 0.7 for the 1–8 Å channel), B is the background counts value, G is the gain with units A/count (equal to 1.87×10^{-15} for GOES-15), and C is a units conversion factor with units of $\mathrm{A/Wm}^{-2}$ (equal to 1.141×10^{-5} for the 0.5–4 Å channel and 3.992×10^{-6} for the 1–8 Å channel). Therefore, for the XRS data used in Chapter 5, half of the irradiance step size as a function of the irradiance was used as an estimate of the uncertainty for each measurement.

2.2 SDO

The *Solar Dynamics Observatory* (SDO) is operated by NASA and has been making observations of the Sun since 2010 (Pesnell et al. 2012). The spacecraft is in an inclined geosynchronous orbit about the Earth, meaning it has a constant view of the Earth-facing side of the Sun. The three instruments carried by SDO are the

Atmospheric Imaging Assembly (AIA), *Extreme Ultraviolet Variability Experiment* (EVE), and *Helioseismic and Magnetic Imager* (HMI).

2.2.1 EVE/ESP

EVE measures the EUV irradiance from the Sun in multiple channels and consists of two sub-instruments (Woods et al. 2012). The first sub-instrument, the Multiple EUV Grating Spectrograph (MEGS), has four channels that measure different parts of the 5–105 nm waveband, with a time cadence of 10 s and a spectral resolution of 0.1 nm. The second sub-instrument is the EUV Spectrophotometer (ESP) (Didkovsky et al. 2012). A thin-film aluminium filter in front of the ESP aperture blocks visible light, and allows EUV and SXR radiation to pass through a diffraction grating and be received by photodiode detectors positioned at the constructive interference peaks of the scattered radiation. Four of the detectors are positioned to receive first order bands of the diffraction grating, with wavebands centred at 17.1, 25.7, 30.4, and 36.6 nm. Another four are at the zeroth order position, and a carbon-titanium-carbon filter between the diffraction grating and these detectors constrains measurements to the 0.1–7 nm (0.18–12.4 keV) waveband. ESP has a very high time cadence of 0.25 s, and unlike MEGS has a near-complete time coverage, which makes this sub-instrument suitable for studying QPPs.

The 0.1–7 nm waveband overlaps with the GOES wavebands, and since this thesis makes use of GOES data in Chapter 5, the ESP data can be used to rule out the possibility that a periodic signal in the GOES data is due to an artefact and is unrelated to the flare (Hayes et al. 2016; Dennis et al. 2017). Flares are also visible in the data from the first order wavebands, but the signal to noise is worse and hence these wavebands are not as well suited to the study of QPPs as the 0.1–7 nm waveband.

Although the time cadence of ESP is 0.25 s, in order to estimate the uncertainties these measurements were binned down to a 1 s cadence, and the standard deviation of the measurements within each 1 s time bin was used as the uncertainty. The disadvantage of this instrument when searching for QPPs is that the waveband is very broad, so much of the fine structure of the flare signal is smeared out due to the Neupert effect.

2.2.2 HMI

HMI makes spatially resolved observations of the Fe I absorption line, where the overall bandpass is 76 mÅ centred at a wavelength of 6173.3 ± 0.1 Å from the whole solar disk with a 1 arc-second resolution. By taking images at two different polarisations and six different positions within this spectral line, four different data types are produced: Doppler velocity, continuum intensity, line-of-sight magnetic flux, and

vector magnetic field (Scherrer et al. 2012). Before entering the HMI instrument, sunlight must first pass through a 50 Å bandpass filter, called the front window. It then enters a refracting telescope, passes through three polarisation selectors, and is reflected from a polarising beamsplitter. The light then passes through a series of filters before being split into two beams that are received by two charge-coupled device (CCD) cameras (Schou et al. 2012). The final series of filters include a blocking filter, a Lyot filter, and two Michelson interferometers. The blocking filter further limits the bandpass to 8 Å while the Lyot filter and Michelson interferometers are tuned to scan across the Fe I line using rotating waveplates. An image is taken for each of the narrowband tunings, and twelve images with different combinations of wavelength and polarisation are used to derive each Doppler velocity and magnetic field map. The magnetic field measurements are made by utilising the Zeeman effect, where the Zeeman splitting is calculated by taking the difference between the energies of the right-hand and left-hand circularly polarised light. Chapter 5 of this thesis makes use of the line-of-sight magnetogram data, which have a cadence of 45 s and a precision of 10 G.

2.3 *Fermi*/GBM

The *Gamma-ray Burst Monitor* (GBM) aboard NASA's *Fermi* satellite (Meegan et al. 2009) measures X- and gamma-ray photons with energies between 4 keV and around 40 MeV. *Fermi* has been operating since 2008, and is in a low Earth orbit with an altitude of 565 km and an inclination of 25.6°. While primarily designed for the detection of gamma-ray bursts, GBM also makes high quality observations of solar flare light curves. GBM consists of 2 bismuth germanate (BGO) and 12 thallium activated sodium iodide (NaI(Tl)) scintillation detectors which all point in different directions, along with a data processing unit and a power box. The NaI detectors measure photons with energies up to 1 MeV, while the BGO detectors measure photons with energies above approximately 200 keV. Since only the most powerful solar flares produce significant count rates above 100 keV, this thesis makes use of the NaI detectors. The diameter of the NaI scintillating crystals is 12.7 cm, and the thickness is 1.27 cm. Photons pass through 0.2 mm of Be and 0.7 mm of Si, which determine the energy range of the transmitted photons, before reaching a NaI detector. Each detector has a photomultiplier tube attached to convert the photons produced by the scintillators into an electric current. Two types of data are produced: CSPEC with 128 energy channels, and CTIME with 8 energy channels. The CSPEC data were used for this thesis, and the energy channels were combined into three energy ranges: 6–25 keV, 25–50 keV, and 50–100 keV. These energy ranges were chosen so that comparisons could be made with data from NASA's *Reuven*

Ramaty High Energy Solar Spectroscopic Imager (RHESSI), however the RHESSI data for the sample of flares examined in Chapter 5 did not show any significant QPP signals using the methods described in Chapter 4. The time cadence of the CSPEC observations is 4.096 s, or 1.024 s when the count rate exceeds a certain threshold and GBM goes into 'trigger' mode for a set amount of time. The trigger threshold is approximately 0.7 photons $\mathrm{cm}^{-2}\,\mathrm{s}^{-1}$ in the 50–300 keV energy range. A better time resolution can be obtained from the CTIME data, with a cadence of 0.256/0.064 s, however this data is noisier and hence it was not found to offer much of a benefit over the CSPEC data for the study of QPPs. Since the different GBM detectors point in different directions, the angle between the detectors and the Sun must be checked, which was done using the IDL Solar Software routine *gbm_get_det_cos*. Data from the most sunward NaI detector at the time of the flare were used with the exception of flares greater than M5 class, where data from the most sunward detector may be subject to discontinuities due to gain changes. Therefore the second most sunward detector was chosen for these flares. Because of the orbit of the *Fermi* satellite, GBM cannot observe solar flares while in the Earth's shadow.

2.4 *Vernov*/DRGE

Hard X-ray (HXR) data were also obtained with the *Detector of the Roentgen and Gamma-ray Emissions* (DRGE) instrument aboard the Russian satellite *Vernov* (Myagkova et al. 2016). The spacecraft had a solar-synchronous orbit with the following parameters: an apogee of 830 km, perigee of 640 km, inclination of 98.4°, and an orbital period of 100 min. It was launched on 2014 July 8 and operated until 2014 December 10. The DRGE instrument included four identical detector blocks (DRGE11, DRGE12, DRGE21 and DRGE22), based on a NaI(Tl)/CsI(Tl) phoswich. The diameter of both scintillators was 13 cm, while the NaI(Tl) thickness was 0.3 cm, and the CsI(Tl) thickness 1.7 cm. These detector blocks were designed for measuring terrestrial gamma flashes and other atmospheric phenomena, so they were directed towards the Earth. The Sun was to the side of the detectors ($\sim$90° from the zenith angle) during the whole period of flare observations, so the effective area of the detectors was only a few cm^2. A more detailed description of the experiment along with a catalogue of HXR solar flares from the active regions NOAA 12172 and 12192 observed by *Vernov* is given in Myagkova et al. (2016). Six flares from this catalogue were used in this thesis: those where the possibility of detecting QPPs appeared most evident on visual inspection. The monitoring parameter 'count rates of all events in NaI' was used, and for solar flare emission this refers to the integral channel of photons with energy >30 keV. The time resolution of the measurements was 1 s. *Vernov* was a polar low-altitude satellite, thus the background conditions

for solar flares were far from optimal, hence two methods of background rejection were used. In the equatorial regions and in the polar caps the background was estimated from the count rates shortly before and after a flare, and in the regions close to the Earth's radiation belts count rates from the previous orbits were taken into account. Poisson counting statistics was assumed, so the uncertainties for each count rate measurement were taken to be equal to the square root of the count rate.

2.5 Nobeyama Radioheliograph

The *Nobeyama Radioheliograph* (NoRH) (Nakajima et al. 1994) is a radio interferometer dedicated to full-disk solar observations consisting of 84 antennas, each with a dish diameter of 80 cm, arranged in a 490 m by 220 m T-shape array. This configuration allows the solar disk to be resolved with a spatial resolution of around 10 arcseconds for 17 GHz observations and 5 arcseconds for 34 GHz, although only the non-spatially resolved correlation data are used in this thesis. NoRH has been operating since 1992, and observations are made between 22:45 and 06:30 UT each day. The temporal resolution of the correlation data is 1 s, and the available wavelengths are 17 and 34 GHz. The 17 GHz data are used in this thesis because only the larger flares can be seen at the 34 GHz microwave frequency, and the 17 GHz microwave frequency tends to show more temporal sub-structure of the flares. The 17 GHz time series data is measured as an 'averaged correlation amplitude' rather than flux, and this correlation data is more sensitive to microwave emission from spatially compact sources, such as flares, rather than the quiet Sun emission. Correlation coefficients are measured between the signals recorded by different antennas in the array, and those corresponding to high spatial frequencies, determined by the antenna spacing, are averaged. The chosen spatial frequency, above which the correlation coefficients are averaged over, corresponds to a source size of 24 arcseconds.

The uncertainty of the data was estimated to be 1.1911749×10^{-5} instrumental units, which is the standard deviation of a flat section of data (see Section 4.5).

2.6 *Kepler*

NASA's *Kepler* mission (Borucki et al. 2010; Koch et al. 2010) made white-light photometric observations of nearly 200,000 astrophysical targets (Huber et al. 2014) inside its 115 $\deg^2$ field of view between 2009 and 2013. The primary purpose of *Kepler* was the detection of dips in the brightness of solar-like stars due to the transit of an Earth-size exoplanet in the habitable zone. Hence most of the stars observed by *Kepler* are on the main sequence, with spectral types ranging from F to M. The

telescope is a Schmidt type that is sensitive to wavelengths in the 423–897 nm range. It has an aperture of 0.95 m, a mirror diameter of 1.4 m, and photons are collected by a CCD array. To give the spacecraft an uninterrupted view of the same patch of sky, it is in an Earth-trailing orbit about the Sun.

The *Kepler* field of view is split between detector pixels that each cover a 3.98×3.98 arcsecond patch of sky. Optimal apertures, or 'postage stamp' images, are defined around each of the target stars, with the size of the aperture chosen such that the signal to noise ratio is maximised (Batalha et al. 2010): hence the image size scales with the target brightness. Only data recorded in pixels within these optimal apertures are stored. For each value in a target light curve, there is a corresponding postage stamp image containing the pixel data, and these image time series are stored in target pixel files (Kinemuchi et al. 2012). The images can be used to check for artefacts in the light curves, for example whether or not a brightness enhancement due to a flare occurs within the point spread function of the target (Maehara et al. 2012).

In order to determine properties of an exoplanet that cannot be seen directly, some properties of its host star must be known. Therefore the *Kepler* mission also provides the *Kepler* Input Catalogue (KIC) (Brown et al. 2011), which contains properties such as the stellar effective temperature ($T_{\rm eff}$), radius ($R_\star$), and surface gravity ($\log g$) for the majority of stars observed. These properties cannot be determined from the *Kepler* data alone, so they were estimated using the Castelli & Kurucz (CK) ATLAS9 stellar atmosphere models (Castelli & Kurucz 2004) and multiple waveband brightness magnitude measurements of the stars. This approach was chosen over a more reliable classification via spectroscopy due to the huge number of targets. The photometric measurements were made especially for the *Kepler* mission with the Fred Lawrence Whipple Observatory 1.2 m telescope. A custom-made filter named $D51$, centred on a wavelength of 510 nm that is sensitive to surface gravity and metallicity, was used and this was combined with measurements using g, r, i, and z filters, similar to those used by the Sloan Digital Sky Survey. These measurements were supplemented with J, H, and K filter measurements from the 2MASS catalogue (Skrutskie et al. 2006) and were then used to calculate seven independent colour magnitudes. These colour magnitudes were compared with synthesised colour magnitudes from the CK stellar atmosphere models, and Bayesian posterior probability maximisation was used to determine stellar parameters based on these model atmospheres. Due to the nature of these parameter estimations, however, many have since been found to be inaccurate. Therefore this thesis makes use of updated stellar parameters from Huber et al. (2014), who collected together improved estimations of the stellar parameters from the scientific literature made using a variety of techniques, such as additional photometry, asteroseismology, spec-

troscopy, and exoplanet transits. This updated catalogue also includes parameters for the stars without estimated parameters in the original KIC.

The majority of data from *Kepler* have a cadence of 30 min, but several thousand stars have also been observed with a 1 min cadence. Despite its primary purpose being to allow the detection of (preferably habitable) exoplanets, the high sensitivity and time resolution of its observations means that it is also proving to be a valuable resource for the study of white-light stellar flares. In addition, the availability of data with a cadence of 1 min makes *Kepler* suitable for studying QPPs with periods greater than a few minutes, allowing for the sample of known stellar flares with QPPs to be increased substantially.

Two types of flux data are available for each light curve: simple aperture photometry (SAP) and pre-search data conditioning simple aperture photometry (PDCSAP). The main difference is that PDCSAP data has had artefacts and systematic trends removed (Kinemuchi et al. 2012). The pipeline module used to produce the PDCSAP flux is designed to optimise the data for the detection of exoplanet transits, however in some cases variations and artefacts that are astrophysical in nature and may be related to flares/QPPs are also removed. Fortunately, SAP flux data is suitable for the study of stellar flares, as the flares can easily be distinguished from most artefacts by comparing with the PDCSAP data, and the timescales of systematic trends are much greater than the durations of the flares. Hence the SAP data was used for the work presented in Chapter 6 of this thesis.

Chapter 3

Data analysis

3.1 Least-squares data fitting

Least-squares fitting is one of the most common approaches to fitting a model to data, and involves minimising the chi-squared statistic for data with uncertainties in the ordinates:

$$\chi^2 = \sum_{n=1}^{N} \left(\frac{X_n - \mu_n}{\sigma_n} \right)^2 , \tag{3.1}$$

where X_n is an observed ordinate, σ_n is the uncertainty in X_n, μ_n is the ordinate value predicted by the model, and N is the number of data points. A minimum in χ^2 occurs when the partial derivatives of χ^2 with respect to the model parameters all equal zero, and χ^2 is used rather than χ so that the partial derivatives can be treated as continuous functions. There are two forms of least-squares fitting: linear and nonlinear. Linear least-squares may be used when the model parameters are linear in the model, which is the case for straight line and polynomial models. For example, when performing a linear least-squares of a linear model, with the form $X_n = mt_n + c$, the χ^2 value to be minimised is

$$\chi^2(m, c) = \sum_{n=1}^{N} \left(\frac{X_n - mt_n - c}{\sigma_n} \right)^2 . \tag{3.2}$$

Then the partial derivatives with respect to the two unknown parameters, m and c, are

$$\frac{\partial \chi^2}{\partial m} = 2m \sum_n \frac{t_n^2}{\sigma_n} + 2c \sum_n \frac{t_n}{\sigma_n} - 2 \sum_n \frac{X_n t_n}{\sigma_n} = 0 , \tag{3.3}$$

and

$$\frac{\partial \chi^2}{\partial c} = 2m \sum_n \frac{t_n}{\sigma_n} + 2c \sum_n \frac{1}{\sigma_n} - 2 \sum_n \frac{X_n}{\sigma_n} = 0 . \tag{3.4}$$

These two simultaneous equations can be solved for m and c to give the best fitting straight line. For nonlinear least-squares fitting, where one or more of the model parameters are not linear in the model (such as a QPP signal modelled as a sinusoidal function), the best fitting parameters cannot usually be calculated analytically. Therefore for the nonlinear case an iterative approach is used, where the partial derivatives of χ^2 are calculated for a set of initial guesses for the parameters, then in each iteration the parameter estimates are adjusted and refined such that χ^2 is minimised. This iterative approach relies on the initial guess parameters being reasonably close to the true best fit parameters. If the model being fitted to $X_n(t_n)$ is a function of t_n with a set of K parameters, $\mathbf{a} = (a_1, a_2, \ldots, a_K)$, then the goal is to find the set of values for $\mathbf{a}$ such that

$$\frac{\partial \chi^2}{\partial a_k} = 0 \tag{3.5}$$

for all $k = 1, 2, \ldots, K$. If it is assumed that the initial guesses for the parameters, $\mathbf{a}^0$, are sufficiently close to the best fit values, so $\mathbf{a} = \mathbf{a}^0 + \delta\mathbf{a}$, then a Taylor expansion can be made of the partial derivatives with the second order and higher terms neglected (Riley et al. 2006):

$$\left.\frac{\partial \chi^2}{\partial a_k}\right|_{\mathbf{a}=\mathbf{a}^0+\delta\mathbf{a}} \approx \left.\frac{\partial \chi^2}{\partial a_k}\right|_{\mathbf{a}=\mathbf{a}^0} + \sum_{l=1}^{K} \left.\frac{\partial^2 \chi^2}{\partial a_k a_l}\right|_{\mathbf{a}=\mathbf{a}^0} \delta a_l \,. \tag{3.6}$$

This Taylor approximation can be set to zero, and the values of $\delta\mathbf{a}$ can be found by solving the set of linear simultaneous equations that result. If $\mathbf{a}^0$ is too far from $\mathbf{a}$ then the first order Taylor approximation is inaccurate, so the partial derivatives that are approximated in Eq. 3.6 will not equal zero. The new parameters that are obtained, $\mathbf{a}^1$, will be closer to $\mathbf{a}$, however, so the process can be repeated to bring the partial derivatives even closer to zero. A successful nonlinear least-squares fit will converge on a minimum value of χ^2, and the iterative process stops when the partial derivatives of χ^2 become sufficiently close to zero. The fit may not converge if poor estimates of the parameters are given initially, or if the model is a poor approximation of the data.

A disadvantage of using least squares fitting rather than other methods is that it is more heavily influenced by outlying points, since the square of the residual is used in the minimisation. Fortunately the data fitted in this thesis do not contain significantly outlying points. Another disadvantage that applies to the nonlinear least squares fitting of more complicated models, where χ^2 has multiple minima, is that the iterative process will converge on the closest local minimum to the initial guess parameters, which may not be the global minimum. Hence this process may not find the true best fitting parameters if initial guess parameters that are not close

enough to the true best fit parameters are used.

This thesis makes use of both linear and nonlinear least-squares methods, to fit linear relationships between different quantities and to fit nonlinear models to flare data. In addition, the calculation of Lomb-Scargle periodograms (that are used in Chapters 4 and 5) involves the least-squares fitting of sinusoids to time series data. This is discussed further in Section 3.2. Another method for fitting models to data is maximum likelihood estimation, which is more general than least-squares fitting because it does not assume that the data uncertainties follow a Gaussian distribution. Instead the data are considered to be drawn from a distribution, according to some model with a particular set of parameters. The 'likelihood' for each data point is the calculated probability density for that data point, and the combined likelihood for the data can be found by multiplying together the likelihoods for each of the individual data points. Hence the likelihood refers to the plausibility of the observed data given the model parameters, and the model parameters can be optimised in order to find the maximum likelihood for generating the observed data. Maximising the likelihood function is equivalent to minimising the corresponding error function, where Eq. 3.1 is an example of an error function, hence if the data are drawn from a Gaussian distribution then maximum likelihood fitting is equivalent to nonlinear least-squares fitting.

For least-squares fitting the optimisation of the model parameters is usually done using a gradient-based approach (as described above, where the gradients are with respect to the model parameters), while for maximum likelihood fitting there may be occasions when the likelihood function is too complicated for a gradient-based approach to be used. In this case a Markov chain Monte Carlo (MCMC) sampling algorithm can be used instead. One of the popular MCMC algorithms is called an ensemble sampler, which makes use of 'random walkers'. These random walkers are initial estimates of the model parameters that are allowed to vary randomly, where each random step is a sample drawn from a known/assumed distribution. The new set of parameters may or may not be accepted, based on whether the calculated likelihood is greater for the new set of parameter guesses, and also based on priors for each parameter, where a prior is a probability distribution that a parameter is expected to follow. This random step process is repeated until the walkers converge on the distribution specified by the likelihood or priors. The MCMC approaches tend to be slower than the gradient-based approaches for least-squares or maximum likelihood fitting, but have the advantage of being more suitable for complicated parameter distributions, where the likelihood functions cannot be solved analytically. MCMC is also more suitable where the likelihood as a function of the parameters is not Gaussian, and hence the uncertainties in the parameters may be asymmetric. In this case an MCMC approach would produce more accurate uncertainty estimates

for the model parameters. In addition, the use of priors means than MCMC sampling is compatible with Bayesian statistics, and extra information about the model parameters can be used to constrain the parameters and reduce their uncertainties.

3.1.1 Monte Carlo simulations

All measurements have an associated level of uncertainty, and these uncertainties must be accounted for when fitting data or testing for correlations. In many situations it is convenient to estimate uncertainties on the parameters of a fitted model, or data that has undergone some kind of operation where standard error propagation cannot be used, using Monte Carlo simulations. Monte Carlo simulations were used to estimate uncertainties associated with fitted models in Chapters 4, 5, and 6, and for each case, the basic approach was as follows. Each value in a set of time series data had a random number added to it, where the random number was drawn from a Gaussian distribution with a mean of zero and a standard deviation equal to the uncertainty associated with that value. In Chapters 4 and 5 the Lomb-Scargle periodogram was calculated for this randomised time series before a model was fitted to it, whereas in Chapter 6 a model was fitted directly to the time series. The parameters and fitted model ordinates were saved, and this process was repeated 10,000 times with a different set of random numbers each time. Having 10,000 repeats was adequate to acquire a sense of how the fitted model parameters and/or ordinates were distributed for the model fits in this thesis, however fewer could be used to reduce computation time, or more could be used to improve accuracy. The fitted model parameters and ordinates used in this thesis followed an approximately Gaussian distribution, so Gaussian models could be fitted to the histograms of the parameters/ordinates obtained from the simulations to give an estimate of the true value and uncertainty for each of the parameters/ordinates.

3.2 Lomb-Scargle periodogram

The Lomb-Scargle (LS) periodogram was proposed independently by both Lomb (1976) and Scargle (1982) as a means to efficiently estimate the spectral power at a particular frequency; hence it can be used for the detection of periodic signals in time series data in a similar manner to Fourier analysis. It has the advantage over other methods of producing power spectra that if the data is unevenly time sampled, the white noise in the LS periodogram follows the same chi-squared, two degrees of freedom (d.o.f.) probability distribution as that of evenly time spaced data (see Section 3.2.1).

The basic approach of the LS periodogram is the least-squares fitting to the data of sinusoidal models with different frequencies, where the periodogram is

constructed from the χ^2 goodness-of-fit statistic at each frequency. More precisely, it is defined as

$$I_X(\omega) = \frac{1}{2}\left\{ \frac{\left(\sum_n X_n \cos\left[\omega(t_n - \tau)\right]\right)^2}{\sum_n \cos^2\left[\omega(t_n - \tau)\right]} + \frac{\left(\sum_n X_n \sin\left[\omega(t_n - \tau)\right]\right)^2}{\sum_n \sin^2\left[\omega(t_n - \tau)\right]} \right\}, \quad (3.7)$$

where X_n is the signal at time t_n, ω is the angular frequency, the sum over n is from 0 to $N-1$, N is the number of samples in the time series, and τ is defined by

$$\tau = \frac{1}{2\omega} \arctan\left(\frac{\sum_n \sin(2\omega t_n)}{\sum_n \cos(2\omega t_n)} \right). \quad (3.8)$$

Another difference between the LS periodogram and the discrete Fourier transform (DFT) is as follows. For the DFT, the length of the time series and time cadence determines the frequency values: often referred to as the 'natural frequencies'. The LS periodogram does not have this restriction, however, and the user is free to specify their own values of ω within the limits of the data. Examples of limitations on the choice of frequencies include a Nyquist-like limit defining the highest frequency observable if the time series data is evenly spaced, and the finite length of the times series: equivalent to imposing a rectangular window function to the time series. Multiplying a time series by a rectangular window function is equivalent to convolving the Fourier transform or periodogram with a sinc function, resulting in the frequency broadening of peaks in the spectrum and the appearance of side lobes. This broadening effect is what limits the frequency spacing in the DFT to $\frac{1}{N\Delta t}$, so if the periodogram is oversampled (the periodogram frequencies are specified to have a higher resolution than the natural frequencies of the DFT), the periodogram powers are no longer independent. The periodogram powers being independent is a requirement for the methods described in Chapter 4, therefore in this thesis the periodogram frequencies used for a particular time series are equal to the natural frequencies of the DFT.

When the time series is evenly sampled, Eq. 3.7 reduces to the classical periodogram:

$$I_X(\omega) = \frac{1}{N}\left\{ \left(\sum_n X_n \cos(\omega t_n)\right)^2 + \left(\sum_n X_n \sin(\omega t_n)\right)^2 \right\}, \quad (3.9)$$

which is equivalent to the squared absolute value of the DFT normalised by N

(provided the frequency values, $f = \frac{\omega}{2\pi}$, used are the same as the natural frequencies of the Fourier transform):

$$I_X(\omega) = \frac{1}{N}\left|\sum_n X_n \exp(-i\omega t_n)\right|^2 , \tag{3.10}$$

where $i = \sqrt{-1}$.

3.2.1 Confidence levels

In terms of assessing the significance of a peak in a power spectrum, Scargle (1982) showed how the false alarm probability can be found for data with white noise. For evenly time-spaced data, the periodogram is equivalent to the Fourier power spectrum with additional normalisation (see Eqs. 3.9 and 3.10), which is equal to the sum of the squares of the real and imaginary parts of the Fourier transform. For a white noise time series, where each value is drawn at random from a Gaussian distribution, the real and imaginary parts of the Fourier transform should also be Gaussian distributed random variables. Squaring a Gaussian distributed random variable results in a chi-squared, one d.o.f. distributed random variable, x, where the chi-squared probability density function for ν degrees of freedom is

$$p_{\chi^2_\nu}(x) = \frac{x^{\frac{\nu}{2}-1}\mathrm{e}^{-x/2}}{2^{\frac{\nu}{2}}\Gamma\left(\frac{\nu}{2}\right)} . \tag{3.11}$$

This links back to Section 3.1, where the square of the residuals between the data and the fitted model follow a chi-squared, one d.o.f. distribution and hence the chi-squared statistic can be used as a goodness-of-fit measurement. Adding together two chi-squared, one d.o.f. distributed variables results in a chi-squared, two d.o.f. distributed random variable. Hence white noise follows a chi-squared, two d.o.f. distribution in the Fourier power spectrum. In addition, Scargle (1982) demonstrated that when using unevenly time spaced data, if the LS periodogram is used rather than the classical periodogram, the noise follows the same distribution. The probability density of a chi-squared, two d.o.f. distributed variable, x, whose distribution has a mean value of two is

$$p_{\chi^2_2}(x) = \frac{1}{2}\mathrm{e}^{-x/2} . \tag{3.12}$$

The probability of having a value X that is greater than some threshold x' is therefore

$$\Pr\left\{X > x'\right\} = \int_{x'}^{\infty} \frac{1}{2}\mathrm{e}^{-x/2}\mathrm{d}x = e^{-x'/2} . \tag{3.13}$$

Since the power spectrum is positive everywhere, x and x' in the above equation are always positive. When considering a power spectrum sampled at $N' = N - 1$

independent frequencies (the Nyquist frequency is neglected as it follows a chi-squared one d.o.f. distribution; Vaughan 2005) the probability is equivalent to

$$\Pr\left\{X > x'\right\} = 1 - (1 - \epsilon_{N'})^{1/N'} \approx \epsilon_{N'}/N' \,, \tag{3.14}$$

where $\epsilon_{N'}$ is the false alarm probability, and the approximation holds when $\epsilon_{N'}$ is small (Chaplin et al. 2002). The false alarm probability is defined as the probability of observing a peak in the power spectrum above some threshold power (Scargle 1982; Horne & Baliunas 1986), and this threshold power can be calculated by equating Eqs. 3.13 and 3.14 and solving for x'. For example, the 99% confidence level in the power spectrum is the power threshold corresponding to a false alarm probability of 0.01, and refers to the level above which there is only a 1% chance of observing a peak in the power spectrum of a Gaussian distributed random (white noise) time series. The above expressions are only valid, however, when considering data with white noise that is chi-squared, two d.o.f. distributed in the power spectrum. This issue is discussed further in Chapter 4.

3.3 Wavelet spectra

A wavelet transform (Daubechies 1990) allows a power spectrum of time series data to be made that gives time evolution information, making it useful when transient or non-stationary periodic signals are present in the data that might otherwise be hidden in a periodogram. The wavelet transform involves multiple convolutions of a chosen wavelet function with the time series data, where for each convolution the width of the wavelet function is changed. The convolution provides time information, while changing the width of the wavelet gives frequency information. It has the advantage over windowed Fourier transforms/periodograms that it does not require a window with a fixed width to be predefined. In addition, the most appropriate choice of window width for one signal may not be the best choice for another, so using a wavelet transform avoids this problem. A potential drawback of both the wavelet and windowed Fourier transforms when compared to conventional Fourier transforms/periodograms is that the uncertainty principle of signal processing ($\Delta t \Delta\omega \geq \frac{1}{2}$) means that the gain of time resolution requires the loss of frequency resolution (and vice versa).

The continuous wavelet transform of a function $X(t)$ is defined as

$$W_X(s, t') = \int_{-\infty}^{\infty} \Psi^*_{s,t'}(t) X(t) \mathrm{d}t \,, \tag{3.15}$$

where $\Psi^*_{s,t'}(t)$ is the complex conjugate of the family of wave functions

$$\Psi_{s,t'}(t) = \frac{1}{\sqrt{s}}\Psi\left(\frac{t-t'}{s}\right), \tag{3.16}$$

which are scaled and translated from a 'mother' wavelet function, $\Psi(t)$, with a scale factor, s, that defines the width/frequency of the wavelet function, and a time shift, t'. Requirements of the mother wavelet function are that it should be localised in time and frequency, it should have a mean of zero:

$$\int_{-\infty}^{\infty} \Psi(t)\mathrm{d}t = 0\,, \tag{3.17}$$

and it should be normalised (Farge 1992):

$$\int_{-\infty}^{\infty} \Psi(t)\Psi^*(t)\mathrm{d}t = 1\,. \tag{3.18}$$

For discrete time series data, X_n, with a time step Δt, the continuous wavelet transform is

$$W_X(s,n') = \sum_{n=0}^{N-1} \Psi^*_{s,n'}(t)X_n\,, \tag{3.19}$$

where the family of wavelet functions is instead written

$$\Psi_{s,n'} = \sqrt{\frac{\Delta t}{s}}\Psi\left[\frac{(n-n')\Delta t}{s}\right]. \tag{3.20}$$

The $\sqrt{\frac{\Delta t}{s}}$ factor ensures that the wavelet functions are normalised, so that the wavelet functions themselves do not affect the amplitudes given by the wavelet transform. To obtain the wavelet power spectrum, the square of the absolute of the wavelet transform should be taken, $|W_X(s,n')|^2$, similar to how the Fourier power spectrum is obtained from the Fourier transform.

The choice of mother wavelet determines the type of signal that is best captured by the wavelet transform, with a wavelet that resembles the signal of interest being most appropriate. Since QPP signals are transient and periodic, this thesis makes use of the Morlet mother wavelet, which consists of a sinusoid modulated by a Gaussian envelope and whose family of wavelet functions is defined as

$$\Psi_{s,t'}(t) = \frac{1}{\pi^{1/4}s^{1/2}}\exp\left(\frac{i\omega_0(t-t')}{s}\right)\exp\left(-\frac{(t-t')^2}{2s^2}\right). \tag{3.21}$$

The most commonly used value for ω_0 is 6 as it satisfies the condition that the wavelet mean should be zero (Torrence & Compo 1998), as stated above, hence it is the value used for the wavelet transforms in this thesis. As mentioned previously,

a range of different scales, s, need to be used to sample different frequencies for the wavelet transform. For this thesis the standard choice of scales were used, as described by Torrence & Compo (1998):

$$s_j = s_0 2^{j\Delta j}\,, \tag{3.22}$$

with $s_0 = 2\Delta t$, $\Delta j = 0.125$, $j = 0, 1, \ldots, J$, and

$$J = \Delta j^{-1} \log_2(N\Delta t/s_0)\,, \tag{3.23}$$

where N is the number of data points in the time series, and Δt is the time cadence.

The algorithm used to calculate the wavelet transform takes advantage of the convolution theorem:

$$\mathcal{F}(x * y) = \mathcal{F}(x)\mathcal{F}(y)\,, \tag{3.24}$$

where x and y are functions, $\mathcal{F}(x)$ denotes the Fourier transform of x, and $x * y$ is the convolution of x with y. This can be rewritten as

$$x * y = \mathcal{F}^{-1}\left[\mathcal{F}(x)\mathcal{F}(y)\right]\,, \tag{3.25}$$

and hence the continuous wavelet transform in Eq. 3.19 can be written

$$W_X(s, n') = \sum_{k=0}^{N-1} \mathcal{F}(\Psi^*_{s,n'})\mathcal{F}(X_n)e^{i\omega_k n'\Delta t}\,, \tag{3.26}$$

where ω_k is the angular frequency and k is the frequency index. The use of fast Fourier transforms means that the wavelet amplitudes for all s and n' can be calculated simultaneously. The fast Fourier transform assumes that the data is cyclic (Torrence & Compo 1998), which is often not the case, so the wavelet transform is likely to produce erroneous powers where it encounters the end of the time series being joined with the beginning. These errors in the calculated powers are referred to as edge effects. Because of the known errors in the calculated powers at early and late times, wavelet power spectra are usually plotted with a 'cone of influence' overlaid, which shows the region where edge effects may be present and hence the calculated powers are unreliable. The edges of the cone of influence are put at the e-folding times of the wavelet function amplitude at each scale. The impact of the edge effects can sometimes be mitigated by padding one end of the time series with zeros or a linear function that joins the first and last values.

3.4 Data detrending

Flare time series data naturally contain a trend, which in this thesis is defined as variations in intensity that are not due to noise or the QPP signal being searched for. In solar flare light curves, the trend is the flare time profile itself, while in stellar flare light curves there may also be contributions to the trend related to differential velocity aberration, where the target star appears to move across on the CCD array as the spacecraft orbits the Sun; orbital motion due to the star being a binary; rotational variability due to starspots; and/or transits.

Aperiodic trends in time series data result in a power spectrum with a power law shape, where there is more power at lower frequencies than higher frequencies. This can hide peaks due to a periodic signal in the spectrum, so it often desirable to detrend the data so that any periodic signals are made more visible in the power spectrum. There are several approaches that can be taken to detrend the data. If a complete theoretical model existed that could describe all flares, then the ideal option would be to fit the model to the flare light curves, and subtract the fitted model in order to detrend. Although most flare light curves follow the same general shape, there is enough variation between them to make finding a general enough model that fits them all accurately very difficult. The problem seems to be worse for solar flares than stellar flares. Solar flares can be observed more easily and more of their fine structure revealed, whereas the intensity and time resolution of stellar flare observations are generally much worse, meaning that only the most powerful stellar flares can be resolved above the noise level, and so their time profile tends to appear simpler than solar flares. Hence the decay phase of stellar flares can often be fitted to a good degree of accuracy using an exponential decay function, plus a low-order polynomial to account for non-flare related trends mentioned in the previous paragraph. Although the work in Chapter 6 ignores the rise phase of the flares observed by *Kepler* due to the lack of data points during that phase, a good fit of the whole time profile of flares that are better resolved can be made by convolving a Gaussian with one or two exponential decays (Gryciuk et al. 2017).

An approach that has been commonly used to detrend solar flare light curves in the past is to smooth the light curve, by convolving it with a rectangular window function, then subtract the smoothed light curve from the original light curve. The convolution of time series data with a rectangular window in equivalent to multiplying the data by a sinc-based function in the Fourier domain, due to the convolution theorem. Auchère et al. (2016) showed that the power spectrum of the detrended time series

$$X_d(t) = X_0(t) - X_0(t) * W(t)\,, \tag{3.27}$$

where $W(t)$ is a rectangular window function, can be written

$$|\mathcal{F}(X_d)|^2 = |\mathcal{F}(X_0)|^2 \, |1 - \mathcal{F}(W)|^2 \tag{3.28}$$

$$= |\mathcal{F}(X_0)|^2 \left(1 - \frac{\sin(\pi\nu\Delta t)}{\pi\nu\Delta t}\right)^2 , \tag{3.29}$$

where ν is the frequency and Δt is the width of the rectangular window function. Hence detrending by smoothing and calculating the power spectrum is equivalent to multiplying the power spectrum of the original data by $(1 - \mathrm{sinc}(\pi\nu\Delta t))^2$. Auchère et al. (2016) also showed that while the impact of this multiplying term is minimal for data with no power law dependence in the power spectrum (which probably would not require detrending in the first place), if there is a power law dependence then the power spectrum is drastically altered. Both the powers of the high and low frequencies are suppressed, while powers around a particular frequency, that depends on the power law index and the width of the rectangular window function, are enhanced. Then, if confidence levels are calculated assuming white noise with no power law dependence in the power spectrum, it can appear that a significant peak is present that is purely an artefact of the detrending method.

Another method that may be used to detrend data is a cubic spline interpolation. For this approach a subset of data points are selected from the time series, and these selected points are usually chosen to be spaced at regular time intervals. Cubic polynomials are then used to interpolate between the selected data points, with the condition that the overall function should be smooth (i.e. that the first and second order derivatives should be continuous everywhere). The cubic spline approach can be very effective for removing gradual trends in data. It has the advantage over using a polynomial fit to the whole time series that high order polynomials are not required to get a sufficiently good fit, which would risk overfitting and introducing artificial oscillatory behaviour into the detrended data. The disadvantage, however, is that rapid background changes in the data, as are usual during the impulsive phase of a flare, are not well fit without increasing the number of data points used for the interpolation, and doing so risks fitting the signal one wishes to detect. There is also the issue of subjectivity when choosing the size of the intervals interpolated over, and the best choice for one flare may not be the best for another when the timescales of the background trends and of QPP signals vary.

Because of the disadvantages with the detrending methods described above, the following chapter describes how one can reliably test for the presence of periodic signals in time series data with trends and/or correlated noise without detrending. This method has been used for the statistical study of QPPs in solar flares described in Chapter 5, while for the study of QPPs in stellar flares in Chapter 6 the simpler flare light curves have been detrended using well fitted models.

3.5 Correlation coefficients

3.5.1 Pearson

The Pearson's correlation coefficient gives a measure of the linear relationship between two variables. It is defined as

$$\rho_{x,y} = \frac{\sum_{i=1}^{N}(x_i - \bar{x})(y_i - \bar{y})}{\sqrt{\sum_{i=1}^{N}(x_i - \bar{x})^2 \sum_{i=1}^{N}(y_i - \bar{y})^2}}, \tag{3.30}$$

where x and y are the two variables, $\bar{x}$ represents the mean of x, and N is the number of values of x and y (Press et al. 1986). The coefficient may have values between -1 and +1, where a value close to -1 indicates a strong negative relationship, close to 0 indicates no correlation, and close to +1 indicates a strong positive relationship. The Pearson's correlation test has the disadvantage of only being a suitable test of linear relationships, and being sensitive to outlying points. For cases where the relationship may be non-linear, and/or there may be outlying points, the Spearman's rank correlation coefficient would be more suited.

3.5.2 Spearman

The Spearman's rank correlation coefficient is defined similarly to the Pearson coefficient, but rather than using the actual values of the variables, it uses their rank (Press et al. 1986):

$$\rho_{x,y} = \frac{\sum_{i=1}^{N}(Rx_i - \bar{Rx})(Ry_i - \bar{Ry})}{\sqrt{\sum_{i=1}^{N}(Rx_i - \bar{Rx})^2 \sum_{i=1}^{N}(Ry_i - \bar{Ry})^2}}. \tag{3.31}$$

The values of x and y are ordered from lowest to highest, then the x_i and y_i values are replaced by their ranking compared to the other values (where the ranking goes from 1 to N). For example, if $x = [4.1, 9.6, 2.4, 0.7, 2.5]$ then the rank of x will be $Rx = [4, 5, 2, 1, 3]$. Using the rank of the variables rather than the actual values of the variables means that the Spearman coefficient is a more reliable test for correlation if the relationship between the two variables is non-linear but still monotonic. It also means that outlying points will have less of an influence on the overall result.

Chapter 4

Significance testing for quasi-periodic pulsations in solar and stellar flares

4.1 Introduction

In the past many different approaches to the detection of QPPs in flares have been taken. Some examples of these include manual identification (e.g. Kane et al. 1983; Asai et al. 2001), searching for a peak in the periodogram or wavelet power spectrum (usually after doing some form of detrending of the flare time series data, e.g. Lipa 1978; Aschwanden et al. 1998; Reznikova & Shibasaki 2011; Kupriyanova et al. 2013; Dennis et al. 2017), and empirical mode decomposition (Kolotkov et al. 2015). More recently, questions have been raised regarding the potential for false detections with some of the detrending methods. This is especially an issue for flare time series data which contain intrinsic coloured noise (McAteer et al. 2007; Gruber et al. 2011), where the data is correlated in time and therefore the spectral power is related to the frequency by a power law ($P \propto f^{-\alpha}$). White noise refers to the case where the power law index, α, is equal to zero, while red noise refers to $\alpha \gtrsim 2$, and pink noise for values of α between zero and two. It should be noted that trends in the data will also contribute towards this power-law dependence, rather than it only being the result of correlated noise. In order to remove this power law behaviour and make peaks due to a periodic component of the signal more prominent in the power spectrum, the flare light curve is often detrended. By removing the longer time-scale flare profile from the time series data, only the shorter time-scale QPPs (if present) and noise should be left. This is usually done by subtracting either a model fitted to the flare profile (e.g. Anfinogentov et al. 2013), a boxcar smoothed version of the time series with a pre-selected boxcar width (e.g. Kupriyanova et al. 2013), or an aperiodic trend

determined by empirical mode decomposition (e.g. Cho et al. 2016). It has been noted, however, that detrending can lead to overestimating the significance of peaks in the power spectrum (Inglis et al. 2015) due to the artificial suppression of other spectral components (Gruber et al. 2011). In addition, Auchère et al. (2016) showed that if a signal with a power-law dependence in its power spectrum is detrended by subtracting a boxcar-smoothed version of the signal from the original signal, before calculating the power spectrum, then the power spectrum will contain what looks like a broad peak. This apparent spectral feature is completely artificial, however, and should not be treated as evidence of a true periodic signal (see Section 3.4).

While the trends in flare time series data cannot be considered to be entirely 'random walk' red noise, since there seems to be a general characteristic shape that flare light curves follow (a rapid rise followed by a more gradual decay), finding the true trend of the flare is a huge challenge in itself when many flares show deviations from the characteristic shape. A model that gives a good fit to the flare profile must be chosen, along with suitable initial estimate parameters, to avoid introducing false signals and altering the underlying probability distribution, which would ultimately lead to the calculation of a misleading confidence level. However some flares being very complex in shape (e.g. Li et al. 2017) makes finding a general model that fits all flares to a satisfactory standard much more difficult. In addition to this, the same flare can have a very different time profile when viewed in different energy bands. On the other hand, if a boxcar smooth is used to detrend the most suitable boxcar width must be chosen for each flare. When undertaking a large-scale study of a number of events a minimal amount of manual intervention is preferable, hence methods that avoid detrending seem more appropriate, such as that used by Inglis et al. (2016). Therefore it is necessary to look into detection methods that do not rely on detrending the data.

The standard approach to testing the significance of a peak in the power spectrum for data with white noise is described in Section 3.2.1. Vaughan (2005) demonstrates a related method that also avoids the need to detrend and takes full account of coloured noise and data uncertainties. They then show how it can be used to test for quasi-periodic signals in X-ray light curves of active galaxies, which have a similar signature to QPPs. In this chapter we build on this method and show in detail how it can be applied to solar flare data, so that peaks in the power spectrum found above a certain confidence level may be considered as candidate QPPs. In Section 4.2 the method of Vaughan (2005) is summarised, a more computationally efficient form of the equation to be solved to determine the confidence level is derived, and a description of how this method can be used to search for QPPs in flare light curve data is given. In Section 4.3 we adapt the method to be used with rebinned power spectra, which can help detect QPPs with a broad peak in the

power spectrum. The results of testing the methods on simulated data are shown in Section 4.4, and in Section 4.5 a few examples are given where the methods have been applied to real solar flare data. A summary of this chapter is given in Section 4.6.

4.2 Confidence levels on power-law power spectra

From Vaughan (2005), if $I(f_k)$ is the periodogram power at a particular frequency, f_k, we have

$$I(f_k) = \mathcal{P}(f_k)\chi^2_2/2\,, \tag{4.1}$$

where $\mathcal{P}(f_k)$ is the 'true' power, and $\chi^2_2/2$ is the chi-squared two d.o.f. distributed noise. For data with coloured noise, the power spectrum will follow a power law, which can be fitted with a straight line when working in log space. Solar flare power spectra often follow a broken power law, since the coloured noise component can fall below the white noise level at high frequencies (Gruber et al. 2011; McAteer et al. 2016). The broken power law model can be written as

$$\log\left[\hat{\mathcal{P}}(f)\right] = \begin{cases} -\alpha\log\left[f\right] + c & \text{if } f < f_{break} \\ -\left(\alpha-\beta\right)\log\left[f_{break}\right] - \beta\log\left[f\right] + c & \text{if } f > f_{break}\,, \end{cases} \tag{4.2}$$

where f_{break} is the frequency at which the power law break occurs, α and β are power law indices and c is a constant. The probability density for $2I_k$ (the factor of two appears because the chi-squared distribution is conventionally defined assuming the values following that distribution have a mean equal to the number of degrees of freedom) can then be written as

$$p_{2I_k}(x) = \frac{1}{2\mathcal{P}_k}\mathrm{e}^{-x/2\mathcal{P}_k}\,, \tag{4.3}$$

where x is a dummy variable representing power in the power spectrum, $\mathcal{P}_k$ is equivalent to $\mathcal{P}(f_k)$.

When fitting the 'true' power spectrum, $\mathcal{P}$, with a broken power law model, $\hat{\mathcal{P}}$, the uncertainties on this fitted model will follow a Gaussian distribution in log space, and hence a log-normal distribution in linear space:

$$p_{\hat{\mathcal{P}}_k}(y) = \frac{1}{\sqrt{2\pi}\,yS_k}\exp\left\{-\frac{\left(\ln[y]-\ln[\mathcal{P}_k]\right)^2}{2S_k^2}\right\}, \tag{4.4}$$

with

$$S_k = \mathrm{err}\left\{\log\left[\hat{\mathcal{P}}(f_k)\right]\right\} \times \ln[10]\,, \tag{4.5}$$

where y is another dummy variable representing power, $\mathrm{err}\left\{\log\left[\hat{\mathcal{P}}(f_k)\right]\right\}$ is the uncertainty on the fitted model in log space, and the ln[10] factor accounts for the fact that the uncertainty is defined in terms of log base ten, whereas the log-normal distribution above is defined (by convention) in terms of log base e. In order to find the uncertainties on the model fitted to flare power spectra, uncertainties on the flare light curve data were used in Monte Carlo simulations. While some instruments that observe the Sun include uncertainties for the data provided, many do not. Fortunately in most cases reasonable estimates of the uncertainties can be made. For example, some X-ray observations of the Sun follow Poisson counting statistics, so the uncertainty on each count rate value can be found by taking the square root of the value. For the radioheliograph data used in Section 4.5, an estimate of the uncertainty can be found by calculating the standard deviation of several hours of flat data, in which no flares occur and there are no other features. For the Monte Carlo simulations, random numbers with a mean of zero and standard deviations equal to the uncertainties on the light curve values are added to each of the light curve values. The periodogram is then found, converted to log space, and a broken power law model is fitted using a least-squares method. This is repeated many times (10,000 times for the examples shown in Section 4.5), and for each iteration the initial guess parameters used in the model fit are allowed to vary, in order to prevent a local rather than a global minimum being found by the least-squares fit (for the examples in Section 4.5 parameters of $\alpha = 2$, $\beta = 1$, $c = -3$ and $f_{break} = 0.1$ were allowed to randomly vary with a standard deviation equal to 10% of the parameter value for each iteration). The distributions of the parameters from the repeated power spectrum fits should be approximately Gaussian, and so for each frequency bin of the power spectrum, the uncertainty on the fitted model value will be Gaussian distributed. Hence the distribution of fitted powers at each frequency index can be fitted by a Gaussian model, and the standard deviation of the Gaussian model can be used as an estimate of the uncertainty of the broken power law model at that index.

The probability density of the ratio $\hat{\gamma}_k = 2I_k/\hat{\mathcal{P}}_k$ (the power spectrum with the coloured noise component removed) can be found from (Curtiss 1941):

$$p_{\gamma_k}(z) = \int_0^{+\infty} |y| p_{2I_k}(zy) p_{\mathcal{P}_k}(y) \mathrm{d}y \,, \tag{4.6}$$

where y and z are dummy variables representing different power levels in the power spectrum. The lower limit of this integral is zero rather than negative infinity because the power spectrum is always positive. Integrating this probability density

between γ_{ϵ_k} and infinity gives the probability that a value $\hat{\gamma_k}$ is greater than γ_{ϵ_k}

$$\Pr\left\{\hat{\gamma_k} > \gamma_{\epsilon_k}\right\} = \frac{1}{\sqrt{8\pi}\, S_k \mathcal{P}_k} \int_{\gamma_{\epsilon_k}}^{\infty} \int_0^{\infty} \exp\left\{ -\frac{\left(\ln[y] - \ln[\mathcal{P}_k]\right)^2}{2S_k^2} - \frac{yz}{2\mathcal{P}_k} \right\} \mathrm{d}y\mathrm{d}z\,. \quad (4.7)$$

Substituting in another dummy variable, $w = y/\mathcal{P}_k$ (with $\mathrm{d}y = \mathcal{P}_k\, \mathrm{d}w$), simplifies this to

$$\Pr\left\{\hat{\gamma_k} > \gamma_{\epsilon_k}\right\} = \frac{1}{\sqrt{8\pi}\, S_k} \int_{\gamma_{\epsilon_k}}^{\infty} \int_0^{\infty} \exp\left\{ -\frac{(\ln\, w)^2}{2S_k^2} - \frac{wz}{2} \right\} \mathrm{d}w\mathrm{d}z\,. \quad (4.8)$$

Since the integrand is well-behaved and contains no discontinuities, the order of integration can be swapped (see Fig. 4.1 for plots of the function for different values of S_k). Then the function can be integrated with respect to z, to get

$$\Pr\left\{\hat{\gamma_k} > \gamma_{\epsilon_k}\right\} = \int_0^{\infty} \frac{1}{\sqrt{2\pi}\, S_k w} \exp\left\{ -\frac{(\ln\, w)^2}{2S_k^2} - \frac{\gamma_{\epsilon_k} w}{2} \right\} \mathrm{d}w\,, \quad (4.9)$$

which can be equated to (see Eq. 3.14 in Section 3.2.1)

$$\Pr\left\{\hat{\gamma_k} > \gamma_{\epsilon_k}\right\} \approx \frac{\epsilon_{N'}}{N'}\,, \quad (4.10)$$

and solved numerically in order to find a γ_{ϵ_k} corresponding to each value of the fitted model power spectrum, $\hat{\mathcal{P}}_k$. Figure 4.2 shows plots of Eq. 4.9 and Eq. 4.10 as a function of γ_{ϵ_k}, and the solution is where the two lines cross. In practise it is helpful to subtract Eq. 4.10 from Eq. 4.9, then the solution will be where this function is equal to zero and a root finding algorithm can be used.

The confidence level would be equal to γ_{ϵ_k} if the spectral powers were independent of the frequency and normalised such that the mean power were equal to the number of degrees of freedom of the chi-squared distribution of the noise (i.e. 2 for the regular power spectra, or $2n$ for the rebinned spectra). Instead we are dealing with power spectra that are not normalised and have a power-law dependence, therefore the final step is to ensure correct normalisation. The regular power spectra could be normalised by multiplying by $2/\langle I_k/\hat{\mathcal{P}}_k\rangle$, in order to have a mean of 2, or alternatively γ_{ϵ_k} can be multiplied by $\langle I_k/\hat{\mathcal{P}}_k\rangle/2$ to account for the lack of normalisation. Here I_k is the original power spectrum, $\hat{\mathcal{P}}_k$ is a broken power law fit to the power spectrum, and $\langle I_k/\hat{\mathcal{P}}_k\rangle$ is the mean of the 'flattened' power spectrum (with the power-law dependence removed). Note that the mean calculated in log space is not the same as the log of the mean calculated in linear space (i.e. $\langle \log \mathcal{P}_k\rangle \neq \log\langle \mathcal{P}_k\rangle$), hence the power spectrum as well as the fit must be converted into linear space before calculating this mean. Finally the power-law dependence needs to be accounted for by multiplying $\gamma_{\epsilon_k}\langle I_k/\hat{\mathcal{P}}_k\rangle/2$ by the power

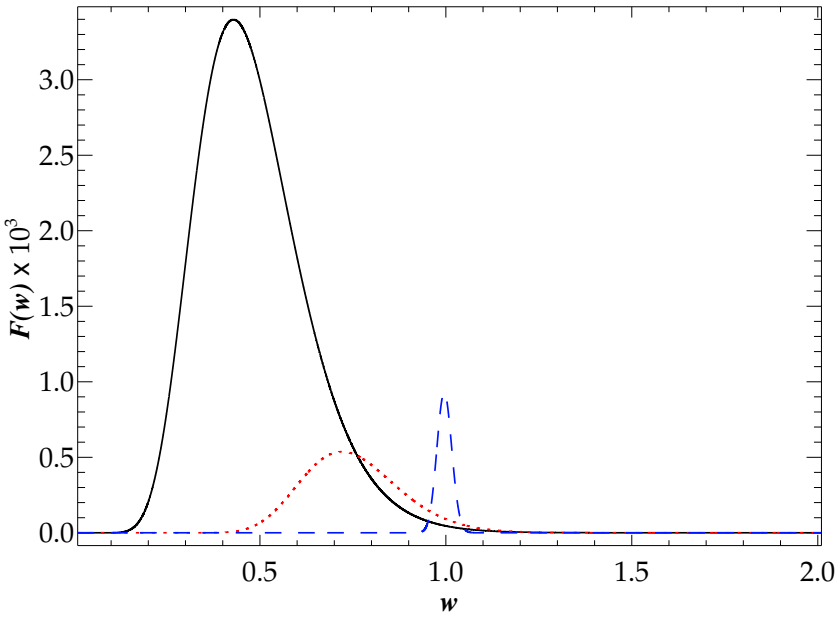

Figure 4.1: Plots of the integrand in Eq. 4.9 as a function of w. The solid black, dotted red and dashed blue lines show the function when S_k is equal to 0.4, 0.2 and 0.02 respectively. The value of γ_{ϵ_k} has arbitrarily been chosen to be equal to 20, which is a typical value.

law fit, or adding if working in log space. Hence the confidence level for the regular power spectrum is equal to $\log[\hat{\mathcal{P}}_k] + \log[\gamma_{\epsilon_k}\langle I_k/\hat{\mathcal{P}}_k\rangle/2]$.

4.3 Confidence levels on rebinned power spectra

Appourchaux (2004) shows how rebinning the power spectrum can improve the detection of short-lived solar acoustic modes, such as wave trains with a highly modulated amplitude, which have power spread across several frequency bins. Van der Klis (1989) and Papadakis & Lawrence (1993) also describe the use of binned or smoothed power spectra in the analysis of X-ray binaries and active galaxies exhibiting quasi-periodic oscillations. A similar method can be applied to candidate QPPs, for example those with exponential or Gaussian damping typical for solar and stellar flares (Pugh et al. 2016; Cho et al. 2016), or those with a small variation of the period. These QPP signals may appear as a broad peak in the power spectrum, with a power spanning more than one frequency bin, and hence considering all of the power contained within the peak (by rebinning the spectrum) rather than separately considering the power in each of the frequency bins will give a better assessment of the significance of the peak.

When summing every n frequency bins, the probability density follows a

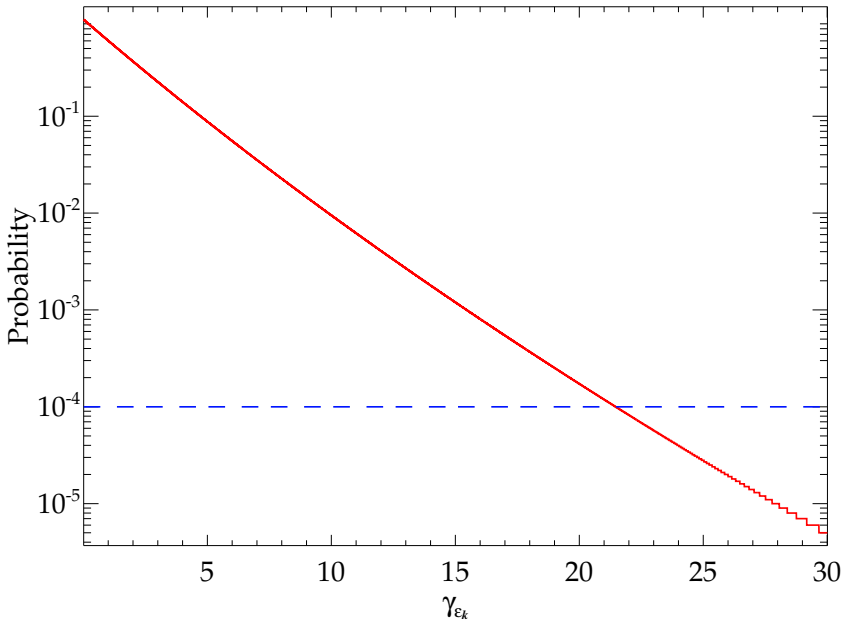

Figure 4.2: Plots of Eq. 4.9 and Eq. 4.10 as a function of γ_{ϵ_k} are shown by the solid red and dashed blue lines respectively. The values of S_k and $\epsilon_{N'}/N'$ have arbitrarily been chosen to be equal to 0.2 and 0.01/100 respectively. The solution we require is where Eq. 4.9 is equal to Eq. 4.10, which corresponds to $\gamma_{\epsilon_k} = 21.467$.

chi-squared $2n$ d.o.f. distribution with a mean equal to $2n$ (Appourchaux 2003):

$$p_{\chi^2_{2n}}(x) = \frac{x^{n-1}\mathrm{e}^{-x/2}}{2^n\Gamma(n)}\,, \tag{4.11}$$

where Γ is the gamma function. Hence the probability distribution followed by the rebinned power spectrum is

$$p_{2nI_k}(x) = \frac{x^{n-1}\mathrm{e}^{-x/2\mathcal{P}_k}}{2^n\mathcal{P}_k^n\Gamma(n)}\,, \tag{4.12}$$

where $\mathcal{P}_k$ is the 'true' rebinned power spectrum which can be fitted by a power law model, $\hat{\mathcal{P}}_k$. Plugging this equation into Eq. 4.6, along with Eq. 4.4 gives

$$p_{\gamma_k}(z) = \int_0^\infty \frac{(yz)^{n-1}}{2^n\mathcal{P}_k^n\Gamma(n)\sqrt{2\pi}\,S_k}\exp\left\{-\frac{(\ln[y]-\ln[\mathcal{P}_k])^2}{2S_k^2} - \frac{yz}{2\mathcal{P}_k}\right\}\mathrm{d}y\,. \tag{4.13}$$

Integrating this probability density from γ_{ϵ_k} up to infinity and substituting $w = y/\mathcal{P}_k$, as before, gives:

$$\Pr\{\hat{\gamma_k} > \gamma_{\epsilon_k}\} = \int_{\gamma_{\epsilon_k}}^\infty\int_0^\infty \frac{(wz/2)^{n-1}}{\sqrt{8\pi}\,S_k\Gamma(n)}\exp\left\{-\frac{(\ln\,w)^2}{2S_k^2} - \frac{wz}{2}\right\}\mathrm{d}w\mathrm{d}z\,. \tag{4.14}$$

By swapping the order of integration and letting $u = wz/2$ (hence $\mathrm{d}z = 2\mathrm{d}u/w$), this equation becomes:

$$\Pr\left\{\hat{\gamma_k} > \gamma_{\epsilon_k}\right\} = \int_0^\infty \frac{2}{\sqrt{8\pi}\, S_k \Gamma(n) w} \exp\left\{-\frac{(\ln\, w)^2}{2S_k^2}\right\} \left\{\int_{w\gamma_{\epsilon_k}/2}^\infty \exp(-u) u^{n-1} \mathrm{d}u\right\} \mathrm{d}w\,, \tag{4.15}$$

which, after writing the internal integral in gamma function notation, becomes:

$$\Pr\left\{\hat{\gamma_k} > \gamma_{\epsilon_k}\right\} = \int_0^\infty \frac{1}{\sqrt{2\pi}\, S_k w} \exp\left\{-\frac{(\ln\, w)^2}{2S_k^2}\right\} \frac{\Gamma(n, w\gamma_{\epsilon_k}/2)}{\Gamma(n)} \mathrm{d}w\,, \tag{4.16}$$

where $\Gamma(n, w\gamma_{\epsilon_k}/2)$ is the upper incomplete gamma function. Like before, this can be solved numerically by equating to Eq. 4.10, and the confidence level in log space is equal to $\log[\hat{\mathcal{P}}_k] + \log[\gamma_{\epsilon_k} \langle I_k/\hat{\mathcal{P}}_k \rangle / 2n]$, where here I_k is the rebinned power spectrum and $\hat{\mathcal{P}}_k$ is the corresponding fitted model.

4.4 Testing the methods on simulated data

Figure 4.3 shows examples where confidence levels have been calculated for synthetic flare time series with QPP signals, and shows how different background trends (which are unknown for real flare data) affect the appearance of a QPP signal in the power spectrum. To create the time series, a polynomial background trend was added to an exponentially damped sinusoid, white noise, and additional red noise. A polynomial was used to represent the flare trend, since the short section of a flare time profile in which a QPP can be seen can often be approximated by a low-order polynomial. The additional red noise was generated by a random walk, where each value in the time series is equal to a normally distributed random number summed with the preceding value. The parameters were chosen to be comparable to flare time series data from the Nobeyama Radioheliograph (see Section 4.5) and, for all of these time series, the sinusoid, white noise and random walk noise terms were kept identical. The top two rows of Fig. 4.3 show time series with different polynomial background trends on the left, and the corresponding power spectra on the right. Despite the different background trends, peaks corresponding to the sinusoidal signals can be seen above the 99% confidence level in the power spectra. The bottom two rows show the same signals as the top two rows, but instead they have higher amplitude background trends. The steeper background trends mean that the sinusoidal signals are no longer seen at a significant level in the power spectra. Therefore, although the method described in Section 4.2 is useful for testing for the presence of a QPP signal when there is some unknown background trend in the data, if the amplitude of the background trend is sufficiently greater than the amplitude

of a QPP signal, the QPP signal will be hidden in the power spectrum.

A scenario where the method described in Section 4.3 results in a peak above the 99% level in the power spectrum, while the method from Section 4.2 does not, is demonstrated in Fig. 4.4. The left panel shows a signal with the same background and noise as the signal in the top left panel of Fig. 4.3, but instead it has a sinusoidal term with a frequency that has a constant mean but a small amount of random variation with time. The result of this is that in the power spectrum, shown in the middle panel of Fig. 4.4, the peak corresponding to the sinusoidal signal is spread across more than one frequency bin, and hence no longer reaches a significant power level. The rebinned power spectrum is shown in the right panel, where the powers in every two frequency bins of the original spectrum have been summed together. Here the peak corresponding to the sinusoidal signal has a power above the 99% confidence level.

4.5 Examples of application to solar flare data

An important consideration when performing a periodogram analysis of time series data to search for a periodic signal that is localised in time (such as a wave train) is the choice of start and end times. For example, if a 5 hour section of a light curve was taken that contained a flare with QPPs that persisted for 30 minutes, then the significance of the peak in the power spectrum corresponding to the QPP signal would be lower than if a 30 minute section of the same light curve, centred around the QPP signal, was used instead. For the following solar flare light curves, the start and end times were chosen manually to best show off candidate QPPs: this was the only aspect of the analysis that was handled manually. An additional issue with the spectral analysis of time series data is the finite duration of the data. For a chosen section of a flare time series, the start and end values are unlikely to be equal to zero, hence there will be spectral leakage when performing some form of discrete Fourier transform, and this reduces the power of a peak in the power spectrum. One way to avoid this effect is to apply a window function, for example a Hann window, to the time series data before calculating the power spectrum. The application of such a window function is, however, not always helpful when searching for low-amplitude transient signals such as QPPs, since any QPP signals will be suppressed near the start and end of the time series, making detection even more challenging. In addition, the application of any window function other than a rectangular window will alter the distribution of noise in the data, and therefore this would need to be taken into account when using the methods described in this chapter. Hence for the following examples, no window function has been applied.

An example of the method described in Section 4.2 being used to confirm

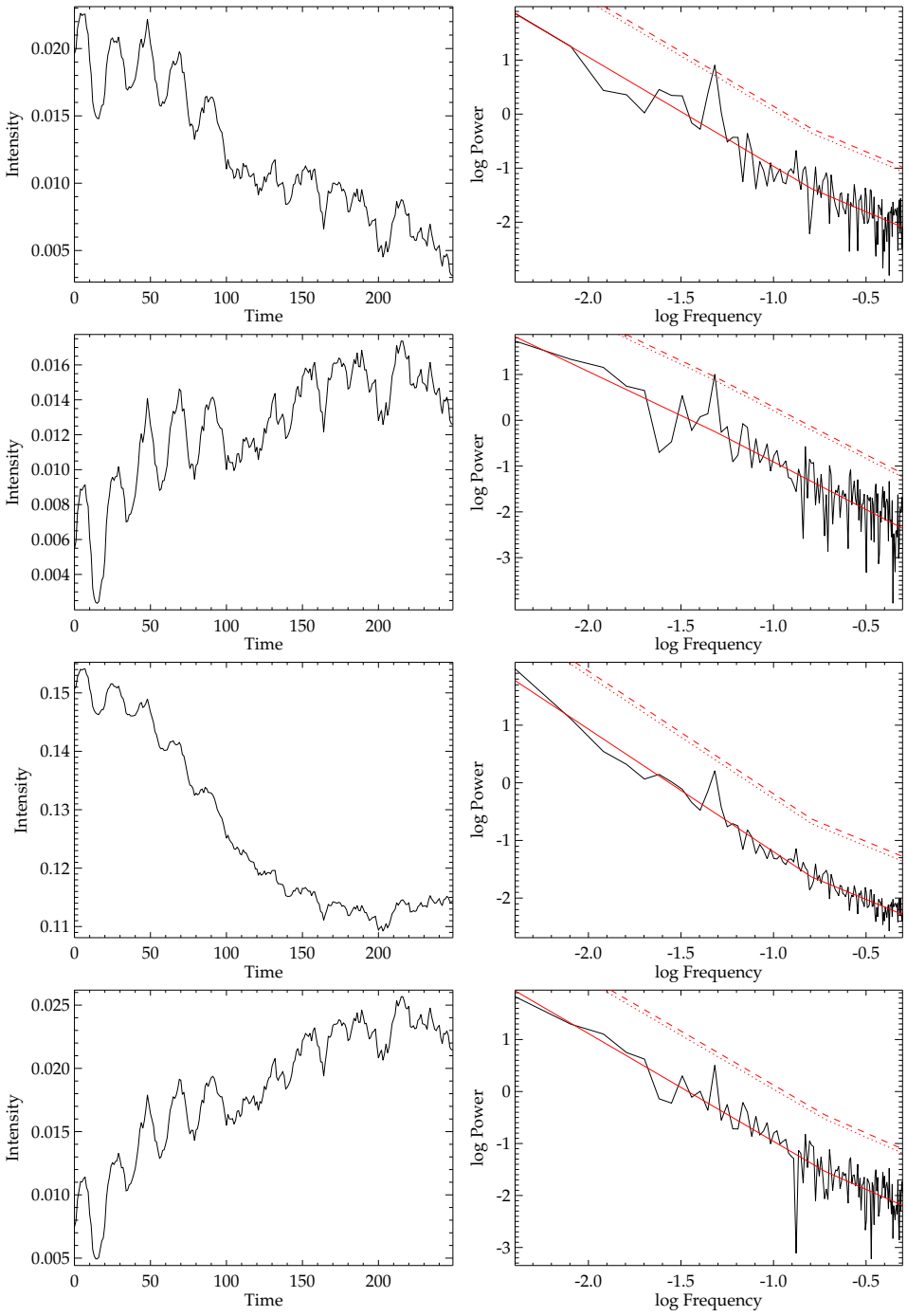

Figure 4.3: Examples of synthetic flare time series with QPPs are given on the left, and on the right are the corresponding power spectra, where the red solid line is a power law fit, and the red dotted and dashed lines correspond to the 95% and 99% confidence levels respectively. Arbitrary units have been used for all plots. The top two rows show two signals with different background trends, both with a peak above the 99% level in the power spectrum. The bottom two rows show the same signals but with steeper background trends, the result of which is that the peaks no longer reach significant levels in the power spectra.

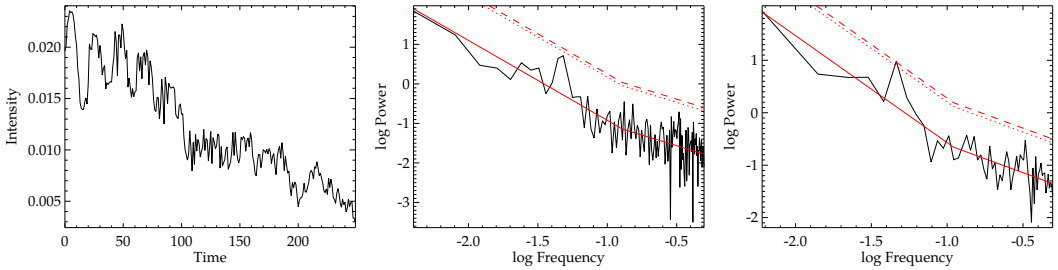

Figure 4.4: Example of how rebinning can help spectral peaks corresponding to certain kinds of periodic signals reach a significant power level. The left panel shows a synthetic time series signal, similar to that in the top left panel of Fig. 4.3, but with a sinusoidal component that has a frequency that fluctuates slightly with time. The middle panel shows the corresponding power spectrum, and the right panel shows the rebinned power spectrum (after summing the powers in every two frequency bins). As before, the red solid line is a power law fit, the red dotted and dashed lines correspond to the 95% and 99% confidence levels respectively, and arbitrary units have been used.

candidate QPPs in a GOES C7.1 class flare, observed between 2014 October 29 23:40 and October 30 00:34 UT, is shown in Fig. 4.5. A section of 17 GHz microwave correlation signal from the Nobeyama Radioheliograph (see Chapter 2) is shown in the left hand panel, and the corresponding Lomb-Scargle periodogram power spectrum is shown on the right. As mentioned in Section 4.2, the correlation data uncertainty was estimated by taking the standard deviation of a flat section of data with no flares, taken from 2016 October 27 00:00 until 05:00 UT. This gave an uncertainty of 1.1911749×10^{-5}. In the periodogram there is a peak with a period of $10.1^{+0.6}_{-0.5}$ s above the 99% confidence level, where the upper and lower uncertainties are taken to be plus or minus half a frequency bin, respectively, on either side of the peak frequency. Visual inspection of the light curve on the left confirms that the pulses have a time spacing approximately equal to this period, hence this can be considered a strong QPP candidate. An example where the method fails to support the possible presence of QPPs in a M8.7 class flare, observed between 2014 October 21 08:09 and 08:15 UT, is shown in Fig. 4.6, where there is no peak in the power spectrum above the 95% level. Although pulsations can be seen in the light curve, these are small in amplitude when compared to the underlying trend in the data, meaning that the trend dominates in the power spectrum and even though the pulsations may be periodic they are not detectable at a significant level.

Another point to note is that although a broken power law model was used to fit these NoRH power spectra in Figs. 4.5 and 4.6, the break cannot be seen. This can be explained by considering the white noise amplitude in the NoRH time series data, which is very small. Hence the frequency at which the white noise would start dominating over the coloured noise in the power spectrum is likely beyond the range

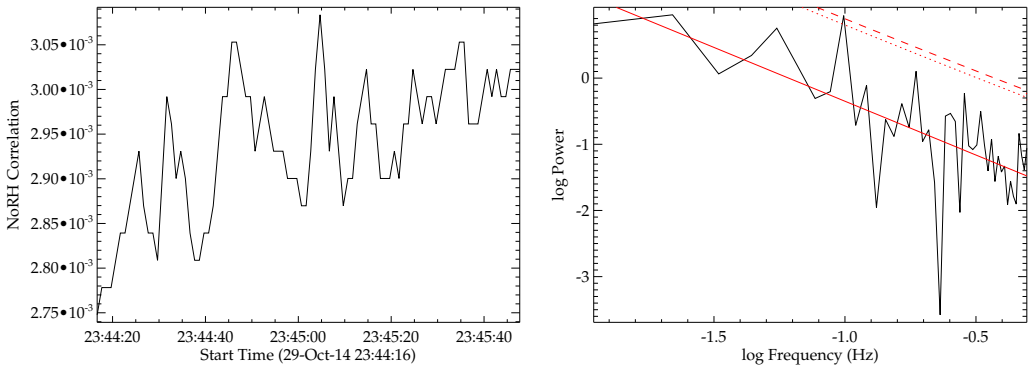

Figure 4.5: *Left:* A section of a GOES C7.1 class flare observed by Nobeyama Radioheliograph. *Right:* The corresponding power spectrum, where the red solid line is a power law fit to the spectrum, the red dotted line represents the 95% confidence level, and the red dashed line the 99% level. One peak is above the 99% level, at a period of $10.1^{+0.6}_{-0.5}$ s.

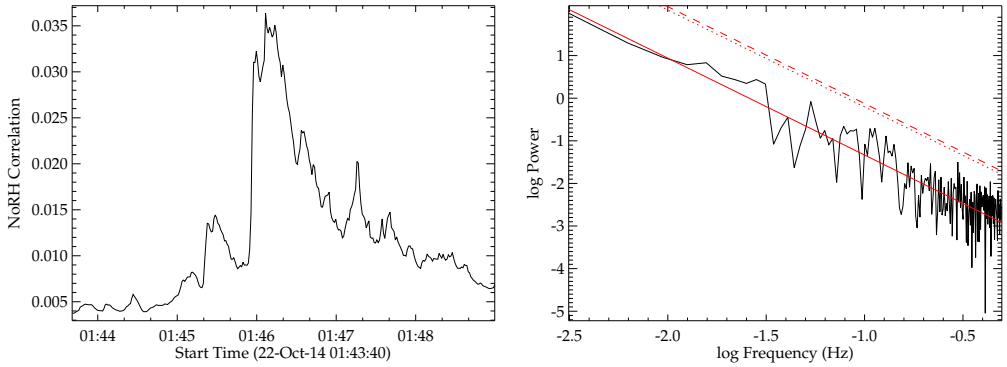

Figure 4.6: As in Fig. 4.5, but for a different flare with a class of M8.7. Although this flare appears to have pulsations there is no peak close to the 95% level in the power spectrum.

of frequencies included in the spectrum.

For the section of the C3.6 class flare observed between 2014 October 24 03:56 and 04:30 UT, shown in Fig. 4.7, again the method described in Section 4.2 fails to show a peak in the power spectrum above the 95% level, however a broad peak can be seen. The rebinned power spectrum is shown in Fig. 4.8, where every three frequency bins have been summed over. Applying the method described in Section 4.3 shows that there is a peak above the 95% confidence level at a period of 15^{+5}_{-3} s, hence this flare can be considered to have candidate QPPs.

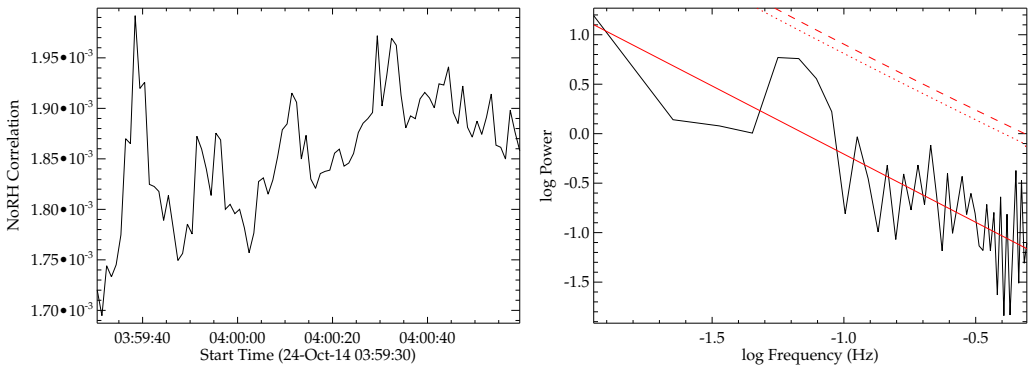

Figure 4.7: As in Fig. 4.5, but for a different flare with a class of C3.6. Here the power spectrum contains a broad peak, which does not reach the 95% confidence level.

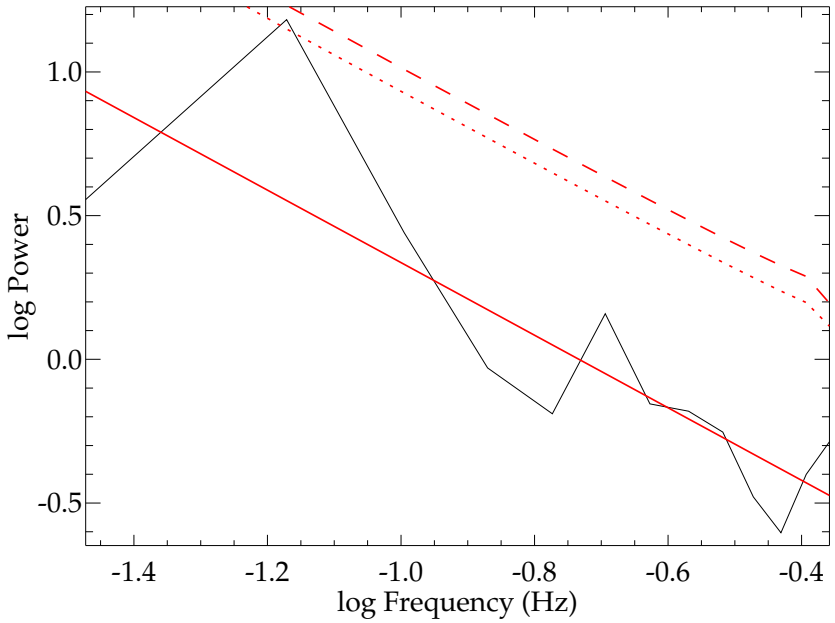

Figure 4.8: The rebinned power spectrum for the flare shown in Fig. 4.7. The peak at a period of 15^{+5}_{-3} s now surpasses the 95% confidence level, which is shown by the red dotted line.

4.6 Summary

We have demonstrated how the method of Vaughan (2005) can be applied to flare time series data in order to test for the presence of QPPs, subject to the careful choice of start and end times. The method has been adapted to be used with rebinned power spectra, which can aid the detection of QPP signals that have a period that varies slightly, or have a modulated amplitude. These methods avoid detrending the data, an approach that has been shown to have the potential to lead to false detections when the detrending is done by smoothing (e.g. Gruber et al. 2011; Auchère et al. 2016). An alternative method that also avoids detrending has been proposed by Inglis et al. (2015), which is discussed further in Chapter 5, therefore future searches for QPPs in flares could make use of both approaches. These methods, however, may not be suitable for searching for non-stationary QPP signals, which have a variable period. The rebinning version of the method can account for weakly non-stationary signals, but if the change in period is too great these signals may not be assessed to be significant. In this case either some form of wavelet analysis (e.g. Kupriyanova et al. 2010) or empirical mode decomposition (e.g. Kolotkov et al. 2015) could be used.

Chapter 5

Properties of quasi-periodic pulsations in solar flares from a single active region

5.1 Introduction

Some of the proposed QPP mechanisms relate the characteristic timescale of the QPPs to a spatial scale: for example, the period of an MHD oscillation of a coronal loop relates to the length or minor radius of the loop. Hence this motivates looking for correlations between the QPP periods and spatial scales of the region from which the flare originates. To do this we chose a set of flares from a single active region (AR), so that any evolution of the QPP properties corresponding to the evolution of the AR properties can be checked for. In addition, focussing on just one AR means that the automatic boundary detection and tracking algorithm from Higgins et al. (2011) can be utilised, which means that calculating AR properties around the time of a particular flare can largely be automated. The AR studied in this work, known as NOAA 12172/12192/12209, was chosen because it produced a large number of flares (a total of 181 GOES class flares), it existed at a time when many high-quality solar observation instruments were operating, and also because it was very long lived, persisting for around three solar rotations. This AR has been the subject of several other studies due to its highly active nature, but also because it is unusual in that none of the X-class flares were accompanied by coronal mass ejections (CMEs), and the few CMEs that did emerge from the AR were relatively small considering the amount of flare activity (Thalmann et al. 2015; Panesar et al. 2016; Liu et al. 2016; Jiang et al. 2016; Drake et al. 2016).

In terms of the detection of the QPPs, Pugh et al. (2017a) demonstrated two variants of the method of Vaughan (2005) to assess the significance of periodic

signals in flares (see Chapter 4). The method accounts for the presence of coloured noise and data uncertainties and does not require any form of detrending. In this chapter the method of Pugh et al. (2017a) is applied to the set of flares from the AR NOAA 12172/12192/12209. The method could complement that used by Inglis et al. (2016), which also avoids detrending and accounts for the presence of coloured noise, but instead involves a power spectrum model comparison. Flare data from GOES/XRS, EVE/ESP, *Fermi*/GBM, *Vernov*/DRGE, and NoRH were used for this study, and details of the data from these instruments are given in Chapter 2.

This chapter is structured as follows. In Section 5.2 the AR magnetogram data used are described. Section 5.3 summarises the QPP detection method, including details of the use of time derivative data and how it impacts on the power spectrum, and also describes how the AR properties were obtained. The results and discussion of the search for the QPPs themselves along with any correlations with flare or AR properties are given in Section 5.4, and finally conclusions are given in Section 5.5.

5.2 Active region observations

Properties of the AR were determined using data from SDO/HMI (see Section 2.2.2). Line of sight magnetogram images were used with a reduced cadence of one hour, and resolution of 1024×1024 pixels. The timescale of the evolution of an AR is typically much greater than an hour, and the reduced resolution does not significantly affect the properties calculated, while it does greatly speed up the calculations. The three time intervals corresponding to the AR's three crossings of the solar disk were chosen to be 2014 September 22 15:00:34 until September 30 08:00:33, 2014 October 19 15:00:30 until October 27 02:00:30, and 2014 November 16 15:00:27 until November 23 08:00:26, where the AR labels during its three crossings are NOAA 12172, NOAA 12192, and NOAA 12209 respectively. Fig. 5.1 shows magnetogram images of the AR during these three time intervals. Note that only times when the AR was within $\pm 60^{\circ}$ of the central meridian line were used. This is because line of sight effects mean the AR magnetogram images near the limb are highly distorted, so when the AR is close to the limb its properties cannot be obtained reliably. Unfortunately many of the flares from the AR occurred outside of these time ranges, so these flares had to be excluded when looking for relationships between the QPP periods and AR properties (see Table 5.1).

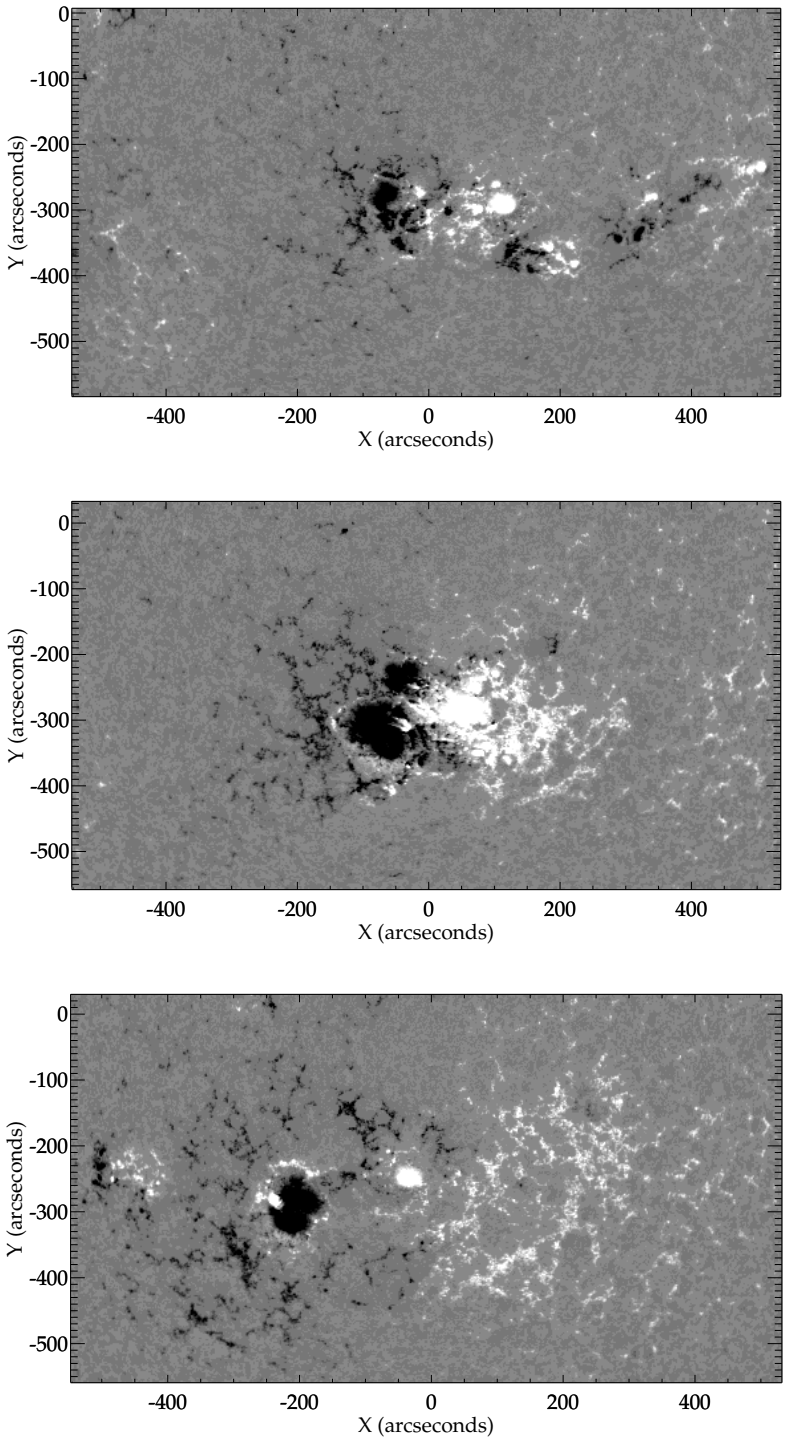

Figure 5.1: HMI magnetogram images of the active region during its three crossings of the solar disk, at 2014 September 26 22:01:30 *(top)*, 2014 October 23 15:01:30 *(middle)*, and 2014 November 19 07:01:30 *(bottom)*.

5.3 Data analysis

The basic outline of our approach to identifying candidate QPPs in the sample of solar flares is as follows. All available light curves for the flares were manually shortened to focus on sections that appeared to show the most variability. Shortening the light curves when searching for QPP signals is often helpful due to the transient nature of QPPs, and also because of the presence of background trends which influence the shape of the power spectrum. Some more complex flares showed variability in more than one section, so these different sections of light curve were analysed separately. The longest allowed light curve durations were the same as the flare durations, and the shortest were 16 times the data time cadence. Because the methods for calculating the confidence levels (see Chapter 4) require even time sampling, to ensure that the spectral powers are independent from each other, any gaps in the data were avoided when manually choosing the time intervals. Additionally, times when there was a switch between trigger mode and non-trigger mode in the *Fermi* data were also avoided. For the light curves from SXR observations, the time derivative was calculated and used for further analysis (see Section 5.3.1).

Lomb-Scargle periodograms were calculated for all of these shortened light curves. No window function was applied to the shortened light curve prior to calculating the periodogram (see Section 4.5). A broken power law model was fitted to the periodograms (see Section 4.2), and model uncertainties at each frequency index were estimated by performing Monte Carlo simulations. The 95% and 99% confidence levels were then calculated (see Section 4.2) taking account of any power-law dependence of the spectrum and uncertainties associated with the model fits. Additionally, rebinned power spectra were calculated in order to better assess the significance of any broader peaks that spanned more than one frequency bin in the regular power spectra (see Section 4.3). For the power spectra with peaks that benefited from rebinning, summing the powers in every 2 or 3 frequency bins (depending on how broad the peak was) was found to give the best results.

Peaks with a period less than four times the cadence or greater than a quarter of the duration of the time series data are not considered as candidate QPP signals, as we do not believe periods in these ranges can be detected reliably without supporting data from another instrument with a higher time resolution. In addition, periods greater than a quarter of the length of the time series data are neglected, as with so few signal repetition cycles it is not possible to be sure that the signal is truly periodic.

The start and end times of the light curves were refined manually in order to maximise the confidence level of any periodic component of the signal. This was done simply by decreasing, then increasing the start time by one data point at a time, to search for a start time which maximised the significance of the peak in

the power spectrum. This iterative process was repeated with the end time, then again with the start time, in order to find the maximum confidence level of the peak. If multiple significant spectral peaks were found then these would be listed separately in the results, although there were no cases where multiple periods in the same section of light curve and same waveband were found. Flares with a peak in the power spectrum above the 95% confidence level were included in the sample of flares with strong candidate QPPs, and used to study the QPP properties.

5.3.1 Time derivative data

Making use of the time derivative of high-precision SXR observations has been shown to be useful for the study of QPPs (Simões et al. 2015; Hayes et al. 2016; Dennis et al. 2017). Taking the derivative will have a significant impact on the power spectrum of time series data, however, and so it is extremely important to understand this impact when assessing the significance of peaks in the power spectrum. One of the most basic numerical approximations to the derivative of time series data is a three-point finite difference, defined as:

$$\dot{X}_n = \frac{X_{n+1} - X_{n-1}}{2\Delta t}, \tag{5.1}$$

where X represents intensity, n is the time index, and Δt is the time cadence. Then the discrete Fourier transform of $\dot{X}$ as a function of time can be written:

$$\mathcal{F}_k(\dot{X}) = \frac{1}{2\Delta t} \sum_{n=0}^{N-1} (X_{n+1} - X_{n-1}) e^{-2\pi i k n/N}, \tag{5.2}$$

where k is the frequency index, ranging from 0 to $N-1$, and N is the number of data points. This expression can be rearranged to:

$$\mathcal{F}_k(\dot{X}) = \frac{1}{2\Delta t} \left(\sum_{n=0}^{N-1} X_{n+1} e^{-2\pi i k n/N} - \sum_{n=0}^{N-1} X_{n-1} e^{-2\pi i k n/N} \right) \tag{5.3}$$

$$= \frac{1}{2\Delta t} \left(\sum_{n=1}^{N} X_n e^{-2\pi i k (n-1)/N} - \sum_{n=-1}^{N-2} X_n e^{-2\pi i k (n+1)/N} \right). \tag{5.4}$$

In the above expression the sums go outside of the data range (the numerical derivative cannot be calculated at the first and last points in the time series), so instead the following expression must be considered:

$$\mathcal{F}_k(\dot{X}) = \frac{1}{2\Delta t} \left(\sum_{n=1}^{N-2} X_n e^{-2\pi i k (n-1)/N} - \sum_{n=1}^{N-2} X_n e^{-2\pi i k (n+1)/N} \right), \tag{5.5}$$

which can then be rearranged to:

$$\mathcal{F}_k(\dot{X}) = \frac{1}{2\Delta t}\left(\sum_{n=1}^{N-2} X_n e^{-2\pi ikn/N} e^{2\pi ik/N} - \sum_{n=1}^{N-2} X_n e^{-2\pi ikn/N} e^{-2\pi ik/N}\right) \tag{5.6}$$

$$= \frac{1}{2\Delta t}\left(e^{2\pi ik/N} - e^{-2\pi ik/N}\right)\sum_{n=1}^{N-2} X_n e^{-2\pi ikn/N} \tag{5.7}$$

$$= \frac{i}{\Delta t}\sin\left(\frac{2\pi k}{N}\right)\mathcal{F}_k(X) = \frac{i}{\Delta t}\sin(\Omega)\mathcal{F}_k(X), \tag{5.8}$$

where Ω is an angular frequency which ranges from 0 to 2π. The Fourier power spectrum is the square of the absolute value of the Fourier transform, so for the power spectrum we have:

$$\left|\mathcal{F}_k(\dot{X})\right|^2 = \frac{1}{(\Delta t)^2}\sin^2(\Omega)\left|\mathcal{F}_k(X)\right|^2. \tag{5.9}$$

The periodogram of evenly spaced data with no oversampling is equivalent to the discrete Fourier power spectrum with additional normalisation, and so this $\sin^2(\Omega)$ multiplying term will appear when the periodogram of time derivative data is calculated. For a perfectly periodic signal, the periodogram of the time derivative of the signal will be equal to $\frac{1}{(\Delta t)^2}\sin^2(\Omega)$ multiplied by the periodogram of the original signal. Flare time series data is not completely periodic, however, and the presence of background trends will have a substantial impact on the power spectra. Taking the time derivative will suppress slowly-varying background trends, and hence if a periodic component of the signal is present it will be more visible in the time derivative power spectrum. Taking the time derivative is most beneficial for SXR flare observations, since the impulsive phase of a flare is best seen in the HXR and microwave/radio wavebands, and the Neupert effect means this phase corresponds to a rise in the SXR emission. Hence QPPs, which are most often seen in the impulsive phase of a flare, tend to appear during the rise of the SXR emission, and this rising trend will make QPPs less visible in the power spectrum. For all SXR observations used in this study, from GOES/XRS and EVE/ESP, the time derivatives of the signals have been used, and the power spectra have been divided by $\sin^2(\Omega)$ before proceeding to calculate the confidence levels. Note that because Ω varies between 0 (at the lowest frequency sampled) and π (at the highest frequency sampled) for the positive frequencies, this means that $\sin^2(\Omega)$ is equal to zero at the edges of the power spectrum, hence the powers at the lowest and highest frequencies of the power spectrum cannot be calculated. In addition, where Ω is close to 0 and π, $\sin^2(\Omega)$ is very small and therefore numerical uncertainties will have a bigger impact. To avoid this, all derivative power spectra have had the first and final 2% of frequencies removed, with the exception of power spectra with less than 50 data points, which

have the first and last points removed.

5.3.2 Active region properties

The processing of the HMI line of sight magnetograms and calculation of some AR properties was done using the *SolarMonitor Active Region Tracking* (SMART) routines provided by Higgins et al. (2011). For each AR crossing of the solar disk (while within around $\pm 60°$ of the central meridian line, since the AR magnetogram images are highly distorted when close to the limb) the processing technique is as follows. First the magnetogram frame where the AR is approximately half way across the solar disk was used to determine a bounding box around the AR. ARs visible on the disk at that time were detected automatically according to Higgins et al. (2011). After selecting the AR of interest, the X and Y coordinate ranges of the SMART detection outline were used to define a box around the AR. Next, the line of sight projection effect of features closer to the limb appearing smaller compared to when closer to the centre of the solar disk is accounted for by differentially rotating the other magnetogram frames to the time where the AR is approximately at the central meridian, using the IDL Solar Software routine *drot_map*. The previously defined box was then used to crop all frames to include only the AR of interest.

In order to estimate the AR photospheric area as a function of time, pixels within the bounding box with an absolute magnetic field strength greater than a threshold value of 70 G were selected. This threshold was chosen as quiet Sun regions tend to have magnetic field values less than this (Higgins et al. 2011). For each selected pixel, the area of the solar surface that the pixel would correspond to if it were located at the disk centre was multiplied by a cosine correction factor, to account for the spherical nature of the Sun meaning that different pixels correspond to different surface areas (McAteer et al. 2005), then the resulting values were summed together to obtain an AR area for a particular magnetogram frame.

The bipole separation is defined as (Mackay et al. 2011):

$$S = |\mathbf{S}(t)| = \left| \frac{\sum_{B_z > +70\,\mathrm{G}} B_z(x,y)\mathbf{R}_{x,y}}{\sum_{B_z > +70\,\mathrm{G}} B_z(x,y)} - \frac{\sum_{B_z < -70\,\mathrm{G}} B_z(x,y)\mathbf{R}_{x,y}}{\sum_{B_z < -70\,\mathrm{G}} B_z(x,y)} \right|, \tag{5.10}$$

where $\mathbf{S}(t)$ is the vector pointing from the centre of one pole to the other, $B_z(x,y)$ is the line of sight magnetic field at pixel position (x,y), and $\mathbf{R}_{x,y}$ is the position vector pointing from the origin to the pixel at (x,y). Once the bipole separation, S, had been calculated it was then converted to a great circle distance in Mm.

Finally, the average magnetic field strength of the active region at the photosphere as a function of time was calculated by summing together the absolute magnetic field strength values of all pixels in a particular magnetogram frame with a magnitude greater than the threshold value of 70 G, then dividing by the number

of pixels with absolute values greater than the threshold.

5.4 Results and discussion

5.4.1 The set of flares with QPPs

Details of all 181 flares used in the analysis are given by Table B.1 in Appendix B.1. These flares were selected from the list of automatically detected flares provided by the NOAA Space Weather Prediction Centre (SWPC)[1], and the spatial location of the flares was checked using SDO Atmospheric Imaging Assembly (AIA) 94 Å difference images provided by SolarMonitor[2] (Gallagher et al. 2002), to ensure that the flares originated from the active region of interest. After searching each of the flares for evidence of QPPs using the methods described in Section 5.3, a total of 37 flares with convincing candidate QPPs were identified, corresponding to 20% of flares in the sample. These flares are summarised in Table 5.1, where the upper and lower uncertainties for each period are taken to be plus or minus half of the corresponding frequency bin width in the power spectrum. Note that for some of these flares, QPPs were found in more than one section of the flare light curve, while there were no cases where multiple significant periods were found in the same section of light curve observed in a particular waveband. The vast majority of the QPPs occurred during the impulsive phase of the flare, with the only exception being the flare labelled '022' in Tables B.1 and 5.1, where the QPPs were predominantly in the decay phase. Plots showing the time series data and power spectra of one of these flares as an example are given in Figs. 5.2 and 5.3, while similar plots for the other 36 flares are shown by Figs. A.1–A.46 in Appendix A.1. A histogram of the QPP periods is given in the left-hand panel of Fig. 5.4, and if a log-normal distribution is assumed (more data is needed to confirm if this model is a good approximation, but similar histograms shown by Inglis et al. (2016) also appear to have a log-normal distribution), then the average QPP period for this set of flares is 20^{+16}_{-9} s. This seems to be consistent with the results of Inglis et al. (2016). The right-hand panel of Fig. 5.4 shows separate histograms for the QPP periods detected by GOES/XRS, and those detected by EVE/ESP, *Fermi*/GBM, NoRH, and *Vernov*/DRGE. The distribution for GOES/XRS appears to be shifted slightly towards longer periods than the other instruments, which could be explained by the other instruments having a higher time resolution and also only capturing the impulsive phase of the flare. GOES/XRS has a lower time resolution and observes both the impulsive and gradual phases of the flare, meaning that the detection of shorter periods is limited by the time resolution, whereas longer periods can be seen more easily.

[1] `http://www.swpc.noaa.gov`
[2] `https://www.solarmonitor.org`

Seven flares (those labelled 056, 072, 104, 106, 135, 142, and 152 in Tables B.1 and 5.1) have a QPP signal from two different instruments above the 95% confidence level in their power spectrum, which rules out the possibility that these signals are due to some instrumental artefact. A further two flares (010 and 024) have peaks just below the 95% level in the EVE/ESP power spectra at the same period as those seen above the 95% level in the GOES/XRS data. On the other hand, three of the flares (010, 037, and 038) have QPPs observed in two different wavebands over the same time range, but with different periods. According to the standard flare model, different wavebands of the emission originate from different positions within the flaring region, so these could be unrelated periodic signals originating from different places, or alternatively they could result from the same process, but be shifted from one another due to changes in the local physical parameters.

It is slightly surprising that the majority of significant QPP detections made by GOES/XRS are not supported by EVE/ESP, considering both instruments observe the Sun near continuously and have overlapping observational wavebands. A possible reason for this is that the EVE/ESP waveband is so wide. QPPs are often more visible in a particular waveband than others (which could relate to the mechanism or spatial origin of the signal), or they could be phase shifted across different wavelengths. These would result in the signal being hidden or blurred in wide waveband observations. The visibility of QPP signals in different wavebands would also explain the other cases where there is a detection in one instrument but not another over the same time range. Alternatively the cause may simply be that the flare signal-to-noise ratio is lower for EVE/ESP than GOES/XRS, thus making any QPP signals in the EVE/ESP data more difficult to detect above the noise level. Also of note are the differences between the two overlapping GOES/XRS wavebands. In most cases a signal can be seen in both wavebands even if it is only above the 95% confidence level threshold in one of the wavebands, while there are a few cases where the signal can only be seen in the power spectrum of one of the wavebands. An explanation of this could be a combination of the Neupert effect resulting in a steeper trend in one of the waveband light curves compared to the other, and that the optimal choice of time interval for one waveband might not be the same as for the other waveband. Pugh et al. (2017a) demonstrated that steeper trends in light curves result in QPP signals having a lower significance in the power spectra. Alternatively there could be a physical reason for the QPP signal appearing stronger in one of the wavebands over the other, based on the QPP mechanism.

Inglis et al. (2016) looked for QPPs in all M- and X-class flares in the GOES/XRS and *Fermi*/GBM data between 2011 February 01 and 2015 December 31, meaning that 44 of those flares are included in our study (flares included in the Inglis et al. (2016) sample are indicated in Table B.1). Rather than shortening

the flare time series to focus on a section showing a potential QPP signal like in this work, Inglis et al. (2016) use the flare start and end times from the GOES catalogue in order to automate their method. Their method involves a model comparison, where three different models are fitted to the flare power spectra, compared by calculating the Bayesian Information Criterion (BIC) for each, and checked for a reasonable goodness of fit. The three models are a single power law plus constant (model S_0), a power law plus Gaussian bump and constant (model S_1), and a broken power law plus constant (model S_2). A lower BIC value means a more favoured model, and Inglis et al. (2016) imposes a selection criterion that model S_1 should have a BIC value that is at least 10 less than those for models S_0 and S_2, so only cases where model S_1 is strongly favoured over models S_0 and S_2 are considered. They also require the models to be fit to the power spectra sufficiently well, based on a goodness-of-fit statistic. We find similar periods (within the 1σ uncertainties) to Inglis et al. (2016) for six flares: 029, 056, 135, 140, 152, 153, and a further seven flares when the selection criteria of Inglis et al. (2016) are relaxed: 049, 054, 085, 104, 105, 117, 161. We consider periods identified with relaxed selection criteria here (all cases where model S_1 is preferred over model S_0) because these are cases where a period identified by the automated method of Inglis et al. (2016) does not quite match their selection criteria, while this study finds the same period to be significant. Therefore we regard these cases as promising and worthy of mention. In addition the same periodic signals as those identified by Myagkova et al. (2016) are found in flares 010, 056, and 135. Different significant periods than Inglis et al. (2016) were found from the same instrument for one flare: 092, and different significant periods from different instruments for one flare: 098. The three flares where there is a significant period identified by Inglis et al. (2016) but not the present study are 075, 115, and 139, and the two flares where the present study finds a significant period whereas Inglis et al. (2016) does not are 008 and 072. For the remaining 24 flares both this work and Inglis et al. (2016) find no convincing evidence of QPPs. We believe that the majority of cases where the results of this work differ from Inglis et al. (2016) can be explained by the different time intervals used or different detection criteria. For example, periods that are less than four times the cadence or greater than a quarter of the length of the time series data are neglected in this study, as these are difficult to detect reliably, whereas Inglis et al. (2016) required a model containing a QPP signal to be sufficiently favoured over two alternative models.

Table 5.1: List of flares with a peak above the 95% confidence level in the power spectrum. The first column contains a numerical label for the flares (see also Table B.1), the second and third columns give the start and end times of the section of the flare where the QPP signal is most visible in the power spectrum, the fourth column is the instrument used, the fifth column is the type of power spectrum in which the signal was detected (the numbers for the rebinned power spectra refer to the number of frequency bins that were summed over, see Section 5.3), the sixth column is the QPP period, and finally the seventh column gives references to other studies that find pulsations in the flare. Flare numbers marked with an asterisk indicate those which occurred while the active region was far enough away from the solar limb so that active region properties could be determined.

Flare no.	Start time	End time	Instrument	Method	Period (s)	References
008*	2014-09-23 23:08:20	2014-09-23 23:13:52	GOES 0.5–4 Å	Regular	$41.2^{+2.7}_{-2.4}$	
010*	2014-09-24 17:49:04	2014-09-24 17:50:18	GOES 1–8 Å	Rebinned (2)	$9.6^{+1.4}_{-1.1}$	2
010*	2014-09-24 17:49:01	2014-09-24 17:49:50	Vernov	Rebinned (2)	$5.8^{+0.8}_{-0.6}$	2
022	2014-10-17 05:23:18	2014-10-17 05:26:35	NoRH	Rebinned (3)	$39.2^{+16.8}_{-9.0}$	
024	2014-10-17 15:35:30	2014-10-17 15:37:54	GOES 1–8 Å	Rebinned (2)	$22.1^{+4.0}_{-3.0}$	
027	2014-10-18 01:04:10	2014-10-18 01:08:30	NoRH	Rebinned (3)	$8.0^{+1.4}_{-1.0}$	
029	2014-10-18 07:36:14	2014-10-18 07:48:48	GOES 1–8 Å	Regular	$50.1^{+1.7}_{-1.6}$	1
030	2014-10-18 13:14:38	2014-10-18 13:15:52	GOES 0.5–4 Å	Regular	$14.3^{+1.6}_{-1.3}$	
035	2014-10-18 19:02:30	2014-10-18 19:06:58	GOES 1–8 Å	Regular	$13.3^{+0.4}_{-0.3}$	2
037	2014-10-19 01:35:00	2014-10-19 01:43:00	GOES 0.5–4 Å	Regular	$79.5^{+7.2}_{-6.1}$	
037	2014-10-19 01:36:28	2014-10-19 01:42:42	NoRH	Regular	$24.9^{+0.9}_{-0.8}$	
038	2014-10-19 04:20:24	2014-10-19 04:24:56	GOES 1–8 Å	Regular	$53.7^{+5.9}_{-4.9}$	

Continued on next page

Table 5.1 – *Continued from previous page*

Flare no.	Start time	End time	Instrument	Method	Period (s)	References
038	2014-10-19 04:20:24	2014-10-19 04:24:56	GOES 0.5–4 Å	Regular	$24.4^{+1.2}_{-1.1}$	
038	2014-10-19 04:41:39	2014-10-19 04:50:00	GOES 0.5–4 Å	Regular	$45.4^{+2.2}_{-2.0}$	
049*	2014-10-20 09:05:45	2014-10-20 09:08:14	GOES 0.5–4 Å	Rebinned (3)	$14.7^{+2.6}_{-1.9}$	1
052*	2014-10-20 14:41:47	2014-10-20 14:43:33	GOES 1–8 Å	Regular	$26.1^{+3.7}_{-2.9}$	
054*	2014-10-20 16:23:02	2014-10-20 16:31:20	GOES 1–8 Å	Regular	$35.4^{+1.3}_{-1.2}$	
056*	2014-10-20 18:57:51	2014-10-20 18:59:01	Fermi 25–50 keV	Rebinned (3)	$13.9^{+6.0}_{-3.2}$	1,2
056*	2014-10-20 18:57:53	2014-10-20 18:59:02	Vernov	Regular	$17.2^{+2.5}_{-1.9}$	1,2
058*	2014-10-20 22:45:18	2014-10-20 22:49:46	GOES 1–8 Å	Rebinned (2)	$48.4^{+10.8}_{-7.5}$	1,3
058*	2014-10-20 22:45:18	2014-10-20 22:49:46	GOES 0.5–4 Å	Rebinned (2)	$48.4^{+10.8}_{-7.5}$	1,3
068*	2014-10-22 01:43:04	2014-10-22 01:46:36	GOES 1–8 Å	Regular	$21.1^{+1.1}_{-1.0}$	
068*	2014-10-22 01:43:04	2014-10-22 01:46:36	GOES 0.5–4 Å	Regular	$21.1^{+1.1}_{-1.0}$	
072*	2014-10-22 14:06:55	2014-10-22 14:12:02	Fermi 50–100 keV	Regular	$30.6^{+1.6}_{-1.4}$	5
072*	2014-10-22 14:06:56	2014-10-22 14:09:30	GOES 1–8 Å	Regular	$30.3^{+3.4}_{-2.8}$	5
072*	2014-10-22 14:15:24	2014-10-22 14:23:40	GOES 0.5–4 Å	Regular	$49.4^{+2.6}_{-2.4}$	5
079*	2014-10-24 02:38:30	2014-10-24 02:41:20	NoRH	Rebinned (2)	$7.9^{+0.4}_{-0.3}$	
081*	2014-10-24 03:59:30	2014-10-24 04:01:00	NoRH	Rebinned (3)	$14.8^{+5.0}_{-3.0}$	

Continued on next page

Table 5.1 – *Continued from previous page*

Flare no.	Start time	End time	Instrument	Method	Period (s)	References
085*	2014-10-24 21:19:38	2014-10-24 21:23:47	GOES 0.5–4 Å	Regular	$49.6^{+5.5}_{-4.5}$	
092*	2014-10-25 17:02:11	2014-10-25 17:10:10	GOES 1–8 Å	Regular	$25.1^{+0.7}_{-0.6}$	1
092*	2014-10-25 17:02:11	2014-10-25 17:10:10	GOES 0.5–4 Å	Regular	$25.1^{+0.7}_{-0.6}$	1
098*	2014-10-26 10:48:52	2014-10-26 10:50:34	Fermi 25–50 keV	Regular	$20.3^{+2.2}_{-1.9}$	
104*	2014-10-26 18:11:18	2014-10-26 18:15:24	GOES 0.5–4 Å	Regular	$20.3^{+0.9}_{-0.8}$	1
104*	2014-10-26 18:12:40	2014-10-26 18:15:28	Fermi 25–50 keV	Regular	$20.9^{+1.4}_{-1.2}$	1
105*	2014-10-26 18:45:04	2014-10-26 18:48:02	GOES 1–8 Å	Regular	$25.2^{+1.9}_{-1.7}$	1
106*	2014-10-26 20:03:42	2014-10-26 20:11:18	GOES 1–8 Å	Rebinned (2)	$36.4^{+3.2}_{-2.7}$	1
106*	2014-10-26 20:03:42	2014-10-26 20:11:18	GOES 0.5–4 Å	Rebinned (2)	$36.4^{+3.2}_{-2.7}$	1
106*	2014-10-26 20:03:38	2014-10-26 20:09:02	Fermi 25–50 keV	Regular	$31.9^{+1.7}_{-1.5}$	1
117*	2014-10-27 17:36:36	2014-10-27 17:37:26	GOES 1–8 Å	Regular	$12.3^{+1.8}_{-1.4}$	1
129	2014-10-29 09:58:00	2014-10-29 10:01:45	EVE	Rebinned (2)	$26.4^{+3.5}_{-2.8}$	1
135	2014-10-29 21:21:33	2014-10-29 21:22:19	Fermi 25–50 keV	Rebinned (3)	$7.5^{+2.5}_{-1.5}$	1,2
135	2014-10-29 21:21:28	2014-10-29 21:22:52	Vernov	Rebinned (3)	$7.6^{+1.2}_{-0.9}$	1,2
138	2014-10-29 23:44:16	2014-10-29 23:45:48	NoRH	Regular	$10.1^{+0.6}_{-0.5}$	
140	2014-10-30 01:28:38	2014-10-30 01:30:30	GOES 1–8 Å	Rebinned (2)	$24.6^{+7.0}_{-4.5}$	1,3

Continued on next page

Table 5.1 – *Continued from previous page*

Flare no.	Start time	End time	Instrument	Method	Period (s)	References
141	2014-10-30 04:22:08	2014-10-30 04:28:00	GOES 1–8 Å	Regular	$21.9^{+0.7}_{-0.7}$	1
142	2014-10-30 05:44:27	2014-10-30 05:45:45	GOES 1–8 Å	Regular	$18.9^{+2.7}_{-2.1}$	
142	2014-10-30 05:44:27	2014-10-30 05:45:43	NoRH	Regular	$18.7^{+2.7}_{-2.1}$	
147	2014-11-13 06:04:59	2014-11-13 06:07:15	NoRH	Regular	$9.0^{+0.3}_{-0.3}$	
152	2014-11-15 11:56:08	2014-11-15 12:02:58	GOES 1–8 Å	Regular	$27.2^{+0.9}_{-0.9}$	1
152	2014-11-15 11:56:08	2014-11-15 12:02:58	GOES 0.5–4 Å	Regular	$27.2^{+0.9}_{-0.9}$	1
152	2014-11-15 11:56:08	2014-11-15 12:02:58	EVE	Regular	$27.3^{+0.9}_{-0.9}$	1
153	2014-11-15 20:42:57	2014-11-15 20:44:28	GOES 0.5–4 Å	Rebinned (2)	$20.0^{+5.7}_{-3.6}$	1
161*	2014-11-16 17:42:46	2014-11-16 17:45:24	GOES 0.5–4 Å	Regular	$19.5^{+1.3}_{-1.2}$	
177*	2014-11-22 06:02:16	2014-11-22 06:04:48	GOES 1–8 Å	Regular	$18.7^{+1.2}_{-1.1}$	
177*	2014-11-22 06:02:16	2014-11-22 06:04:48	GOES 0.5–4 Å	Regular	$18.7^{+1.2}_{-1.1}$	

References. (1) Inglis et al. (2016); (2) Myagkova et al. (2016); (3) Cho et al. (2016); (5) Kuznetsov et al. (2016)

5.4.2 Comparing QPP and flare properties

Figures 5.5 and 5.6 show a weak correlation of the QPP period with the flare amplitude in the GOES 1-8 Å waveband and a moderate correlation with the flare duration, which is consistent with the flare amplitude being correlated with the duration (e.g. Lu et al. 1993; Veronig et al. 2002). The flare durations were estimated from the GOES 1-8 Å data, and were taken as the time between when the intensity begins increasing above the base level and when the intensity returns to the base level. Duplicate points, where the same QPP signal can be seen in multiple instruments or wavelength ranges, are omitted. This apparent correlation may be due to observational constraints, however, since the short periods tend to be more easily visible in the shorter duration flares, while the detection of long periods is only possible in the longer duration flares. In addition, Inglis et al. (2016) found no correlation between the period and GOES class for a larger sample of flares.

Figure 5.7 shows a positive correlation between the QPP period and the duration of the QPP signal, for which the time interval that gave the most significant peak in the power spectrum is used (see Section 5.3). Fitting a linear model gives a relationship:

$$\log P = (0.62 \pm 0.03) \log \tau - (0.07 \pm 0.07), \tag{5.11}$$

where P is the period and τ is the QPP signal duration time. Observational constraints mean that the maximum detectable period will depend on the time interval being used, so longer periods will require longer durations, however this does not explain why short periods with longer durations are not seen. We also note that the relationship is different from the period versus decay time relationships found by Cho et al. (2016) and Pugh et al. (2016), although these studies focussed on a specific class of QPP signals—those which show a decay—whereas many of the QPP signals included in the present study do not show a clear decay, and appear more like a set of periodic pulses rather than a harmonic signal.

A plot of QPP period against the time at which the QPP signal occurs is shown in Fig. 5.8, where there is no clear trend in how the periods change with time. It can be seen that the majority of the QPPs were found during the AR's second crossing of the solar disk (as NOAA 12192), but this is simply because most of the flares occurred during this time as shown by the grey shaded region.

5.4.3 Comparing QPP and active region properties

Figures 5.9–5.11 show scatter plots of the QPP period with total area, bipole separation distance, and average photospheric magnetic field strength of the AR around the time of the QPP signal onset, respectively. These plots show no correlation between the QPP periods and AR properties, which, if the characteristic timescale

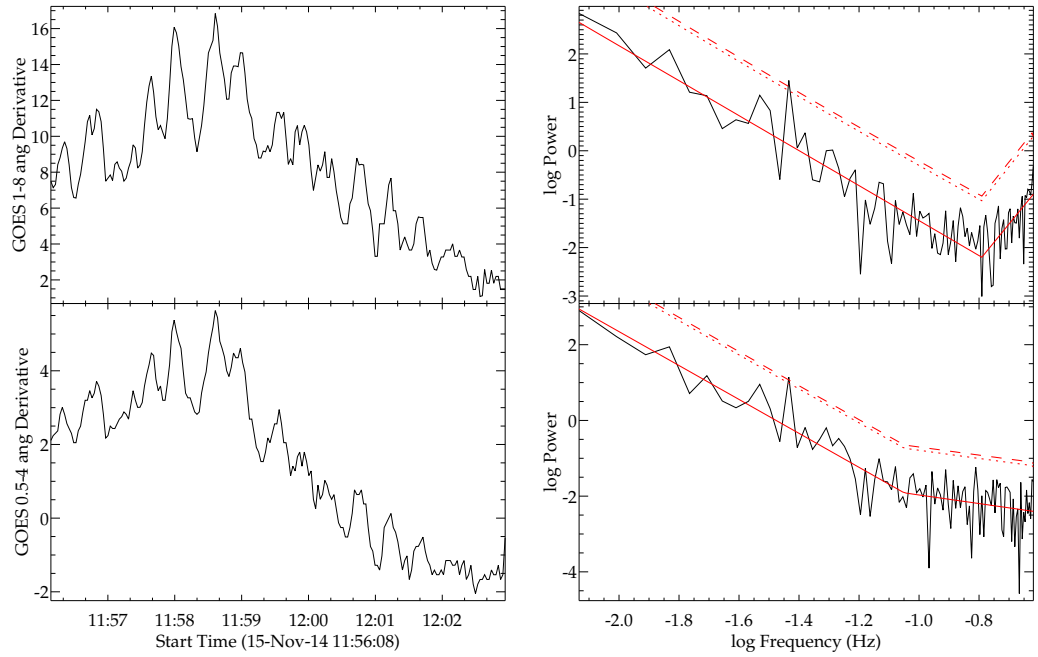

Figure 5.2: *Left:* The time derivatives of a section of flare 152 observed by GOES/XRS, where the top panel shows the 1–8 Å emission and the bottom panel the 0.5–4 Å emission. *Right:* The corresponding power spectra, where the red solid lines are broken power law fits to the spectra, the red dotted lines represent the 95% confidence levels, and the red dashed lines the 99% levels. One peak in each is above the 99% level, at a period of 27.2 ± 0.9 s.

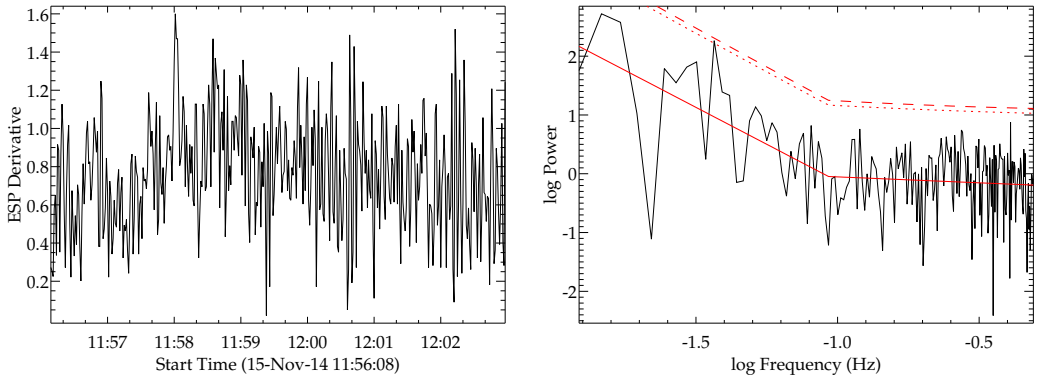

Figure 5.3: *Left:* The time derivative of a section of flare 152 observed by EVE/ESP. *Right:* The corresponding power spectrum, where the red solid line is a broken power law fit to the spectrum, the red dotted line represents the 95% confidence level, and the red dashed line the 99% level. One peak is above the 95% level, at a period of 27.3 ± 0.9 s.

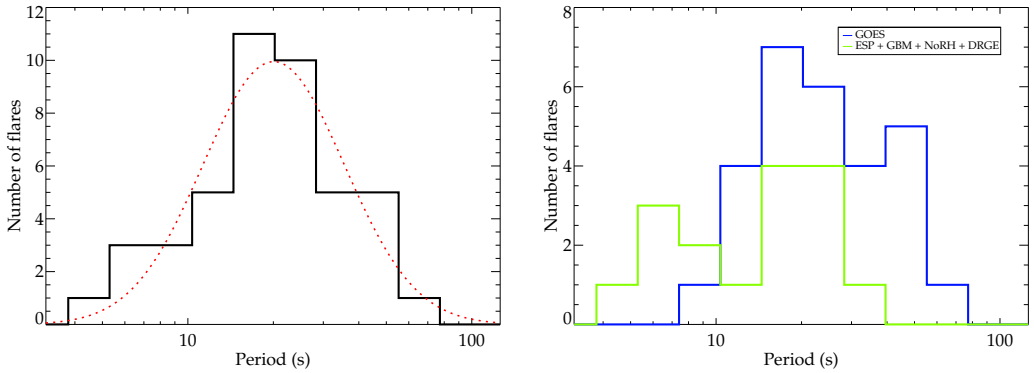

Figure 5.4: Histograms of the QPP periods. *Left:* The black solid line shows all QPP periods combined, and the dotted red line shows a Gaussian fit to the overall distribution which corresponds to an average QPP period of 20^{+16}_{-9} s for the set of flares examined. *Right:* The same histogram but with the QPP periods separated based on which instrument was used. The blue line shows the QPP periods detected in the GOES/XRS wavebands with a 2 s cadence, and the green line shows those detected by EVE/ESP, *Fermi*/GBM, NoRH, and *Vernov*/DRGE with a 1 s cadence. The distribution for GOES/XRS appears to be shifted slightly towards longer periods than the other instruments.

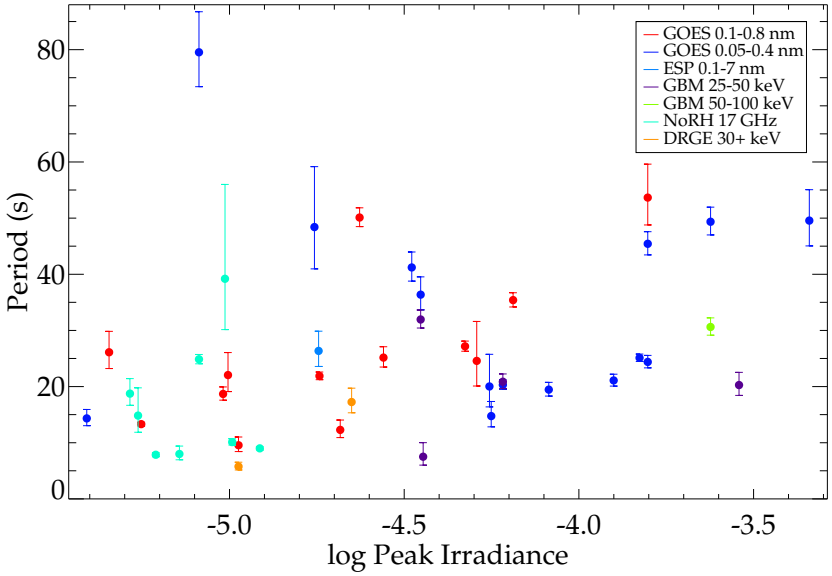

Figure 5.5: QPP periods plotted against the peak GOES/XRS 1-8 Å irradiance, where the different colours correspond to the different instruments and wavebands used to observe the flares. The Pearson correlation coefficient is 0.33, suggesting a very slight positive correlation.

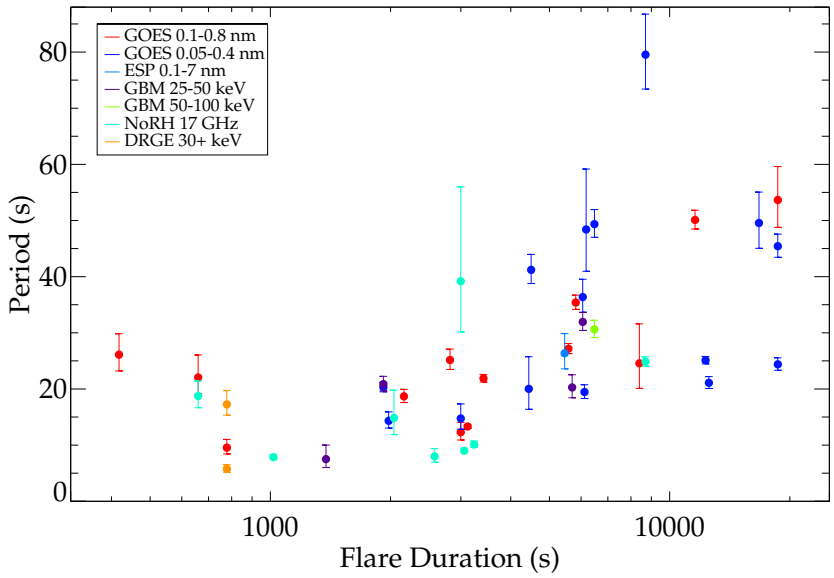

Figure 5.6: QPP periods plotted against the duration of the flares. The Pearson correlation coefficient is 0.59, suggesting a positive correlation.

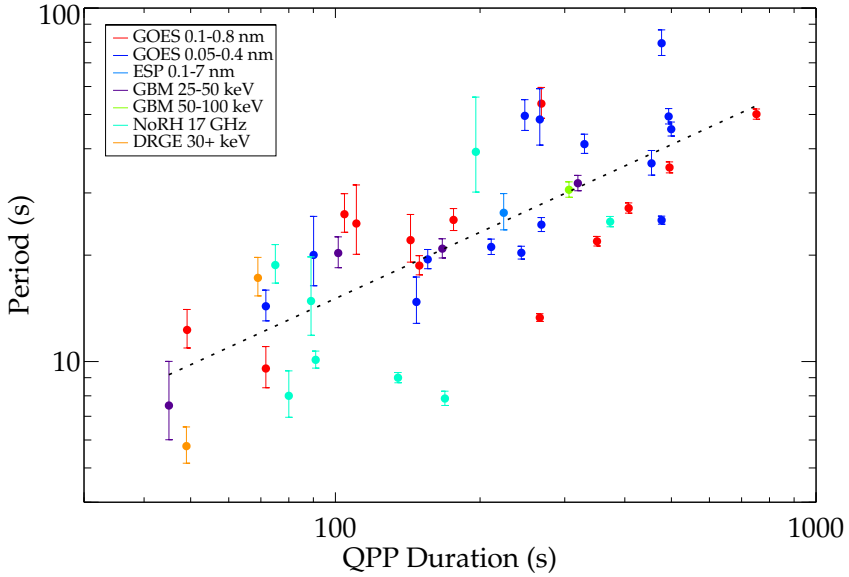

Figure 5.7: QPP periods plotted against the duration of the QPP signal. The Pearson correlation coefficient of 0.76 shows a positive correlation. The black dotted line shows a linear fit.

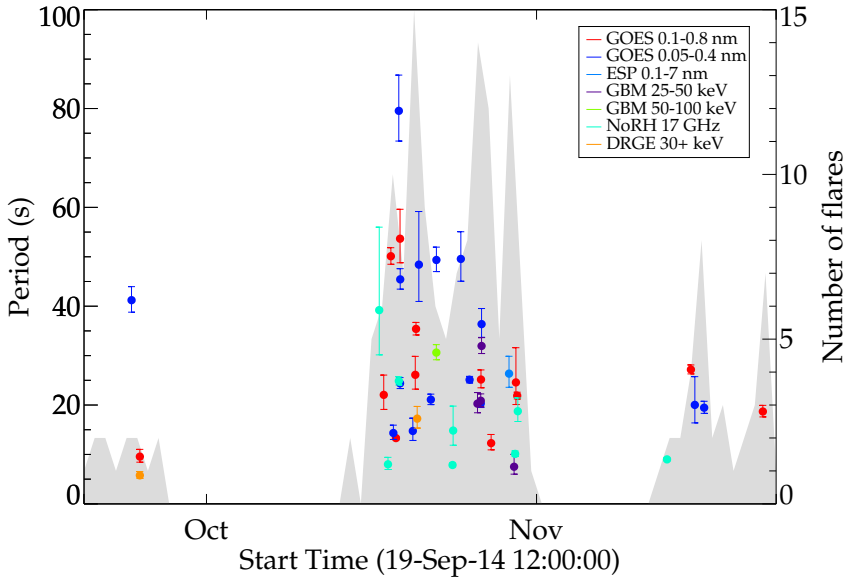

Figure 5.8: QPP periods plotted against the approximate time at which the QPP signal begins. There is no obvious trend suggesting that there is no characteristic timescale which is evolving with time. The grey shaded region indicates the number of flares that occurred on a particular day.

of the QPPs is assumed to be related to a characteristic length scale, suggests that the fine structure of the AR may be important since different structures within the AR will have different length scales. Another possibility is that for different QPP mechanisms, the characteristic length scale has a different relationship with the characteristic timescale, and that different mechanisms are responsible for different QPP signals.

5.5 Conclusions

In this chapter we have shown that 37 out of 181 flares (around 20%) from a single active region show good evidence of having stationary or weakly non-stationary QPPs using methods that limit the potential for false detections, and using data from several different instruments observing different wavelength ranges. This is likely to be a lower limit for the true number of flares in the sample with QPPs, however. For example, the presence of background trends due to the flare itself can mask QPP signals in the power spectrum (Pugh et al. 2017a), the QPPs could be non-stationary (where the period drifts with time, e.g. Kupriyanova et al. 2010) and hence would not have a well defined peak in the power spectrum, the QPPs could be too low amplitude or have the wrong period to be detectable with the instruments operating at the time, or lower quality QPP signals could have been missed during

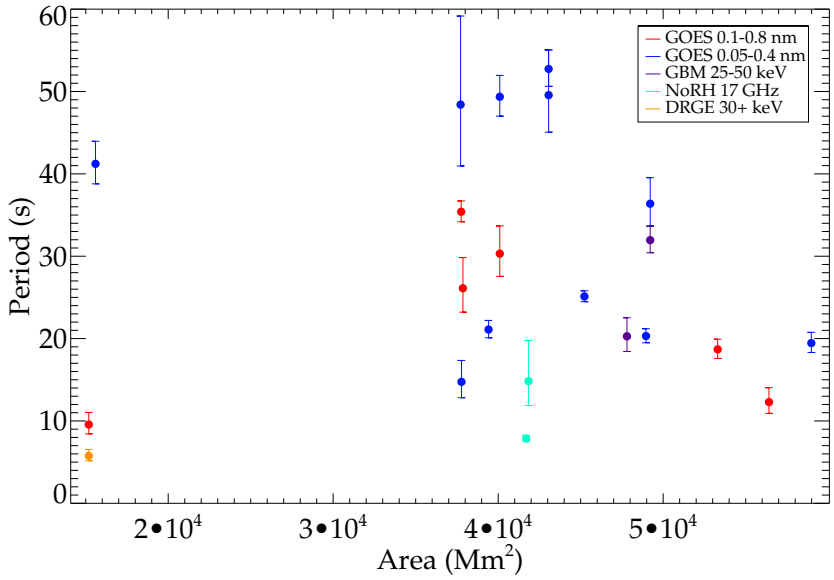

Figure 5.9: QPP periods plotted against the area of the AR at the time of the flare. The Pearson correlation coefficient is 0.05, suggesting no correlation.

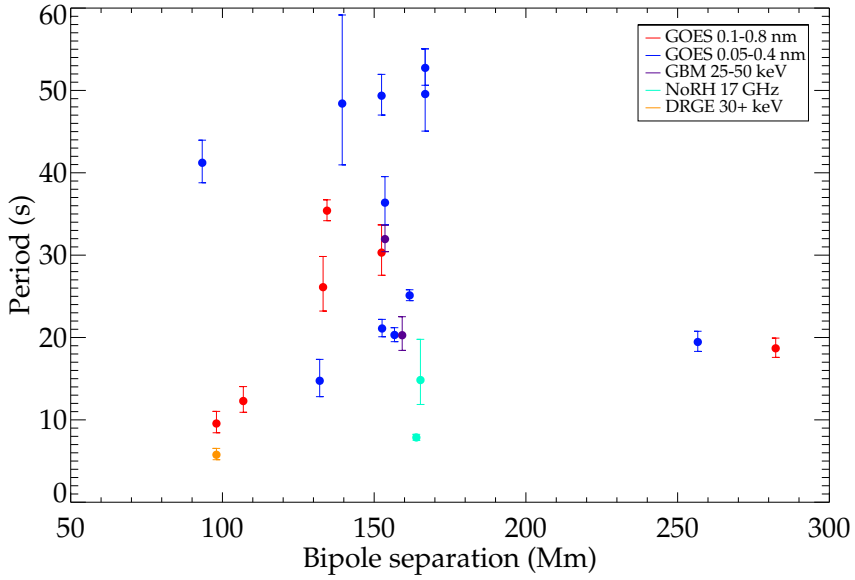

Figure 5.10: QPP periods plotted against the separation of the centres of positive and negative magnetic flux in the AR at the time of the flare. The Pearson correlation coefficient is 0.01, suggesting no correlation.

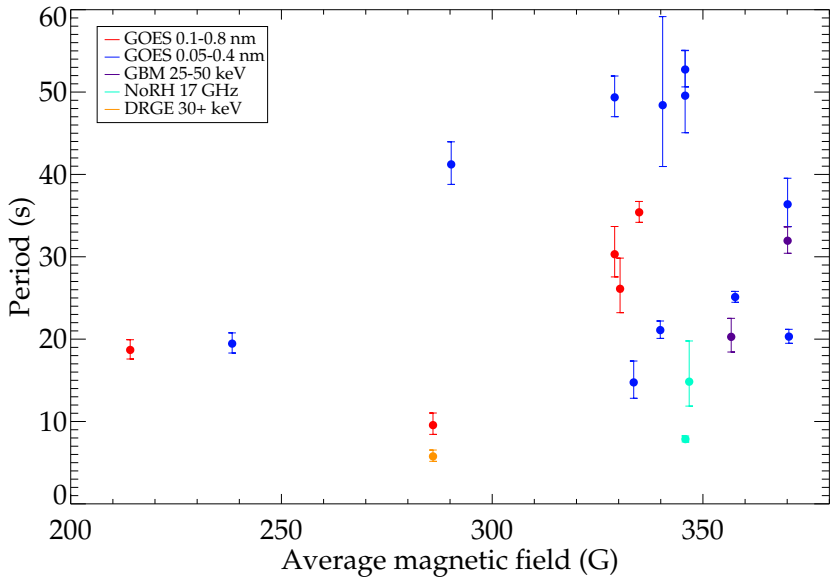

Figure 5.11: QPP periods plotted against the average magnetic field strength of the AR at the time of the flare. The Pearson correlation coefficient is 0.19, suggesting no correlation.

the manual search stage. Additionally we show how taking the time derivative of light curve data, which has previously been shown to be useful when searching for QPPs (Simões et al. 2015; Hayes et al. 2016; Dennis et al. 2017), impacts the power spectrum, and suggest how this can be accounted for when searching for periodic signals. Out of the 44 flares in this sample that overlap with those included by Inglis et al. (2016), we find the same periods in 6 (or 13 if the selection criteria used by Inglis et al. (2016) are relaxed) and agree with the lack of evidence of a QPP signal in a further 24. For the other flares either only one method identifies a periodic signal, or the periods identified by the different methods are different. The mean period for the QPPs in our sample is 20^{+16}_{-9} s. A significant correlation between the period and QPP duration was also found, and while the possibility that observational constraints may be the cause should be acknowledged, it is unclear whether this could fully explain the strong correlation.

Three properties of the AR from which the flares originate (namely area, bipole separation and average photospheric magnetic field strength) have been tracked over time, to test for any correlation with the QPP periods. No correlations were found, which could either suggest that the small-scale structure within the AR is more important, that different mechanisms act in different cases, or that the sausage mode is responsible for the QPPs, since the oscillation period may be only weakly dependent on the length of the hosting coronal loop for the sausage mode (Nakariakov et al. 2012).

Chapter 6

Quasi-periodic pulsations in white-light flares observed with *Kepler*

6.1 Introduction

The first observation of oscillations in a stellar flare was made by Rodono (1974), on the star HII 2411. Since then occasional observations of QPPs in different stars have been made in the optical (Mathioudakis et al. 2003), ultraviolet (Welsh et al. 2006), microwave (Zaitsev et al. 2004) and X-ray (Mitra-Kraev et al. 2005) wavebands. Recently, Anfinogentov et al. (2013) found QPPs in a megaflare on the dM4.5e star YZ CMi, observed in white light, that looked very similar to oscillations in solar flares that were concluded to be the result of standing slow magnetoacoustic modes. This suggests that this mechanism, where the oscillations cause plasma parameters to vary and hence modulate the acceleration of precipitating non-thermal electrons, applies for a wide range of flare energies, including superflares. So far no other evidence has been found to suggest any major differences between solar and stellar QPPs, indicating that the basic physical processes responsible for the energy releases (e.g. magnetic reconnection) are the same.

The first 7 flares in the *Kepler* data showing quasi-periodic variability were reported by Balona et al. (2015), with periods ranging from 4.8 to 14 min. The periods were not found to correlate with any global stellar parameter, suggesting that they could be QPPs in the impulsive energy release itself. Maehara et al. (2015) also noted that several flares showed QPP-like signatures in their study of superflares on solar-type stars, and Davenport et al. (2014) classified 15.5% of flares detected in the *Kepler* light curves of the highly active star GJ 1243 (KIC 9726699) as being complex, due to them having multiple peaks. In addition to this, Davenport

et al. (2014) found that a broken power-law fitted the distribution of flare durations very well, but this broken power-law model could not fully reproduce the observed fraction of complex flares as a function of duration. They concluded that this could be due to some of the apparent complex flares being the superposition of multiple independent flares, hence they fitted the complex flares with a model based on the superposition of multiple flare shapes. While large amplitude QPP could result in some of these complex flare profiles, those that are well fitted by this model and whose multiple peaks are not periodic are likely to be sympathetic flares.

Several studies have shown that hotter stars flare less frequently (e.g. Candelaresi et al. 2014). Other results have also suggested that hotter, more luminous stars produce flares with higher energies; for example, Pettersen et al. (1984) found a correlation between the cumulative flare energy distribution and stellar temperature using data from 7 stars. A large-scale study of M dwarfs also found that the higher luminosity flares were less likely to occur on the cooler, redder stars (Kowalski et al. 2009): a result that was supported by Walkowicz et al. (2011) using *Kepler* Quarter 1 observations of cool stars. The large data set from *Kepler* allows us to investigate this possible dependency of the flare energy on stellar parameters further, and recently Balona (2015) found a strong positive correlation between flare energy and stellar radius/luminosity. Since it is thought that the magnetic field of early-type stars tends to be weaker than that of late-type stars, this result suggested that the flaring AR size scales with the size of the star, as $E \approx L^3 B^2 / 8\pi$, where E is the total magnetic energy stored in the AR, L is the characteristic size of the AR, and B is the magnetic field strength. Balona (2015) also found that the flare energy scales with the host star radius cubed, much like how the energy stored in an AR scales with L^3, providing further support to this idea. Hence it was suggested that the relationship between flare energy and stellar radius could be used to constrain the magnetic field strength of the AR that produced the flare. This approach should be treated with caution, however, as it is the free magnetic energy stored in an AR which gives an upper limit on the possible flare energy, rather than the total magnetic energy.

In this chapter we present the largest collection of stellar flares exhibiting QPPs studied to date, all observed by the *Kepler* mission. Section 6.2 gives details about the analysis methods used. We derive parameters of the QPPs and investigate whether there is a relationship between the QPP period and stellar temperature, radius, rotation period and surface gravity in Section 6.3. The distribution of QPP periods is also studied, and any dependencies on other properties of the flare, namely the total energy and QPP decay time, are checked for. Section 6.3.2 provides extra detail on one of the flares that appears to exhibit QPPs with multiple periods, and Section 6.3.3 explores possible correlations between the flare energy and stellar

parameters. Finally, a summary is given in Section 6.4.

6.2 Data analysis

6.2.1 Identifying decaying oscillations in the flares

Stars classified as A- to M-type observed in short-cadence mode by *Kepler* (see Section 2.6) were searched for flares using an automated algorithm. This method, similar to that used by Walkowicz et al. (2011), involved removing long-duration trends in the SAP light curves by smoothing them over an interval of 100 min, and subtracting the smoothed version from the original light curve. Using a smoothing interval much longer than this would not sufficiently remove trends due to short period eclipsing binaries. Any time locations where more than two consecutive data points had values greater than 4.5 times the standard deviation of the detrended light curve were then flagged. Light curves containing candidate flares were checked by eye for the characteristic flare shape—a rapid rise in flux followed by a more gradual decline—and any flares showing potential signs of QPPs were analysed using the wavelet and autocorrelation techniques, which allow for the detection of non-stationary QPPs. We chose to focus on QPPs in the decline phase of the flare, as the rise phase of the flare usually happens on a much shorter timescale, and hence fewer data points are available in which to search for a signal. Note that a slightly different terminology for the flare phases is used in this chapter. We refer to the phase where the white-light emission increases to a peak as the rise phase, and the phase where the white-light emission decreases back the background value as the decline phase. This is because white-light emission of solar flares occurs entirely during the impulsive phase of the flare, and although it is not yet clear whether the same is true for stellar superflares it cannot be assumed that the decline of the white-light emission of a stellar flare coincides with the decay phase based on the SXR emission (see Section 1.2.1). QPPs have been detected in the rise phase of some solar flares (e.g. Fárník et al. 2003), however, and there is evidence of additional peaks in the rise phase of some of the flares observed by *Kepler*, so this could be the subject of a further study. The SAP data were used rather than the PDCSAP light curves, which have systematic artefacts removed, because some PDCSAP light curves were found to have artificial periodicities introduced. The target pixel files were also inspected to check that the flares were not due to contamination from a nearby object (within 4 arcseconds from the target, the size of 1 *Kepler* pixel), by ensuring that the pixels showing the flare coincided with the target point spread function. Our sample of flares includes those found by Balona et al. (2015), and those described as having complex structure by Davenport et al. (2014) and Maehara et al. (2015), however not all flares identified by these authors were considered to be

QPP flares. Flares with two peaks were omitted as it is not possible to determine whether there is a characteristic timescale when only two peaks are present. In addition to this, it is not possible to know whether the two peaks are part of the same flare, or are due to separate flares in different ARs. On the other hand, it is far less likely that more than two flares occurred in separate ARs at around the same time. Only flares exhibiting some kind of periodic behaviour in the wavelet spectrum and autocorrelation function were included in our sample.

On 2016 February 4, a problem with the *Kepler* short-cadence data pixel calibration was reported, affecting around half of the targets and meaning that those affected may have signals introduced by other stars falling on the same CCD column. Fortunately, in most cases the amount of contamination is very small compared to the target signal. The long-cadence data are unaffected, so in order to assess the reliability of the data used in this chapter the short-cadence and long-cadence target pixel files were compared, and in nearly all cases the contamination was not visible. The long-cadence and short-cadence light curves were also compared, to ensure that the flares studied appeared in both. The stars where a small amount of contamination was visible in the target pixel data are KIC 2852961 (although the QPPs can also be seen in the long-cadence data for this star), KIC 5475645, KIC 10206340 and KIC 11560431, so results from these stars should be treated with caution until the problem is fixed in next data release.

Performing a wavelet transform on a time series gives a map of non-stationary power as a function of time and period, where the period has a range from double the time step up to the total duration of the time series (see Section 3.3). Unlike a windowed Fourier transform, there is no temporal scale imposed by defining a window size. Instead, the wavelet function is scaled for each time step, so that the full range of possible periods can be mapped accurately. The disadvantage of this method is that the resolution is generally poor, and there is an intrinsic uncertainty relating to the choice of mother wavelet and number of oscillations present in the mother wavelet (De Moortel et al. 2004). In this study the Morlet wavelet with the default wavenumber of 6 was chosen, to give better period resolution but lower time resolution. The wavelet transforms were used to identify periodicities above the 99% confidence level in the flare decline phases, with a duration greater than the period. In order to estimate the QPP period from the wavelet plot, along with the associated uncertainty, the global wavelet spectrum (a time-average of the wavelet spectrum) was plotted, and a Gaussian line profile fitted to the peak corresponding to the periodic signal in the data.

The autocorrelation function (the correlation of a sample with itself) as a

function of time lag is defined as:

$$P(l) = \frac{\sum_{i=0}^{N-l-1} (x_i - \bar{x})(x_{i+l} - \bar{x})}{\sum_{i=0}^{N-1} (x_i - \bar{x})^2}, \tag{6.1}$$

where $x_i (i = 0, ..., N-1)$ is a time series, $\bar{x}$ is the mean of the time series, and l is the time lag. In this study, the time lags used ranged from zero to half the duration of the flare decline time series, with a spacing equal to the cadence of the data. The autocorrelation function of a periodic signal is also periodic, but noise is substantially suppressed, so it is useful for enhancing any stable periodic signals in the data and determining their quality.

6.2.2 Modelling the flares

Most of the stellar flares identified in this study have fairly simple time profiles compared to the solar flares in the previous chapter, hence the stellar flare trends can be modelled very well with a simple analytical function. In order to make any periodic behaviour easier to identify in the wavelet spectra and autocorrelation functions, the fitted decline trends can be removed from the flare decline light curves. As discussed in Section 3.4, the subtraction of an appropriate fitted model should not affect the underlying noise distribution, so detrending in this way does not introduce any additional risk of false detections. The following expressions were used to fit the flare decline trends using a least-squares method:

$$F(t) = A_0 e^{-t/t_0} + Bt + C, \tag{6.2}$$

or,

$$F(t) = A_0 e^{-t/t_0} + B(t - D)^2 + C, \tag{6.3}$$

where F is the flux, t is time, and A_0, t_0, B, C, D are constants. In some cases a simple exponential decay fits the flare decline very well, however most light curves have underlying trends, albeit with timescales much longer than that of the flare. These trends can be the result of differential velocity aberration, orbital motion due to the star being a binary, transits of an eclipsing binary or large exoplanet, and/or rotational variability due to starspots. To account for this, additional terms appear in the above expressions, where in Eq. 6.2 a linear term is added and in Eq. 6.3 a parabolic term is added. For the cases where there was no background trend, B was set to zero. Previous research has found that many *Kepler* flares are better fitted with a two-phase exponential decay model rather than a single exponential decay

(Davenport et al. 2014). In solar flares there are different regimes during the decay phase where either conductive or radiative post-flare cooling dominates (e.g. Cargill et al. 1995), resulting in two different exponential decays of the thermal emission. It is not yet clear if this could also apply to stellar flare white-light emission, however, which should only occur during the flare impulsive phase if it is equivalent to solar flare white-light emission. Because the focus of this study is the QPPs, and since a simple single exponential model for the flare decline gave good fits, the impact of the inclusion of a second exponential component on the QPP parameters obtained would have been minor. Furthermore, the QPPs disrupt the smooth shape of the flare decline, making it difficult to accurately fit a two-component model. Hence a more simplistic model seemed more appropriate for this study. Whether Eq. 6.2 or Eq. 6.3 was used to fit the flare decline was decided based on the shape of the light curve in the vicinity of the flare. Both of these trend functions are aperiodic, and hence their subtraction from the original light curve cannot introduce artificial periodicities.

Figure 6.1 shows stages of the analysis of a single flare on the star KIC 12156549. The decline phase light curve of this flare is shown in the top left panel, and the top right panel shows the same light curve after the flare decline trend has been subtracted. Performing a wavelet transform on the detrended light curve gives the contour plot in the bottom right panel, which shows a prominent feature above the 99 % confidence level at a period of around 45 min, and suggests the presence of an oscillatory signal. Finally, the bottom left panel shows the autocorrelation of the detrended light curve, and more clearly shows a decaying sinusoidal signal. A fit to this plot gives a period of (46 ± 1) min.

The majority of flares with a QPP-like signal in the light curve and wavelet plot either had a non-constant period, or did not decay in a straight-forward manner, meaning that the QPPs could not easily be fitted. Some of the flares, however, did have a QPP signal that appeared to be a stable decaying oscillation (i.e. a decaying signal that undergoes at least two cycles of oscillation and has a constant period) in their wavelet and autocorrelation plots. For these 11 flares (shown in Figs. 6.1 and A.47-A.56) the QPPs were fitted simultaneously with the underlying decline trend of the flare, using one of the following expressions combined with either Eq. 6.2 or 6.3:

$$F(t) = A \exp\left(\frac{-(t-B)}{\tau_e}\right) \cos\left(\frac{2\pi}{P}t + \phi\right), \tag{6.4}$$

or

$$F(t) = A \exp\left(\frac{-(t-B)^2}{2\tau_g^2}\right) \cos\left(\frac{2\pi}{P}t + \phi\right), \tag{6.5}$$

where P is the period, ϕ is the phase, τ_e and τ_g are the exponential and Gaussian

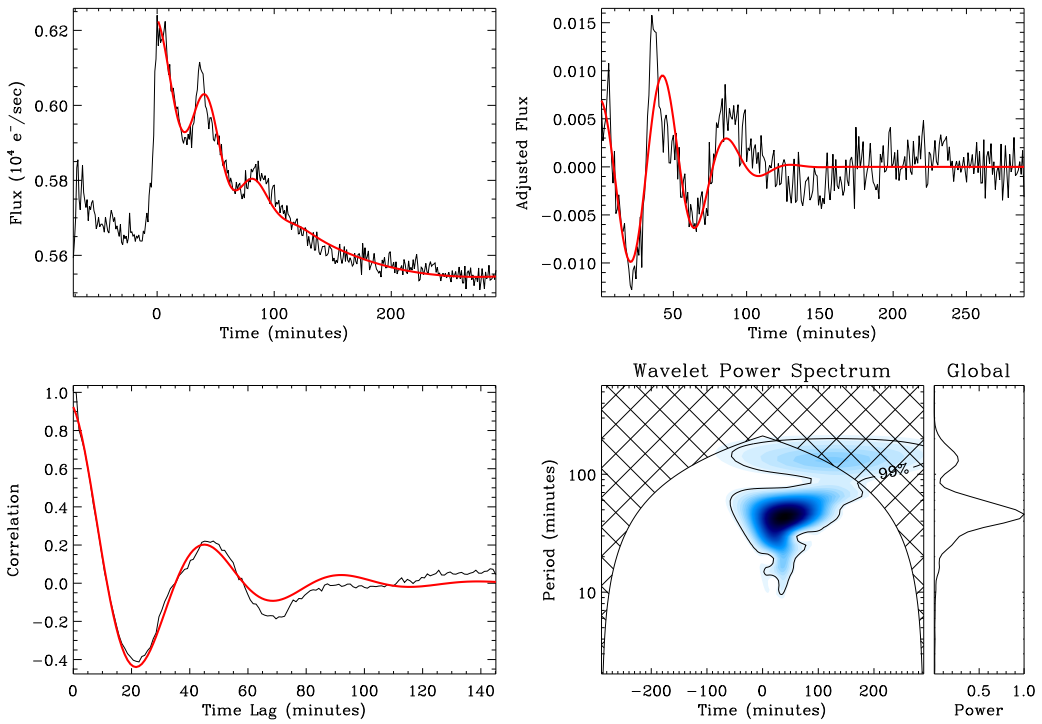

Figure 6.1: *Top left:* Light curve showing the decline phase of a flare on KIC 12156549, where start time is at the flare peak (BJD 55287.92 for this flare). The red overplotted line shows the result of a least-squares fit to the flare decline combined with the QPPs. *Top right:* The same light curve as in Fig. 6.1, but with a fit to the flare decline trend subtracted in order to emphasise short-term variability. The red overplotted line shows a decaying sinusoidal fit. *Bottom left:* The autocorrelation function of the time series shown in the top right panel, with a fitted exponentially decaying sinusoid shown in red. *Bottom right:* The wavelet spectrum of the time series in the top right plot, which has been padded with zeros at the beginning in order to bring the feature of interest into the centre of the cone of influence. The spectrum shows a feature at a period of around 45 min. The far-right panel shows the global wavelet spectrum.

damping times, respectively, and A, B are constants. An exponential decay is a natural assumption when considering damped harmonic oscillators and has already been identified in stellar flares (e.g. Anfinogentov et al. 2013), however some MHD oscillations (such as kink modes) may also have a Gaussian damping profile. This was first discovered in numerical simulations by Pascoe et al. (2012), then justified analytically by Hood et al. (2013), and shown in observations by Pascoe et al. (2016). The choice of which decay profile to use when fitting the flares was made based on the reduced chi-squared goodness-of-fit test, although for two of the flares the Gaussian modulated fit (Eq. 6.5) did not converge, hence the exponential decay model was chosen (Eq. 6.4). These fits allowed a more precise estimation of the QPP period to be obtained, along with an estimation of the QPP decay time. Uncertainties for these fitted parameters are based on the uncertainties of *Kepler* flux values, and were obtained by performing 10,000 Monte Carlo simulations. The error resampling method was used, where for each simulated sample a set of random numbers was drawn from the error distributions for each of the *Kepler* SAP flux values. These 10,000 simulated samples were fitted using Eq. 6.4 or 6.5, where the initial parameters used for these fits were the same as those obtained by fitting the original light curve. Gaussian functions were then fitted to the resulting histograms of the fitted parameters, in order to obtain a robust estimate of the value and uncertainty of each parameter. The red overplotted line in Fig. 6.1 shows the fit to the flare on KIC 12156549, which gave a QPP period of (44.6 ± 0.6) min. Figures A.47–A.56 in Appendix A.2 show the analysis of the other flares with stable decaying oscillations.

6.2.3 Calculating flare energies

The energies of the superflares were estimated using a similar method to Shibayama et al. (2013). The flare luminosity ($L_{\rm flare}$) is a function of time, and integrating with respect to time gives the total energy radiated ($E_{\rm flare}$):

$$E_{\rm flare} = \int_{\rm flare} L_{\rm flare}(t)\,{\rm d}t. \tag{6.6}$$

The bolometric flare luminosity can be calculated from the Stefan-Boltzmann relation, assuming that the emission can be approximated by a blackbody spectrum:

$$L_{\rm flare}(t) = \sigma T_{\rm flare}^4 A_{\rm flare}(t), \tag{6.7}$$

where σ is the Stefan-Boltzmann constant, $T_{\rm flare}$ is the effective temperature of the flare, and $A_{\rm flare}$ is the area covered by the flare. The ratio of the measured flare flux and stellar flux should be equal to the ratio of the flare luminosity and stellar luminosity, since $L = 4\pi d^2 F$ (where d is the distance to the star and F is the

measured flux), and the observed flare and stellar luminosities can be written as:

$$L_{\mathrm{flare,obs}} = A_{\mathrm{flare}}(t) \int r_\lambda B_{\lambda(T_{\mathrm{flare}})}\, \mathrm{d}\lambda, \tag{6.8}$$

and

$$L_{\star,\mathrm{obs}} = \pi R_\star^2 \int r_\lambda B_{\lambda(T_{\mathrm{eff}})}\, \mathrm{d}\lambda, \tag{6.9}$$

where λ is the wavelength, r_λ is the *Kepler* instrument response function, $B_{\lambda(T)}$ is the Planck function, and $R_\star$ is the stellar radius. Hence we can write:

$$\frac{\Delta F(t)}{F(t)} = \frac{A_{\mathrm{flare}}(t) \int r_\lambda B_{\lambda(T_{\mathrm{flare}})}\, \mathrm{d}\lambda}{\pi R_\star^2 \int r_\lambda B_{\lambda(T_{\mathrm{eff}})}\, \mathrm{d}\lambda}, \tag{6.10}$$

where $\frac{\Delta F}{F}$ is the change in flux due to the flare, normalised by the underlying stellar flux. This expression can be used to find $A_{\mathrm{flare}}(t)$, which can then be used to find $L_{\mathrm{flare}}(t)$ and E_{flare}. The underlying trend in the light curve is approximately linear in the vicinity of a flare, since the duration of the flare is typically short compared to the timescale of light curve modulation due to the rotation of the star. Hence, the flare amplitude, $\frac{\Delta F}{F}$, was found by subtracting each value of the linear interpolation between the flare start and flare end from the corresponding measured flux values, and then dividing the resulting values by the corresponding linear interpolation values. Uncertainties of the flare energies were estimated by performing Monte Carlo simulations with the stellar temperature and radius uncertainties (given in Table 6.1), as well as the estimated uncertainty of the flare temperature, which was taken to be $9000 \pm 500\,\mathrm{K}$ (Hawley & Fisher 1992; Hawley et al. 2003; Kretzschmar 2011). Other sources of uncertainty include assuming that the star and flare behave like blackbody radiators, defining the flare start and end (for example, the exponential decay nature of the flare decline makes it difficult to determine exactly when the flare has ended), the flux uncertainties, and the limited cadence of the data when performing the integration in Eq. 6.6. The latter three uncertainties will be much smaller than the others, hence have a negligible effect on the flare energy uncertainty.

6.2.4 Stellar parameters

The surface temperature, radius, rotation period, surface gravity and Kepler magnitude for each of the stars with evidence of QPPs in one or more flares is given in Table 6.1. The stellar temperatures, radii and surface gravities are taken from Huber et al. (2014), and the Kepler magnitudes are taken from the Kepler Input Catalogue. Stellar rotation periods were obtained following the method described in Armstrong et al. (2016), which we summarise here. We use the PDCSAP detrended

Kepler data for this step (Stumpe et al. 2012; Smith et al. 2012), and note that this can attenuate signals arising from rotation periods over approximately 21 days (García et al. 2013). Rotation periods are determined using both the autocorrelation function and a wavelet analysis, the latter to ensure the period arises from the entire duration of the data rather than a single isolated region in time. These are calculated as described in Section 6.2.1. Rotation periods are extracted from the autocorrelation function by first smoothing it with a Gaussian filter with a standard deviation the same as the strongest detected peak, truncated at 3.1σ. The first 4 harmonics of this peak are then identified, and a linear fit performed to the peak periods, as well as the maximum peak and the origin. The gradient and error of this fit then gives our autocorrelation function period and its error. We then confirm this extracted period visually against the *Kepler* light curve. This follows the similar method proposed and tested in McQuillan et al. (2014). While the wavelet analysis, due to its nature, gives less precise period measurements, we extract the wavelet period for comparison, as performed in, for example, García et al. (2014); Mathur et al. (2014). The wavelet power is summed over the time axis, giving the global wavelet spectrum. This is fit by the sum of several Gaussian profiles, with the given period found from the largest amplitude peak and its error from the half width at half maximum of this peak.

Table 6.1: Parameters of the stars that have a flare showing evidence of QPPs. For each star the Kepler Input Catalogue (KIC) number is given, along with the temperature, radius, two estimates of the rotation period obtained using different methods, surface gravity and the Kepler magnitude (K_p). Temperatures, radii and surface gravities were taken from Huber et al. (2014), with the exception of KIC 9726699, for which the temperature and radius are based on its M4 classification (Reid et al. 2004). The note EB indicates that the star is an eclipsing binary, which prevented some rotation periods from being obtained without the use of a more complex modelling procedure. [(a)] For this star, the rotation period was obtained by Davenport et al. (2015).

KIC	Temp. (K)	Radius ($R_\odot$)	Rot. per. from wavelet (days)	Rot. per. from autocorr. (days)	$\log g$ (cm/s^2)	K_p	Notes
2852961	4882^{+126}_{-118}	$5.910^{+3.154}_{-2.027}$	35.5 ± 4.8	35.505 ± 0.054	$2.888^{+0.355}_{-0.313}$	10.146	Subgiant
3128488	4565^{+123}_{-127}	$0.546^{+0.037}_{-0.041}$	6.09 ± 0.73	6.171 ± 0.014	$4.698^{+0.055}_{-0.032}$	11.667	
3540728	5015^{+173}_{-168}	$0.559^{+0.031}_{-0.034}$	2.10 ± 0.25	2.1472 ± 0.0018	$4.697^{+0.048}_{-0.028}$	12.596	
4671547	4175^{+160}_{-184}	$0.657^{+0.038}_{-0.057}$	8.03 ± 0.96	8.2215 ± 0.0048	$4.649^{+0.039}_{-0.041}$	11.293	
4758595	3573^{+88}_{-77}	$0.400^{+0.080}_{-0.050}$	19.5 ± 2.7	19.51 ± 0.16	$4.858^{+0.060}_{-0.100}$	12.148	
5475645	5513^{+171}_{-141}	$0.708^{+0.193}_{-0.046}$	7.27 ± 0.87	7.504 ± 0.012	$4.627^{+0.029}_{-0.161}$	11.205	
6184894	5388^{+175}_{-142}	$0.717^{+0.172}_{-0.069}$	2.60 ± 0.32	2.640 ± 0.014	$4.560^{+0.072}_{-0.216}$	13.028	
6437385	5727^{+180}_{-224}	$2.061^{+1.476}_{-1.270}$	13.4 ± 1.6	13.6154 ± 0.0016	$3.707^{+0.757}_{-0.360}$	11.539	
7664485	5510^{+166}_{-134}	$0.762^{+0.221}_{-0.054}$	3.12 ± 0.38	3.145 ± 0.016	$4.594^{+0.029}_{-0.177}$	13.264	
7885570	5587^{+165}_{-134}	$0.756^{+0.316}_{-0.053}$	0.85 ± 0.10	0.9139 ± 0.0062	$4.593^{+0.031}_{-0.246}$	11.679	EB
7940533	5495^{+169}_{-133}	$0.798^{+0.320}_{-0.070}$	3.82 ± 0.46	3.9032 ± 0.0031	$4.543^{+0.045}_{-0.244}$	12.862	EB

Continued on next page

Table 6.1 – *Continued from previous page*

KIC	Temp. (K)	Radius ($R_\odot$)	Rot. per. from wavelet (days)	Rot. per. from autocorr. (days)	$\log g$ (cm/s^2)	K_p	Notes
8226464	6028^{+153}_{-160}	$1.535^{+0.707}_{-0.490}$	3.08 ± 0.37	3.130 ± 0.014	$4.044^{+0.318}_{-0.228}$	11.468	
8414845	5693^{+162}_{-134}	$0.899^{+0.388}_{-0.121}$	1.88 ± 0.22	1.8889 ± 0.0072	$4.436^{+0.111}_{-0.275}$	13.298	
8915957	5518^{+138}_{-123}	$2.652^{+2.406}_{-0.354}$	46.8 ± 5.8	46.40 ± 0.58	$3.467^{+0.121}_{-0.429}$	10.918	Subgiant
9641031	6126^{+147}_{-166}	$1.176^{+0.459}_{-0.204}$	–	–	$4.285^{+0.160}_{-0.236}$	9.177	EB
9652680	5825^{+145}_{-146}	$0.835^{+0.314}_{-0.067}$	1.41 ± 0.17	1.430 ± 0.014	$4.555^{+0.032}_{-0.267}$	11.210	
9655129	5334^{+173}_{-141}	$0.810^{+0.458}_{-0.095}$	–	–	$4.492^{+0.091}_{-0.471}$	13.805	EB
9726699	3100^{+150}_{-300}	$0.26^{+0.13}_{-0.06}$	–	0.592596 ± 0.00021^a	5.283	12.738	
9821078	4268^{+136}_{-140}	$0.680^{+0.030}_{-0.058}$	–	9.792 ± 0.015	$4.602^{+0.048}_{-0.017}$	14.117	EB
9946017	6799^{+172}_{-220}	$2.892^{+0.885}_{-1.555}$	1.41 ± 0.17	1.430 ± 0.014	$3.655^{+0.529}_{-0.182}$	11.146	
10206340	5759^{+112}_{-120}	$0.945^{+0.183}_{-0.056}$	2.25 ± 0.28	2.28150 ± 0.00065	$4.481^{+0.039}_{-0.160}$	11.203	EB
10459987	5153^{+146}_{-135}	$0.649^{+0.095}_{-0.042}$	5.98 ± 0.74	6.048 ± 0.023	$4.658^{+0.030}_{-0.084}$	10.625	
10528093	5334^{+170}_{-140}	$0.746^{+0.190}_{-0.079}$	12.2 ± 1.5	12.1180 ± 0.0089	$4.536^{+0.079}_{-0.270}$	13.563	
11551430	5648^{+108}_{-91}	$1.605^{+0.377}_{-0.345}$	4.10 ± 0.52	4.1652 ± 0.0036	$4.019^{+0.183}_{-0.132}$	10.691	
11560431	5367^{+223}_{-175}	$0.828^{+0.322}_{-0.082}$	3.06 ± 0.37	3.1609 ± 0.0052	$4.514^{+0.060}_{-0.245}$	9.694	
11560447	5105^{+147}_{-152}	$0.593^{+0.042}_{-0.038}$	–	0.4891 ± 0.0020	$4.665^{+0.050}_{-0.037}$	10.834	EB

Continued on next page

Table 6.1 – *Continued from previous page*

KIC	Temp. (K)	Radius ($R_\odot$)	Rot. per. from wavelet (days)	Rot. per. from autocorr. (days)	$\log g$ (cm/s^2)	K_p	Notes
11610797	6140^{+140}_{-193}	$1.048^{+0.591}_{-0.090}$	1.58 ± 0.19	1.6303 ± 0.0026	$4.455^{+0.039}_{-0.348}$	11.535	
11665620	4683^{+132}_{-132}	$0.573^{+0.043}_{-0.045}$	0.358 ± 0.042	0.32693 ± 0.00038	$4.676^{+0.058}_{-0.034}$	14.242	
12102573	4474^{+161}_{-137}	$0.745^{+0.029}_{-0.057}$	2.71 ± 0.32	2.74038 ± 0.00065	$4.561^{+0.046}_{-0.022}$	11.815	
12156549	5888^{+350}_{-356}	$1.043^{+0.464}_{-0.191}$	3.61 ± 0.42	6.653 ± 0.014	$4.373^{+0.137}_{-0.280}$	15.886	

6.3 Results and discussion

Out of the 1439 flares detected on 216 different stars, 56 (around 4%) are found to have pronounced QPP-like signatures in the light curve, of which 11 (around 0.8% of the original flare sample) show evidence of stable decaying oscillations. The host stars range from F- to M-type. We note that 1439 is a lower estimate for the total number of flares, since low amplitude flares are not detected by the automated search. All available short cadence light curves for the flaring stars were checked by eye, however, to ensure that no flares with a QPP-like signature were missed. Details of the flares containing QPP-like signatures are given in Table 6.2, where the periods of the 11 flares with stable oscillations were obtained using the method described in Section 6.2.2, and for the other flares the period was estimated using the global wavelet spectrum. A complete list of parameters obtained from the flare fits are given by Table B.2 in Appendix B.2.

Table 6.2: Parameters of the flares showing evidence of a QPPs. The KIC number of the star is given along with the approximate time at which the flare occurs (given as the Barycentric Julian Date), the QPP period, and an estimate of the energy released during the flare.

KIC	Time (Barycentric Julian Date)	Period (min)	Flare energy (erg)
2852961	55238.22	68 ± 2	$(7.5^{+10.3}_{-4.3}) \times 10^{35}$
2852961	55240.27	93^{+27}_{-21}	$(1.4^{+2.0}_{-0.8}) \times 10^{37}$
3128488	54990.32	19^{+5}_{-4}	$(1.6^{+0.5}_{-0.4}) \times 10^{34}$
3540728	55751.38	43^{+13}_{-10}	$(2.4^{+0.8}_{-0.6}) \times 10^{34}$
3540728	55807.25	36.7 ± 0.3	$(4.1^{+1.4}_{-1.0}) \times 10^{34}$
4671547	55090.04	$4.6^{+0.9}_{-0.7}$	$(1.8^{+0.8}_{-0.5}) \times 10^{33}$
4758595	56219.15	49^{+35}_{-20}	$(1.6^{+0.9}_{-0.6}) \times 10^{33}$
5475645	55095.92	16.2 ± 0.9	$(1.3^{+0.6}_{-0.4}) \times 10^{34}$
5475645	56330.43	41^{+13}_{-10}	$(1.8^{+0.9}_{-0.6}) \times 10^{34}$
6184894	56243.87	57 ± 1	$(2.2^{+1.1}_{-0.7}) \times 10^{34}$
6184894	56291.77	56^{+29}_{-19}	$(3.5^{+1.8}_{-1.2}) \times 10^{34}$
6437385	55391.10	27^{+6}_{-5}	$(5.1^{+17.9}_{-4.0}) \times 10^{35}$
6437385	55393.76	40.9 ± 0.3	$(6.1^{+20.2}_{-4.7}) \times 10^{35}$
7664485	56107.70	54^{+14}_{-11}	$(3.3^{+1.6}_{-1.1}) \times 10^{34}$

Continued on next page

Table 6.2 – *Continued from previous page*

KIC	Time (Barycentric Julian Date)	Period (min)	Flare energy (erg)
7664485	56119.79	62 ± 4	$(2.7^{+1.4}_{-0.9}) \times 10^{34}$
7885570	55010.88	30^{+9}_{-7}	$(2.4^{+1.4}_{-0.9}) \times 10^{34}$
7940533	55317.42	65^{+12}_{-15}	$(7.9^{+5.2}_{-3.1}) \times 10^{34}$
8226464	55012.10	61 ± 2	$(2.2^{+2.7}_{-1.2}) \times 10^{35}$
8414845	56217.91	39 ± 7	$(3.2^{+2.4}_{-1.4}) \times 10^{34}$
8414845	56285.43	87^{+18}_{-15}	$(5.7^{+4.3}_{-2.5}) \times 10^{34}$
8414845	56293.70	24^{+16}_{-10}	$(2.5^{+1.8}_{-1.0}) \times 10^{34}$
8915957	55152.31	45^{+16}_{-12}	$(8.4^{+11.4}_{4.8}) \times 10^{34}$
9641031	55614.55	23.7 ± 0.2	$(6.9^{+5.6}_{-3.1}) \times 10^{34}$
9652680	55085.13	75 ± 2	$(6.0^{+3.6}_{-2.3}) \times 10^{34}$
9655129	56149.04	78 ± 5	$(3.4^{+3.0}_{-1.6}) \times 10^{34}$
9726699	55382.78	22.0 ± 0.4	$(2.9^{+3.7}_{-1.6}) \times 10^{32}$
9726699	55401.16	24.2 ± 0.1	$(5.5^{+7.9}_{-3.2}) \times 10^{31}$
9726699	55409.48	13^{+5}_{-3}	$(7.8^{+11.2}_{-4.6}) \times 10^{31}$
9726699	55749.56	29^{+6}_{-5}	$(1.6^{+2.1}_{0.9}) \times 10^{32}$
9726699	55999.77	9.16 ± 0.02	$(2.6^{+3.8}_{1.5}) \times 10^{33}$
9726699	56082.84	44^{+16}_{-12}	$(1.6^{+2.2}_{-0.9} \times 10^{32}$
9821078	55487.25	42^{+8}_{-12}	$(6.0^{+2.2}_{-1.6}) \times 10^{33}$
9946017	55217.57	29.1 ± 0.4	$(6.9^{+12.2}_{-4.4}) \times 10^{35}$
10206340	55076.74	39^{+21}_{-14}	$(2.5^{+1.0}_{-0.7}) \times 10^{34}$
10459987	55158.15	12.9 ± 0.3	$(2.5^{+0.9}_{-0.7}) \times 10^{33}$
10459987	56189.39	55^{+16}_{-13}	$(1.8^{+0.6}_{-0.5}) \times 10^{33}$
10528093	56214.53	87^{+29}_{-22}	$(2.4^{+1.3}_{-0.8}) \times 10^{34}$
10528093	56262.77	74^{+34}_{-23}	$(1.4^{+0.8}_{-0.5}) \times 10^{35}$
11551430	55004.60	21^{+7}_{-5}	$(1.4^{+1.0}_{-0.6}) \times 10^{35}$
11551430	55024.13	28^{+8}_{-6}	$(1.3^{+0.8}_{-0.5}) \times 10^{35}$
11551430	55031.05	38 ± 5	$(3.4^{+2.2}_{-1.3}) \times 10^{35}$
11551430	55031.96	35^{+9}_{-7}	$(1.7^{+1.1}_{-0.7}) \times 10^{35}$

Continued on next page

Table 6.2 – *Continued from previous page*

KIC	Time (Barycentric Julian Date)	Period (min)	Flare energy (erg)
11551430	56117.13	33^{+8}_{-7}	$(3.3^{+2.1}_{-1.3}) \times 10^{35}$
11551430	56134.74	23^{+5}_{-4}	$(2.6^{+1.7}_{-1.0}) \times 10^{35}$
11551430	56166.63	71^{+40}_{-25}	$(2.3^{+1.5}_{-0.9}) \times 10^{35}$
11551430	56208.35	41^{+19}_{-13}	$(4.3^{+2.9}_{-1.7}) \times 10^{35}$
11551430	56264.09	13^{+4}_{-3}	$(4.5^{+3.0}_{-1.8}) \times 10^{35}$
11551430	56270.75	17^{+9}_{-6}	$(4.7^{+3.1}_{-1.9}) \times 10^{35}$
11560431	56150.68	$9.5^{+3.2}_{-2.4}$	$(2.1^{+1.5}_{-0.9}) \times 10^{33}$
11560431	56193.12	25^{+6}_{-5}	$(3.1^{+2.1}_{-1.3}) \times 10^{33}$
11560447	55947.44	21^{+5}_{-4}	$(5.8^{+2.0}_{-1.5}) \times 10^{34}$
11610797	54981.63	12 ± 2	$(1.1^{+0.9}_{-0.5}) \times 10^{35}$
11665620	55762.95	20^{+8}_{-6}	$(4.2^{+1.4}_{-1.0}) \times 10^{34}$
12102573	55086.03	37^{+9}_{-7}	$(3.7^{+1.3}_{-0.9}) \times 10^{33}$
12156549	55287.92	44.6 ± 0.6	$(5.0^{+4.7}_{-2.4}) \times 10^{35}$
12156549	55347.20	28^{+9}_{-7}	$(5.4^{+5.3}_{-2.7}) \times 10^{35}$

6.3.1 Properties of the QPPs

Figure 6.2 shows scatter plots of the period of the 56 flares showing a QPP-like signal with various stellar parameters: namely surface temperature, radius, rotation period and surface gravity. The surface gravity is dependent on the temperature and radius, but is included for completeness. None of the correlation coefficients suggest a relationship between the QPP period and the global stellar parameters, implying that the pulsations are related to a local, rather than global, phenomenon. Nor is there strong evidence of a correlation between the QPP period and total flare energy, as shown in the left-hand panel of Fig. 6.3, which is consistent with the results of Chapter 5. Since the flare energy scales with stellar temperature, radius, and surface gravity, as shown in Section 6.3.3, it follows that if the QPP period does not relate to any stellar parameter, then it should not relate to the flare energy either. In all of these plots, no distinction can be made between the flares with high-quality, stable decaying oscillations, and those which are quasi-periodic. The QPP decay times were also checked for any dependency on the stellar parameters

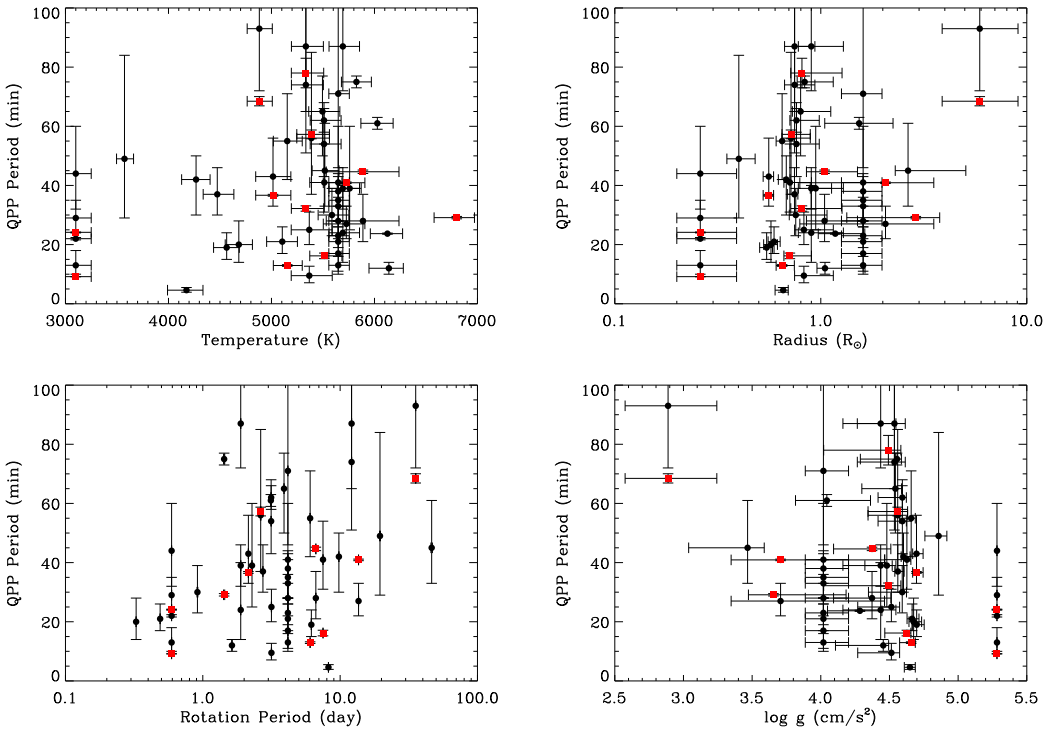

Figure 6.2: *Top left:* Scatter plot of stellar effective temperature and QPP period. The Pearson correlation coefficient is 0.184, with a p-value of 0.086, and the Spearman coefficient is 0.077, with a p-value of 0.567. *Top right:* Scatter plot of stellar radius and QPP period. The Pearson correlation coefficient is 0.312, with a p-value of 0.009, and the Spearman coefficient is 0.172, with a p-value of 0.200. *Bottom left:* Scatter plot of stellar rotation period and QPP period. The Pearson correlation coefficient is 0.357, with a p-value of 0.003, and the Spearman coefficient is 0.246, with a p-value of 0.073. *Bottom right:* Scatter plot of stellar surface gravity and QPP period. The Pearson correlation coefficient is -0.281, with a p-value of 0.017, and the Spearman coefficient is -0.193, with a p-value of 0.151. In all plots, the red square points indicate the flares with a stable decaying oscillation, and the black round points indicate the quasi-periodic flares.

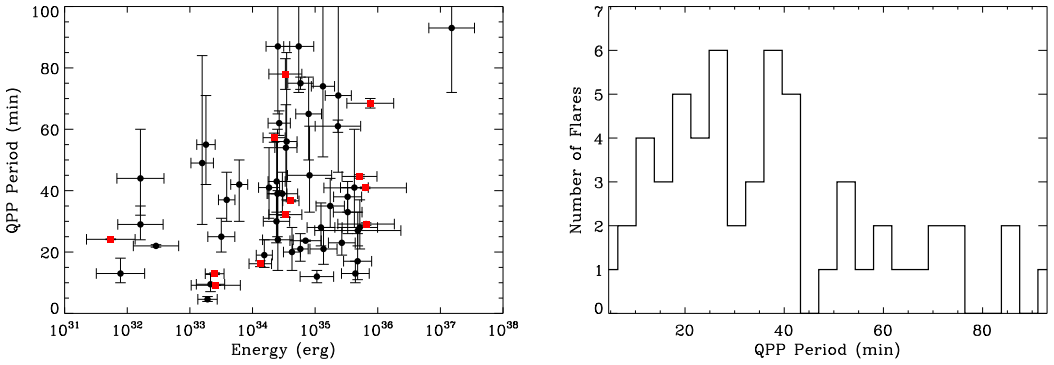

Figure 6.3: *Left:* Scatter plot of flare energy and QPP period. The Pearson correlation coefficient is 0.333, with a p-value of 0.005, and the Spearman coefficient is 0.219, with a p-value of 0.102. The red points indicate the flares with a high-quality, stable decaying oscillation. *Right:* Histogram showing the distribution of QPP periods.

or flare energy, but no correlations were found.

A histogram of the distribution of periods is given in the right-hand panel of Fig. 6.3. While the detectable range of periods is limited by the cadence of the data and the duration of the flare, the plot shows that apart from the majority of flares having a period less than 45 min, there does not appear to be a clear preference for a particular period range. Even for the cases where several QPP flares are detected on the same star, there is still a wide range of periods, as shown in Table 6.2. This is consistent with the solar case, where a wide range of QPP periods are detected in solar flares (see Chapter 5 and Nakariakov & Melnikov 2009).

Properties of the flares with stable decaying oscillations are given by Table 6.3, with a complete list of parameters given by Table B.3 in Appendix B.2. A scatter plot of the oscillation period and the oscillation decay time for these flares is given in the left-hand panel of Fig. 6.4, where the flares with exponentially damped oscillations do not show a correlation, but those with Gaussian modulated oscillations do. Due to the limited sample size, however, future observations will be needed to confirm this. Fitting a linear model for the flares with Gaussian modulated oscillations, as shown by the red line in the left-hand panel of Fig. 6.4, gives the following expression:

$$\log \tau_g = (1.31 \pm 0.06) \log P - (0.46 \pm 0.07). \tag{6.11}$$

The above expression is close to the relationship $\tau \sim P$, which has been derived both theoretically and observationally for standing kink and slow magnetoacoustic oscillations of solar coronal loops, and corresponds to damping due to resonant absorption (also referred to as mode coupling) for kink waves (e.g. Ofman & As-

chwanden 2002; Aschwanden et al. 2003; Goddard et al. 2016; Cho et al. 2016) or thermal conduction for slow magnetoacoustic waves (Ofman & Wang 2002). The same damping mechanism can be responsible for the two types of damping profile; for example, for kink modes a low density contrast between the oscillating coronal loop and the background plasma results in weak mode coupling, and hence a Gaussian damping profile of the oscillations, while a high density contrast would result in strong mode coupling and hence exponential damping (Pascoe et al. 2016). It is still possible that the exponentially damped oscillations could show a similar relationship with more data, since the decay time is not expected to scale perfectly with the period; both the decay time and period should also depend on other properties of the oscillating coronal structure.

The right-hand panel of Fig. 6.4 shows that the decay times are not correlated with the amplitude of the QPPs (normalised by the stellar flux at the base of the flare, so that the brightness of the star does not influence the amplitude) suggesting that the majority of these flares have a linear QPP signal, since a non-linear signal would result in higher amplitude QPPs being damped more strongly. There was also no evidence that the QPP period correlated with the amplitude.

Table 6.3: Parameters of the flares showing evidence of a stable decaying oscillation. The KIC number of the star is given along with the approximate time at which the flare occurs, the period of oscillation, the decay time, the damping profile type that best fits the oscillations, and an estimate of the energy released during the flare. Note that KIC 9655129 is included twice as two separate periods were detected (Pugh et al. 2015). We also note that while the period obtained for the flare on KIC 9946017 is very close to the *Kepler* long cadence time period of 29.4 min, the same period was not detected elsewhere in the light curve.

KIC	Time (Barycentric Julian date)	Period from wavelet (min)	Period from fit (min)	Oscillation decay time (min)	Decay profile	Flare energy (erg)
2852961	55238.22	60^{+16}_{-13}	68 ± 2	26 ± 2	Gaussian	8.3×10^{35}
3540728	55807.25	36^{+10}_{-8}	36.7 ± 0.3	17.2 ± 0.8	Gaussian	4.2×10^{34}
5475645	55095.92	16^{+5}_{-4}	16.2 ± 0.9	9 ± 2	Gaussian	1.3×10^{34}
6184894	56243.87	52^{+16}_{-12}	57 ± 1	59 ± 8	Gaussian	2.3×10^{34}
6437385	55393.76	39^{+13}_{-10}	40.9 ± 0.3	26.5 ± 0.4	Gaussian	6.8×10^{35}
9655129	56149.04	78^{+23}_{-17}	78 ± 5	58 ± 15	Exponential	3.6×10^{34}
9655129	56149.04	32 ± 7	32 ± 1	65 ± 37	Exponential	3.6×10^{34}
9726699	55401.16	28^{+9}_{-7}	24.2 ± 0.1	133 ± 33	Exponential	5.5×10^{31}
9726699	55999.77	8 ± 2	9.16 ± 0.02	4.87 ± 0.03	Gaussian	2.6×10^{33}
9946017	55217.57	30^{+8}_{-6}	29.1 ± 0.4	53 ± 6	Exponential	7.1×10^{35}
10459987	55158.15	13^{+3}_{-2}	12.9 ± 0.3	10 ± 1	Exponential	1.8×10^{33}
12156549	55287.92	45^{+14}_{-11}	44.6 ± 0.6	36 ± 2	Gaussian	5.4×10^{35}

6.3.2 Observation of multiple periods in a flare

In this section we focus on a rare example of a flare showing evidence of two periods of oscillation, which occurred on KIC9655129, a K-type eclipsing binary star. While at this stage it is difficult to tell from which of the binary stars the flare originates, the conclusions of this study do not rely upon the stellar spectral type. This star has a low contamination factor of 0.035, meaning that little of the light detected comes from surrounding objects. Multiple period QPPs are of great interest because they impose additional constraints on the plasma parameters, have implications for the underlying QPP mechanisms, and have interesting seismological implications (e.g. Van Doorsselaere et al. 2007; Inglis & Nakariakov 2009; Van Doorsselaere et al. 2011). Detections of multiple period QPPs are only very occasionally made in solar flares (e.g. Inglis & Nakariakov 2009), owing to the lower amplitudes of higher harmonics, and they are even rarer in stellar flares, most likely due to the noise level of the data. Only two examples in stellar flares have been reported previously, both of which were detected in different wavebands to the flare presented in this section. The first case was found in the microwave band by Zaitsev et al. (2004), which had one quasi-periodic component with a period that varied from 0.5 to 2 s during the flare, and the other was a series of pulses with a period of 0.5 s. The second case was found in the X-ray band by Srivastava et al. (2013), which had periods of 21.0 and 11.5 min. For these two cases the detected periods are different to the ones found in our study, and the flares themselves may or may not be superflares, since the flare amplitudes were not specified. Moreover, a white-light emission burst is considered to be a signature of a superflare.

A section of the short cadence light curve from KIC9655129 containing the flare of interest, which occurred on 2012 August 9^{th}, is shown in the left-hand panel of Fig. 6.5. The periodic modulation of the light curve is due to this star being a binary, and the dip is where one star eclipses the other. The three small peaks near the centre are flares, and the right-hand panel of Fig. 6.5 shows the decline phase of the central flare.

The left-hand panel of Fig. 6.6 shows the de-trended light curve. The wavelet spectrum, shown in the right-hand panel of Fig. 6.6, has a clear feature at a period of 78^{+23}_{-17} min, which is above the 99% confidence level (as defined by Torrence & Compo 1998). There is also a feature above the 99% level at a period of around 250 min, which can be ignored as its duration is roughly equal to its period, so cannot be considered to be an oscillatory pattern. The small short-period features are due to noise in the data. The high-power spectral feature appears to split into two bands, suggesting the presence of two different periodic signals.

To examine a possible second periodic signal, we subtracted the signal given by Eq. 6.4 with the best-fitting coefficients from the de-trended original light curve,

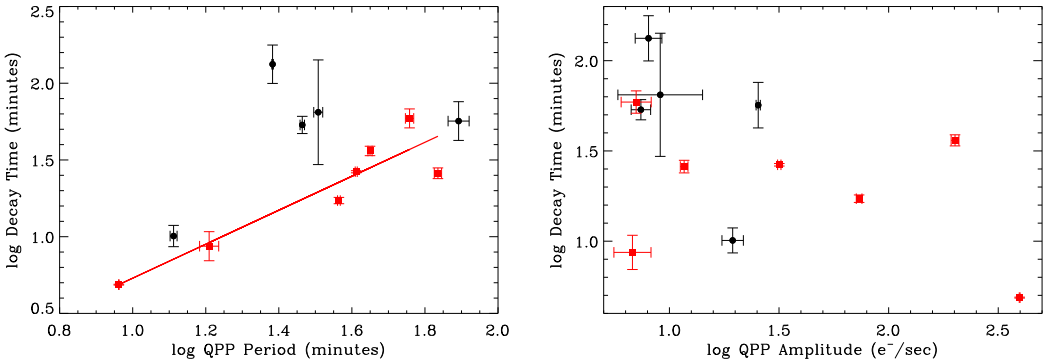

Figure 6.4: *Left:* Scatter plot of QPP period and QPP decay time, where only flares with a stable periodic signal and an exponential or Gaussian decay profile were used. Those with an exponential decay profile are shown in black, and those with a Gaussian profile are shown in red. For the exponential decay profile flares, the Pearson correlation coefficient is 0.042, with a p-value of 0.378, and the Spearman coefficient is 0.300, with a p-value of 0.624. For the Gaussian modulated flares, the Pearson correlation coefficient is 0.737, with a p-value of 0.000, and the Spearman coefficient is 0.786, with a p-value of 0.036. *Right:* Scatter plot of normalised QPP amplitude and QPP decay time. The Pearson correlation coefficient is -0.371, with a p-value of 0.002, and the Spearman coefficient is -0.364, with a p-value of 0.245.

and then performed a wavelet transform on the resultant time series. The remnant signal is shown in the left-hand panel of Fig. 6.7, with a decaying sinusoidal fit overplotted in red. Despite the noise in this plot, several cycles of the oscillation can be seen near the start, and this becomes more clear when a wavelet transform is performed, as shown in the right-hand panel of Fig. 6.7. The bright band above the 99% confidence level shows a second period of 32 ± 7 min. There is also evidence of a possible third periodic signal at around 19 min, but it requires a more complex fit.

Figure 6.8 shows the result of fitting all parameters simultaneously and performing 10,000 Monte Carlo simulations, using a fitting function combining Eq. 6.2 with the two periodic signals, described by Eq. 6.4. Histograms for the two fitted periods are shown in Fig. 6.9. These have been fitted with Gaussian functions to give values of 78 ± 5 and 32 ± 1 min, which are in good agreement with the values obtained using the wavelet and autocorrelation methods. The same Monte Carlo simulations were used to evaluate correlations between the different fitted parameters. No strong correlations were found between the periods themselves (Pearson's correlation coefficient of 0.08), or between the periods and their corresponding decay times (Pearson's correlation coefficient of 0.19 for the longer period and 0.29 for the shorter period), suggesting that they are independent. Although the longer period was found to be slightly correlated with the decay time of the flare itself (t_0 in Eq. 6.2), with a Pearson's correlation coefficient of 0.5, over 99% of the fitted values

were within the range of 78^{+23}_{-17} min indicated by the wavelet analysis, suggesting that the data de-trending has not significantly influenced the results.

The significance of finding a multi-period QPP is that it is a strong indication that MHD oscillations are the cause of the QPPs in this flare. Multiple periods are difficult to explain with the load/unload mechanisms whereas harmonics are a common feature of resonators, and different types of wave (see Section 1.3.1) have different characteristic periods and damping times. There is, however, a possibility that the QPP signal detected in the flare is non-linear, and such a signal could readily be produced by a self-oscillation (Nakariakov et al. 2012). A non-linear signal, for example a sawtooth wave, can be constructed by the superposition of different sine/cosine waves (a Fourier series expansion), hence its Fourier/wavelet spectrum would have multiple peaks. In this case the phase difference between the sinusoidal components at a particular point in time would be 2π less than the phase difference at a point one cycle of the fundamental harmonic ahead of the first point. On the other hand, if the signals belong to different MHD modes or their spatial harmonics, they may have phases disconnected from one another. To check whether the detected periodic signals are time harmonics of the same non-linear signal, the phases of oscillation of the two periodic signals were found by fitting Eq. 6.4, with a period equal to 78 min, to the de-trended light curve (shown in Fig. 6.6), and fitting the shorter-period signal to the de-trended light curve with the fitted longer-period signal subtracted (shown in Fig. 6.7). The phases were found to be 3.8 ± 0.1 radians for the longer-period signal, and 0.6 ± 0.2 radians for the shorter-period signal, giving a phase difference of 3.2 ± 0.2 radians at the time $t = 0$. After one cycle of the longer-period signal the phase difference is 5.7 ± 0.2 radians, and after two cycles it is 14.6 ± 0.2 radians. Since these phase differences do not differ by a factor of 2π, this suggests that the signal is linear and that the shorter-period signal is a spatial harmonic of the longer-period signal, or the result of a different MHD mode. Also, the decay time of the shorter-period signal is 77 ± 29 min, compared to 80 ± 12 min for the longer-period signal. If this shorter-period signal were a higher harmonic of a non-linear signal, it would be expected to decay faster than the fundamental harmonic. Indeed it is possible that the shorter-period signal decays faster than the main oscillation due to the associated uncertainties, but it is more likely the case that they are similar in duration.

Considering the ratio of the periods; for a uniform medium the fundamental and second harmonics might be expected to be a factor of two different, whereas here the periods have a ratio of 2.4 ± 0.4. While some MHD modes are dispersionless or weakly dispersive (e.g. torsional and slow magnetoacoustic), others are highly dispersive (e.g. kink and sausage) and so the ratio of the periods of their spatial harmonics can be non-integer (Inglis & Nakariakov 2009). Also stratification of the

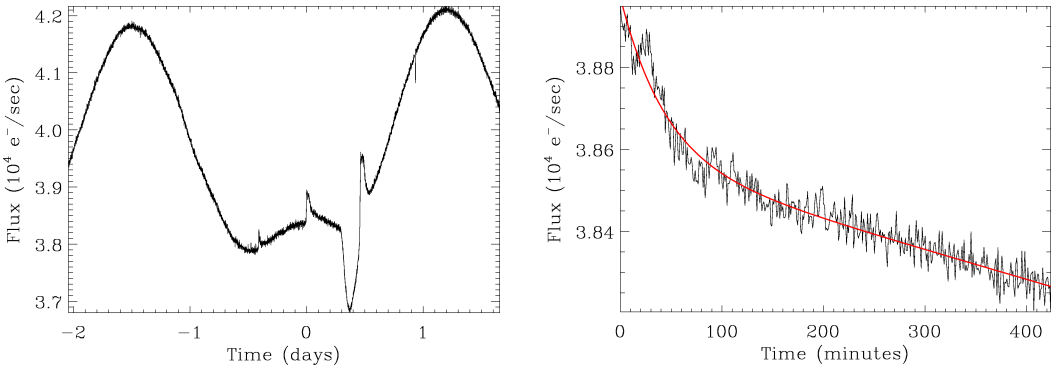

Figure 6.5: *Left:* A section of the short cadence light curve of KIC9655129 from Quarter 14b, which contains three flares. *Right:* A shorter section of the light curve, showing the decline phase of the central flare in the plot on the left. The peak intensity of the flare is at time, $t = 0$. The red overplotted line is the result of a least-squares fit to the flare decline, as detailed in Section 6.3.

plasma density due to gravity, along with the geometry of coronal loops, means that the plasma density and magnetic field strength vary along the loop, and hence it is most likely that the wave frequency does not scale linearly with the wavelength for spatial harmonics. Therefore this ratio is consistent with the findings in the previous paragraph, and the presence of spatial harmonics. While we cannot use this information to conclusively identify the mechanism behind the QPPs, sausage modes can be excluded, as their characteristic periods are much shorter than those detected here (Nakariakov et al. 2012).

6.3.3 Flare energy scaling laws

The correlations of QPP parameters with stellar parameters and flare energies were studied in Section 6.3.1, and so in this section the dependency of the total flare energy on stellar parameters is examined. Plotting the flare energy against stellar surface temperature (as shown in the top left panel of Fig. 6.10) shows a strong positive correlation. While the Pearson correlation coefficient does not seem to be reliable for this case, due to the outlying points, the Spearman correlation coefficient and associated p-value shows a strong correlation, supporting previous findings, and fitting a straight line gives the following expression:

$$\log E = (9.2 \pm 0.4) \log T_\star + (0 \pm 2). \tag{6.12}$$

A similarly strong relationship is found between the flare energy and stellar radius (top right panel of Fig. 6.10), and the fitted expression is in excellent agreement with the relationship of $\log E = 3 \log R_\star / R_\odot + 34.14$ found by Balona (2015), despite the

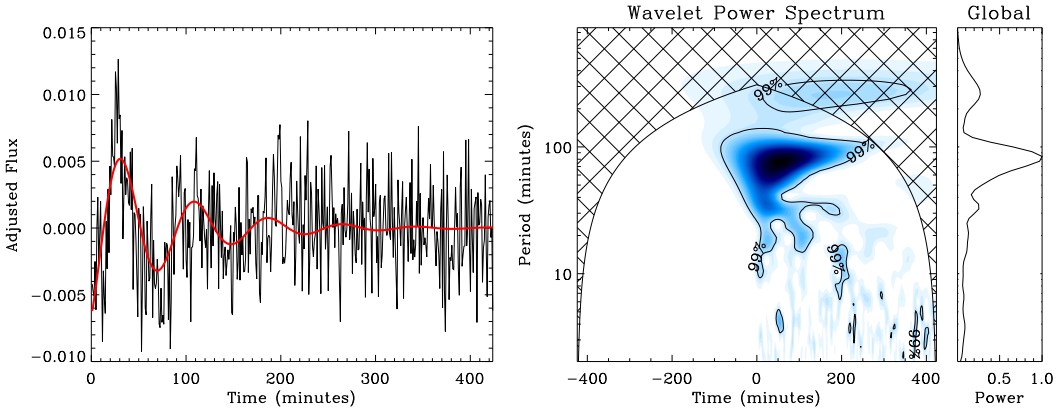

Figure 6.6: *Left:* The de-trended decline phase of the flaring light curve, with a fit to the main periodic signal overplotted in red. *Right:* Corresponding wavelet spectrum. The bright feature has a period of 78^{+23}_{-17} min. The far-right panel shows the global wavelet spectrum. The beginning of the time series used to produce the wavelet spectrum have been padded with zeros in order to bring the features of interest into the centre of the cone of influence. The peak of the flare is at the time $t = 0$.

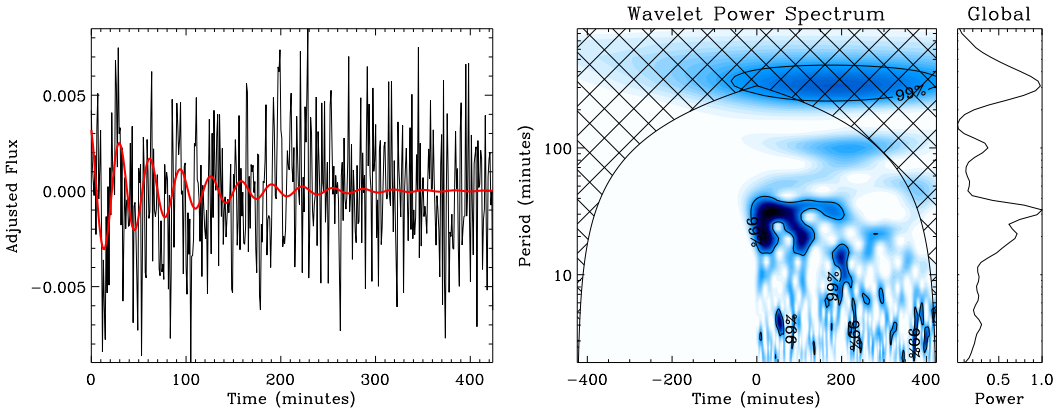

Figure 6.7: *Left:* The de-trended light curve in the left panel of Fig. 6.6 with a fit to the main periodic signal subtracted. Fitting the shorter-period signal gives the curve overplotted in red. *Right:* Corresponding wavelet spectrum, showing a second period of 32 ± 7 min. The far-right panel shows the global wavelet spectrum. The beginning of the time series used to produce the wavelet spectrum have been padded with zeros in order to bring the features of interest into the centre of the cone of influence. The peak of the flare is at the time $t = 0$.

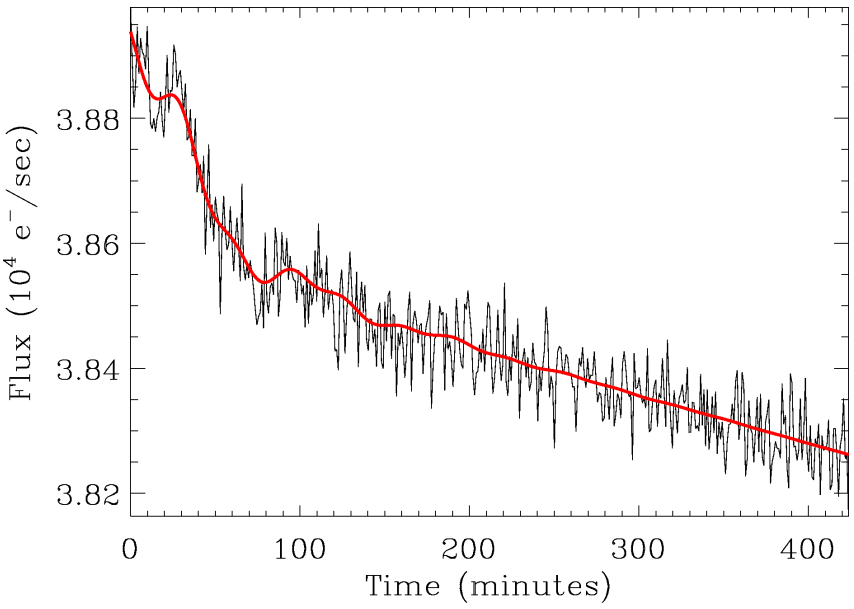

Figure 6.8: The flare decline light curve with the red overplotted curve showing the result of a least-squares fit to the flare decline, along with the two periodic signals.

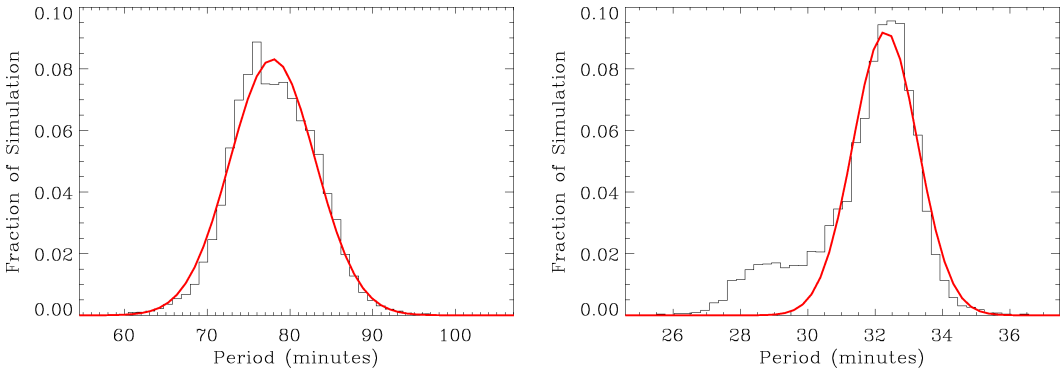

Figure 6.9: Histograms showing the results of Monte Carlo simulations for the main *(left)* and secondary *(right)* periods. The red overplotted curves show Gaussian fits, which have been used to estimate values of 78 ± 5 min for the longer period, and 32 ± 1 min for the shorter period.

smaller sample size used:

$$\log E = (3.0 \pm 0.1) \log R_\star / R_\odot + (34.70 \pm 0.03). \tag{6.13}$$

No correlation was found between the flare energy and stellar rotation period, as shown in the bottom left panel of Fig. 6.10, which is in agreement with previous findings (Maehara et al. 2012; Candelaresi et al. 2014). The bottom right panel of Fig. 6.10 shows that the flare energy correlates negatively with stellar surface gravity, which is to be expected if larger, hotter main sequence stars tend to have a lower surface gravity. Fitting a linear expression gives:

$$\log E = (-1.88 \pm 0.08) \log g + (42.9 \pm 0.4). \tag{6.14}$$

Since no correlations were found between the QPP period and any stellar parameters or the flare energy, the relationships derived above are unlikely to have any bearing on the future study of QPPs in stellar flares. They may, however, have implications for the study of superflares: in particular, the likelihood of a superflare occuring on the Sun (Shibata et al. 2013).

6.4 Conclusions

Correlations between QPP periods in stellar flares and various parameters of the host stars were studied. The periods were not found to depend on any global stellar parameters, suggesting that they are related to local properties of the flaring site or AR only, rather than being the result of the leakage of global oscillations such as p- or g-modes (the periods of which are determined by stellar parameters). This supports the idea that the QPPs observed in stellar flares are akin to those in solar flares, and that coronal seismology techniques can be applied in the stellar context provided the mechanism responsible for the QPPs can be determined. The period was also found to be independent of the flare energy, again suggesting that QPPs in stellar superflares can be used to learn about the local conditions in flaring ARs, in much the same way as QPPs in solar flares. Another observational finding that supports the possible association of QPPs with MHD oscillations is the presence of a characteristic decay of the detected QPP signal in many cases, which is consistent with solar flare QPP light curves and spatially resolved oscillations of coronal plasma structures, observed in the extreme ultraviolet and microwave bands. This apparent independence of the QPP parameters from other observables makes them a potentially important independent diagnostic tool.

As expected from the theory of coronal loop oscillations, the QPP damping time was related to the period by a power law. Only the flares with Gaussian

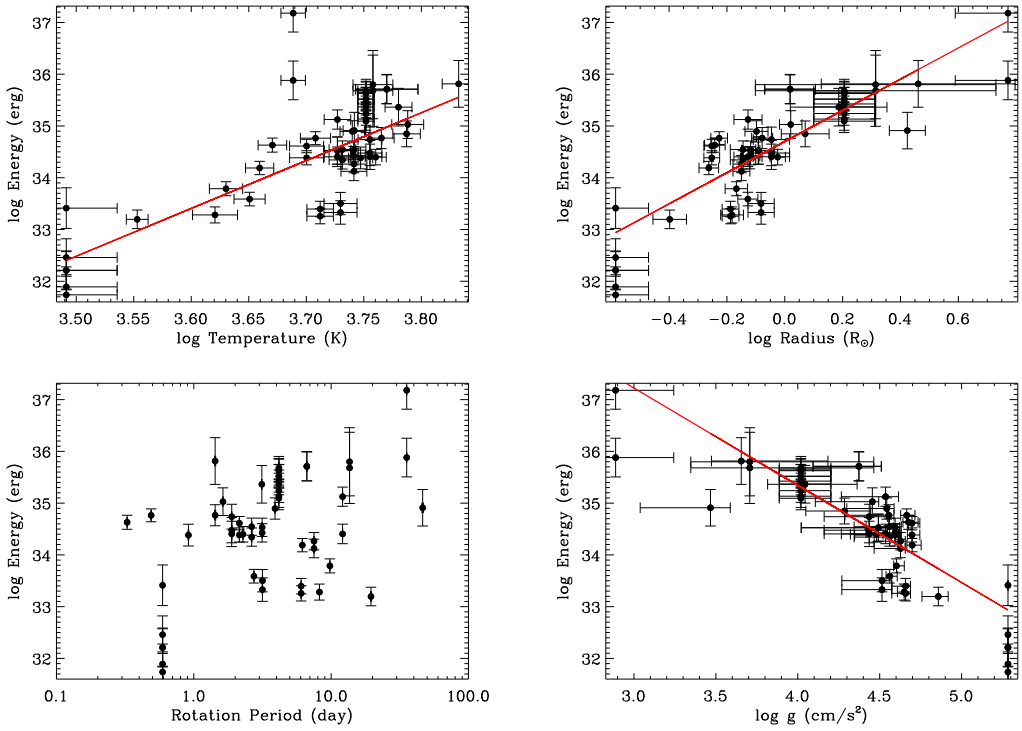

Figure 6.10: *Top left:* Scatter plot of stellar temperature and flare energy. The Pearson correlation coefficient is -0.001, with a p-value of 0.496, and the Spearman coefficient is 0.669, with a p-value of 10^{-8}. *Top right:* Scatter plot of stellar radius and flare energy. The Pearson correlation coefficient is 0.651, with a p-value of 6×10^{-9}, and the Spearman coefficient is 0.858, with a p-value of 10^{-17}. *Bottom left:* Scatter plot of stellar rotation period and flare energy. The Pearson correlation coefficient is 0.472, with a p-value of 8×10^{-5}, and the Spearman coefficient is 0.360, with a p-value of 0.007. *Bottom right:* Scatter plot of stellar surface gravity and flare energy. The Pearson correlation coefficient is -0.468, with a p-value of 10^{-4}, and the Spearman coefficient is -0.858, with a p-value of 10^{-17}.

modulated QPPs showed a statistically significant correlation with a small p-value (where a p-value less than 0.05 indicates that the null hypothesis, i.e. that there is no correlation, should be rejected). On the other hand, the flares with exponentially damped QPPs showed no clear correlation, and the calculated p-value indicated that the correlation coefficient was not statistically significant, although we observe that the damping time does increase with the period overall. A larger sample size is necessary to confirm this finding.

It should be noted that the flares studied in this chapter are all observed in white-light, and the origin of white-light emission in solar flares is currently not well understood. The QPP mechanisms discussed in Section 1.3 apply to microwave and X-ray emission via the gyrosynchrotron mechanism and bremsstrahlung, respectively, or thermal emission in the extreme ultraviolet and soft X-ray wavebands. Multiple wavelength observations of solar flares have, however, found that the white-light emission tends to be strongly associated with hard X-ray emission (Matthews et al. 2003; Fletcher et al. 2007), and so it is expected that the same QPP mechanisms apply.

QPPs in the light curve of a flare on KIC9655129 showed evidence of the coexistence of two periods of oscillation, namely 78 ± 5 min and 32 ± 1 min. These are consistent with the presence of two spatial harmonics due to the dispersive nature of guided magnetohydrodynamic waves. Further evidence suggesting that these periodic signals are not components of a non-linear signal was found by comparing the phase differences and decay times. While it is possible that these oscillations could be instrumental or astrophysical artefacts, there is no evidence of periods less than several hours in the rest of the data. Multiple periods are much more likely to be associated with MHD wave mechanisms of QPPs, rather than load/unload mechanisms, so this is one step towards understanding the physics at play, and further suggests that the underlying physics in solar and stellar flares could be similar. It is also possible that one periodic signal is due to a load/unload mechanism, and the other due to an MHD oscillation.

Chapter 7

Summary

This thesis has presented two out of the three currently existing statistical studies of QPPs in solar and stellar flares, making use of a variety of different datasets. These studies can inform future research attempting to link observations with theoretical models. In this chapter a summary of the work presented in this thesis is given (Sections 7.1–7.3), along with some ideas for how this work can be further developed (Section 7.4).

7.1 Significance testing for QPPs in solar and stellar flares

Chapter 4 is based on Pugh et al. (2017a), and begins with an overview of different methods that have previously been used for the detection of QPPs. It also gives a brief discussion of how the inappropriate use of certain methods can lead to false detections. In order to avoid the potential pitfalls of some methods and minimise the possibility of false detections, a method of calculating confidence levels on power spectra with a power law dependence is suggested, based on the work of Vaughan (2005). The power law dependence of the power spectrum is an intrinsic feature of flare light curves, and is the result of red noise and/or trends in the data. The method also accounts for data uncertainties. In Section 4.2 the method of Vaughan (2005) is outlined in detail, and a simplified form of the equation given by Vaughan (2005) is derived. The method is adapted to be more suitable for the detection of QPPs in flares by using a broken power law model to fit the power spectrum, rather than a single power law model. A suggestion of how to go about estimating the uncertainties on the fitted broken power law model is also given.

Section 4.3 shows a variation of the method described in the previous section. Rebinning the power spectrum has previously shown to be beneficial for detecting broad peaks, with power spread across more than one frequency bin in the regular

power spectrum, and for QPPs this could be caused by modulation of the QPP signal amplitude or variation of the QPP period. This section shows for the first time how the method of Vaughan (2005) can be applied to rebinned power spectra, and derives the equation that allows the confidence levels to be calculated.

The two sections that follow show examples of this method being used for the detection of QPP signals. Section 4.4 gives five examples of synthetic data with QPP signals added. It demonstrates that the method can successfully detect QPP signals, but finds that steep background trends in the data can hide real QPP signals. The final example in this section has a synthetic QPP signal with a varying period. While the QPP signal is not found to be significant in the regular power spectrum, the rebinning method described in Section 4.3 does detect the signal at a significant level. Three more examples are given in Section 4.5, where real solar flare data from NoRH is used. The first of these examples shows a QPP signal that is found to be highly significant in the regular power spectrum, while for contrast the second example shows a solar flare that appears to contain pulsations, but the pulsations are not found to be periodic. The third example shows a QPP signal that is not found to be significant in the regular power spectrum, but is significant in the rebinned power spectrum.

7.2 Properties of QPPs in solar flares from a single AR

Chapter 5 is based on Pugh et al. (2017b). The introduction gives a motivation for the study, which is to check for a relationship between several AR properties and the QPP periods for the first time. If a relationship can be found then this would be a huge step forward towards linking the observations with theory, which is necessary if QPPs are to be used for coronal seismology. Descriptions of the chosen AR, the flares it produced, and the data used are also given. Section 5.2 gives more detail on the AR observations, and Section 5.3 describes how the flares were searched for QPP signals. Section 5.3.1 gives a further variant on the method described in the previous chapter, which is specific to time derivative data. Taking the time derivative of SXR flare data is beneficial for the detection of QPPs, since QPPs are most often seen in the impulsive phase of the flare, where the SXR flux steadily rises. Hence there are steep trends in the sections of data most likely to contain QPP signals. Taking the time derivative is a non-subjective way to suppress steady background trends and thus improves the visibility of more variable components of the signal. It will, however, alter the probability distribution of the noise in the power spectrum, but fortunately the alteration can be described analytically and can therefore be accounted for when calculating the confidence levels. The final aspect of the data analysis is given in Section 5.3.2, which details how three different AR properties

(photospheric area, bipole separation distance, and average magnetic field strength) were determined from the HMI line-of-sight magnetogram data.

The results of this study are given in Section 5.4, which begins with an overview of the set of flares found to have significant QPP signals. This includes a histogram showing how the periods are distributed, and a table containing the list of flares found to have significant QPP signals, with details of the time interval over which the detection was made, the instrument that provided the data for the detection, and the QPP period with estimated uncertainties. It is noted that seven QPP signals can be detected identically in the data from two instruments, ruling out the possibility that instrument artefacts could be the source of the QPP signals. A comparison of the data from GOES/XRS and EVE/ESP was made, since the wavebands used overlap. Despite the data being of a similar quality, there are far fewer significant QPP signals detected in the EVE/ESP data than in the GOES/XRS. This is concluded to be due to the much broader waveband used by EVE/ESP, which includes EUV emission that is less well suited for seeing QPP signals. Comparisons are made with the results of the only other statistical study of QPPs in solar flares, made by Inglis et al. (2016), and general agreement is found between the two studies. Correlations between the QPP period and flare properties were checked for. There is no correlation between the QPP period and flare intensity, while there is a moderate correlation with the flare duration that is attributed to an observational bias. A relationship between the QPP period and the duration of the QPP signal was also checked for, and this shows a strong correlation. Again this can, at least in part, be explained by observational bias. The final part of Section 5.4 shows the results of tests for relationships between the QPP period and the three different AR properties. No correlations were found, suggesting that if there is a link between the QPP period and some spatial scale, then the scales of the flaring site may be more important than those of the AR as a whole.

7.3 QPPs in white-light flares observed with *Kepler*

The majority of the work presented in Chapter 6 is based on Pugh et al. (2016). For this study an automated flare detection method was used to search for flaring stars in the short-cadence *Kepler* data, which has a time cadence of 1 min (Section 6.2.1). Once a list of flare stars observed in the short-cadence mode had been put together, their light curves were searched by eye for flares that showed multiple peaks, or some sort of variability in the flare decline phase. We chose to focus only on the decline phase, as the rise phase tends to occur on a timescale of just a few minutes, and hence is not usually sufficiently well resolved in the *Kepler* data for the identification of QPPs. The flares that showed some evidence of pulsations in their light curves

were selected for further analysis, and the wavelet transform and autocorrelation function were used to determine whether the pulsations were quasi-periodic. Those flares that showed evidence of periodic behaviour using both of these techniques were then fitted with a simple model function, with the flare decline phase modelled by a decaying exponential, the QPP signal modelled by a decaying sinusoid, and the background trend modelled by a linear or quadratic function (Section 6.2.2). Out of the 56 flares that show evidence of a QPP signal in the wavelet and autocorrelation plots, only 11 can be fit sufficiently well with the simple model, and these were referred to as exhibiting stable decaying oscillations. For the decaying sinusoid part of the function, which models the QPP signals, it is found that some QPP signals are better fit with an exponential decay whereas others are better fit with a Gaussian modulation, based on a chi-squared goodness-of-fit test. For the 11 flares with stable decaying oscillations, QPP periods and decay times were determined from these fits, with uncertainties estimated by performing Monte Carlo simulations. For the remaining flares showing evidence of QPPs, the periods and uncertainties were estimated by fitting a Gaussian model to the peak in the global wavelet spectrum corresponding to the QPP signal. Section 6.2.3 describes how the total energy released during each of the flares was estimated. Details of several global parameters for the host stars are given in Section 6.2.4, along a description of how the rotation periods were estimated.

Scatter plots of the QPP periods and four different stellar parameters are shown in Section 6.3.1, which show no evidence of correlations. This lack of correlation is consistent with solar flares, where solar QPPs show a wide range of different periods that appear to be independent of the parameters of the host star, and suggests that the stellar QPP periods do not relate to some global oscillation of the host star. There was also no correlation found between the QPP period and flare energy, which again is consistent with solar flare QPP studies (for example, see Fig. 5.5). For the flares with stable decaying oscillations, a scatter plot of the QPP period and decay time could be made. While no correlation is seen for the flares with exponentially decaying QPPs, there does appear to be a correlation for those with Gaussian modulated QPPs, although a larger sample is needed to confirm this. The relationship is approximately linear, and hence could be consistent with kink or slow magnetoacoustic waves being the cause of the QPPs. A more detailed analysis of one of the flares is given in Section 6.3.2, which is based on Pugh et al. (2015), since this flare showed evidence of containing a QPP signal with two periods occurring simultaneously. This flare could be fitted with a model that included two decaying sinusoids with different periods. The period ratio was found to be around 2.4, which is consistent with harmonics of MHD modes, whose period ratios can be non-integer since some modes are dispersive, and the plasma parameters within a coronal loop

can vary slightly with height. At this stage it is not possible to rule out that the two periods could be caused by two different mechanisms, rather than harmonics, however. In the final part of the results, Section 6.3.3 shows that the flare energy correlates with the stellar effective temperature, radius, and surface gravity, while there is no correlation between the flare energy and the stellar rotation period.

7.4 Future work

The work in this thesis has contributed to understanding the general properties of QPPs in both solar and stellar flares, and has provided evidence that they are of the same nature. The precise nature of QPPs remains ill-defined, however, and the mechanisms causing them are still unknown. These open questions mean that QPPs are a highly active research topic, and fortunately there are several research avenues relating to the research in this thesis that can be taken to help further our understanding. These are outlined below.

- **Automated significance testing for power spectra**

  The method described in Chapter 4 can be used to calculate accurate confidence levels for power spectra of flare light curves, and thus minimise the possibility of false detections. While the method was largely automated, the one step that required manual intervention was the choice of start and end times for the section of time series data used to calculate the power spectrum. This step is important as different time intervals will give different power spectra, and tests on synthetic data show that whether or not a peak in the power spectrum, corresponding to a true transient periodic signal, is assessed to be significant depends on the choice of time interval. This step can be time consuming, as different combinations of start and end times must be tried to see which gives the most significant peak in the power spectrum. Although the human eye may still be one of the best tools for judging whether flare time series data show signs of a QPP signal, a computer could cycle through all possible combinations of start and end time, within limits. These limits could include a maximum time interval based on the duration of the flare itself, and a minimum time interval based on the time cadence of the data.

- **Significance testing for wavelet power spectra**

  The method described in Chapter 4 to calculate confidence levels for rebinned power spectra can be used for the detection of weakly non-stationary QPP signals. This approach may not be the most appropriate for non-stationary QPP signals with a more substantial period drift, however, although additional tests on synthetic data should be made to better gauge the performance for

these cases. A wavelet power spectrum may be a better place to start for non-stationary QPP signals, since time evolution information is given, and issues relating to the choice of start and end times of the time series data (mentioned in the previous point) are avoided. The significance of a signal seen in the wavelet power spectrum should be assessed, and Auchère et al. (2016) showed how improvements can be made to the confidence levels provided by the commonly used wavelet code from Torrence & Compo (1998). These confidence levels do not account for data uncertainties, however, hence a method could be developed to calculate confidence levels on wavelet power spectra that account for both a power law dependence and data uncertainties. This would require the discrete wavelet transform to used, because the probability density function used to calculate the confidence levels requires the spectral powers to be independent, which is not the case for the continuous wavelet transform (such as that from Torrence & Compo 1998).

- **Relating QPP and flaring site properties**

  The research presented in Chapter 5 can be extended by using different data sets to estimate the spatial scales of the flaring regions themselves, rather than those of the whole AR. In particular, AIA 1600 Å images can be used to estimate the areas and lengths of flare ribbons (Toriumi et al. 2017), and these areas can be used to calculate average photospheric magnetic field strengths of the flaring sites from the corresponding HMI data. In addition, since the work in Chapter 5 focused on a set of flares from just one AR, the sample of flares could be expanded to include those from many different ARs. One starting point could be to use the sample of solar flares with significant QPP signals identified by Inglis et al. (2016).

- **QPPs in stellar flares observed by *Kepler***

  There is also scope for extending the work presented in Chapter 6. A fairly simple automated routine was used to detect flares in the *Kepler* data, whereas more recent works have employed more sophisticated techniques for the detection of flares (Davenport 2016; Van Doorsselaere et al. 2017). An automated version of the method described in Chapter 4 could be applied to the catalogues of stellar flares from Davenport (2016) and Van Doorsselaere et al. (2017) with the aim of increasing the number of QPPs detected in stellar flares and improving the statistics. More recent data from the K2 mission can also be searched for QPPs in stellar flares, and in addition the upcoming Transiting Exoplanet Survey Satellite (TESS) mission will provide data suitable for the detection of QPPs. Furthermore, systematic searches for QPPs in stellar flares observed by the XMM-Newton, Chandra, and GALEX satellites

have yet to be made. Although the signal-to-noise ratio of the data from these telescopes tends to be worse than the more recent *Kepler* data, the fact that they make X-ray or ultraviolet observations is beneficial for the study of stellar flares, as more direct comparisons with X-ray and ultraviolet observations of solar flares can be made. *Kepler* and TESS make white-light observations, and although white-light flares are observed on the Sun, the emission mechanism is unknown. In addition, at present no white-light solar flares have been sufficiently well resolved for the detection of QPPs.

Appendix A

Additional figures

A.1 Properties of quasi-periodic pulsations in solar flares from a single active region

This section shows light curves and corresponding power spectra for the other solar flares from Chapter 5 found to have significant QPP signals. Additional information about these flares can be found in Table B.1, and a summary of the detected QPP signals can be found in Table 5.1.

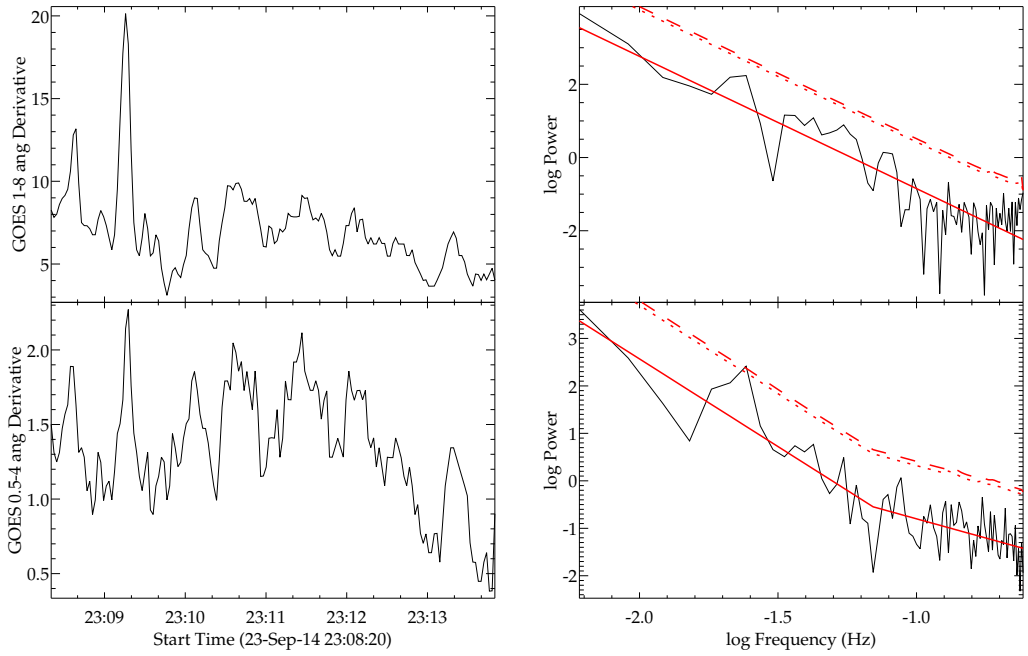

Figure A.1: Similar to Fig. 5.2, with GOES/XRS data for flare 008.

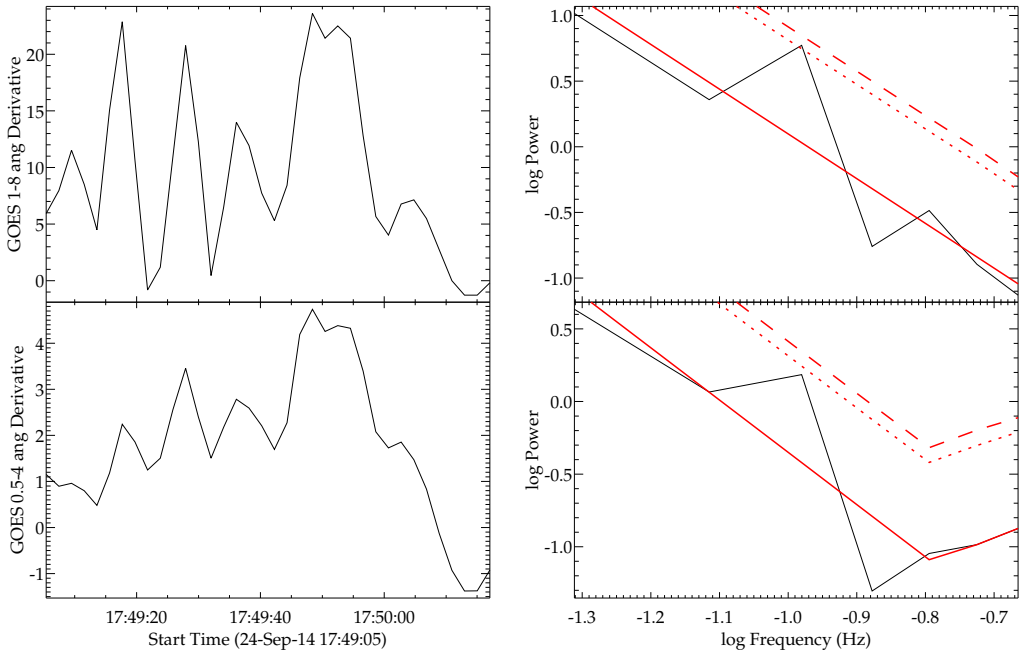

Figure A.2: Similar to Fig. 5.2, with GOES/XRS data for flare 010.

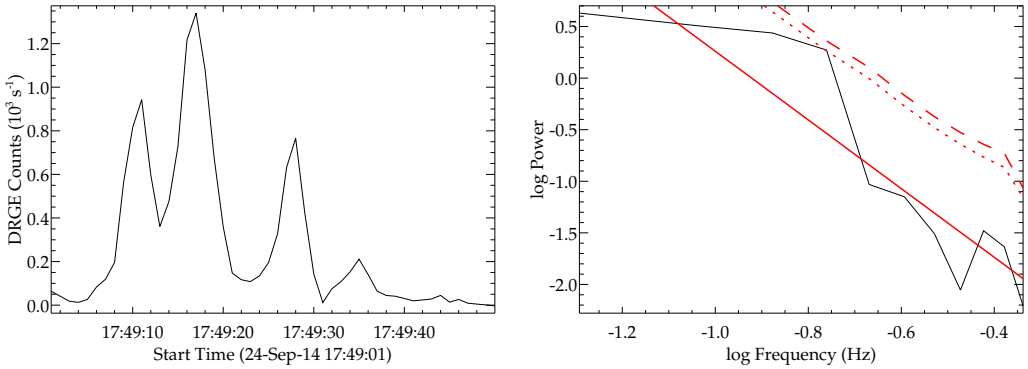

Figure A.3: Similar to Fig. 5.2, with *Vernov*/DRGE data for flare 010.

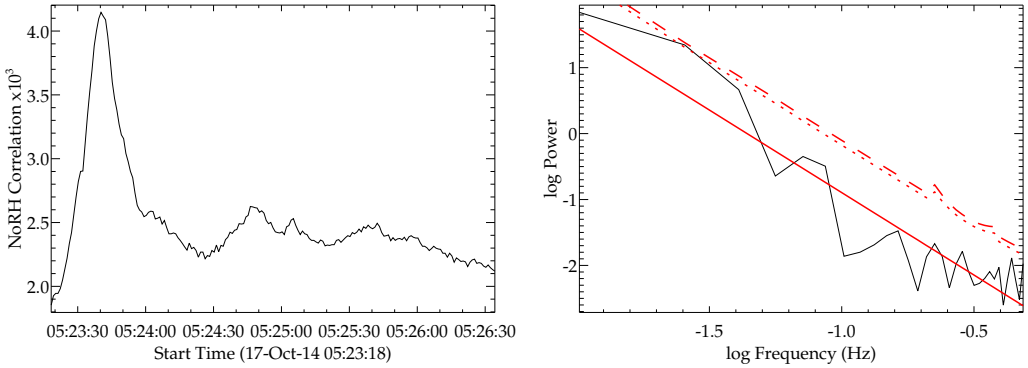

Figure A.4: Similar to Fig. 5.2, with NoRH data for flare 022.

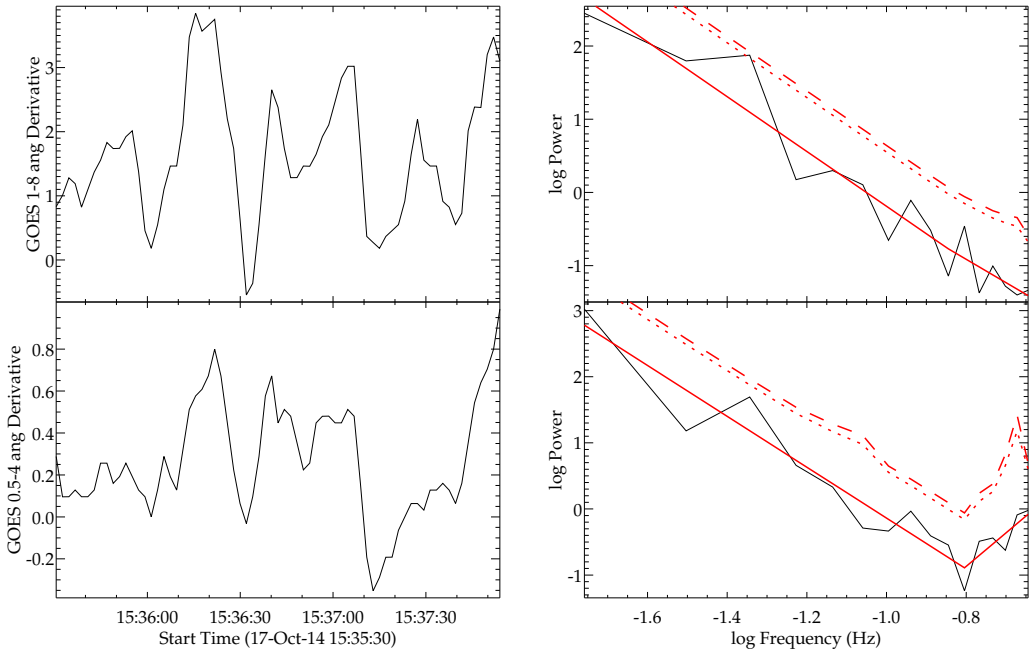

Figure A.5: Similar to Fig. 5.2, with GOES/XRS data for flare 024.

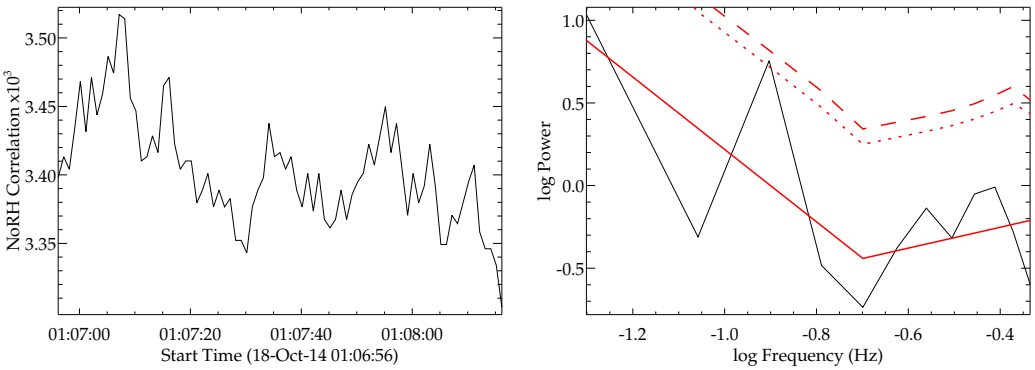

Figure A.6: Similar to Fig. 5.2, with NoRH data for flare 027.

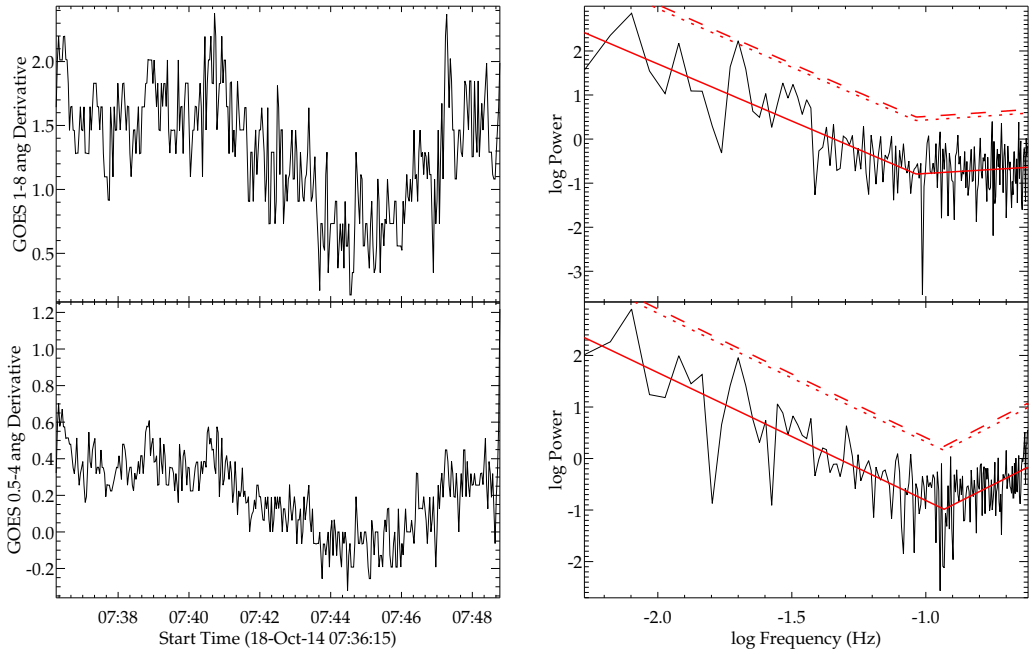

Figure A.7: Similar to Fig. 5.2, with GOES/XRS data for flare 029.

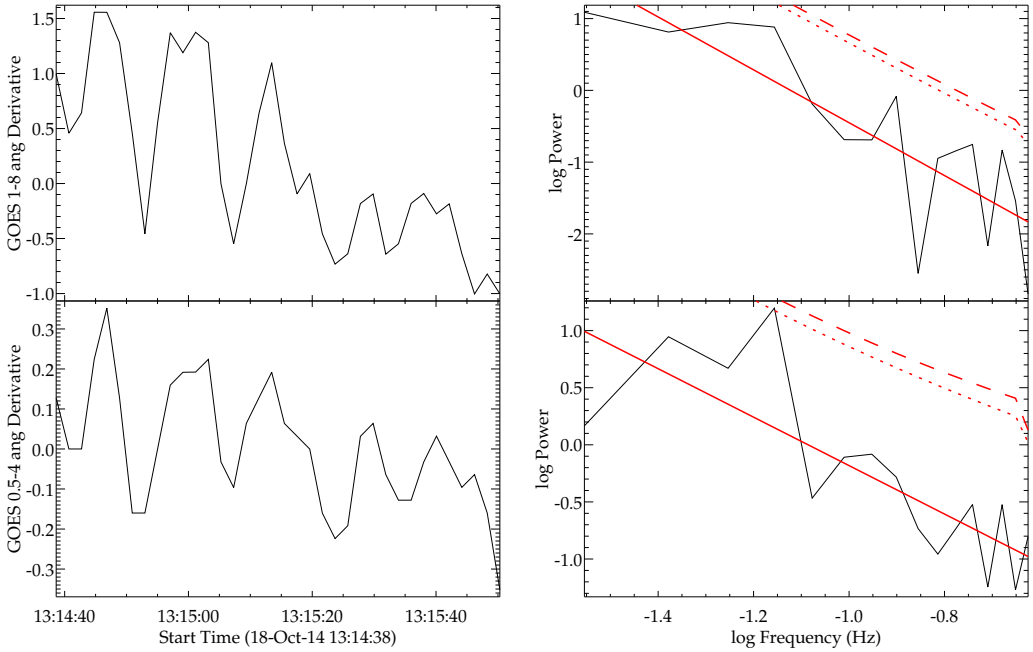

Figure A.8: Similar to Fig. 5.2, with GOES/XRS data for flare 030.

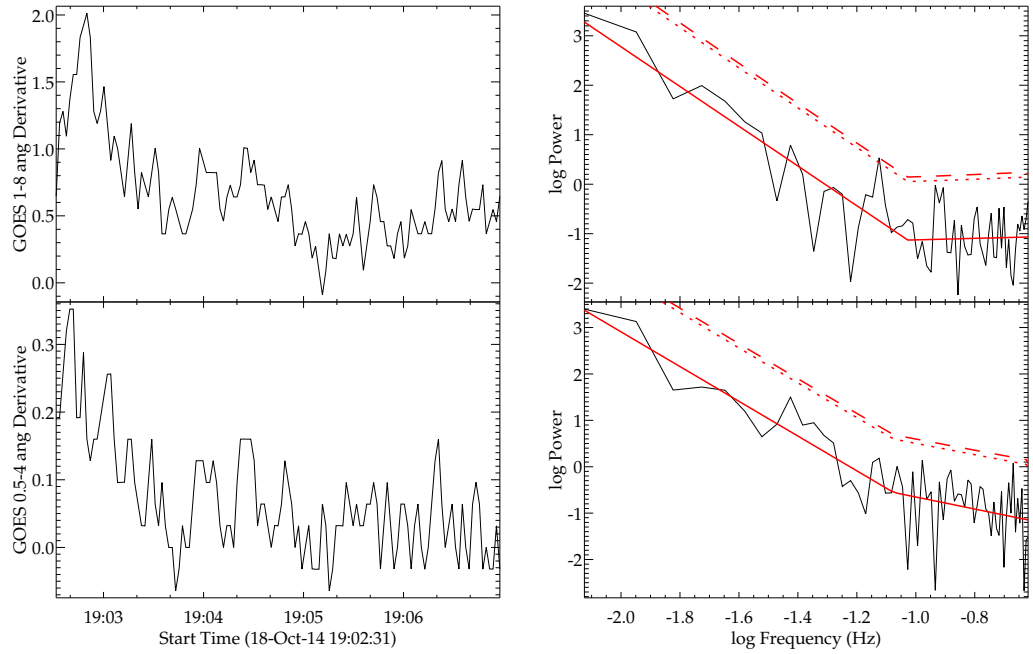

Figure A.9: Similar to Fig. 5.2, with GOES/XRS data for flare 035.

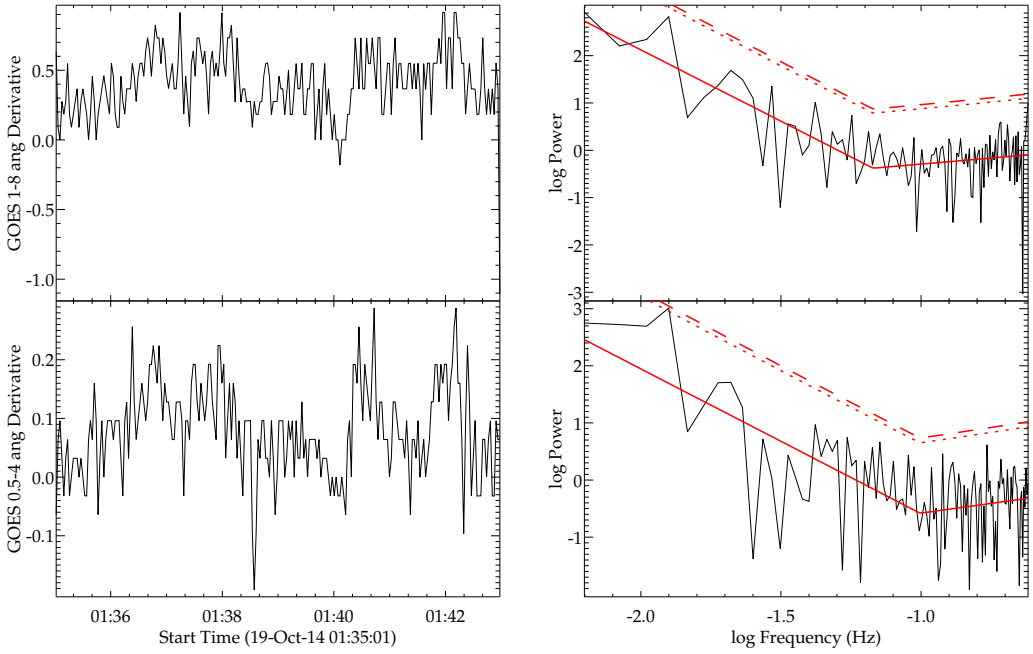

Figure A.10: Similar to Fig. 5.2, with GOES/XRS data for flare 037.

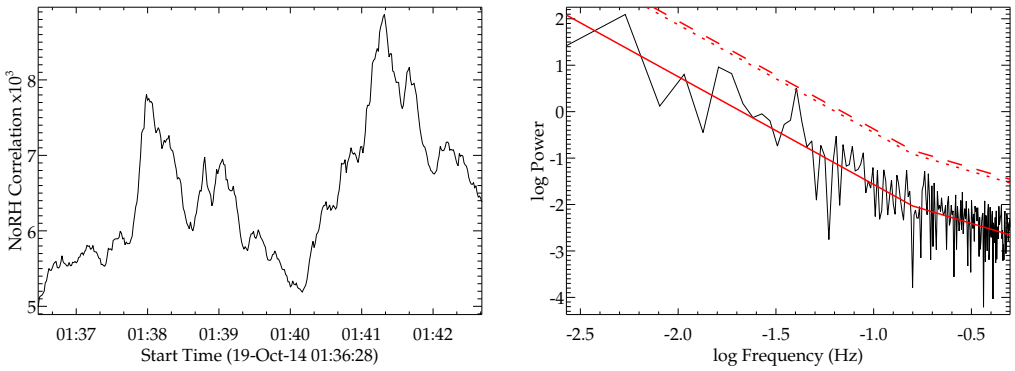

Figure A.11: Similar to Fig. 5.2, with NoRH data for flare 037.

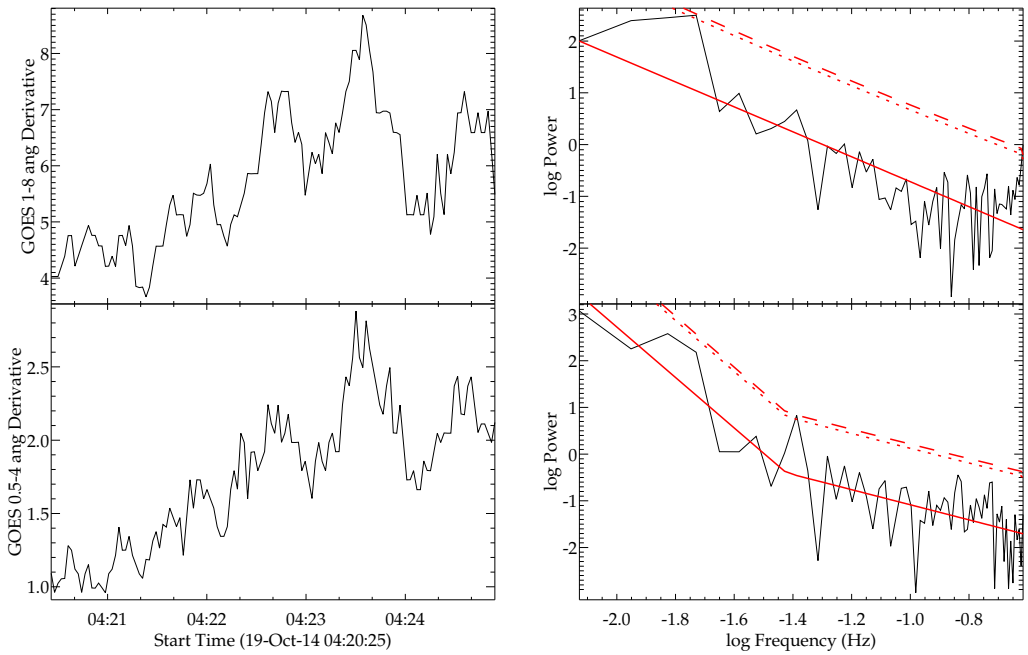

Figure A.12: Similar to Fig. 5.2, with GOES/XRS data for flare 038.

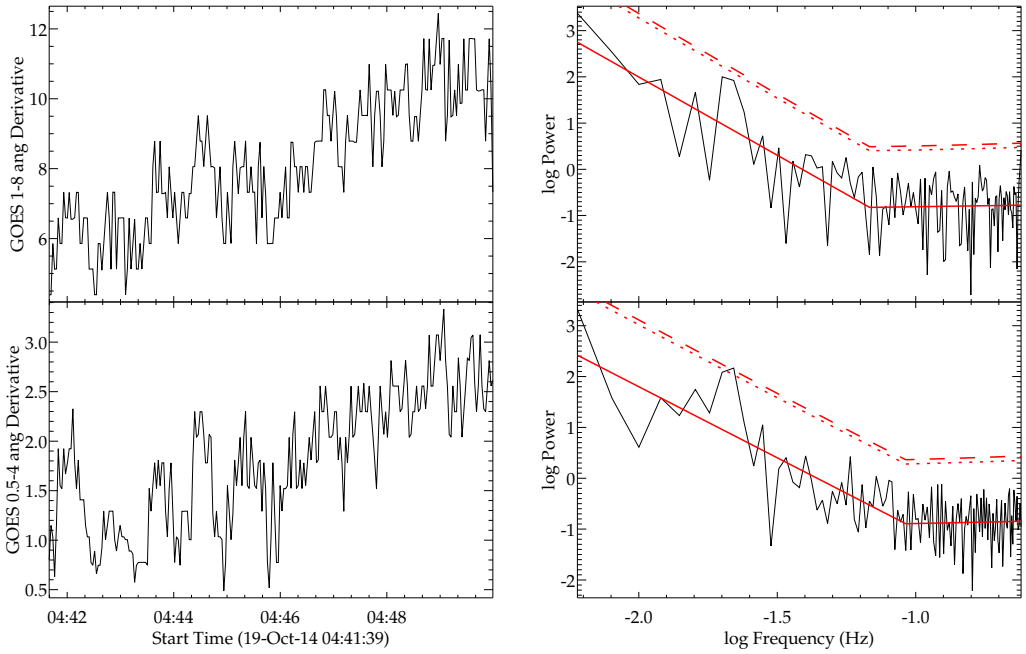

Figure A.13: Similar to Fig. 5.2, with GOES/XRS data for flare 038.

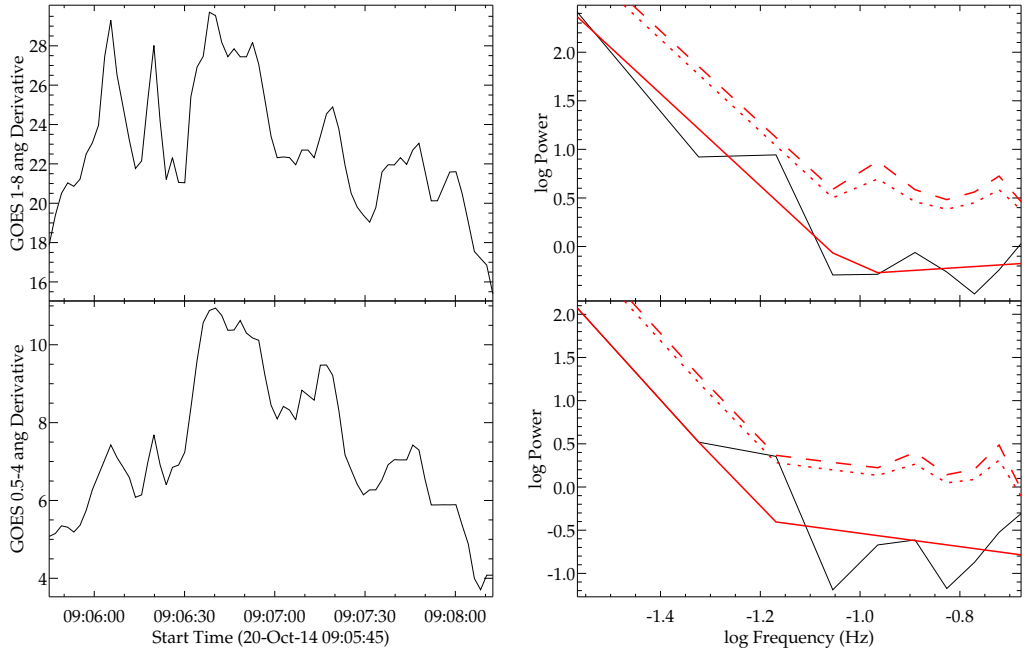

Figure A.14: Similar to Fig. 5.2, with GOES/XRS data for flare 049.

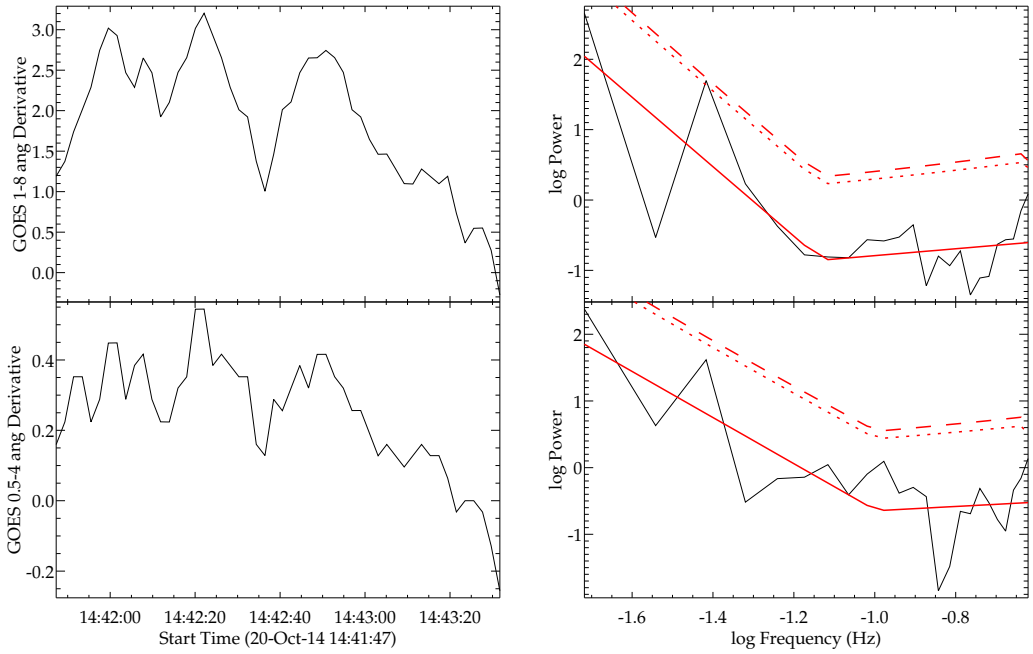

Figure A.15: Similar to Fig. 5.2, with GOES/XRS data for flare 052.

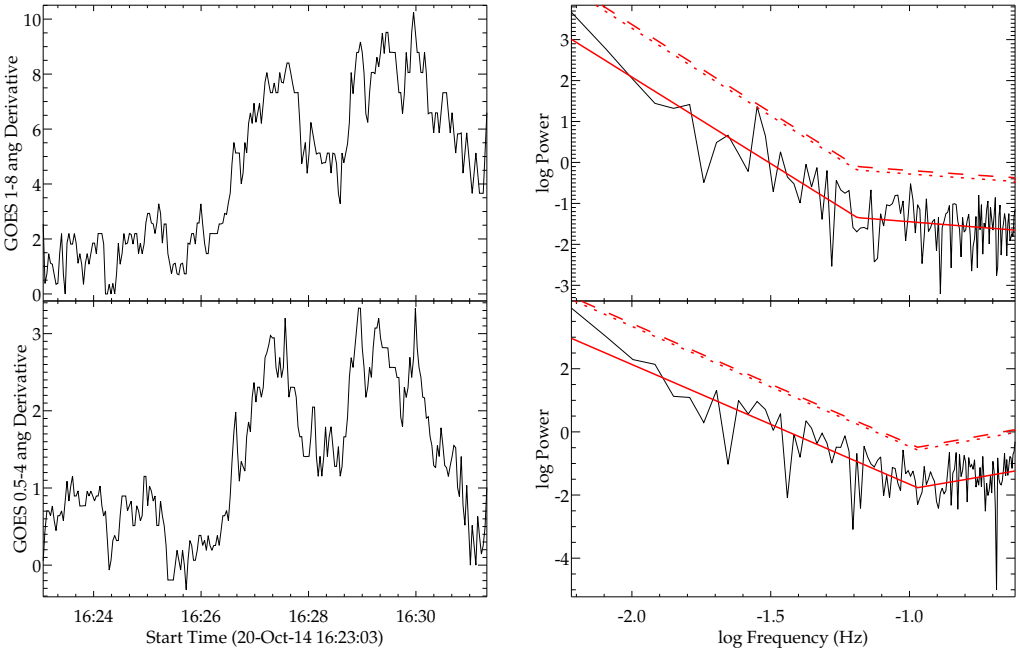

Figure A.16: Similar to Fig. 5.2, with GOES/XRS data for flare 054.

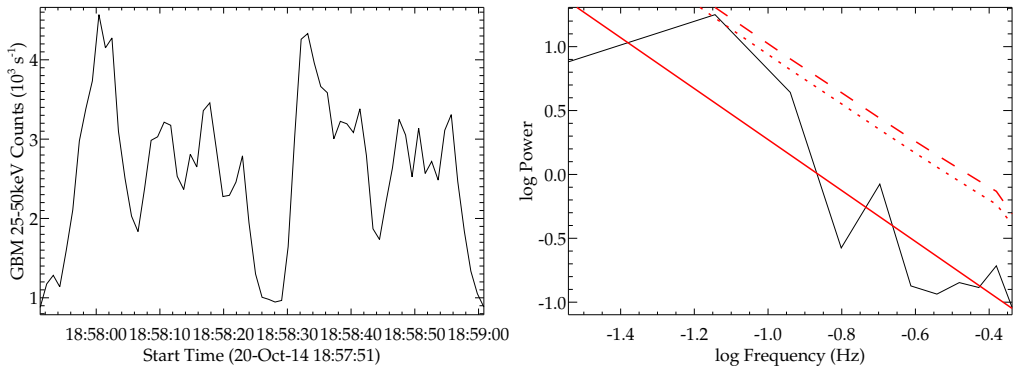

Figure A.17: Similar to Fig. 5.2, with *Fermi*/GBM 25–50 keV data for flare 056.

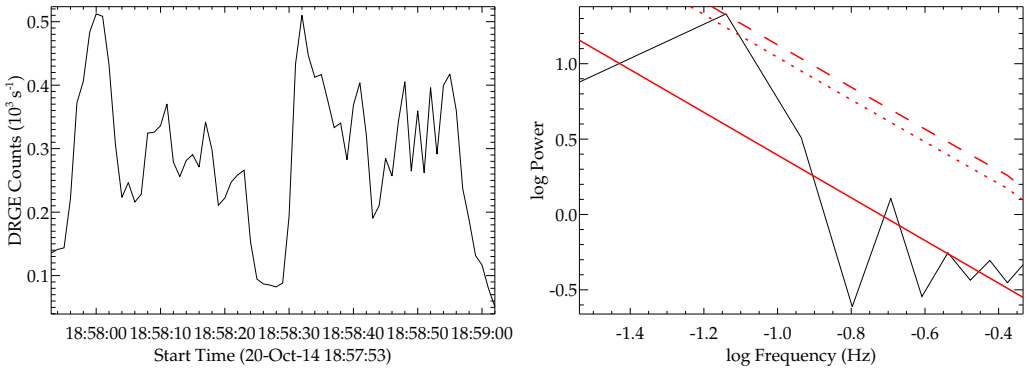

Figure A.18: Similar to Fig. 5.2, with *Vernov*/DRGE data for flare 056.

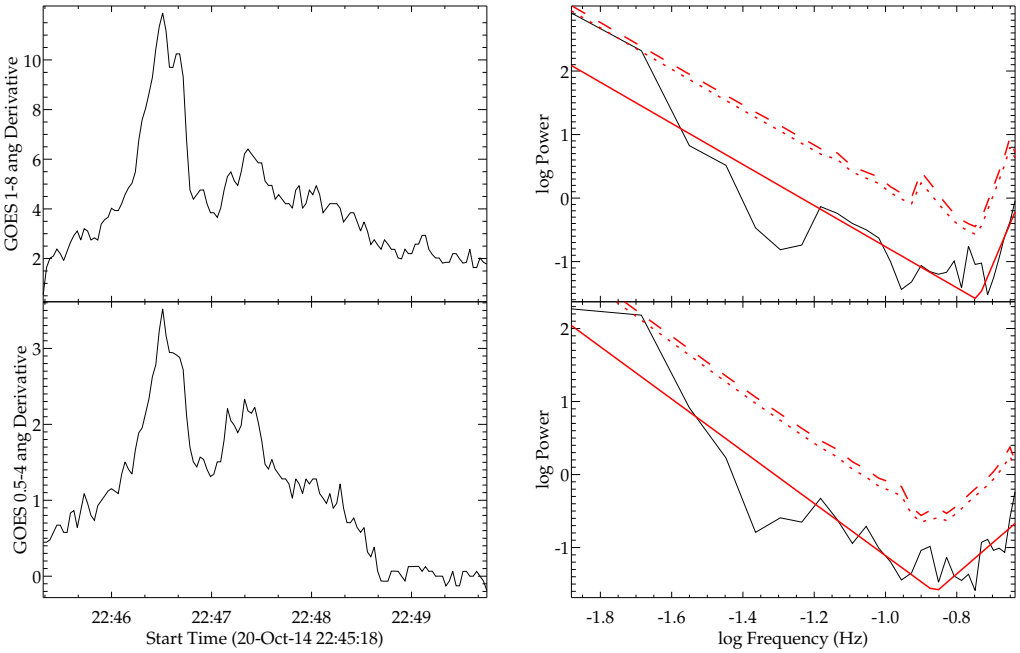

Figure A.19: Similar to Fig. 5.2, with GOES/XRS data for flare 058.

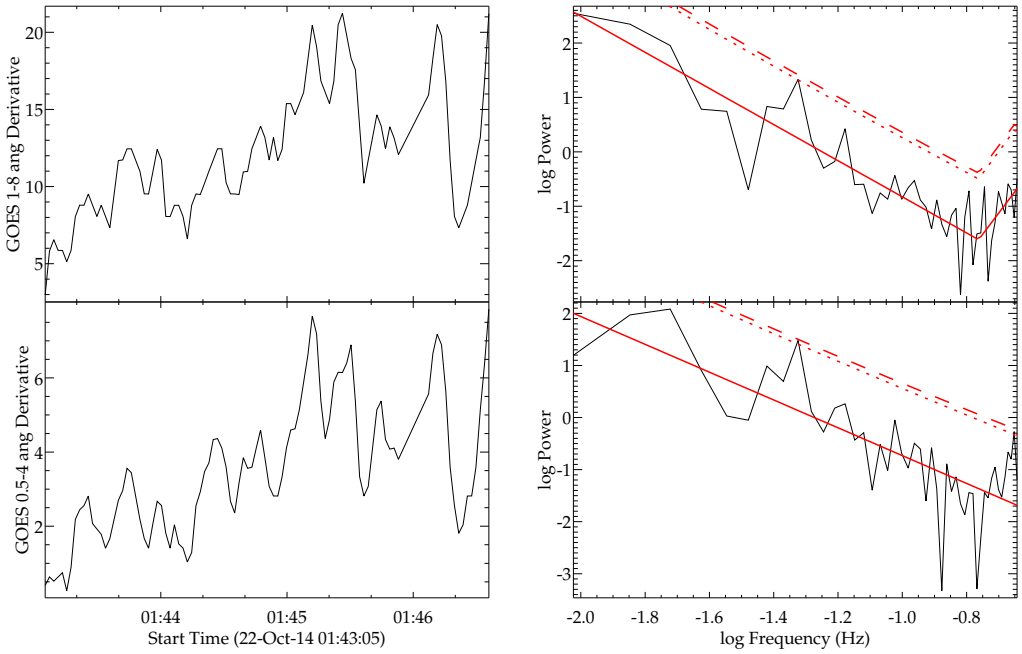

Figure A.20: Similar to Fig. 5.2, with GOES/XRS data for flare 068.

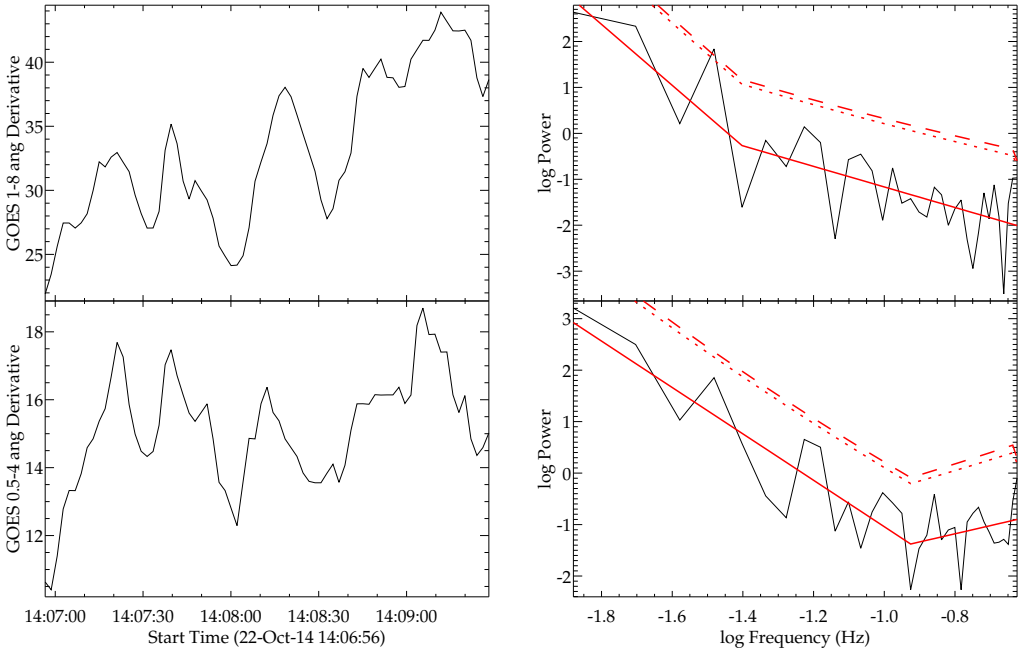

Figure A.21: Similar to Fig. 5.2, with GOES/XRS data for flare 072.

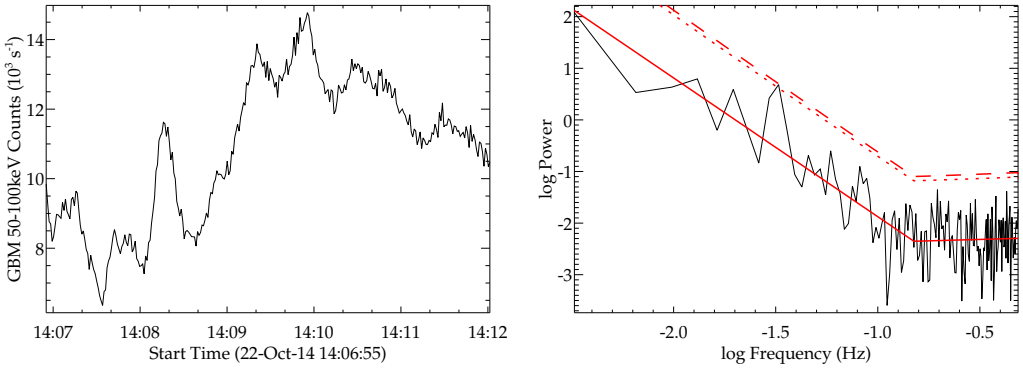

Figure A.22: Similar to Fig. 5.2, with *Fermi*/GBM data for flare 072.

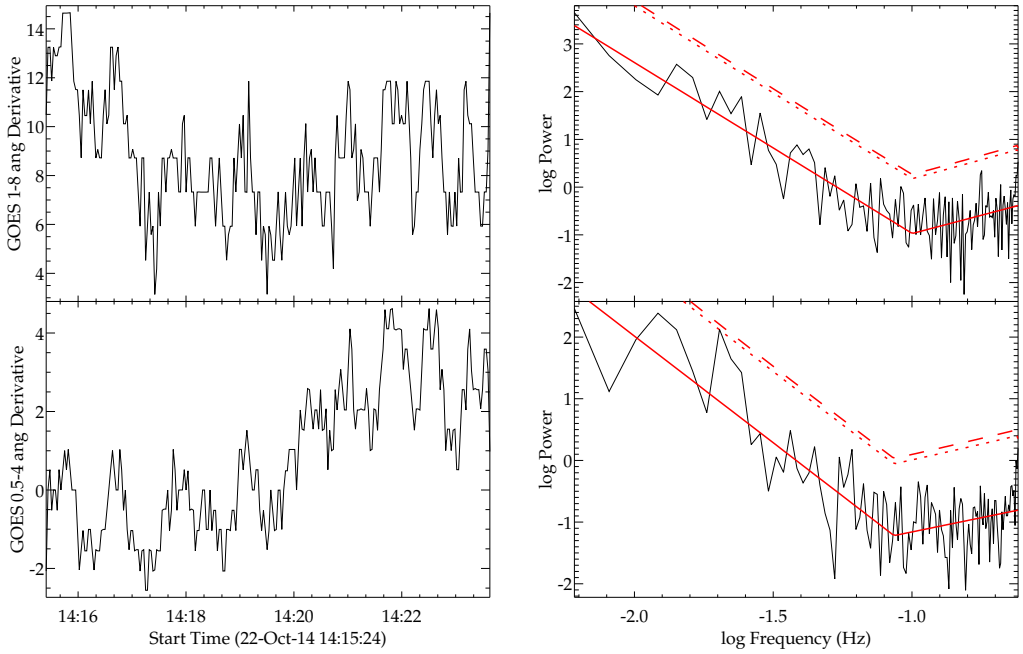

Figure A.23: Similar to Fig. 5.2, with GOES/XRS data for flare 072.

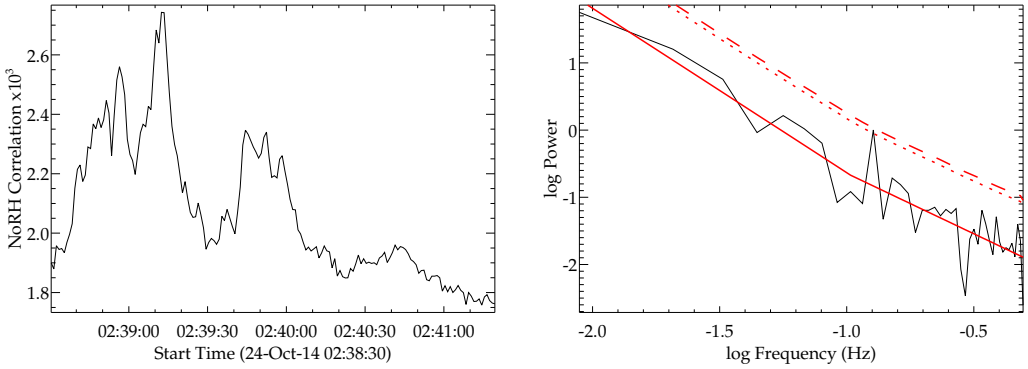

Figure A.24: Similar to Fig. 5.2, with NoRH data for flare 079.

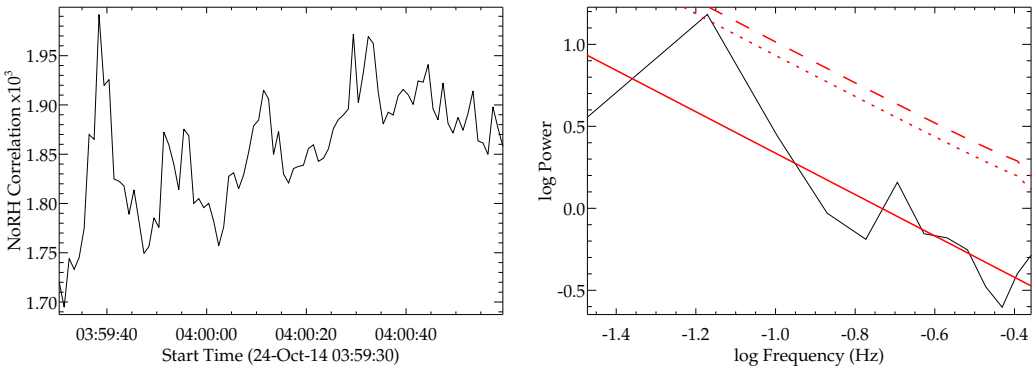

Figure A.25: Similar to Fig. 5.2, with NoRH data for flare 081.

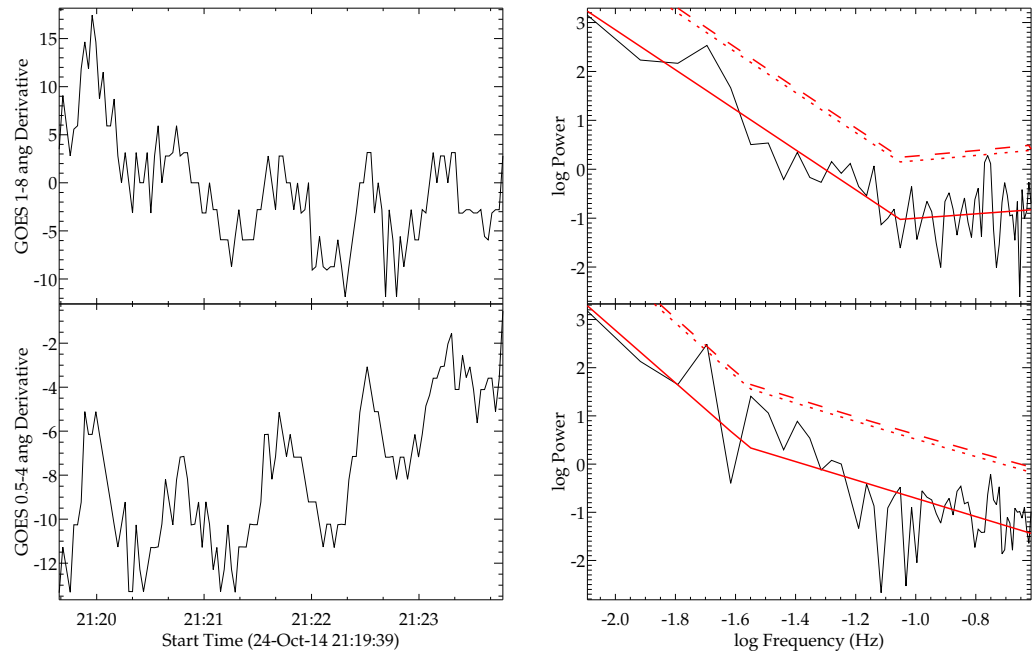

Figure A.26: Similar to Fig. 5.2, with GOES/XRS data for flare 085.

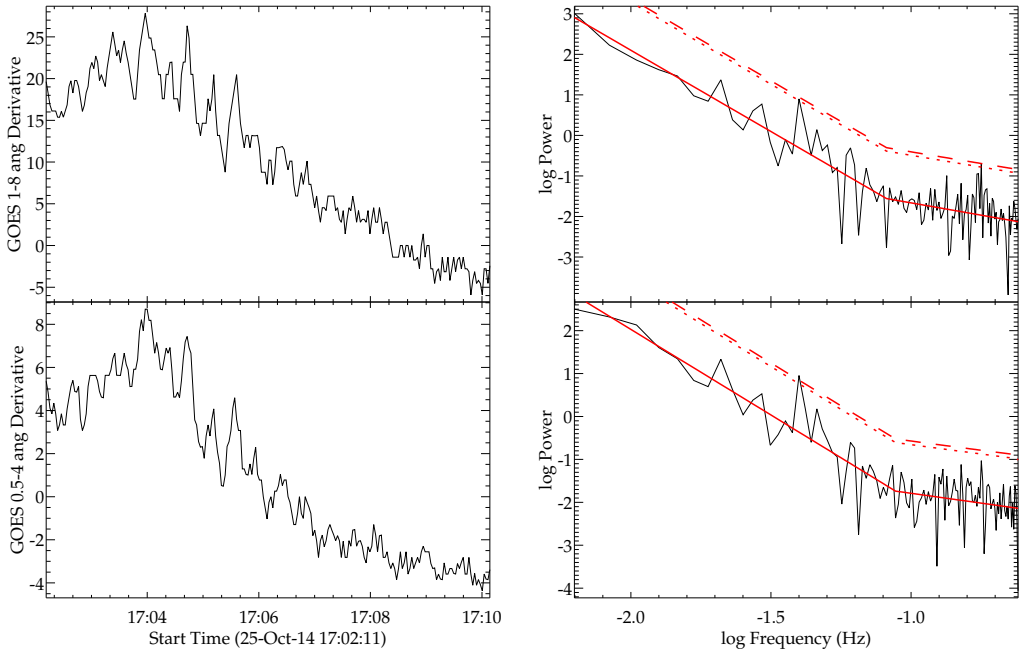

Figure A.27: Similar to Fig. 5.2, with GOES/XRS data for flare 092.

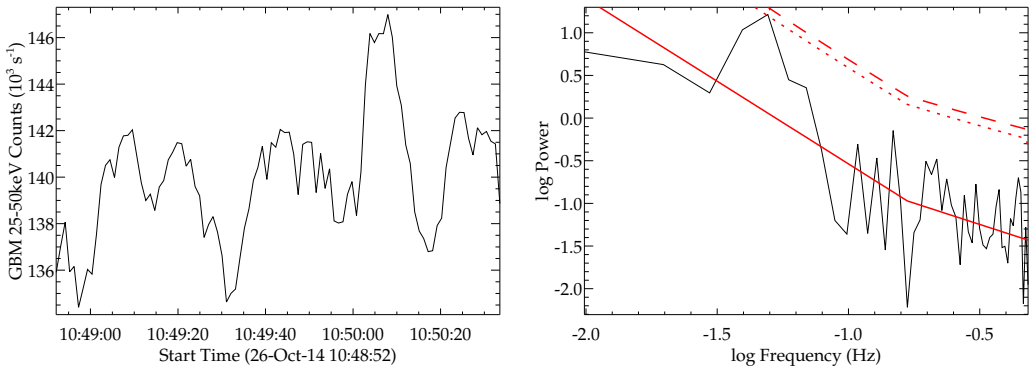

Figure A.28: Similar to Fig. 5.2, with *Fermi*/GBM data for flare 098.

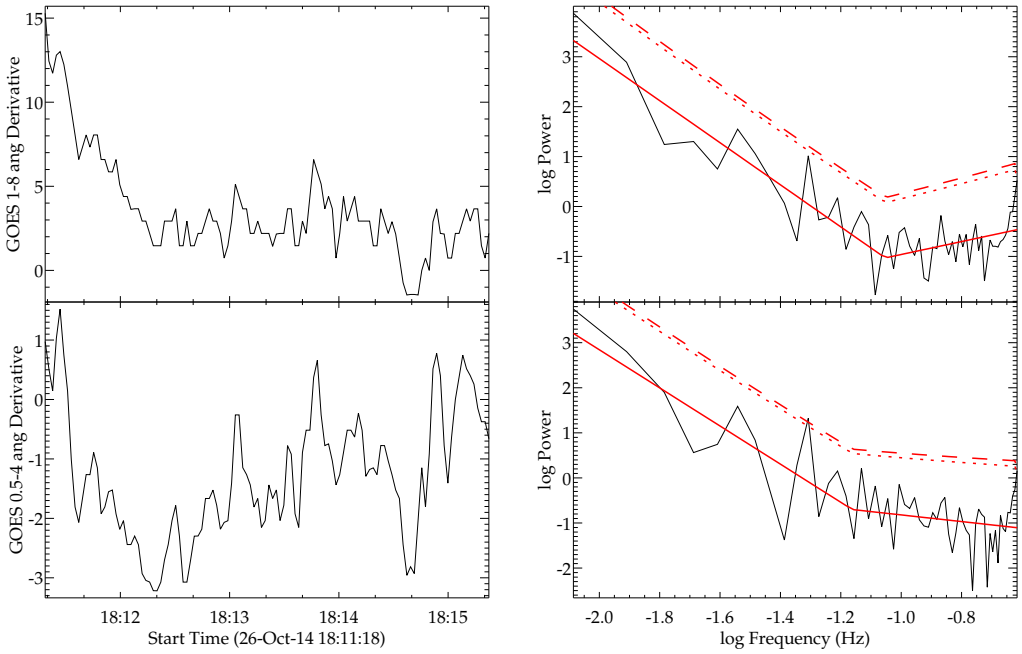

Figure A.29: Similar to Fig. 5.2, with GOES/XRS data for flare 104.

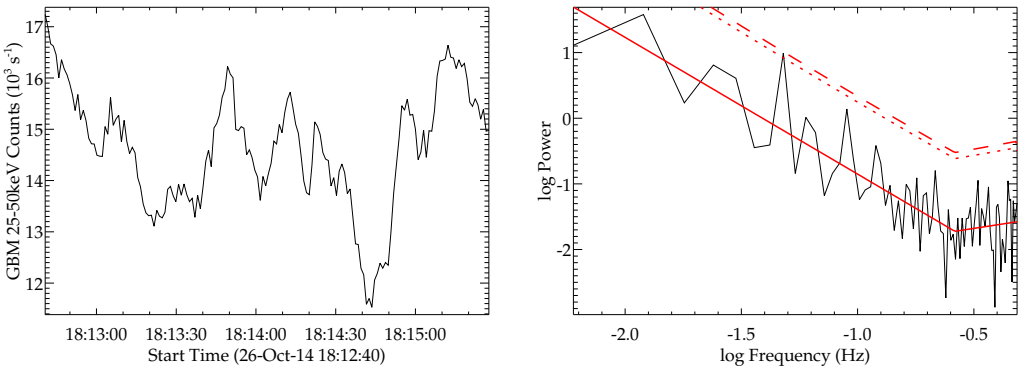

Figure A.30: Similar to Fig. 5.2, with *Fermi*/GBM data for flare 104.

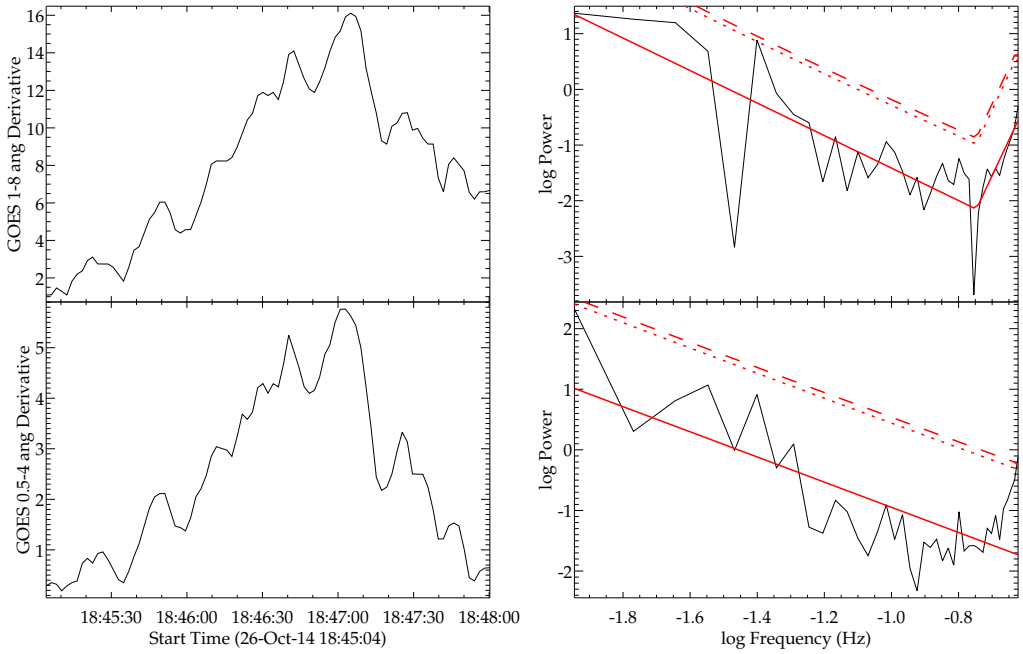

Figure A.31: Similar to Fig. 5.2, with GOES/XRS data for flare 105.

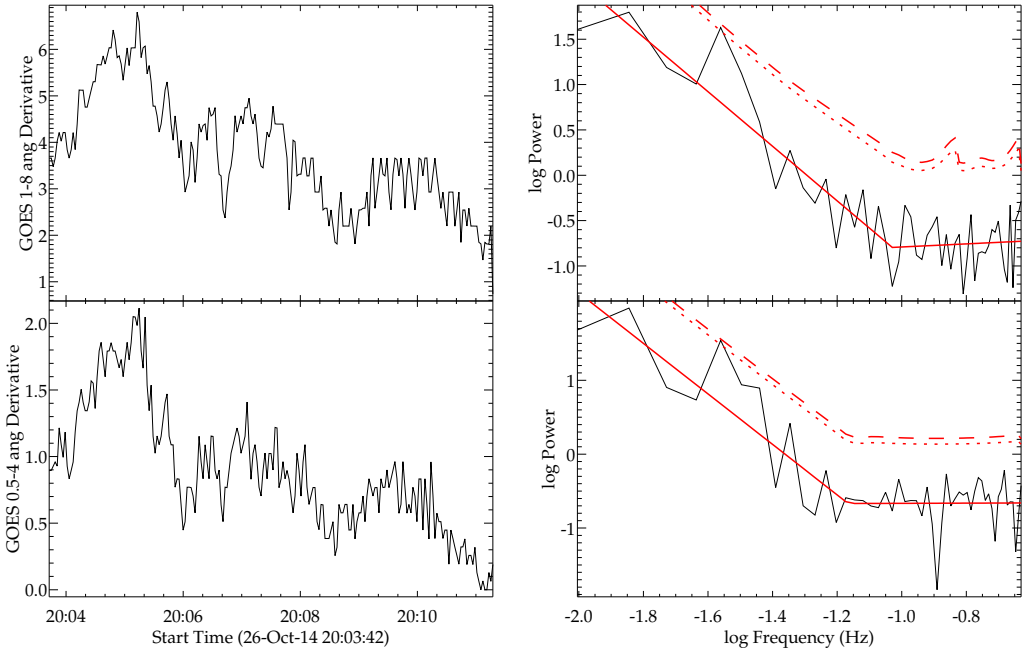

Figure A.32: Similar to Fig. 5.2, with GOES/XRS data for flare 106.

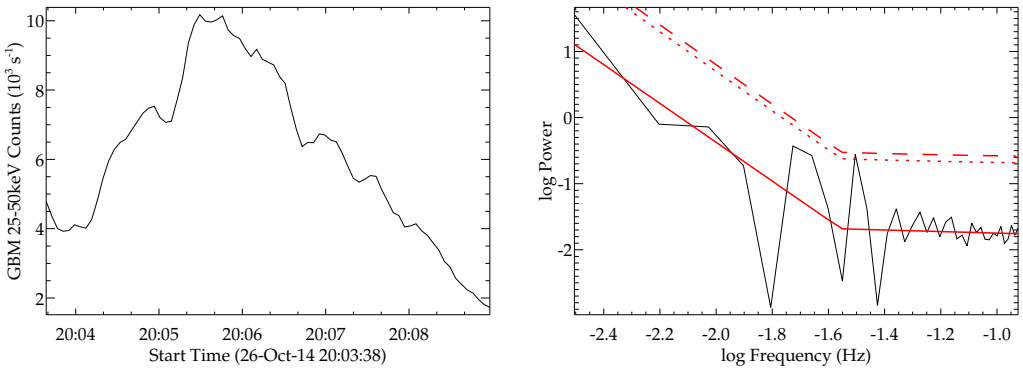

Figure A.33: Similar to Fig. 5.2, with *Fermi*/GBM data for flare 106.

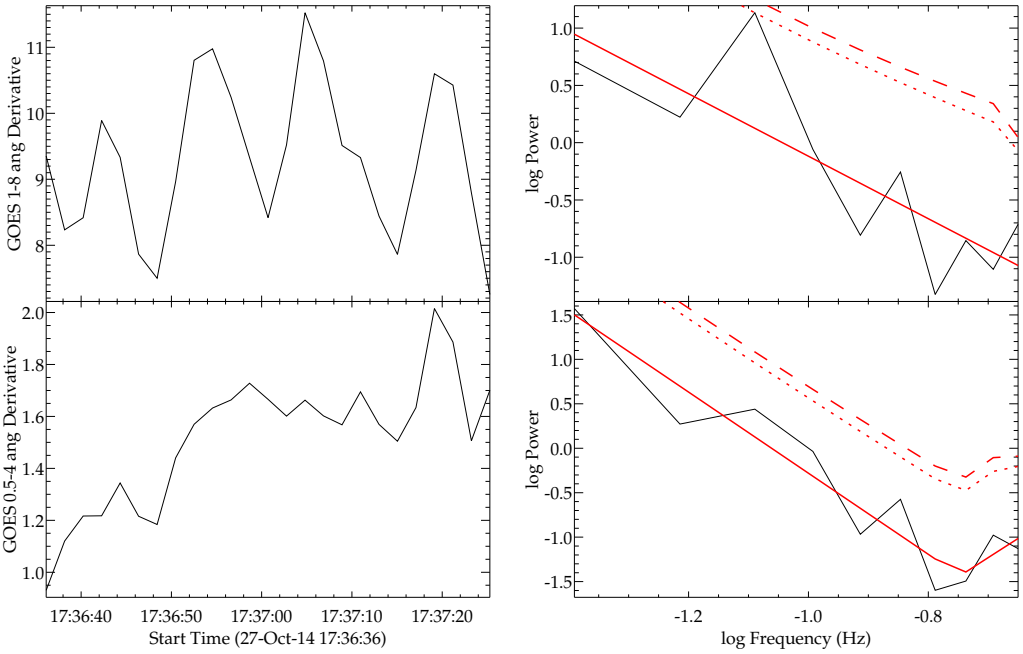

Figure A.34: Similar to Fig. 5.2, with GOES/XRS data for flare 117.

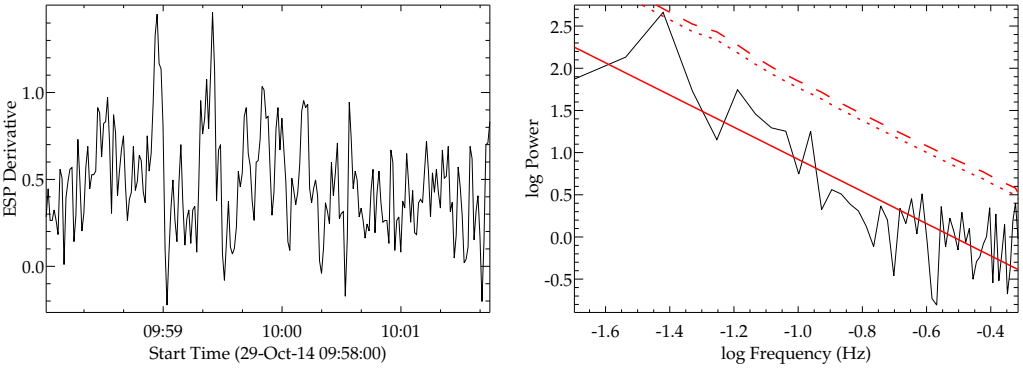

Figure A.35: Similar to Fig. 5.2, with EVE/ESP data for flare 129.

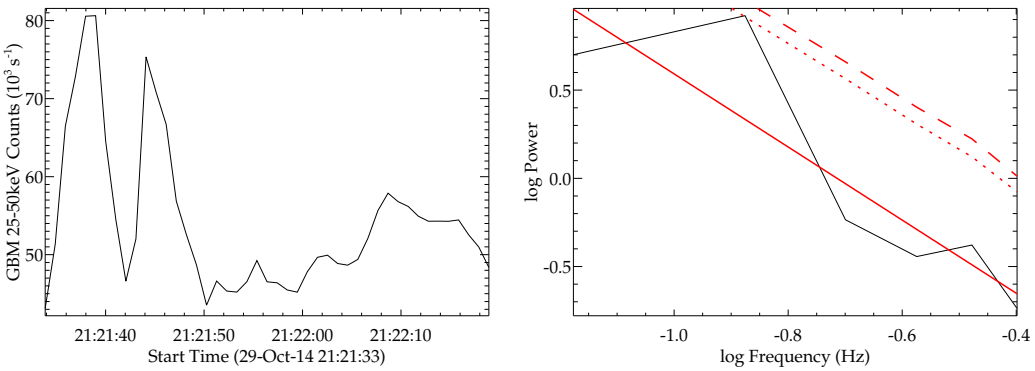

Figure A.36: Similar to Fig. 5.2, with *Fermi*/GBM data for flare 135.

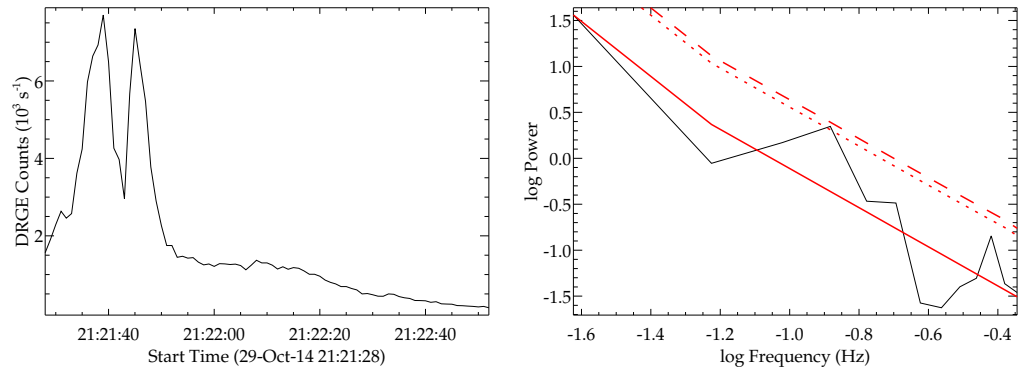

Figure A.37: Similar to Fig. 5.2, with *Vernov*/DRGE data for flare 135.

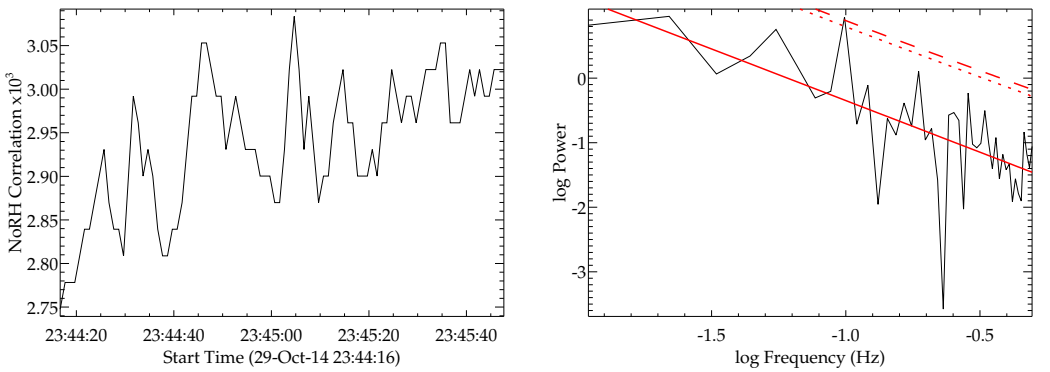

Figure A.38: Similar to Fig. 5.2, with NoRH data for flare 138.

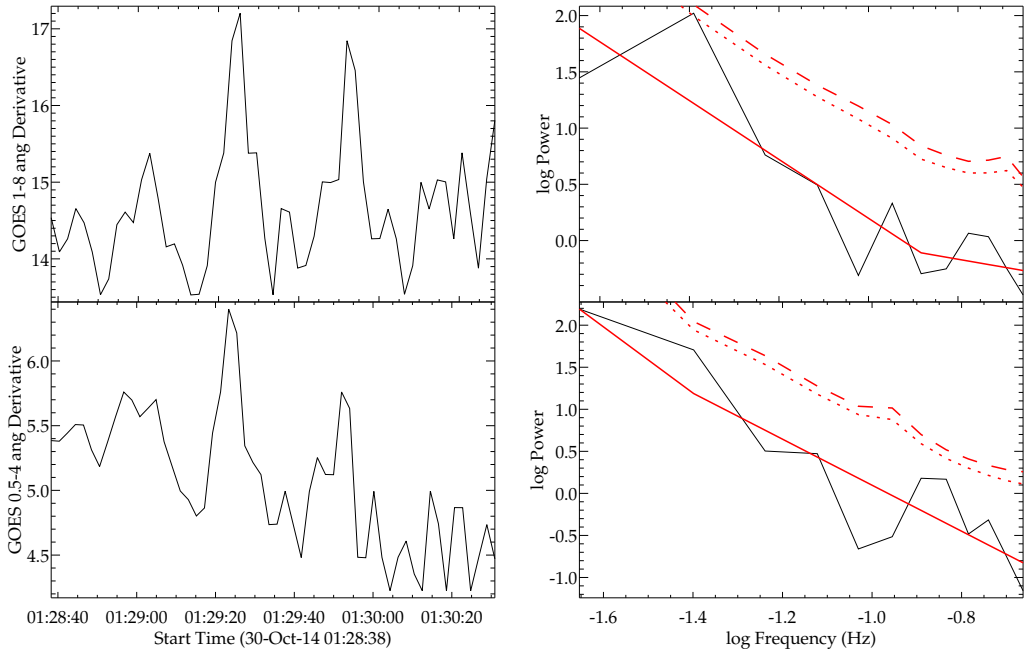

Figure A.39: Similar to Fig. 5.2, with GOES/XRS data for flare 140.

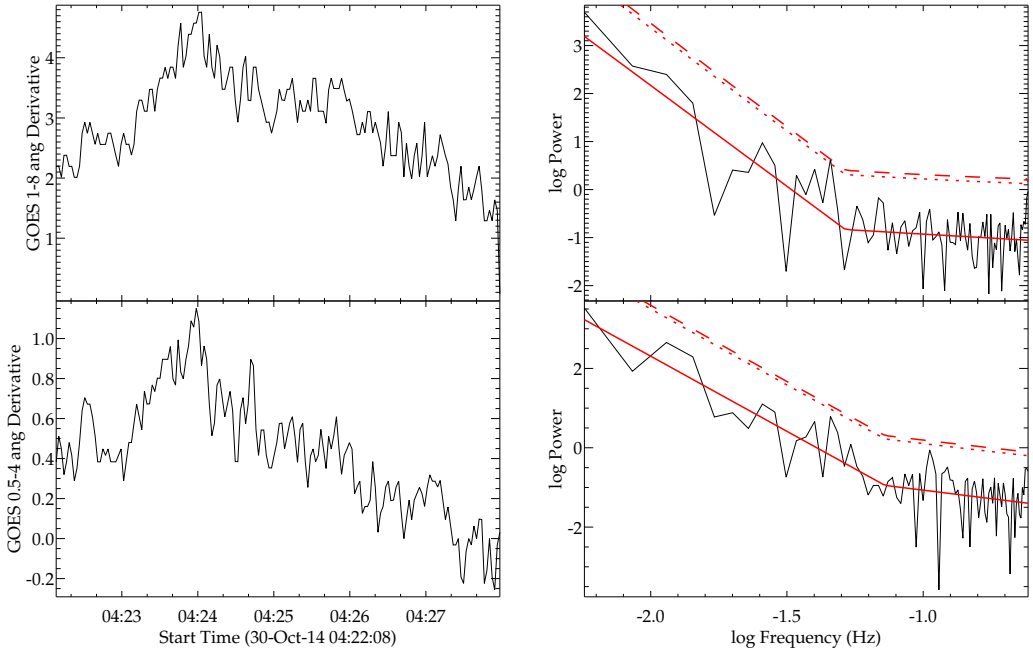

Figure A.40: Similar to Fig. 5.2, with GOES/XRS data for flare 141.

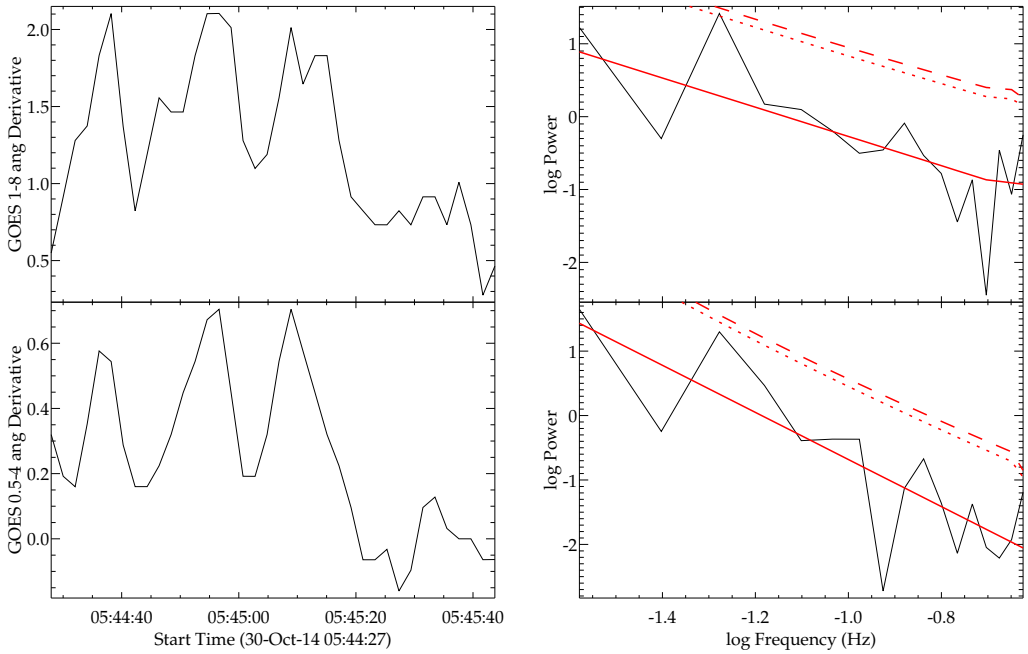

Figure A.41: Similar to Fig. 5.2, with GOES/XRS data for flare 142.

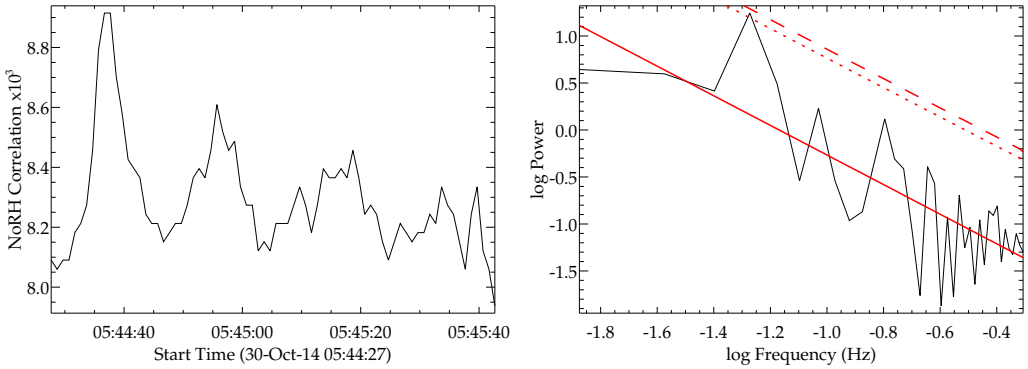

Figure A.42: Similar to Fig. 5.2, with NoRH data for flare 142.

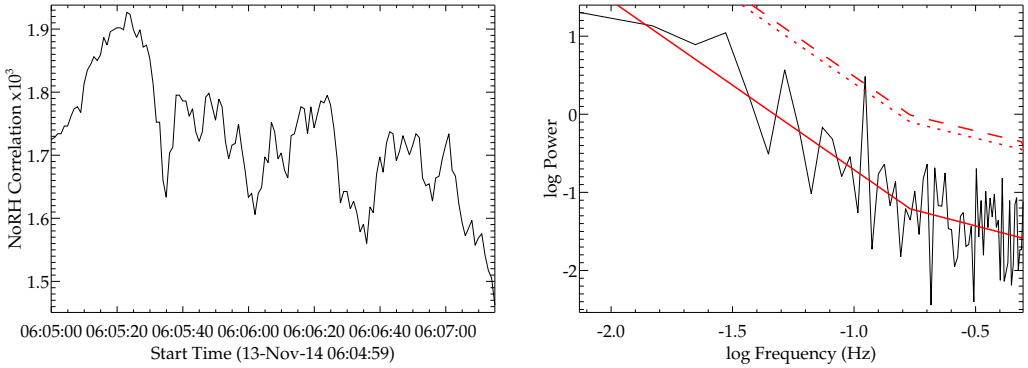

Figure A.43: Similar to Fig. 5.2, with NoRH data for flare 147.

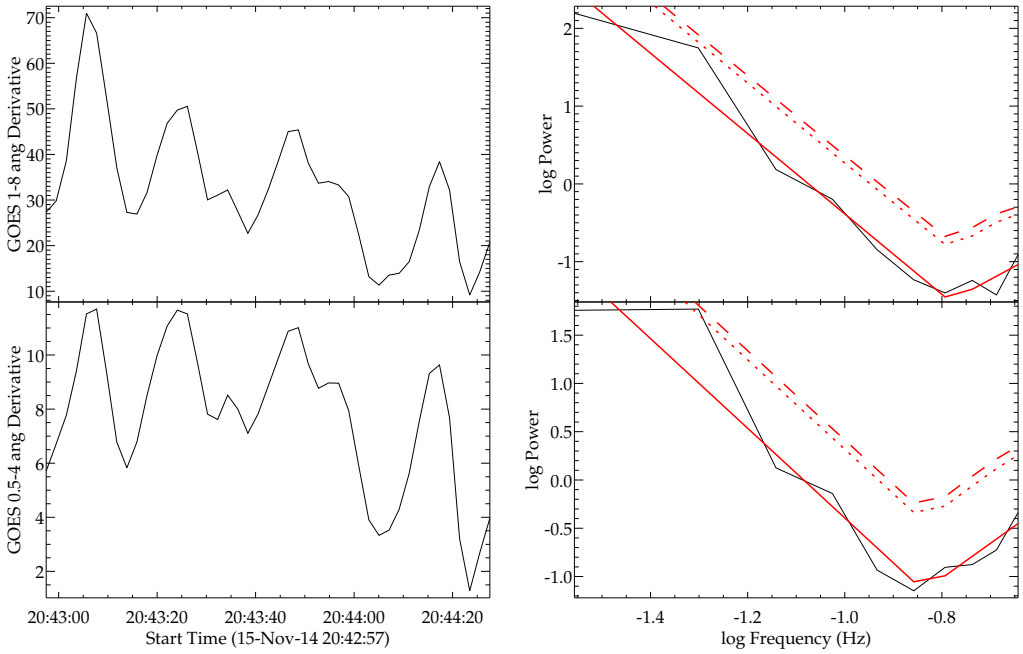

Figure A.44: Similar to Fig. 5.2, with GOES/XRS data for flare 153.

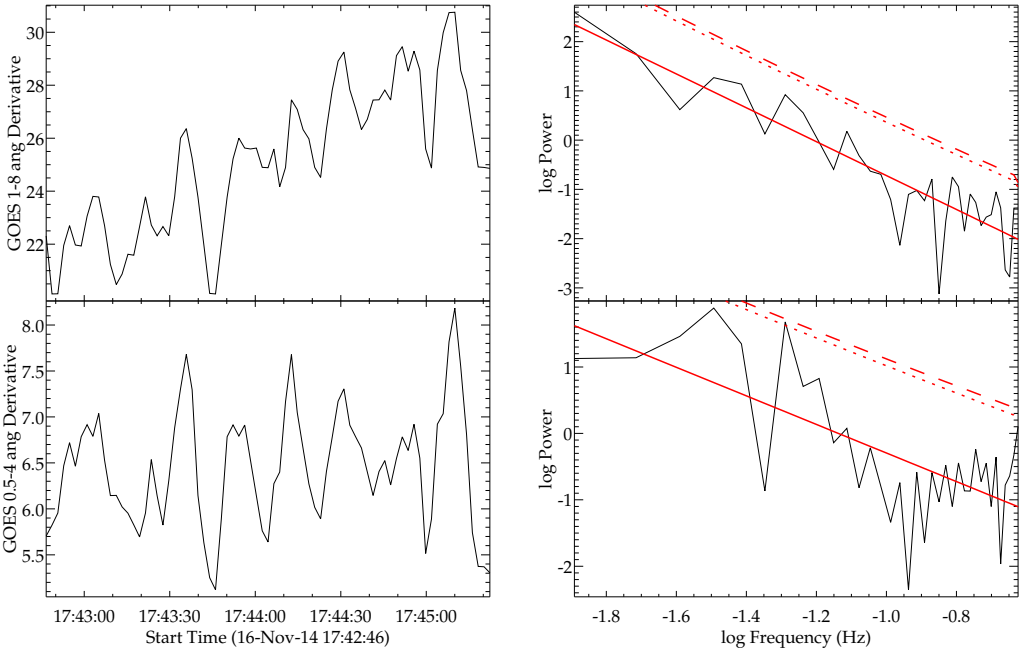

Figure A.45: Similar to Fig. 5.2, with GOES/XRS data for flare 161.

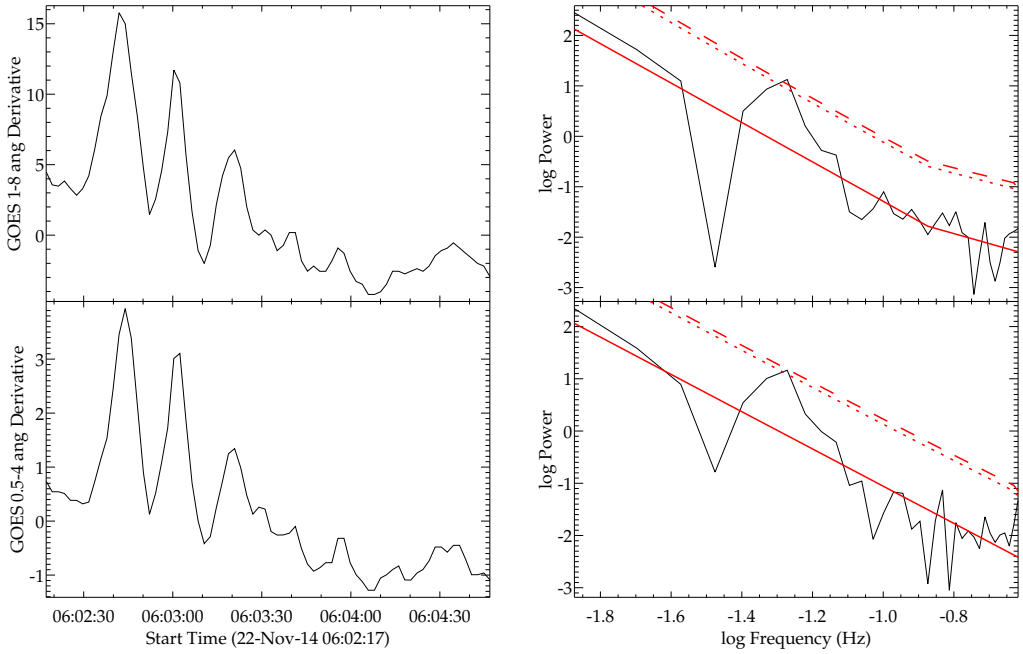

Figure A.46: Similar to Fig. 5.2, with GOES/XRS data for flare 177.

A.2 Quasi-periodic pulsations in white-light flares observed with *Kepler*

In this section plots are included for the other stellar flares with stable decaying oscillations from Chapter 6, and as summarised in Table 6.3. The plots are equivalent to those described in Section 6.2.2 for the star KIC 12156549.

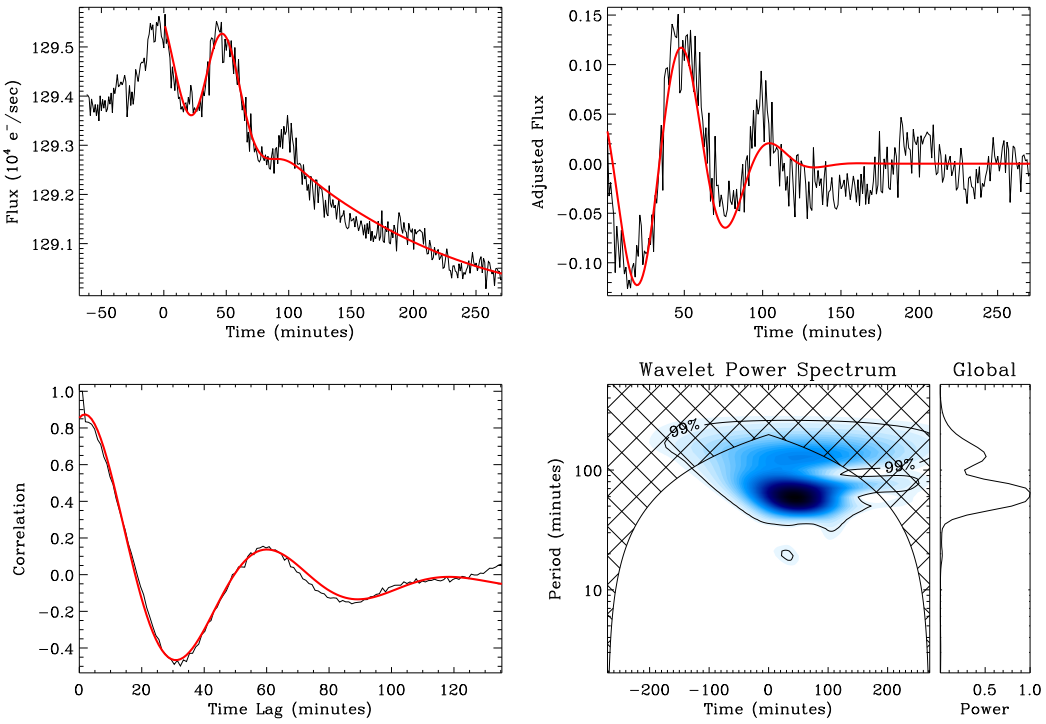

Figure A.47: KIC 2852961, start time (BJD): 55238.22.

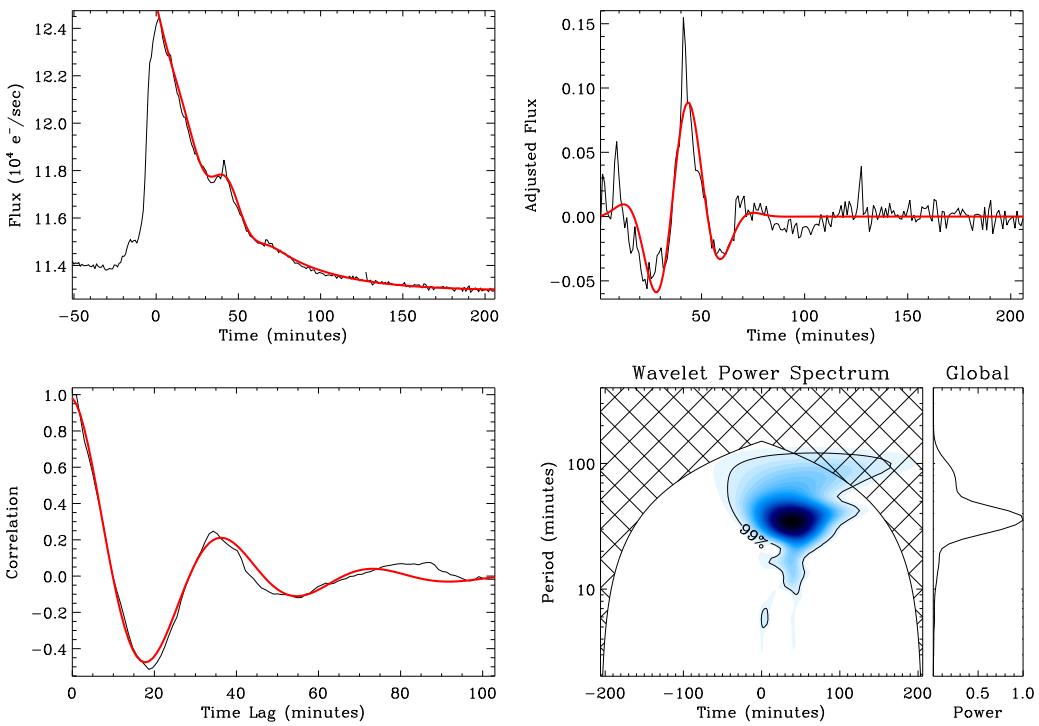

Figure A.48: KIC 3540728, start time (BJD): 55807.25.

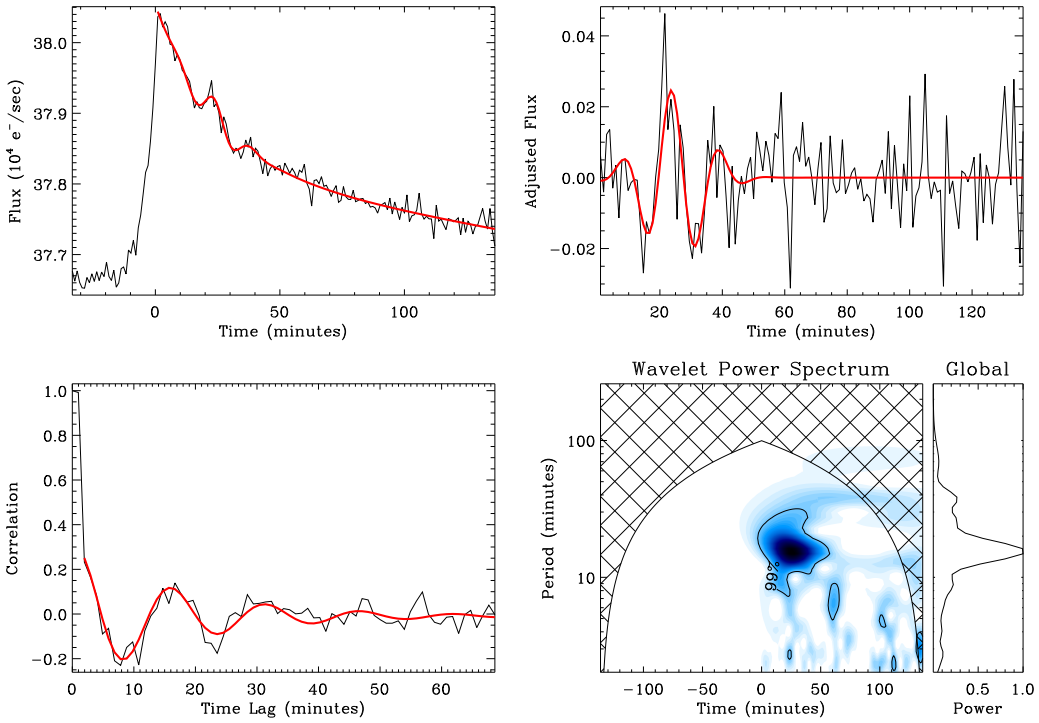

Figure A.49: KIC 5475645, start time (BJD): 55095.92.

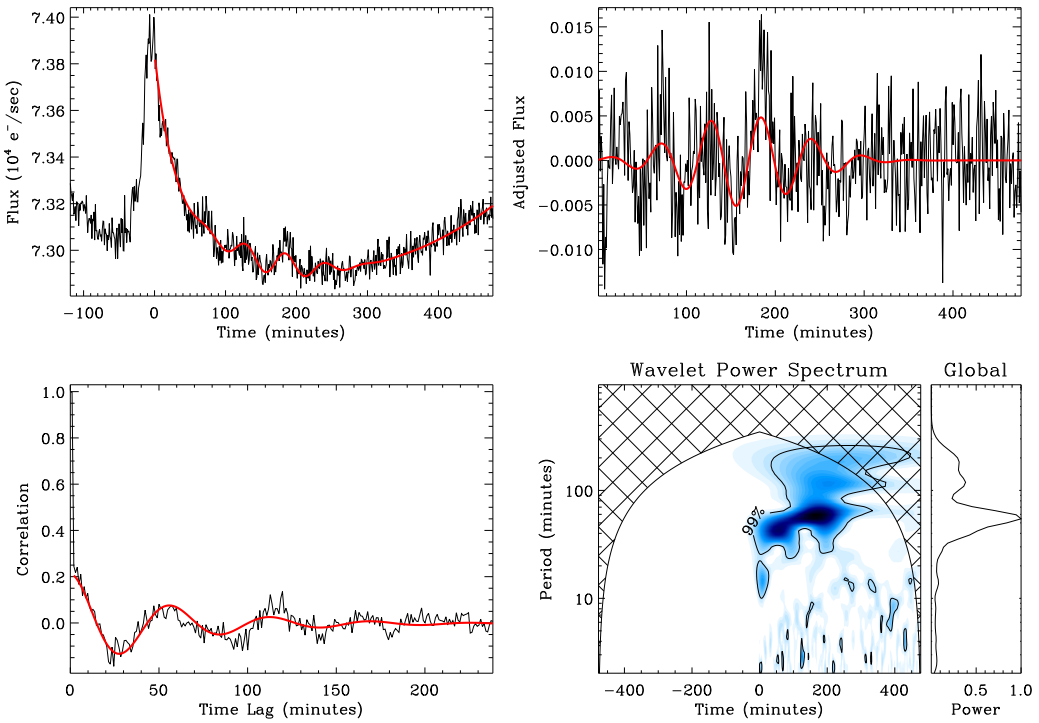

Figure A.50: KIC 6184894, start time (BJD): 56243.87. The substantial underlying trend in the light curve is due to starspot modulation.

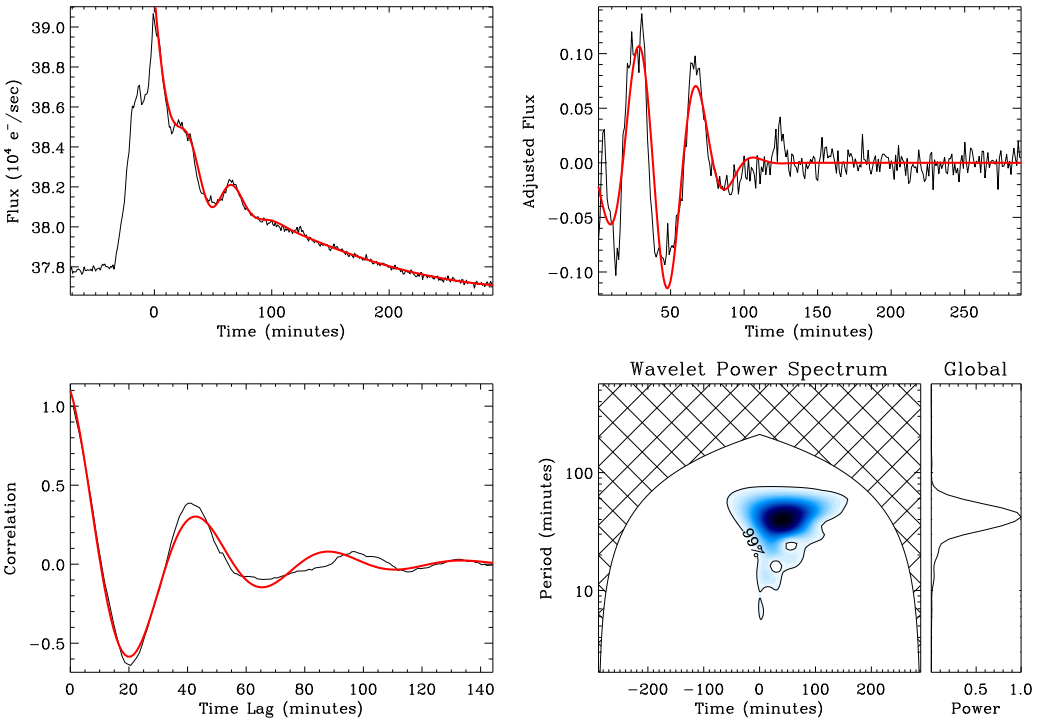

Figure A.51: KIC 6437385, start time (BJD): 55393.76.

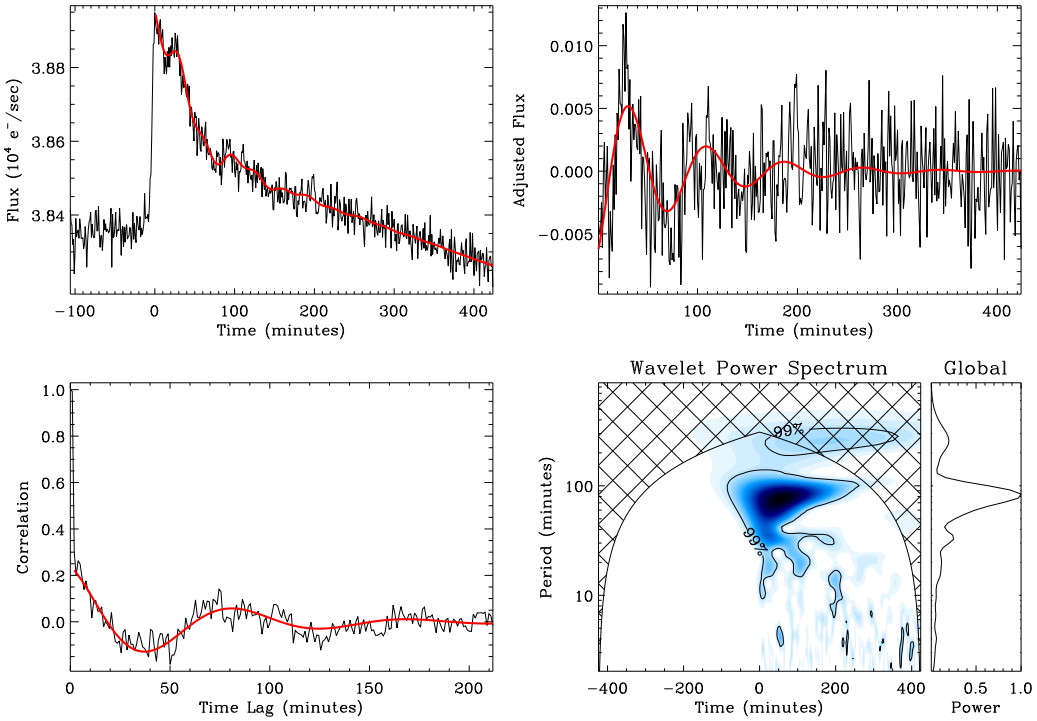

Figure A.52: KIC 9655129, start time (BJD): 56149.04.

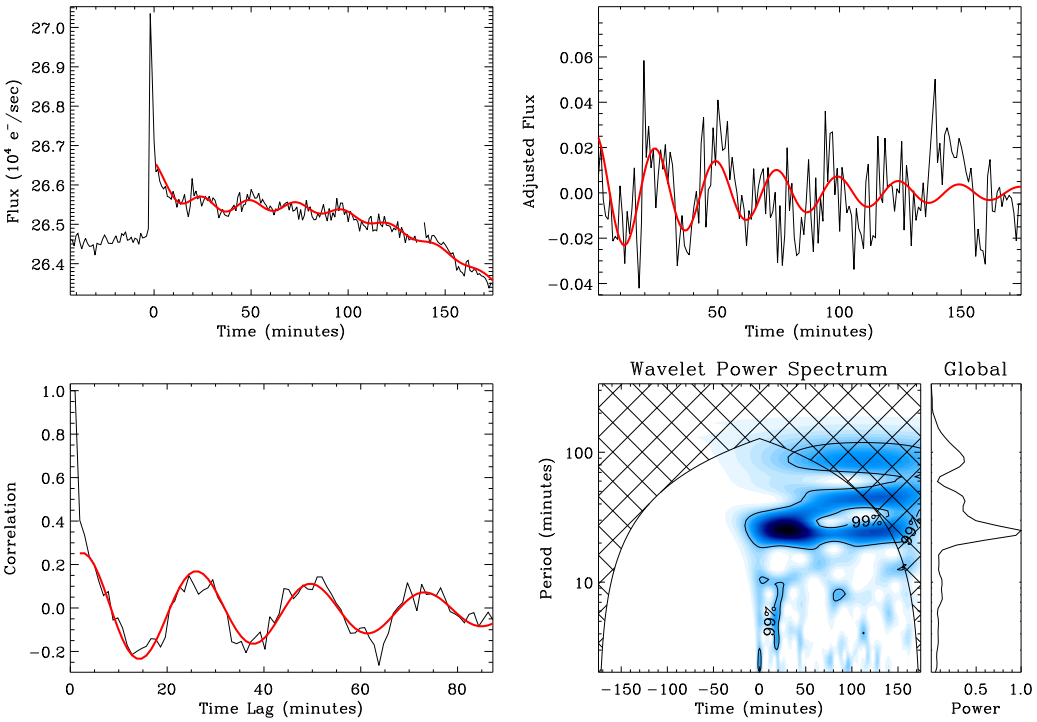

Figure A.53: KIC 9726699, start time (BJD): 55401.16.

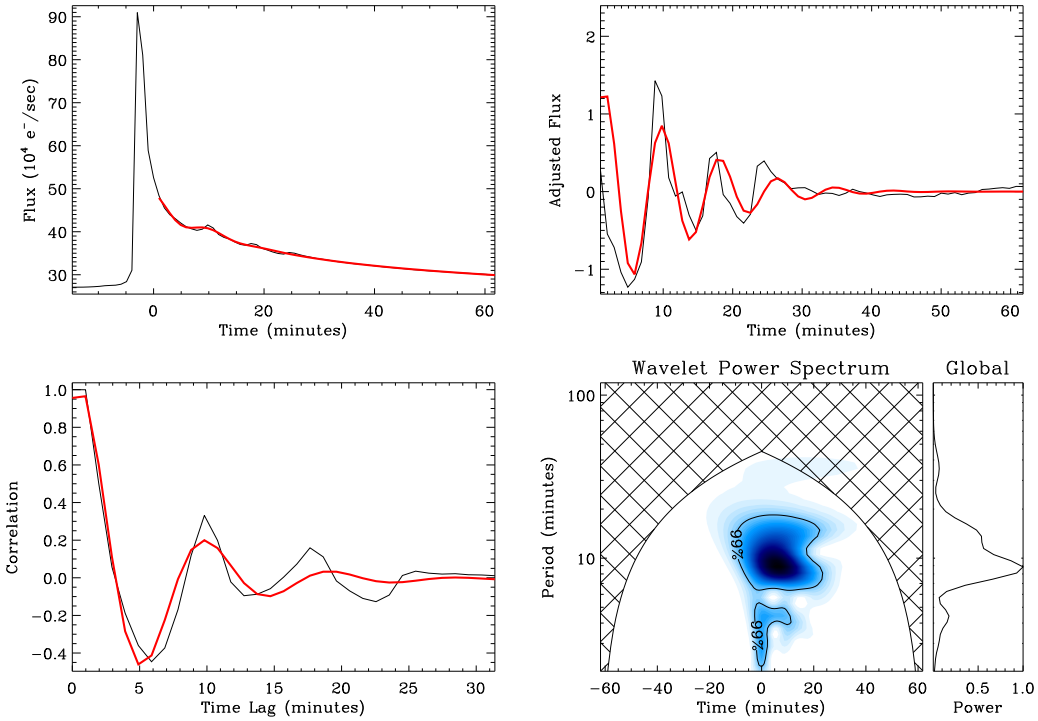

Figure A.54: KIC 9726699, start time (BJD): 55999.77.

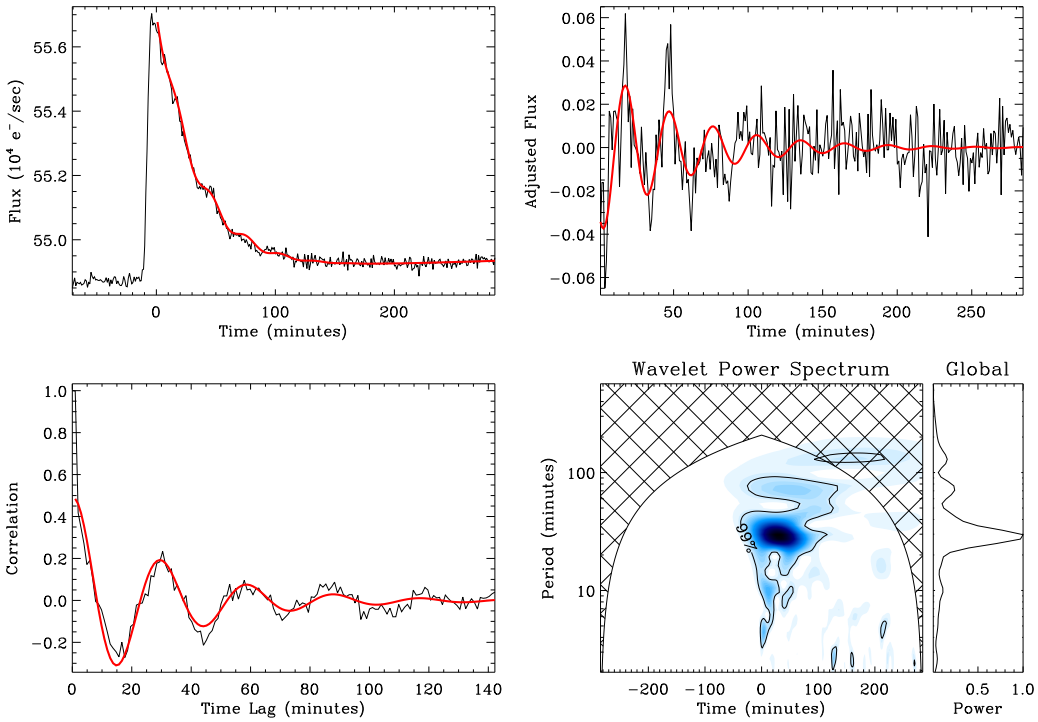

Figure A.55: KIC 9946017, start time (BJD): 55217.57.

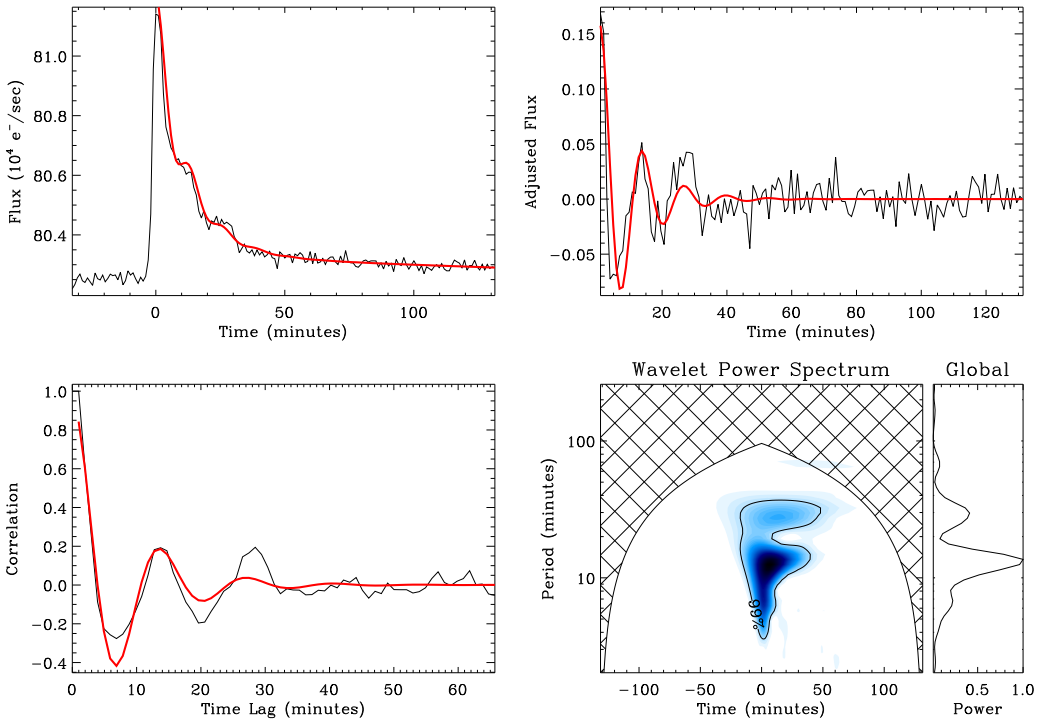

Figure A.56: KIC 10459987, start time (BJD): 55158.15.

Appendix B

Additional tables

B.1 Properties of quasi-periodic pulsations in solar flares from a single active region

The table in this section gives information about each of the flares included in the sample used for the study presented in Chapter 5.

Table B.1: Summary table of the 181 flares from the chosen active region. The first column contains a numerical label for each flare, the second and third columns are the flare start and end times (UT), the fourth column is the flare GOES class, the fifth the approximate position on the solar disk. The sixth column shows which instruments, other than GOES/XRS and EVE/ESP, observed the flare, where *R*, *F*, *N*, *V* correspond to RHESSI, *Fermi*/GBM, NoRH, and *Vernov*/DRGE respectively, and *(part)* indicates that only part of the flare was observed by that instrument. Finally, the seventh column contains references to other studies that include the flare.

Flare no.	Start time	End time	GOES class	Coordinates	Other instruments	References
001	2014-09-19 18:03	2014-09-19 19:52	C3.3	S10E84		
002	2014-09-20 12:44	2014-09-20 13:50	C1.1	S13E88	R(part), F(part)	
003	2014-09-20 17:10	2014-09-20 17:38	C1.1	S12E88	R(part), F(part)	
004	2014-09-21 01:46	2014-09-21 02:14	C1.2	S13E85	R, F, N	
005	2014-09-21 07:10	2014-09-21 07:43	C2.0	S12E78		
006	2014-09-22 19:28	2014-09-22 20:30	C1.6	S16E61		
007	2014-09-23 15:29	2014-09-23 15:44	C1.1	S14E47	F(part)	
008	2014-09-23 23:05	2014-09-24 00:20	M2.3	S14E32	R, F(part), N	1
009	2014-09-24 16:04	2014-09-24 16:18	C1.8	S13E23		
010	2014-09-24 17:48	2014-09-24 18:01	C7.0	S13E23	R, V	2
011	2014-09-25 19:20	2014-09-25 21:51	C3.2	S16E17	R(part), F(part)	
012	2014-09-26 03:54	2014-09-26 10:00	C8.7	S08E08	N(part)	
013	2014-09-26 13:53	2014-09-26 14:01	C4.2	S11E06	F	

Continued on next page

Table B.1 – *Continued from previous page*

Flare no.	Start time	End time	GOES class	Coordinates	Other instruments	References
014	2014-10-14 18:12	2014-10-14 19:01	M1.1	S12E88	F(part)	1
015	2014-10-14 19:07	2014-10-15 08:30	M2.2	S11E88		1
016	2014-10-16 07:34	2014-10-16 08:02	C7.7	S14E88	R(part)	
017	2014-10-16 08:38	2014-10-16 10:02	C6.4	S11E88	R(part), F(part)	
018	2014-10-16 13:01	2014-10-16 13:09	M4.3	S13E88	R(part), V	1,2
019	2014-10-16 18:04	2014-10-16 18:23	C2.0	S15E88	F	
020	2014-10-16 20:12	2014-10-16 21:14	C2.9	S13E88	R(part), F(part)	
021	2014-10-17 03:12	2014-10-17 03:45	C3.9	S17E87	R(part), N	2
022	2014-10-17 04:58	2014-10-17 05:48	C6.6	S15E88	F, N	2
023	2014-10-17 12:45	2014-10-17 13:11	C3.6	S13E88	R(part)	
024	2014-10-17 15:35	2014-10-17 15:46	C6.7	S13E75	R, F(part)	
025	2014-10-17 19:30	2014-10-17 19:42	C6.3	S13E72	F	
026	2014-10-17 20:45	2014-10-17 21:29	C2.3	S13E83	F(part)	
027	2014-10-18 00:55	2014-10-18 01:38	C5.0	S12E80	R, F(part), N	
028	2014-10-18 06:45	2014-10-18 07:00	C3.7	S13E68	F	
029	2014-10-18 07:02	2014-10-18 10:15	M1.6	S14E82	R(part), F(part)	1

Continued on next page

Table B.1 – *Continued from previous page*

Flare no.	Start time	End time	GOES class	Coordinates	Other instruments	References
030	2014-10-18 13:03	2014-10-18 13:36	C2.6	S14E66	R(part), F	
031	2014-10-18 14:23	2014-10-18 14:34	C1.7	S08E61		
032	2014-10-18 16:01	2014-10-18 16:13	C2.6	S12E69	F(part)	
033	2014-10-18 17:03	2014-10-18 17:10	C2.1	S12E69	R, F(part)	
034	2014-10-18 17:11	2014-10-18 17:47	C2.7	S11E68	R(part)	
035	2014-10-18 19:01	2014-10-18 19:53	C3.8	S16E66	F(part), V	2
036	2014-10-18 19:54	2014-10-18 20:35	C6.7	S07E58	R, F(part)	
037	2014-10-19 01:17	2014-10-19 03:42	C5.7	S12E65	R(part), F(part), N	
038	2014-10-19 04:00	2014-10-19 09:11	X1.1	S14E64	F(part), N(part)	1,2
039	2014-10-19 11:07	2014-10-19 11:49	C4.2	S12E57	R(part), F(part)	
040	2014-10-19 12:11	2014-10-19 12:42	C5.8	S12E57	R(part)	
041	2014-10-19 15:52	2014-10-19 16:18	C3.9	S16E52	R(part), F(part)	
042	2014-10-19 17:31	2014-10-19 17:49	C4.7	S12E52	R(part), F(part)	
043	2014-10-19 20:22	2014-10-19 20:45	C2.1	S13E50		
044	2014-10-20 00:51	2014-10-20 01:07	C2.5	S18E37	R(part)	
045	2014-10-20 02:00	2014-10-20 02:25	C2.8	S18E36	R, F, N	

Continued on next page

Table B.1 – *Continued from previous page*

Flare no.	Start time	End time	GOES class	Coordinates	Other instruments	References
046	2014-10-20 02:26	2014-10-20 02:49	C3.2	S15E43	R(part), F(part), N	
047	2014-10-20 03:31	2014-10-20 04:27	C5.4	S15E43	R, F(part), N	
048	2014-10-20 05:37	2014-10-20 06:17	C9.0	S12E46	R(part), N	
049	2014-10-20 09:01	2014-10-20 09:51	M3.9	S16E42	F(part)	1
050	2014-10-20 11:20	2014-10-20 11:33	C2.8	S11E44	R(part), F	
051	2014-10-20 13:58	2014-10-20 14:14	C2.7	S11E43	F(part)	
052	2014-10-20 14:41	2014-10-20 14:48	C3.1	S15E36	R, F	
053	2014-10-20 14:57	2014-10-20 15:59	C8.6	S14E40	R(part), F(part)	
054	2014-10-20 16:01	2014-10-20 17:38	M4.5	S14E39	R(part), F(part)	1
055	2014-10-20 18:44	2014-10-20 18:55	C6.2	S19E45		
056	2014-10-20 18:56	2014-10-20 19:09	M1.4	S15E46	R(part), F(part), V	1,2
057	2014-10-20 19:55	2014-10-20 21:05	M1.7	S14E36	R(part), F(part)	1,3
058	2014-10-20 22:45	2014-10-21 00:28	M1.2	S14E36	R(part), F(part), N(part)	1,3
059	2014-10-21 02:13	2014-10-21 02:35	C4.2	S10E36	R(part), F(part), N	
060	2014-10-21 06:01	2014-10-21 06:33	C5.7	S10E34	R(part), F(part), N	
061	2014-10-21 06:55	2014-10-21 07:13	C2.9	S14E27	R(part), F	

Continued on next page

Table B.1 – *Continued from previous page*

Flare no.	Start time	End time	GOES class	Coordinates	Other instruments	References
062	2014-10-21 08:09	2014-10-21 08:15	C3.1	S10E29	R, F	
063	2014-10-21 12:26	2014-10-21 12:34	C4.4	S18E36	R(part), F(part)	
064	2014-10-21 13:37	2014-10-21 13:42	M1.2	S14E35		1
065	2014-10-21 18:54	2014-10-21 19:56	C4.0	S13E23	R(part), F(part)	
066	2014-10-21 20:12	2014-10-21 21:00	C6.5	S20E30	R(part), F(part)	
067	2014-10-21 21:56	2014-10-21 22:44	C3.4	S16E21	R, F(part)	
068	2014-10-22 01:15	2014-10-22 04:44	M8.7	S13E21	R(part), F(part), N	1,4
069	2014-10-22 05:13	2014-10-22 05:42	M2.7	S15E14	F(part), N	1
070	2014-10-22 09:07	2014-10-22 09:49	C4.6	S16E12	R(part), F(part)	
071	2014-10-22 12:01	2014-10-22 12:58	C3.2	S18E13	R(part)	
072	2014-10-22 14:02	2014-10-22 15:50	X1.6	S14E13	R(part), F(part)	1,4,5,6,7
073	2014-10-22 16:54	2014-10-22 17:07	C5.7	S19E17	R(part)	
074	2014-10-23 04:16	2014-10-23 05:07	C3.7	S13E06	R(part), F, N	
075	2014-10-23 09:46	2014-10-23 10:14	M1.1	S16E03	F(part)	1
076	2014-10-23 15:02	2014-10-23 16:45	C4.6	S08W01	R(part), F(part)	
077	2014-10-23 17:42	2014-10-23 18:43	C5.9	S13W01	R(part), F(part)	

Continued on next page

Table B.1 – *Continued from previous page*

Flare no.	Start time	End time	GOES class	Coordinates	Other instruments	References
078	2014-10-23 19:13	2014-10-23 19:23	C3.3	S20E04	F(part)	
079	2014-10-24 02:35	2014-10-24 02:52	C4.2	S19W01	R, F, N	
080	2014-10-24 02:54	2014-10-24 03:24	C3.4	S20W02	R(part), F, N	
081	2014-10-24 03:56	2014-10-24 04:30	C3.6	S21W00	R, F(part), N	
082	2014-10-24 07:39	2014-10-24 08:31	M4.0	S19W05	R(part), F(part)	1,4
083	2014-10-24 09:53	2014-10-24 12:32	C3.6	S14W07	F(part)	
084	2014-10-24 14:47	2014-10-24 17:05	C5.1	S16W15	R(part), F(part)	
085	2014-10-24 20:46	2014-10-25 01:25	X3.1	S22W21	R(part), F(part)	1,5
086	2014-10-25 04:07	2014-10-25 04:25	C4.4	S09W07	R(part), F, N	
087	2014-10-25 07:22	2014-10-25 09:10	C9.2	S16W25	R(part), F(part)	
088	2014-10-25 09:44	2014-10-25 10:11	C4.6	S11W22	R(part)	
089	2014-10-25 12:14	2014-10-25 13:04	C3.2	S13W22	R(part), F	2
090	2014-10-25 14:57	2014-10-25 15:18	C5.1	S13W23	R, F(part)	8
091	2014-10-25 15:47	2014-10-25 16:24	C9.7	S13W23	R(part), F(part)	8
092	2014-10-25 16:35	2014-10-25 20:00	X1.0	S10W22	R(part), F(part)	1,8
093	2014-10-25 23:21	2014-10-26 00:06	C8.4	S13W28	R(part), F, N	

Continued on next page

Table B.1 – *Continued from previous page*

Flare no.	Start time	End time	GOES class	Coordinates	Other instruments	References
094	2014-10-26 01:10	2014-10-26 01:26	C3.1	S14W29	F(part), N	
095	2014-10-26 05:10	2014-10-26 05:37	C2.8	S13W30	R, F, N	
096	2014-10-26 05:42	2014-10-26 06:08	C4.0	S14W31	F, N	2
097	2014-10-26 06:09	2014-10-26 06:55	C9.5	S14W31	R(part), F(part), N(part)	
098	2014-10-26 10:35	2014-10-26 12:10	X2.0	S14W37	R(part), F(part)	1
099	2014-10-26 13:05	2014-10-26 13:54	C9.2	S13W35	R, F(part)	
100	2014-10-26 15:06	2014-10-26 15:52	C5.2	S16W42	R(part), F	
101	2014-10-26 15:52	2014-10-26 16:09	C3.5	S13W39	R	
102	2014-10-26 17:07	2014-10-26 17:46	M1.0	S13W38	R(part), F(part)	1
103	2014-10-26 17:56	2014-10-26 18:07	C7.8	S14W38	R, F(part)	
104	2014-10-26 18:08	2014-10-26 18:40	M4.2	S14W37	R(part), F	1
105	2014-10-26 18:41	2014-10-26 19:28	M1.9	S13W38	R(part)	1
106	2014-10-26 19:54	2014-10-26 21:35	M2.4	S15W45	R(part), F(part)	1
107	2014-10-26 21:45	2014-10-26 23:00	C8.3	S14W43	R(part), F(part)	
108	2014-10-27 00:03	2014-10-27 01:03	M7.1	S12W42	R(part), F(part), N	1,2,9
109	2014-10-27 01:45	2014-10-27 02:16	M1.0	S13W45	R, F(part), N	1,3

Continued on next page

Table B.1 – *Continued from previous page*

Flare no.	Start time	End time	GOES class	Coordinates	Other instruments	References
110	2014-10-27 03:34	2014-10-27 04:13	M1.3	S13W45	R(part), F(part), N	1,3
111	2014-10-27 05:02	2014-10-27 05:16	C3.4	S13W44	R, N	2
112	2014-10-27 05:21	2014-10-27 06:11	C4.9	S16W50	R(part), F, N	
113	2014-10-27 06:57	2014-10-27 07:12	C9.6	S14W46	R(part), F	
114	2014-10-27 07:12	2014-10-27 07:30	C9.6	S13W46	F	
115	2014-10-27 09:55	2014-10-27 11:05	M6.7	S15W51	R(part), F(part)	1
116	2014-10-27 14:05	2014-10-27 16:56	X2.0	S18W57	R(part)	1,2
117	2014-10-27 17:30	2014-10-27 18:20	M1.4	S21W51	R, F(part)	1
118	2014-10-27 21:18	2014-10-27 21:45	C5.4	S13W53	F	
119	2014-10-27 22:52	2014-10-27 23:30	C4.6	S13W54	F, N	
120	2014-10-28 02:02	2014-10-28 03:14	M3.4	S17W65	R(part), F(part)	1
121	2014-10-28 06:07	2014-10-28 06:37	C4.2	S11W56	R, N	
122	2014-10-28 08:21	2014-10-28 08:34	C6.5	S19W62	R(part), F	
123	2014-10-28 11:03	2014-10-28 11:21	C5.3	S15W61	R	
124	2014-10-28 13:55	2014-10-28 15:15	M1.6	S16W74	R	1
125	2014-10-29 03:11	2014-10-29 03:21	C3.3	S13W69	R, N	2

Continued on next page

Table B.1 – *Continued from previous page*

Flare no.	Start time	End time	GOES class	Coordinates	Other instruments	References
126	2014-10-29 03:31	2014-10-29 05:12	C8.4	S16W79	R(part), F(part), N	2
127	2014-10-29 06:04	2014-10-29 08:02	M1.0	S14W77	R(part), N(part)	1
128	2014-10-29 08:12	2014-10-29 09:22	C6.5	S19W62		
129	2014-10-29 09:54	2014-10-29 11:25	M1.2	S18W77	R(part), F(part)	1
130	2014-10-29 13:57	2014-10-29 14:07	C5.5	S14W75	R	
131	2014-10-29 14:25	2014-10-29 15:21	M1.4	S13W77	R(part), F(part)	1
132	2014-10-29 16:07	2014-10-29 17:03	M1.0	S14W82	F(part)	1
133	2014-10-29 18:49	2014-10-29 18:57	M1.3	S13W77	R	1,10
134	2014-10-29 19:32	2014-10-29 20:19	C6.8	S08W89	R(part), F(part)	10
135	2014-10-29 21:21	2014-10-29 21:44	M2.3	S09W88	R(part), F(part), V	1,2,10
136	2014-10-29 23:01	2014-10-29 23:16	C2.7	S14W86	R, F(part), N	2
137	2014-10-29 23:20	2014-10-29 23:35	C3.6	S14W88	R, N	
138	2014-10-29 23:40	2014-10-30 00:34	C7.1	S13W88	F(part), N	
139	2014-10-30 00:35	2014-10-30 01:00	M1.3	S14W81	R, F(part), N, V	1,2
140	2014-10-30 01:20	2014-10-30 03:40	M3.5	S14W88	R(part), F(part), N	1,3
141	2014-10-30 04:18	2014-10-30 05:15	M1.2	S08W89	R(part), F(part), N	1

Continued on next page

Table B.1 – *Continued from previous page*

Flare no.	Start time	End time	GOES class	Coordinates	Other instruments	References
142	2014-10-30 05:42	2014-10-30 05:53	C3.5	S14W88	R, N	
143	2014-10-30 12:38	2014-10-30 13:05	C2.9	S13W88	R(part), F(part)	
144	2014-10-30 15:19	2014-10-30 16:37	C9.7	S13W88	R(part), F(part)	
145	2014-10-31 00:32	2014-10-31 02:30	C8.2	S15W88	R(part), F(part), N	
146	2014-11-12 09:21	2014-11-12 09:35	C1.4	S13E88	F(part)	
147	2014-11-13 05:39	2014-11-13 06:30	C8.4	S10E80	F, N	
148	2014-11-13 19:20	2014-11-13 19:27	C1.4	S14E78	R	
149	2014-11-14 07:45	2014-11-14 08:35	C5.4	S12E77	R(part), F(part)	
150	2014-11-14 23:27	2014-11-15 00:20	C2.0	S11E67	R(part), F(part), N	
151	2014-11-15 06:11	2014-11-15 06:24	C1.1	S12E65	R, F(part), N	
152	2014-11-15 11:47	2014-11-15 13:20	M3.2	S11E62	R(part), F(part)	1
153	2014-11-15 20:41	2014-11-15 21:55	M3.7	S14E63		1
154	2014-11-15 23:31	2014-11-16 00:49	C2.7	S12E45	R(part), F(part), N	
155	2014-11-16 01:12	2014-11-16 01:28	C1.4	S10E45	R, F(part), N	
156	2014-11-16 07:29	2014-11-16 09:08	C3.9	S11E51	R(part), F(part)	
157	2014-11-16 09:09	2014-11-16 09:31	C2.0	S12E50	R, F(part)	

Continued on next page

Table B.1 – *Continued from previous page*

Flare no.	Start time	End time	GOES class	Coordinates	Other instruments	References
158	2014-11-16 10:00	2014-11-16 10:21	C2.4	S12E50	R(part)	
159	2014-11-16 13:40	2014-11-16 13:56	C1.5	S15E38	F(part)	
160	2014-11-16 16:41	2014-11-16 17:19	C3.9	S12E47	R(part)	
161	2014-11-16 17:35	2014-11-16 19:17	M5.7	S12E46	R(part), F(part)	1
162	2014-11-16 22:02	2014-11-16 22:16	C2.4	S12E43	F(part)	
163	2014-11-17 06:03	2014-11-17 06:11	C1.7	S16E43	R(part), N	
164	2014-11-17 18:20	2014-11-17 18:56	C1.6	S11E33	R(part), F(part)	
165	2014-11-18 08:02	2014-11-18 08:45	C1.8	S10E26	R(part)	
166	2014-11-18 14:15	2014-11-18 18:05	C1.9	S12E21		
167	2014-11-18 19:23	2014-11-18 19:45	C1.3	S12E05	R, F	
168	2014-11-19 18:57	2014-11-19 19:20	C2.4	S12E05	R, F	
169	2014-11-20 19:37	2014-11-20 20:50	C2.5	S12W08	R(part), F(part)	
170	2014-11-20 21:01	2014-11-20 22:00	C1.3	S12W27	F(part)	
171	2014-11-21 01:54	2014-11-21 02:39	C1.4	S11W13	F(part), N	
172	2014-11-21 04:44	2014-11-21 04:54	C1.9	S12W13	R, F, N	
173	2014-11-21 23:29	2014-11-21 23:45	C1.1	S13W20	R, F(part), N	

Continued on next page

Table B.1 – *Continued from previous page*

Flare no.	Start time	End time	GOES class	Coordinates	Other instruments	References
174	2014-11-22 00:08	2014-11-22 00:51	C2.3	S14W26	R(part), F(part), N	
175	2014-11-22 00:56	2014-11-22 02:35	C8.1	S12W25	R(part), F(part), N	
176	2014-11-22 03:36	2014-11-22 04:02	C2.4	S12W26	R(part), F(part), N	
177	2014-11-22 05:58	2014-11-22 06:34	C6.5	S13W23	R(part), F(part), N	
178	2014-11-22 09:51	2014-11-22 11:05	C1.5	S11W31	R(part), F(part)	
179	2014-11-22 13:22	2014-11-22 14:03	C2.1	S23W43	R(part)	
180	2014-11-22 17:09	2014-11-22 17:36	C3.1	S12W33	R(part), F(part)	
181	2014-11-23 05:30	2014-11-23 06:08	C2.4	S16W43	R, N	

References. (1) Inglis et al. (2016); (2) Myagkova et al. (2016); (3) Cho et al. (2016); (4) Kuhar et al. (2016); (5) Kuznetsov et al. (2016); (6) Bamba et al. (2017b); (7) Lee et al. (2017); (8) Bamba et al. (2017a); (9) Li et al. (2017); (10) Yurchyshyn et al. (2017).

B.2 Quasi-periodic pulsations in white-light flares observed with *Kepler*

The tables in this section contain all parameters for the fitted flare decay and QPP signal models for each of the flares studied in Chapter 6.

Table B.2: Flare decay fit parameters of the flares showing evidence of QPPs. The KIC number of the star is given along with the approximate time at which the flare occurs and the fit parameters, as described by Eqs. 6.2 and 6.3.

KIC	Time (Barycentric Julian Date)	Amplitude, A_0 (10^{-4} e$^-$/sec)	Decay time, t_0 (min)	B (10^{-4} e$^-$sec^{-1}min^{-1} or 10^{-4} e$^-$sec^{-1}min^{-2})	C (10^{-4} e$^-$/sec)	D (min)
2852961	55238.22	0.76	241.556	0.00	128.79	-
2852961	55240.27	7.96	460.718	0.00	127.25	-
3128488	54990.32	1.20	25.132	-4.84×10^{-4}	25.68	-
3540728	55751.38	0.15	4.547	2.23×10^{-6}	11.39	-283.47
3540728	55807.25	1.16	39.078	0.00	11.29	-
4671547	55090.04	0.52	18.065	0.00	38.61	-
4758595	56219.15	0.71	21.292	-5.58×10^{-4}	16.54	-
5475645	55095.92	0.23	27.553	-5.23×10^{-4}	37.81	-
5475645	56330.43	0.24	87.865	-2.81×10^{-5}	40.14	-
6184894	56243.87	0.07	28.996	3.87×10^{-7}	7.29	-228.22
6184894	56291.77	0.17	10.913	5.61×10^{-7}	7.34	-667.77
6437385	55391.10	0.71	152.034	-7.79×10^{-6}	38.84	-
6437385	55393.76	0.67	16.882	5.47×10^{-6}	37.69	-346.91
7664485	56107.70	0.05	79.561	-2.03×10^{-5}	5.73	-

Continued on next page

Table B.2 – *Continued from previous page*

KIC	Time	Amplitude	Decay time	B	C	D
7664485	56119.79	0.17	11.105	6.95×10^{-7}	5.72	-252.56
7885570	55010.88	0.28	20.804	-4.06×10^{-6}	32.32	-82.97
7940533	55317.42	0.22	47.852	0.00	10.10	-
8226464	55012.10	0.49	50.559	-5.95×10^{-4}	34.20	-
8414845	56217.91	0.09	46.991	-6.53×10^{-7}	6.28	-147.58
8414845	56285.43	0.08	118.071	3.20×10^{-7}	6.14	-601.68
8414845	56293.70	0.09	38.782	2.44×10^{-4}	6.12	-
8915957	55152.31	0.15	53.075	-7.52×10^{-5}	52.50	-
9641031	55614.55	3.70	19.189	-1.13×10^{-3}	309.36	-
9652680	55085.13	1.48	21.007	-1.34×10^{-6}	45.88	-89.16
9655129	56149.04	0.04	43.862	-7.25×10^{-5}	3.86	-
9726699	55382.78	1.02	11.445	-3.12×10^{-3}	27.36	-
9726699	55401.16	0.13	6.317	-9.19×10^{-6}	26.55	-37.87
9726699	55409.48	0.09	26.260	-5.26×10^{-6}	26.47	118.58
9726699	55749.56	0.48	14.658	-1.82×10^{-3}	26.57	-
9726699	55999.77	14.66	23.487	-1.38×10^{-2}	29.69	-

Continued on next page

Table B.2 – *Continued from previous page*

KIC	Time	Amplitude	Decay time	B	C	D
9726699	56082.84	0.37	5.486	-3.66×10^{-3}	26.21	-
9821078	55487.25	0.10	13.639	-3.91×10^{-5}	3.14	-
9946017	55217.57	0.79	36.529	1.73×10^{-4}	54.89	-
10206340	55076.74	1.97	128.953	-1.49×10^{-5}	60.20	-335.74
10459987	55158.15	0.72	12.437	-3.26×10^{-4}	80.33	-
10459987	56189.39	0.26	7.122	-8.09×10^{-4}	78.42	-
10528093	56214.53	0.07	59.488	0.00	4.84	-
10528093	56262.77	0.25	54.927	-4.33×10^{-5}	4.82	-
11551430	55004.60	1.04	34.201	-3.28×10^{-4}	85.27	-
11551430	55024.13	1.24	71.061	0.00	83.92	-
11551430	55031.05	2.71	63.622	0.00	85.21	-
11551430	55031.96	1.38	34.188	-4.11×10^{-4}	84.91	-
11551430	56117.13	0.71	135.828	-8.01×10^{-4}	79.85	-
11551430	56134.74	1.44	66.907	-5.11×10^{-4}	78.16	-
11551430	56166.63	1.39	55.898	-1.26×10^{-6}	79.69	-251.91
11551430	56208.35	3.94	50.695	-7.49×10^{-4}	79.84	-

Continued on next page

Table B.2 – *Continued from previous page*

KIC	Time	Amplitude	Decay time	B	C	D
11551430	56264.09	2.14	109.713	0.00	78.66	-
11551430	56270.75	6.29	40.643	-1.10×10^{-3}	79.68	-
11560431	56150.68	0.53	12.627	2.51×10^{-4}	202.90	-
11560431	56193.12	0.72	13.623	-1.32×10^{-3}	201.47	-
11560447	55947.44	3.84	4.803	-2.01×10^{-2}	72.76	-
11610797	54981.63	0.95	54.170	0.00	33.65	-
11665620	55762.95	0.17	17.923	4.49×10^{-6}	2.66	-188.60
12102573	55086.03	0.02	3.932	3.63×10^{-6}	23.03	-217.59
12156549	55287.92	0.08	111.846	3.66×10^{-5}	0.54	-
12156549	55347.20	0.06	66.821	0.00	0.52	-

Table B.3: QPP fit parameters of the 11 flares showing evidence of stable decaying oscillations. The KIC number of the star is given along with the approximate time at which the flare occurs and the fit parameters, as described by Eqs. 6.4 and 6.5.

KIC	Time (Barycentric Julian date)	Amplitude, A (10^{-4} e$^-$/sec)	Decay time, τ_e or τ_g (min)	B (min or min^{-2})	Period, P (min)	Phase, ϕ	Decay profile
2852961	55238.22	0.146 ± 0.006	27 ± 2	35 ± 2	67 ± 1	1.64 ± 0.08	Gaussian
3540728	55807.25	0.091 ± 0.003	14.4 ± 0.7	39.0 ± 0.4	37.1 ± 0.4	5.27 ± 0.08	Gaussian
5475645	55095.92	0.026 ± 0.005	9 ± 2	23 ± 2	16.2 ± 0.9	3.8 ± 0.6	Gaussian
6184894	56243.87	0.0051 ± 0.0008	59 ± 8	165 ± 14	57 ± 1	5.0 ± 0.5	Gaussian
6437385	55393.76	0.120 ± 0.002	26.5 ± 0.4	39.6 ± 0.7	40.9 ± 0.3	8.46 ± 0.04	Gaussian
9655129	56149.04	0.0026 ± 0.0003	57.5 ± 14.6	2 ± 6	78 ± 5	3.7 ± 0.3	Exponential
9655129	56149.04	0.0010 ± 0.0002	65.1 ± 36.5	-3 ± 12	32 ± 1	0.5 ± 0.4	Exponential
9726699	55401.16	0.030 ± 0.003	129 ± 34	-48 ± 14	24.2 ± 0.1	0.1 ± 0.1	Exponential
9726699	55999.77	2.261 ± 0.016	8.89 ± 0.05	-3.6 ± 0.1	10.93 ± 0.01	6.830 ± 0.006	Gaussian
9946017	55217.57	0.045 ± 0.002	54 ± 6	-6 ± 3	29.1 ± 0.4	2.6 ± 0.1	Exponential
10459987	55158.15	0.158 ± 0.009	10 ± 1	-0.1 ± 0.6	12.9 ± 0.3	6.2 ± 0.1	Exponential
12156549	55287.92	0.0103 ± 0.0004	36 ± 2	28 ± 2	44.6 ± 0.6	0.37 ± 0.07	Gaussian

Bibliography

Alfvén H., 1942, Nature, 150, 405

Anfinogentov S., Nakariakov V. M., Mathioudakis M., Van Doorsselaere T., Kowalski A. F., 2013, ApJ, 773, 156

Anglada-Escudé G., et al., 2016, Nature, 536, 437

Appourchaux T., 2003, A&A, 412, 903

Appourchaux T., 2004, A&A, 428, 1039

Armstrong D. J., Pugh C. E., Broomhall A., Brown D. J. A., Lund M. N., Osborn H. P., Pollacco D. L., 2016, MNRAS, 455, 3110

Asai A., Shimojo M., Isobe H., Morimoto T., Yokoyama T., Shibasaki K., Nakajima H., 2001, ApJ, 562, L103

Aschwanden M. J., Kliem B., Schwarz U., Kurths J., Dennis B. R., Schwartz R. A., 1998, ApJ, 505, 941

Aschwanden M. J., Nightingale R. W., Andries J., Goossens M., Van Doorsselaere T., 2003, ApJ, 598, 1375

Auchère F., Froment C., Bocchialini K., Buchlin E., Solomon J., 2016, ApJ, 825, 110

Aulanier G., Démoulin P., Schrijver C. J., Janvier M., Pariat E., Schmieder B., 2013, A&A, 549, A66

Balona L. A., 2015, MNRAS, 447, 2714

Balona L. A., Broomhall A.-M., Kosovichev A., Nakariakov V. M., Pugh C. E., Van Doorsselaere T., 2015, MNRAS, 450, 956

Bamba Y., Inoue S., Kusano K., Shiota D., 2017a, ApJ, 838, 134

Bamba Y., Lee K.-S., Imada S., Kusano K., 2017b, ApJ, 840, 116

Batalha N. M., et al., 2010, ApJ, 713, L109

Benz A. O., 2017, Living Reviews in Solar Physics, 14, 2

Borucki W. J., et al., 2010, Science, 327, 977

Brown J. C., 1971, Sol. Phys., 18, 489

Brown T. M., Latham D. W., Everett M. E., Esquerdo G. A., 2011, AJ, 142, 112

Bushby P., Mason J., 2004, Astronomy and Geophysics, 45, 4.07

Candelaresi S., Hillier A., Maehara H., Brandenburg A., Shibata K., 2014, ApJ, 792, 67

Cannon A. J., Pickering E. C., 1901, Annals of Harvard College Observatory, 28, 129

Cargill P. J., Mariska J. T., Antiochos S. K., 1995, ApJ, 439, 1034

Carmichael H., 1964, NASA Special Publication, 50, 451

Carrington R. C., 1859, MNRAS, 20, 13

Castelli F., Kurucz R. L., 2004, ArXiv Astrophysics e-prints,

Chabrier G., Baraffe I., 1997, A&A, 327, 1039

Chaplin W. J., Elsworth Y., Isaak G. R., Marchenkov K. I., Miller B. A., New R., Pinter B., Appourchaux T., 2002, MNRAS, 336, 979

Chen P. F., Priest E. R., 2006, Sol. Phys., 238, 313

Cho I.-H., Cho K.-S., Nakariakov V. M., Kim S., Kumar P., 2016, ApJ, 830, 110

Cuntz M., Saar S. H., Musielak Z. E., 2000, ApJ, 533, L151

Curtiss J. H., 1941, Ann. Math. Statist., 12, 409

Daubechies I., 1990, IEEE Transactions on Information Theory, 36, 961

Davenport J. R. A., 2016, ApJ, 829, 23

Davenport J. R. A., et al., 2014, ApJ, 797, 122

Davenport J. R. A., Hebb L., Hawley S. L., 2015, ApJ, 806, 212

Davenport J. R. A., Kipping D. M., Sasselov D., Matthews J. M., Cameron C., 2016, ApJ, 829, L31

De Moortel I., Nakariakov V. M., 2012, Philosophical Transactions of the Royal Society of London Series A, 370, 3193

De Moortel I., Munday S. A., Hood A. W., 2004, Sol. Phys., 222, 203

Degenaar N., Miller J. M., Kennea J., Gehrels N., Reynolds M. T., Wijnands R., 2013, ApJ, 769, 155

Dennis B. R., Zarro D. M., 1993, Sol. Phys., 146, 177

Dennis B. R., Tolbert A. K., Inglis A., Ireland J., Wang T., Holman G. D., Hayes L. A., Gallagher P. T., 2017, ApJ, 836, 84

Didkovsky L., Judge D., Wieman S., Woods T., Jones A., 2012, Sol. Phys., 275, 179

Dikpati M., Gilman P. A., 2007, New Journal of Physics, 9, 297

Dolla L., et al., 2012, ApJ, 749, L16

Dorman B., Nelson L. A., Chau W. Y., 1989, ApJ, 342, 1003

Doyle J. G., et al., 2018, MNRAS, 475, 2842

Drake J. F., Swisdak M., Che H., Shay M. A., 2006, Nature, 443, 553

Drake J. J., Cohen O., Garraffo C., Kashyap V., 2016, in Kosovichev A. G., Hawley S. L., Heinzel P., eds, IAU Symposium Vol. 320, Solar and Stellar Flares and their Effects on Planets. pp 196–201 (arXiv:1610.05185), doi:10.1017/S1743921316000260

Duncan R. C., 1998, ApJ, 498, L45

Farge M., 1992, Annual Review of Fluid Mechanics, 24, 395

Fárník F., Karlický M., Švestka Z., 2003, Sol. Phys., 218, 183

Fletcher L., Hudson H. S., 2008, ApJ, 675, 1645

Fletcher L., Hannah I. G., Hudson H. S., Metcalf T. R., 2007, ApJ, 656, 1187

Foullon C., Verwichte E., Nakariakov V. M., Fletcher L., 2005, A&A, 440, L59

Gallagher P. T., Moon Y.-J., Wang H., 2002, Sol. Phys., 209, 171

García R. A., Ceillier T., Mathur S., Salabert D., 2013, in Shibahashi H., Lynas-Gray A. E., eds, Astronomical Society of the Pacific Conference Series Vol. 479, Progress in Physics of the Sun and Stars: A New Era in Helio- and Asteroseismology. p. 129 (arXiv:1307.4163)

García R. A., et al., 2014, A&A, 572, A34

Gillon M., et al., 2017, Nature, 542, 456

Goddard C. R., Nisticò G., Nakariakov V. M., Zimovets I. V., 2016, A&A, 585, A137

Gopalswamy N., Mikić Z., Maia D., Alexander D., Cremades H., Kaufmann P., Tripathi D., Wang Y.-M., 2006, Space Sci. Rev., 123, 303

Gosling J. T., Hildner E., MacQueen R. M., Munro R. H., Poland A. I., Ross C. L., 1976, Sol. Phys., 48, 389

Green J. L., Boardsen S., 2006, Advances in Space Research, 38, 130

Green L. M., Kliem B., Wallace A. J., 2011, A&A, 526, A2

Gruber D., et al., 2011, A&A, 533, A61

Gryciuk M., Siarkowski M., Sylwester J., Gburek S., Podgorski P., Kepa A., Sylwester B., Mrozek T., 2017, Sol. Phys., 292, 77

Guidoni S. E., DeVore C. R., Karpen J. T., Lynch B. J., 2016, ApJ, 820, 60

Hambaryan V. V., Neuhäuser R., 2013, MNRAS, 430, 32

Hanser F. A., Sellers F. B., 1996, in Washwell E. R., ed., Proc. SPIEVol. 2812, GOES-8 and Beyond. pp 344–352, doi:10.1117/12.254082

Hathaway D. H., 2010, Living Reviews in Solar Physics, 7, 1

Hawley S. L., Fisher G. H., 1992, ApJS, 78, 565

Hawley S. L., et al., 1995, ApJ, 453, 464

Hawley S. L., et al., 2003, ApJ, 597, 535

Hayashi M. R., Shibata K., Matsumoto R., 1996, ApJ, 468, L37

Hayes L. A., Gallagher P. T., Dennis B. R., Ireland J., Inglis A. R., Ryan D. F., 2016, ApJ, 827, L30

Hayes L. A., Gallagher P. T., McCauley J., Dennis B. R., Ireland J., Inglis A., 2017, Journal of Geophysical Research (Space Physics), 122, 9841

Hermes J. J., et al., 2015, ApJ, 810, L5

Higgins P. A., Gallagher P. T., McAteer R. T. J., Bloomfield D. S., 2011, Advances in Space Research, 47, 2105

Hirayama T., 1974, Sol. Phys., 34, 323

Hodgson R., 1859, MNRAS, 20, 15

Hollands M. A., Gänsicke B. T., Koester D., 2015, MNRAS, 450, 681

Hood A. W., Ruderman M., Pascoe D. J., De Moortel I., Terradas J., Wright A. N., 2013, A&A, 551, A39

Horne J. H., Baliunas S. L., 1986, ApJ, 302, 757

Huang J., Tan B., Zhang Y., Karlický M., Mészárosová H., 2014, ApJ, 791, 44

Huber D., et al., 2014, ApJS, 211, 2

Hudson H. S., 1972, Sol. Phys., 24, 414

Hudson H. S., Wolfson C. J., Metcalf T. R., 2006, Sol. Phys., 234, 79

Huppenkothen D., et al., 2013, ApJ, 768, 87

Inglis A. R., Nakariakov V. M., 2009, A&A, 493, 259

Inglis A. R., Ireland J., Dominique M., 2015, ApJ, 798, 108

Inglis A. R., Ireland J., Dennis B. R., Hayes L., Gallagher P., 2016, ApJ, 833, 284

Ip W.-H., Kopp A., Hu J.-H., 2004, ApJ, 602, L53

Jiang C., Wu S. T., Yurchyshyn V., Wang H., Feng X., Hu Q., 2016, ApJ, 828, 62

Judge P. G., Tritschler A., Chye Low B., 2011, ApJ, 730, L4

Kahler S. W., 1992, ARA&A, 30, 113

Kane S. R., Kai K., Kosugi T., Enome S., Landecker P. B., McKenzie D. L., 1983, ApJ, 271, 376

Karoff C., et al., 2016, Nature Communications, 7, 11058

Karovska M., Schlegel E., Hack W., Raymond J. C., Wood B. E., 2005, ApJ, 623, L137

Khodachenko M. L., et al., 2007, Astrobiology, 7, 167

Kinemuchi K., Barclay T., Fanelli M., Pepper J., Still M., Howell S. B., 2012, PASP, 124, 963

Kliem B., Karlický M., Benz A. O., 2000, A&A, 360, 715

Koch D. G., et al., 2010, ApJ, 713, L79

Kolotkov D. Y., Nakariakov V. M., Kupriyanova E. G., Ratcliffe H., Shibasaki K., 2015, A&A, 574, A53

Kopp R. A., Pneuman G. W., 1976, Sol. Phys., 50, 85

Kowalski A. F., Hawley S. L., Hilton E. J., Becker A. C., West A. A., Bochanski J. J., Sesar B., 2009, AJ, 138, 633

Kretzschmar M., 2011, A&A, 530, A84

Krucker S., Hudson H. S., Jeffrey N. L. S., Battaglia M., Kontar E. P., Benz A. O., Csillaghy A., Lin R. P., 2011, ApJ, 739, 96

Kuhar M., Krucker S., Martínez Oliveros J. C., Battaglia M., Kleint L., Casadei D., Hudson H. S., 2016, ApJ, 816, 6

Kupriyanova E. G., Melnikov V. F., Nakariakov V. M., Shibasaki K., 2010, Sol. Phys., 267, 329

Kupriyanova E. G., Melnikov V. F., Shibasaki K., 2013, Sol. Phys., 284, 559

Kuznetsov S. A., Zimovets I. V., Morgachev A. S., Struminsky A. B., 2016, Sol. Phys., 291, 3385

Lammer H., et al., 2007, Astrobiology, 7, 185

Lecavelier des Etangs A., et al., 2012, A&A, 543, L4

Lee K.-S., Imada S., Watanabe K., Bamba Y., Brooks D. H., 2017, ApJ, 836, 150

Li D., Zhang Q. M., Huang Y., Ning Z. J., Su Y. N., 2017, A&A, 597, L4

Lingam M., Loeb A., 2017, ApJ, 848, 41

Lipa B., 1978, Sol. Phys., 57, 191

Liu K., Zhang J., Wang Y., Cheng X., 2013, ApJ, 768, 150

Liu Y., et al., 2014, Scientific Reports, 4, 3728

Liu L., et al., 2016, ApJ, 826, 119

Lockwood G. W., Skiff B. A., Henry G. W., Henry S., Radick R. R., Baliunas S. L., Donahue R. A., Soon W., 2007, ApJS, 171, 260

Lomb N. R., 1976, Ap&SS, 39, 447

Lu E. T., Hamilton R. J., McTiernan J. M., Bromund K. R., 1993, ApJ, 412, 841

Mackay D. H., Green L. M., van Ballegooijen A., 2011, ApJ, 729, 97

Maehara H., et al., 2012, Nature, 485, 478

Maehara H., Shibayama T., Notsu Y., Notsu S., Honda S., Nogami D., Shibata K., 2015, Earth, Planets, and Space, 67, 59

Martínez Oliveros J.-C., et al., 2012, ApJ, 753, L26

Masuda S., Kosugi T., Hara H., Tsuneta S., Ogawara Y., 1994, Nature, 371, 495

Mathioudakis M., Seiradakis J. H., Williams D. R., Avgoloupis S., Bloomfield D. S., McAteer R. T. J., 2003, A&A, 403, 1101

Mathur S., et al., 2014, A&A, 562, A124

Matthews S. A., van Driel-Gesztelyi L., Hudson H. S., Nitta N. V., 2003, A&A, 409, 1107

Matthews S. A., Harra L. K., Zharkov S., Green L. M., 2015, ApJ, 812, 35

McAteer R. T. J., Gallagher P. T., Ireland J., Young C. A., 2005, Sol. Phys., 228, 55

McAteer R. T. J., Young C. A., Ireland J., Gallagher P. T., 2007, ApJ, 662, 691

McAteer R. T. J., Aschwanden M. J., Dimitropoulou M., Georgoulis M. K., Pruessner G., Morales L., Ireland J., Abramenko V., 2016, Space Sci. Rev., 198, 217

McLaughlin J. A., Hood A. W., 2004, A&A, 420, 1129

McLaughlin J. A., De Moortel I., Hood A. W., Brady C. S., 2009, A&A, 493, 227

McLaughlin J. A., Thurgood J. O., MacTaggart D., 2012a, A&A, 548, A98

McLaughlin J. A., Verth G., Fedun V., Erdélyi R., 2012b, ApJ, 749, 30

McLaughlin J. A., Nakariakov V. M., Dominique M., Jelínek P., Takasao S., 2018, Space Sci. Rev., 214, 45

McQuillan A., Mazeh T., Aigrain S., 2014, ApJS, 211, 24

Meegan C., et al., 2009, ApJ, 702, 791

Mekhaldi F., et al., 2015, Nature Communications, 6, 8611

Metcalf T. R., Alexander D., Hudson H. S., Longcope D. W., 2003, ApJ, 595, 483

Mitra-Kraev U., Harra L. K., Williams D. R., Kraev E., 2005, A&A, 436, 1041

Miyake F., Nagaya K., Masuda K., Nakamura T., 2012, Nature, 486, 240

Miyake F., Masuda K., Nakamura T., 2013, Nature Communications, 4, 1748

Moore R. L., Sterling A. C., Hudson H. S., Lemen J. R., 2001, ApJ, 552, 833

Munro R. H., Gosling J. T., Hildner E., MacQueen R. M., Poland A. I., Ross C. L., 1979, Sol. Phys., 61, 201

Murray M. J., van Driel-Gesztelyi L., Baker D., 2009, A&A, 494, 329

Myagkova I. N., Bogomolov A. V., Kashapova L. K., Bogomolov V. V., Svertilov S. I., Panasyuk M. I., Kuznetsova E. A., Rozhkov G. V., 2016, Sol. Phys., 291, 3439

Nakajima H., et al., 1994, IEEE Proceedings, 82, 705

Nakariakov V. M., Melnikov V. F., 2009, Space Sci. Rev., 149, 119

Nakariakov V. M., Ofman L., 2001, A&A, 372, L53

Nakariakov V. M., Verwichte E., 2005, Living Reviews in Solar Physics, 2, 3

Nakariakov V. M., Zimovets I. V., 2011, ApJ, 730, L27

Nakariakov V. M., Foullon C., Verwichte E., Young N. P., 2006, A&A, 452, 343

Nakariakov V. M., Inglis A. R., Zimovets I. V., Foullon C., Verwichte E., Sych R., Myagkova I. N., 2010, Plasma Physics and Controlled Fusion, 52, 124009

Nakariakov V. M., Hornsey C., Melnikov V. F., 2012, ApJ, 761, 134

Nakariakov V. M., et al., 2016, Space Sci. Rev., 200, 75

Narain U., Ulmschneider P., 1990, Space Sci. Rev., 54, 377

Neupert W. M., 1968, ApJ, 153, L59

Notsu Y., Honda S., Maehara H., Notsu S., Shibayama T., Nogami D., Shibata K., 2015a, PASJ, 67, 32

Notsu Y., Honda S., Maehara H., Notsu S., Shibayama T., Nogami D., Shibata K., 2015b, PASJ, 67, 33

Ofman L., Aschwanden M. J., 2002, ApJ, 576, L153

Ofman L., Wang T., 2002, ApJ, 580, L85

Ohki K., Hudson H. S., 1975, Sol. Phys., 43, 405

Panesar N. K., Sterling A. C., Moore R. L., 2016, ApJ, 822, L23

Papadakis I. E., Lawrence A., 1993, MNRAS, 261, 612

Parenti S., 2014, Living Reviews in Solar Physics, 11, 1

Parks G. K., Winckler J. R., 1969, ApJ, 155, L117

Pascoe D. J., Nakariakov V. M., Arber T. D., 2007, A&A, 461, 1149

Pascoe D. J., Hood A. W., de Moortel I., Wright A. N., 2012, A&A, 539, A37

Pascoe D. J., Goddard C. R., Nisticò G., Anfinogentov S., Nakariakov V. M., 2016, A&A, 585, L6

Pavlov A. K., Blinov A. V., Konstantinov A. N., Ostryakov V. M., Vasilyev G. I., Vdovina M. A., Volkov P. A., 2013, MNRAS, 435, 2878

Payne C. H., 1925, PhD thesis, RADCLIFFE COLLEGE.

Pedersen M. G., Antoci V., Korhonen H., White T. R., Jessen-Hansen J., Lehtinen J., Nikbakhsh S., Viuho J., 2017, MNRAS, 466, 3060

Penn M., Krucker S., Hudson H., Jhabvala M., Jennings D., Lunsford A., Kaufmann P., 2016, ApJ, 819, L30

Pesnell W. D., Thompson B. J., Chamberlin P. C., 2012, Sol. Phys., 275, 3

Pettersen B. R., 1989, Sol. Phys., 121, 299

Pettersen B. R., Coleman L. A., Evans D. S., 1984, ApJS, 54, 375

Press W. H., Flannery B. P., Teukolsky S. A., 1986, Numerical Recipes: The Art of Scientific Computing. Cambridge University Press

Pugh C. E., Nakariakov V. M., Broomhall A.-M., 2015, ApJ, 813, L5

Pugh C. E., Armstrong D. J., Nakariakov V. M., Broomhall A.-M., 2016, MNRAS, 459, 3659

Pugh C. E., Broomhall A.-M., Nakariakov V. M., 2017a, A&A, 602, A47

Pugh C. E., Nakariakov V. M., Broomhall A.-M., Bogomolov A. V., Myagkova I. N., 2017b, A&A, 608, A101

Reid I. N., et al., 2004, AJ, 128, 463

Reznikova V. E., Shibasaki K., 2011, A&A, 525, A112

Riley K., Hobson M., Bence S., 2006, Mathematical Methods for Physics and Engineering: A Comprehensive Guide, 3rd ed edn. Cambridge University Press, https://books.google.co.uk/books?id=Mq1nlEKhNcsC

Rodono M., 1974, A&A, 32, 337

Rubenstein E. P., Schaefer B. E., 2000, ApJ, 529, 1031

Scargle J. D., 1982, ApJ, 263, 835

Schaefer B. E., King J. R., Deliyannis C. P., 2000, ApJ, 529, 1026

Scherrer P. H., et al., 2012, Sol. Phys., 275, 207

Schou J., et al., 2012, Sol. Phys., 275, 229

Segura A., Walkowicz L. M., Meadows V., Kasting J., Hawley S., 2010, Astrobiology, 10, 751

Severino G., 2017, The Structure and Evolution of the Sun. Springer International Publishing AG, doi:10.1007/978-3-319-64961-0

Shibata K., Magara T., 2011, Living Reviews in Solar Physics, 8, 6

Shibata K., Masuda S., Shimojo M., Hara H., Yokoyama T., Tsuneta S., Kosugi T., Ogawara Y., 1995, ApJ, 451, L83

Shibata K., et al., 2013, PASJ, 65, 49

Shibayama T., et al., 2013, ApJS, 209, 5

Simões P. J. A., Hudson H. S., Fletcher L., 2015, Sol. Phys., 290, 3625

Simões P. J. A., Kerr G. S., Fletcher L., Hudson H. S., Giménez de Castro C. G., Penn M., 2017, A&A, 605, A125

Simon T., Linsky J. L., Schiffer III F. H., 1980, ApJ, 239, 911

Skrutskie M. F., et al., 2006, AJ, 131, 1163

Smalley B., 2004, in Zverko J., Ziznovsky J., Adelman S. J., Weiss W. W., eds, IAU Symposium Vol. 224, The A-Star Puzzle. pp 131–138 (arXiv:astro-ph/0408222), doi:10.1017/S1743921304004478

Smith J. C., et al., 2012, PASP, 124, 1000

Solanki S. K., 2003, A&A Rev., 11, 153

Spruit H. C., 1982, Sol. Phys., 75, 3

Srivastava A. K., Lalitha S., Pandey J. C., 2013, ApJ, 778, L28

Steiner O., 2005, A&A, 430, 691

Stumpe M. C., et al., 2012, PASP, 124, 985

Sturrock P. A., 1966, Nature, 211, 695

Sun X., et al., 2015, ApJ, 804, L28

Takasao S., Shibata K., 2016, ApJ, 823, 150

Thalmann J. K., Su Y., Temmer M., Veronig A. M., 2015, ApJ, 801, L23

Thurgood J. O., Pontin D. I., McLaughlin J. A., 2017, ApJ, 844, 2

Toriumi S., Schrijver C. J., Harra L. K., Hudson H., Nagashima K., 2017, ApJ, 834, 56

Torrence C., Compo G. P., 1998, Bulletin of the American Meteorological Society, 79, 61

Van Ballegooijen A. A., Martens P. C. H., 1989, ApJ, 343, 971

Van Doorsselaere T., Nakariakov V. M., Verwichte E., 2007, A&A, 473, 959

Van Doorsselaere T., Nakariakov V. M., Young P. R., Verwichte E., 2008, A&A, 487, L17

Van Doorsselaere T., De Groof A., Zender J., Berghmans D., Goossens M., 2011, ApJ, 740, 90

Van Doorsselaere T., Kupriyanova E. G., Yuan D., 2016, Sol. Phys., 291, 3143

Van Doorsselaere T., Shariati H., Debosscher J., 2017, ApJS, 232, 26

Van Driel-Gesztelyi L., Green L. M., 2015, Living Reviews in Solar Physics, 12, 1

Van der Klis M., 1989, ARA&A, 27, 517

Vaughan S., 2005, A&A, 431, 391

Vernazza J. E., Avrett E. H., Loeser R., 1976, ApJS, 30, 1

Veronig A., Temmer M., Hanslmeier A., Otruba W., Messerotti M., 2002, A&A, 382, 1070

Vida K., Kővári Z., Pál A., Oláh K., Kriskovics L., 2017, ApJ, 841, 124

Walkowicz L. M., et al., 2011, AJ, 141, 50

Watanabe K., Krucker S., Hudson H., Shimizu T., Masuda S., Ichimoto K., 2010, ApJ, 715, 651

Webb D. F., Howard T. A., 2012, Living Reviews in Solar Physics, 9, 3

Welsh B. Y., et al., 2006, A&A, 458, 921

Willson R. C., Hudson H. S., 1988, Nature, 332, 810

Woods P. M., Kouveliotou C., Göğüş E., Finger M. H., Swank J., Smith D. A., Hurley K., Thompson C., 2001, ApJ, 552, 748

Woods T. N., et al., 2011, ApJ, 739, 59

Woods T. N., et al., 2012, Sol. Phys., 275, 115

Yashiro S., Gopalswamy N., Akiyama S., Michalek G., Howard R. A., 2005, Journal of Geophysical Research (Space Physics), 110, 12

Yurchyshyn V., Kumar P., Abramenko V., Xu Y., Goode P. R., Cho K.-S., Lim E.-K., 2017, ApJ, 838, 32

Zaitsev V. V., Stepanov A. V., 1982, Soviet Astronomy Letters, 8, 132

Zaitsev V. V., Stepanov A. V., 2008, Physics Uspekhi, 51, 1123

Zaitsev V. V., Stepanov A. V., Urpo S., Pohjolainen S., 1998, A&A, 337, 887

Zaitsev V. V., Kislyakov A. G., Stepanov A. V., Kliem B., Furst E., 2004, Astronomy Letters, 30, 319

Zweibel E. G., Yamada M., 2009, ARA&A, 47, 291